PONTIFICIA UNIVERSIDAD CATOLICA DE CHILE
SCHOOL OF ENGINEERING

TOWARD RESILIENT AND SUSTAINABLE COMMUNITIES: PERFORMANCE EVALUATION OF LIGHT FRAME TIMBER RESIDENTIAL STRUCTURES SUBJECTED TO SEISMIC AND HURRICANE HAZARDS

DIEGO NICOLAS VALDIVIESO CASCANTE

Thesis submitted to the Pontificia Universidad Católica de Chile and University of Colorado Boulder in partial fulfillment of the requirements for the Degree Doctor in Engineering Sciences and Doctor of Philosophy

Advisor:
ABBIE B. LIEL
PABLO GUINDOS BRETONES
DIEGO LOPEZ-GARCIA GONZALEZ

Santiago de Chile, April 2024

PONTIFICIA UNIVERSIDAD CATOLICA DE CHILE

SCHOOL OF ENGINEERING

TOWARD RESILIENT AND SUSTAINABLE COMMUNITIES: PERFORMANCE EVALUATION OF LIGHT FRAME TIMBER RESIDENTIAL STRUCTURES SUBJECTED TO SEISMIC AND HURRICANE HAZARDS

DIEGO NICOLÁS VALDIVIESO CASCANTE

Members of the Committee:

DIEGO LÓPEZ-GARCÍA

PABLO GUINDOS

ABBIE B. LIEL

JOSE LUIS ALMAZÁN

RODRIGO ASTROZA

PETER DECHENT

AMY JAVERNICK-WILL

WIL V. SRUBAR

YADRAN ETEROVIC

Thesis submitted to the Pontificia Universidad Católica de Chile and University of Colorado Boulder in partial fulfillment of the requirements for the Degree Doctor in Engineering Sciences and Doctor of Philosophy

Santiago of Chile, April, 2024

To my girlfriend Valeria, for her understanding and companionship throughout this journey, joining me in every new adventure that came my way.

To my beloved family, for being by my side throughout my life, supporting all my decisions, and providing the necessary support to successfully complete this segment of my life's journey.

To my friends from Chile, for all the moments of joy and support they have offered me throughout my doctoral journey.

To my cherished animal family, who have accompanied me in this challenge both in Chile and the United States, especially my dog Holley for her emotional support in the United States and for the joyful and not-so-joyful moments during our stay in the USA.

To my friends in the USA, for giving me all the support during my adventure in the USA, making my stay more enjoyable with all those moments of joy and laughter.

To my advisors in Chile and my advisor in the USA, for their great support and emotional guidance, and for the moments we shared (usually with one of them) eating ramen and looking forward to what the future holds.

I am grateful to each of my students over the past years; seeing their abilities transform as I have worked with them has filled me with joy and fuels my desire to continue and now conclude my doctoral journey, thinking about how I can transform future generations with the tools I have gained and will gain in the future.

I am thankful to my colleagues at Simpson Strong-Tie, both in Chile and the USA, for their support during the time I worked with them, both emotionally and financially, to successfully complete this work. I also thank the various companies involved in wood construction in Chile that supported the development of this thesis in one way or another, as well as the constant support from CENAMAD+CIM-UC, who welcomed me with open arms to pursue my doctoral studies at the center.

ACKNOWLEDGEMENTS

Financial support was provided by ANID (Doctorado Nacional 2018–21180074), VRI-UC, ANID BASAL FB210015 (CENAMAD), ANID FONDECYT #1201841 project, CORFO award 21SN-182547, and the National Science Foundation Awards #1901808 and #2207295. The opinions, findings, and conclusions presented in this thesis do not necessarily represent those of the funding institutions.

I express my profound gratitude to Professor Amy Javernick-Will, Professor Jose Luis Almazan, Luis Perez, Matias Alarcon, Raul Araya, Sebastian Carcamo, Juan Acevedo, Professor Franco Benedetti, Professor Alexander Opazo, Salvador Correa, Thomas Schussler, John Hindman, Jorge Lagos, Nicol Lopez, Jairo Montano, Bryan Palominos, Sergio Quezada, Esteban Reyes, Diego Quizanga, and the DICTUC team, each of whom played a vital role at different stages of this thesis.

Finally, I express my profound gratitude for the support from the private sector, which was instrumental to the success of my research project. Special thanks to Simpson Strong-Tie, Tecno Fast, Adyacente, Etex Group, Patagual Home, and E2E. I also acknowledge the support of the laboratories at Universidad Federico Santa Maria and Universidad del Bio Bio for their assistance with the testing campaign.

TABLE OF CONTENTS

LIST OF FIGURES

LIST OF TABLES

ABSTRACT

This thesis offers an in-depth analysis of the structural behavior and modeling of light-frame timber structures. Emphasis is placed on accurate modeling of the actual 3D behavior, as opposed to the typical simplified 2D modeling currently applied in practice. The main objective is to get a better understanding of the structural response against seismic and hurricane hazards in Chile and Puerto Rico, respectively. By such enhanced understanding the community resilience in these environmentally sensitive regions might be improved, and at the same time timber construction might become more competitive and viable as a sustainable alternative. Emphasizing sustainability, this research addresses the significant role of timber in reducing the housing deficit and curbing global greenhouse gas emissions.

More specifically, the 3D analysis of light-frame timber structures delves into their system effects, i.e., in-depth examination of the influence of the transverse shear walls, the out-of-plane bending stiffness of the diaphragms, and the gravity loads on wood-frame shear walls. It combines experimental and numerical methods to investigate the behavior of non-planar shear walls and the impact of finish layers (such as Type X gypsum wallboard used for fire protection) on the lateral response of planar shear walls. The findings highlight the need to refine current analytical and numerical models (mostly 2D models that ignore system effects) for safer and more effective designs under extreme lateral loading.

A key aspect of the research presented in this thesis is the evaluation of the vulnerability of informally constructed light-frame timber houses in Puerto Rico subjected to hurricanes. It proposes tailored mitigation strategies and employs a performance-based wind procedure to assess hurricane wind-related risks. The potential impacts of climate change are also considered.

This thesis integrates various aspects of timber building behavior under seismic and hurricane wind loads, challenging conventional design approaches and advocating for sustainable and socially responsible practices. The conclusions and recommendations set a path for developing robust, efficient, and sustainable building practices in areas prone to natural hazards. Future research is expected to expand on the system effects and finish layer effects to develop the information needed by practitioners and academics to fully consider such effects in the analysis of timber structures. Future research should also focus on developing comprehensive climate change models for multi-hazard risk assessment, thereby promoting resilience in vulnerable communities globally.

Keywords: System effects, Non-planar shear walls, Transverse shear walls, Out-of-plane bending stiffness of diaphragms, Wood frame construction, Light-frame timber buildings, Multi-layered, Gypsum wallboard, Structural vulnerability, Climate change scenarios, Earthquake hazard, Hurricane hazard, Wind engineering.

RESUMEN

Esta tesis ofrece un análisis profundo sobre el comportamiento estructural y la modelización de estructuras de entramado ligero de madera. Destaca la importancia de un modelado en 3D que refleje con precisión el comportamiento real, frente a las aproximaciones simplificadas en 2D comúnmente usadas en el ámbito profesional. El objetivo principal de esta tesis es profundizar en el entendimiento de las respuestas estructurales ante riesgos sísmicos y huracanados en Chile y Puerto Rico, respectivamente. Esta mayor comprensión podría potenciar la resiliencia de las comunidades en estas zonas ambientalmente sensibles, haciendo al mismo tiempo que la construcción con madera sea más competitiva y factible como opción sostenible en el tiempo. Centrándose en la sostenibilidad, este estudio subraya el importante papel de la madera en la disminución del déficit habitacional y en la reducción de las emisiones de gases de efecto invernadero a nivel mundial.

Más específicamente, el análisis 3D de estructuras de entramado ligero de madera examina los efectos de sistema, es decir, evalúa el efecto de los muros transversales en los muros no planares, la rigidez a la flexión fuera del plano de los diafragmas y las cargas gravitacionales sobre los muros de entramado ligero de madera. Esta tesis combina métodos experimentales y numéricos para investigar tanto el comportamiento de los efectos de sistema como el efecto de las capas no estructurales (como las placas de yeso Tipo X utilizadas para protección al fuego) en la respuesta lateral de los muros de entramado ligero de madera. Los hallazgos destacan la necesidad de refinar los modelos analíticos y numéricos actuales (principalmente modelos 2D que ignoran los efectos de sistema) para diseños más seguros y efectivos bajo cargas laterales extremas. Un aspecto clave de la investigación presentada en esta tesis es la evaluación de la vulnerabilidad de las casas de entramado ligero de madera construidas informalmente en Puerto Rico sujetas a vientos huracanados. Se sugieren medidas de mitigación específicas y se emplea una evaluación

basada en desempeño para evaluar los riesgos relacionados con los vientos huracanados. También se consideran los posibles impactos del cambio climático en la frecuencia e intensidad de los huracanes en la isla.

Esta tesis integra varios aspectos del comportamiento de los edificios de madera bajo cargas sísmicas y de vientos huracanados, desafiando los enfoques de diseño convencionales y abogando por prácticas sostenibles y socialmente responsables. Las conclusiones y recomendaciones establecen un camino para el desarrollo de prácticas de construcción robustas, eficientes y sostenibles en áreas propensas a amenazas naturales. Se espera que investigaciones futuras expandan sobre los efectos de sistema y los efectos de las capas no estructurales para desarrollar la información necesaria para que los profesionales y académicos consideren tales efectos en el análisis de estructuras de madera. Las investigaciones futuras también deberían centrarse en desarrollar modelos integrales de cambio climático para la evaluación del riesgo ante múltiples amenazas, promoviendo así la resiliencia en comunidades vulnerables a nivel global.

Palabras Claves: Efectos de sistema, Muros no planares, Muros transversales, Rigidez a la flexión fuera del plano de los diafragmas, Construcción de estructuras de madera, Edificios de entramado ligero madera, Multiples capas, Placa de yeso, Vulnerabilidad estructural, Escenarios de cambio climático, Peligro sísmico, Peligro de huracán, Ingeniería de viento.

1. INTRODUCTION

1.1. Overview

Timber structures have been extensively used in North America and Europe, but now they are also being increasingly promoted in rapidly developing countries of Latin America and the Caribbean. These regions include countries in which there are: a) very strong housing demands; and b) very significant natural hazards such as hurricanes and strong earthquakes. Hazard-induced disasters have caused economic losses in the tens of billions of U.S. dollars on a global scale since the 1990s (Botzen et al., 2019). Specifically, the loss of residential structures is particularly impactful for community recovery (Peacock et al., 2018), due to housing's critical role in maintaining social networks and providing a sense of normalcy and security, which are essential for the overall resilience and rebuilding of communities in the aftermath of disasters (Comerio, 1998; Fothergill & Peek, 2004; Viveiros & Sturtevant, 2014; Mukherji, 2017; Rivera-Crespo & Colón Rodríguez, 2021). Timber structures have the potential to improve the performance of residential homes. Timber structures are more sustainable than other alternatives, particularly the reinforced concrete and masonry commonly used in Latin America, in terms of embodied energy consumption, carbon sequestration, and recycling potential (Kremer & Symmons, 2015), recognizing that the construction industry is one of the largest contributors to greenhouse gas emissions (Mao et al., 2013). Nevertheless, enhancing disaster resilience within the residential building sector involves adopting sustainable building practices and materials that not only reduce emissions but also ensuring structures are better equipped to withstand future hazard events. This dissertation aims to provide a deep understanding of the structural response of light-frame timber structures considering Chilean and Puerto Rican challenges for the development of resilient structures under earthquake and hurricane hazard events, respectively. Resilience here refers to "the degree to which the social system is capable of organizing itself to increase the capacity for learning from past disasters for better future protection and to improve risk reduction measures" (UNISDR, 2005).

Light Frame Timber Building (LFTB) is one of the new structural systems currently evaluated by the Chilean construction industry, public authorities, and academia to enhance the sustainability of the Chilean mid-rise building inventory. Industrialized timber construction can contribute significantly to sustainability and resilience goals. At present, however, LFTBs in Chile do not have more than 4 stories due to restrictive seismic design standards. In addition, the configuration of residential buildings in Chile is different from configurations found in other countries (Estrella, Guindos, et al., 2021; Berwart et al., 2022). The key difference is the Chilean buildings' floor plan pattern referred to in the literature as the "fish-bone" pattern (Westenenk et al., 2013; Ugalde & Lopez-Garcia, 2020), where strong wood-frame shear walls (Estrella et al., 2020) and floor/roof diaphragms are used as both lateral- and gravitational-load resisting system. In highly seismic-prone areas, such as Chile, it is essential to design resilient LFTBs with adequate structural and non-structural components to limit damage and repair costs after earthquake events. However, LFTBs have typically been analyzed considering analytical/numerical models based on isolated 2D assemblies (Leung et al., 2010; Pei & van de Lindt, 2011; W. Pang & Hassanzadeh Shirazi, 2013; S. I. Carcamo, 2017; S. Carcamo et al., 2018; M. M. Bagheri, 2018; M. Bagheri et al., 2019; AWC, 2021), which strongly limits the understanding of the real lateral behavior. Among other shortcomings, such analytical/numerical models consider neither the presence of multiple finish layers such as gypsum wallboard, nor the potential reduction of overturning due to the effects of the transverse shear walls, nor the out-of-plane bending stiffness of the diaphragms in non-planar shear wall configurations (i.e., L-, T-, or U-shaped shear walls). As a result, wood-frame shear walls are designed with a strong configuration, featuring framing members and sturdy end studs supported by conventional hold-down devices or a continuous rod system. They utilize wood structural panels, typically oriented strand board, on both sides, with closely spaced nails for secure attachment. Additionally, these walls often include one or two layers of type X gypsum wallboard for fire protection, fastened through the sheathing to the framing (see Figure 4.1).

This dissertation investigates experimentally and numerically the effects of the transverse shear walls, the out-of-plane bending stiffness of the diaphragms and the gravity load on non-planar shear walls (**Chapters 2 and 3**), and the contribution of Type X GWB layers to the lateral response of planar multi-layered shear walls (**Chapters 4 and 5**) in LFTBs with strong shear walls. The goal is to enhance 3D understanding of the lateral behavior of LFTBs and, in doing so, contribute to the development of more accurate analytical/numerical models that will provide practicing engineers with the ability to accurately predict story drift demands, force demands, and seismic performance. Such refined models are essential to support the increased development of resilient buildings through cost-effective structural design. The analysis approach adopted in this thesis focuses on buildings with high wall density used for mid-rise residential construction in Chile.

Another hazard event with major consequences beyond earthquakes are tropical hurricanes. Hurricanes are climate-related hazard events that affect housing through the compromise of structural integrity and induction of economic losses due to damage to both the building's structure and contents as the envelope fails (Ellingwood et al., 2004; Talbot et al., 2022; Vickery, Quayyum, et al., 2023). These events disproportionately affect resource-limited communities (Rivera-Crespo & Colón Rodríguez, 2021; Talbot et al., 2022). Puerto Rico is one hazard prone area where much of the population lives in informally-constructed light-frame timber houses. Previous research (Hinojosa & Meléndez, 2018; Cruzado & Pacheco-Crosetti, 2018; Goldwyn, Javernick-Will, & Liel, 2022; Goldwyn, Vega, et al., 2022; Goldwyn, Javernick-Will, Liel, & Koschmann, 2022; Murray et al., 2023) has shown that informally-constructed housing is potentially vulnerable to both hurricane and earthquake events, but such vulnerability varies widely depending on housing characteristics. This study aims to support resilient informally-constructed light-frame timber houses subjected to hurricane winds for current and future climate change scenarios in Puerto Rico by proposing, evaluating, and prioritizing accessible and cost-effective mitigation strategies for wind hazards that are consistent with community needs (**Chapter 6**). Performance is assessed through a component-based static wind procedure, supported by component testing, and quantified in terms of the lifetime risk of wind-related roof or wall failure. For the development of resilient informally-constructed housing, it is necessary to consider the available resources, risk perceptions, and construction knowledge of households and builders, as these factors determine design and construction choices that may enhance or reduce the community resilience. This holistic approach, which also accounts for the social feasibility of lateral strengthening, is expected to bring the theoretical understanding gained by this research into the real world application.

1.2. Dissertation Organization and Research Questions

This dissertation adopts a paper-based format. **Chapters 2** to **6** present 5 journal articles (one journal article per chapter) that describe the research generated by this thesis. Table 1.1 provides an overview of the publication status, identified research gaps, research questions, and methodologies of the journal articles presented in each chapter. The overarching motivation for all chapters is to gain a comprehensive understanding of the behavior of light frame timber buildings under seismic and hurricane wind loads, which is crucial for fostering resilient and sustainable communities in Chile and Puerto Rico. The key contributions of this dissertation and the main conclusions of each chapter are covered in **Chapter 7**. Additionally, **Appendix A** features a co-authored journal article that addresses the quest for resilient light-frame timber buildings under seismic conditions, focusing on the use of cost-effective frictional isolation devices. **Appendix B** contains a compilation of abstracts of conference papers that were generated from this research (links to those papers are also provided). **Appendix C** and **D** offer supplementary information about the discoveries presented in this dissertation related to the work developed in Puerto Rico.

Table 1.1. Summary of gaps, questions, methods, and submission status for each chapter

Gaps/Needs	Research Question (s)	Methodology	Supporting Information
Chapter 2. Valdivieso, D., Almazan, J.L, Lopez-Garcia, D. , Montano, J., Liel, A., & Guindos, P. (2024). System effects in T-shaped timber shear walls: effects of transverse walls, diaphragms, and axial loading. *Earthquake Engineering & Structural Dynamics*. https://doi.org/10.1002/eqe.4125			
Scarce experimental and numerical data on system effects in non-planar wood-frame shear walls. Need for specific details on the connections between perpendicular walls.	(i) How significant is the contribution of system effects to the lateral response of wood-frame shear walls?	Experimental and numerical evaluation of two potential options for wall-to-wall perpendicular connections, as well as of the lateral response of both a planar and a T-shaped wood-frame shear wall.	

Gaps/Needs	Research Question (s)	Methodology	Supporting Information
Chapter 3. Valdivieso, D., Quizanga, D., Almazan, J.L, Guindos, P., Lopez-Garcia, D. , Liel, A., Lopez, N., & Hernandez, F. (Under Review). Shake table testing for system effects analysis in a 1:2 scale three-story light frame timber building. *Earthquake Spectra,* resubmitted 02/24.			
Insufficient experimental data exists to develop a better understanding and modeling techniques for the complex interactions and effects observed in light-frame timber buildings, particularly in those designed for large seismic loads.	(i) How significant is the influence of system effects on the dynamic properties of light frame timber buildings? (ii) What do system effects mean for design implications? (iii) How effectively does the current analytical model, which relies on isolated stacked planar shear walls, represent the lateral behavior of multi-layered wood-frame shear walls?	Shake table tests and numerical analyses of light-frame timber buildings that have U- and L-shaped non-planar shear walls. Evaluation of system effects and of potential enhancements to existing numerical models.	Appendix A. *Shaking table test of a timber building equipped with a novel cost-effective, impact-resilient seismic isolation system.*

Gaps/Needs	Research Question (s)	Methodology	Supporting Information
Chapter 4. Valdivieso, D., Guindos, P., Montaño, J., & Lopez-Garcia, D. (2023). Experimental investigation of multi-layered strong wood-frame shear walls with nonstructural Type X gypsum wallboard layers under cyclic load. *Engineering Structures*, 282, 115797. https://doi.org/10.1016/j.engstruct.2023.115797			
Lack of experimental and numerical evidence on how finish layers, used for fire protection, influence the lateral response of wood-frame strong shear walls.	(i) What is the influence of Type X finish layers used for fire protection on the lateral response of multi-layered strong wood-frame shear walls? (ii) How effectively does the current analytical model represent the lateral behavior of multi-layered wood-frame shear walls?	Investigation of multi-layered wood-frame shear walls with Type X GWB finish layers through connection-level and full-scale monotonic/cyclic testing. Comparison of numerical and analytical predictions with test data.	

Gaps/Needs	Research Question (s)	Methodology	Supporting Information
Chapter 5. Valdivieso, D., Lopez-Garcia, D., Liel, A., & Guindos, P. (Under Review). Reinforcement effects and parametric study of the lateral response of multi-layered wood-frame shear walls: an experimental and numerical investigation. *Journal of Structural Engineering,* Submitted 06/23.			
The reinforcing effect of finish layers, intended for fire protection, on wood frame strong shear walls remains unexplored, both experimentally and numerically. Furthermore, there is an absence of numerical and experimental data to assess the variables controlling the response of multi-layered strong shear walls, which is crucial for developing design guidelines for engineering practitioners.	(i) What is the reinforcement effect of deeply fastened Type X GWB on the cyclic lateral performance of strong shear walls? (ii) How do various parameters such as wall aspect ratio, number of Type X GWB layers, multi-layered connection type, and overturning anchorage systems, influence the performance of multi-layered strong shear walls? (iii) How effectively does the current analytical model represent the lateral behavior of multi-layered wood-frame shear walls?	Experimental (monotonic and cyclic) tests and numerical simulations to assess the reinforcement effect of finish layers on multi-layered strong shear walls, including a parametric analysis.	

Gaps/Needs	Research Question (s)	Methodology	Supporting Information
Chapter 6. Valdivieso, D., Liel, A., Javernick-Will, A., Goldwyn, B., Lopez-Garcia, D., & Guindos, P. (under review). Potential for Mitigating Hurricane Wind Impact on Informally-Constructed Homes in Puerto Rico under Current and Future Climate Scenarios. *International Journal of Disaster Risk Reduction.* Submitted 03/24.			
Exploring community-engaged mitigation strategies to bolster the resilience and sustainability of informally constructed light-frame timber houses in Puerto Rico against hurricane winds stands as a critical area for research. This inquiry should integrate considerations of climate change and existing building practices to offer comprehensive solutions.	(i) What are the mitigation measures necessary for the reduction of damage due hurricanes in informally constructed houses? (ii) Are these mitigation measures feasible for Puerto Ricans? (iii) What is the annual failure probability of informally constructed houses before and after mitigation measures? (iv) Are these values acceptable, according to building codes and standards? What is the potential impact of climate change on these risks?	Reliability analysis through a component-based performance-based wind engineering assessment of informally constructed light frame timber house typologies under current and projected climate conditions.	Appendix C. *Questionnaire used in interviews with local NGO builders and hardware store employees to identify barriers in implementing proposed mitigation measures.(English).* Appendix D. *Workshop Documentation*

2. CHAPTER 2 - SYSTEM EFFECTS IN T-SHAPED TIMBER SHEAR WALLS: EFFECTS OF TRANSVERSE WALLS, DIAPHRAGMS, AND AXIAL LOADING

2.1. Introduction

The lateral configuration of timber buildings is based on the fundamental principle that shear walls (SWs) are the only structural members that take lateral forces. SWs take in-plane lateral forces only (i.e., planar SWs), and the lateral strength and stiffness of each SW are not influenced by any other structural member (i.e., the lateral response of each SW is independent of the remaining structure). This concept is advocated in the design methodologies outlined by the "Special Design Provisions for Wind and Seismic" SDPWS (AWC, 2021) and by Eurocode 5 (EN, 2004): "Design of timber structures". While this traditional assumption had limited implications in the past for the design of low-rise structures, it may significantly affect the design of contemporary and future mid- and high-rise timber buildings. Notably, tests conducted on multistory timber buildings have revealed that the actual lateral stiffness of timber structures might exceed the theoretical stiffness (Paevere, 2002; Collins et al., 2005b; van de Lindt, Pei, Pryor, et al., 2010; Winkel & Smith, 2010; Tomasi et al., 2015). This stiffness may be due to gypsum wallboards and facade finishes (Filiatrault et al., 2002; Uang & Gatto, 2003; Chen et al., 2016; Valdivieso, Guindos, et al., 2023), and system (coupling) effects due to other structural members (Paevere, 2002; Collins et al., 2005b; van de Lindt, Pei, Pryor, et al., 2010; Winkel & Smith, 2010; Pei & van de Lindt, 2011; Tomasi et al., 2015). System effects refer here to interactions of planar SW with other structural assemblies that cause its behavior to deviate from the theoretical behavior of an isolated, cantilever planar assembly. In reality, the ability of SWs to bend freely is constrained at least by transverse shear walls (TSWs), by out-of-plane flexural (F) stiffness of diaphragms (DIA) or FDIA, and by axial loading (AXL). TSWs cause stiffening and strengthening effects because they have some resistance to non-planar loading and because they restrain planar SWs from uplifting. The extent of this influence depends on the stiffness of the connection between SWs and TSWs (i.e., SW-to-TSWs connection). FDIA, which results from the connection between the SWs and the diaphragms above, further restricts uplift through out-of-plane flexural stiffness. The gravitational load on the SWs restricts uplift too, thus enhancing shear stiffness and possibly generating other beneficial effects. These considerations, however, are entirely neglected in the light frame timber building (LFTB) structural typology. The impact of these system effects becomes even more significant when considering that they not only increase structural stiffness, but also potentially alter the kinematics of the buildings, including overturning. The design of LFTBs considering cumulative deformations due to bending and rocking, as presented by Leung et al. (2010), might indicate that the structure is excessively flexible. Counterintuitively, this approach may result in non-conservative designs because seismic design forces might be underestimated. On the other hand, gross overestimations of uplift might greatly increase the cost of anchorage systems, which ultimately leads to inefficient structural designs. Despite several studies highlighting the potential impact of system effects on the design of timber structures (discussed in the subsequent section), this aspect has received limited attention in practical investigations, particularly in terms of experimental analysis. The scarcity of research may be attributed to the challenges associated with reliable testing and measurement of these effects, as well as with difficult integration into practical design considerations (Benedetti et al., 2022). This study aims to contribute to this field by conducting experimental tests on T-shaped wood-frame SW assemblies, with and without diaphragms. The investigated assembly comprises a combination of a T-shaped SW and a planar SW, allowing for separate evaluation of the contributions made by perpendicular walls and diaphragms. Moreover, the potential effects of axial loading in multistory buildings are also investigated. This research focuses on system effects in LFTBs.

2.2. Relation to previous research

This section provides a comprehensive review of the current state of knowledge regarding the coupling effects of TSWs, FDIA, and AXL.

2.2.1. Previous research on the influence of TSWs

A better understanding of TSWs in non-planar SWs assemblies has been identified as critical to the lateral behavior of LFTBs (McDowall, 1984; Boughton, 1988; G. Foliente, 1995; Seible et al., 1999; Pei & van de Lindt, 2011; Benedetti et al., 2022). Experimental evaluations have been conducted to characterize the mechanical properties of both conventional wood-frame TSWs (Sugiyama & Isono, 1983; Suzuki, 1990; J. Dolan & Heine, 1997; Kochkin & McKee, 2001) and transverse partition walls (J. Dolan & Heine, 1997; Kochkin & McKee, 2001; Hopkins et al., 2014). Here, conventional SWs is a term coined by (Estrella et al., 2020) to indicate SWs usually used in low-rise buildings. However, these previous studies primarily examined if wood-frame TSWs could replace anchorage hardware (e.g., hold-downs) for restraining planar SW overturning, without extensively analyzing their impact on wood-frame SWs' lateral behavior. Results indicate that wood-frame TSWs can enhance the racking stiffness of a planar wood-frame SW, eliminating the need for hold-downs. Additionally, experiments with double T-shaped partition walls revealed increments in peak strength (up to 16%), elastic stiffness (up to 54%), and residual capacity with respect to those of planar partition walls (Hopkins et al., 2014). In Collins et al. (2005a) and G. Foliente et al. (2000), an experimental study on an L-shaped wood-frame house demonstrated significant load sharing among structural components, primarily attributed to transverse end walls and the roof system (i.e., system effects). Furthermore, Collins et al. (2005a) and G. Foliente et al. (2000) noted that the load-sharing behavior under elastic conditions is sensitive to the details of the connection between the walls (i.e., SW-to-TSW connection) and the roof system. However, contrary to previous studies (Sugiyama & Isono, 1983; Suzuki, 1990; J. Dolan & Heine, 1997; Kochkin & McKee, 2001), the numerical study from Collins et al. (2005a), Collins et al. (2005b) and G. Foliente et al. (2000) concluded that TSWs do not impact the hysteretic response of conventional SWs (G. Foliente et al., 2000; Collins et al., 2005a, 2005b). In Girhammar and Källsner (2008), an analytical procedure to quantify the tying-down effect of wood-frame TSWs on the load-carrying capacity of partially anchored conventional wood-frame

SWs was proposed, revealing that TSWs can enhance the lateral in-plane load-carrying capacity of SWs. The extent of improvement diminishes with decreasing wall aspect ratio (e.g., up to a 100% increase for SWs with a 1:2 aspect ratio and up to a 32% increase for SWs with a 1:0.5 aspect ratio). However, this procedure solely considered the uplift strength and stiffness of wood-frame TSWs, disregarding the out-of-plane strength and stiffness. Hence, additional experimental investigations remain necessary, particularly on strong wood-frame SWs (Guinez et al., 2019; Estrella et al., 2020; Estrella, Malek, et al., 2021) that are crucial for multistory LFTBs. Apart from kinematics that are different from that of conventional SWs, strong SWs also tend to be subjected to greater axial loading (Guinez et al., 2019; Estrella et al., 2020; Estrella, Malek, et al., 2021), and are therefore more susceptible to potential influences of axial loading. In this regard, Benedetti et al. (2022) presented an initial approach to evaluate the system effect of strong wood-frame SWs with axial loading using a refined numerical model. The study revealed that the relevance of the rocking component of the lateral response of SWs diminishes due to the influence of TSWs, underscoring the importance of considering the TSW effect in design practices. However, such effects cannot be adequately evaluated using two-dimensional or simplified models (Benedetti et al., 2022). Thus, there is a lack of knowledge on the cyclic behavior of strong wood-frame non-planar SWs that are typically required in mid-rise multistory buildings. In addition, studies primarily focused on cross-laminated timber (CLT) structures, which have higher out-of-plane stiffness than conventional wood frame SWs, have examined the impact of TSWs on the lateral behavior of CLT SWs (Stoner, 2020; E. Ruggeri et al., 2022). Numerical analyses by E. Ruggeri et al. (2022) highlighted the substantial contribution of CLT TSWs, leading to higher rocking stiffness (up to 75%) and lateral capacity (up to 100%) and thereby altering the rocking behavior of CLT SWs. The TSW's effect in CLT SWs is influenced by factors such as the TSW location, the SW-to-TSW connection, and the presence of hold-downs (Stoner, 2020; E. Ruggeri et al., 2022). These findings may underscore the significance of stiff connections between TSWs and planar SWs to effectively consider them as a system to restrain uplift forces. E. Ruggeri et al. (2022) emphasized the need for experimental validation to gain a deeper understanding of the interaction mechanism between TSWs and SWs. Hence, research on the TSWs effect and the role of the SW-to-TSW connection are rather necessary for any timber structural system.

2.2.2. Previous research of the influence of the FDIA

The role of out-of-plane bending diaphragm stiffness in restraining the overturning of wood-frame SWs is understudied and not addressed in current design standards. Numerical models by M. Bagheri et al. (2019) suggested that virtually any diaphragm would possess sufficient out-of-plane bending stiffness to be considered fully rigid when evaluating deflections in wood-frame SWs, indicating the potential importance of diaphragms in reducing cumulative overturning deformations. However, current mechanical models lack the ability to predict the influence of the FDIA, as they assume that walls behave as isolated planar SWs with flexible out-of-plane diaphragms (Pei & van de Lindt, 2009; Leung et al., 2010; Pei & van de Lindt, 2011; Tamagnone et al., 2020; AWC, 2021). In other words, current mechanical models assume that diaphragms have null flexural stiffness. Further research, both experimental and numerical, is warranted to investigate the overlooked influence of the FDIA effect on complex assemblies. Progress in this topic has had more breadth for CLT assemblies. In the study of an I-shaped CLT non-planar SW, the inclusion of FDIA together with CLT TSWs demonstrated a positive effect on initial lateral stiffness (up to 155% increase) and peak strength (up to 60% increase) with respect to those of a planar SW, without change to the failure mechanism and deformation capacity (Stoner, 2020). However, the quantification of the individual contributions of TSWs and FDIA was not conducted, and the specimen was solely tested under in-plane loading conditions. Additionally, in Tamagnone et al. (2020) the influence of the FDIA effect on the lateral response of planar CLT SWs was found to be minimal because the behavior was found to be governed primarily by the stiffness of the wall-to-diaphragm connection. Flexible connections led to wall detachment (which limited the FDIA effect), while overly stiff connections altered the kinematic response of the wall. Conversely, in D'Arenzo et al. (2021) diaphragm-to-wall interaction was shown to increase the rocking stiffness of planar segmented CLT SWs and modify their kinematic behavior, with the increment in rocking stiffness depending on floor bending stiffness and withdrawal stiffness of the connections. As a result, the uplift restriction of timber diaphragms is an effect that also needs more investigation for any timber structural system.

2.2.3. Previous research on the influence of the AXL

The influence of high gravitational forces and overturning moments on the behavior of planar strong wood-frame SWs was investigated by Orellana et al. (2021). The study revealed significant improvements in stiffness (up to 141%), load-carrying capacity (up to 37%), equivalent viscous damping (up to 104%), and ductility (up to 55%) compared to those of strong wood-frame planar SWs without gravity load. The increased engineering parameters were attributed to potential modifications in OSB sheathing-to-frame connections and to the interaction within framing members, including an unidentified inner frictional phenomenon. Furthermore, the inclusion of AXL in a midrise LFTB resulted in a 6.7% decrease in the fundamental period and a 51.4% increase in building strength (Orellana et al., 2021). However, the combined effect of AXL, TSWs, and FDIA was not addressed. Another study on CLT structures (E. Ruggeri et al., 2022) observed that the influence of CLT TSWs diminishes when the AXL effect on CLT non-planar SWs is considered, while Tamagnone et al. (2020) found that the AXL effect, together with the FDIA effect, can modify the kinematic response of planar segmented CLT SWs (from coupled to uncoupled behavior). Thus, axial effects are also understudied in any timber assemblies.

2.3. Scope

This research focuses on evaluating the combined system effects of TSWs, FDIA, and AXL on the lateral response of strong wood-frame SWs expected to be included in midrise multistory LFTBs located in high seismic regions. The objective is to elucidate the potential influence of system effects on the performance of real structures and to make contributions to future developments of design methods suitable for engineering practice.

Experimental evaluation of such system effects has predominantly been either estimated out of the entire building response in shaking table tests or by planar assemblies (for the AXL effect), which allows neither for an in-depth comprehension of their effects nor to elucidate the sole contribution of each of the three aforementioned potential influences, namely TSWs, FDIA, and AXL effects.

2.4. Materials and methods

Two sets of tests were performed in this research: tests on connections between the SWs and the TSWs, and tests on a full-scale T-shaped SW assembly. In both cases, specimens were subjected to monotonic and/or cyclic loading. Connection tests were conducted to evaluate two potential methods for connecting SWs to TSWs, enabling the TSW effect in non-planar SWs. Meanwhile, assembly tests were employed to analyze the impact of TSWs, FDIA, and AXL on the performance of strong wood-frame SWs.

2.4.1. Connections

Two configurations of SW-to-TSW connections were tested in this study. Both configurations were designed to provide high vertical stiffness in order to assess the potential of the connection in reducing uplift demands on the overturning restraint system. The connections consisted of screwed and slotted configurations, which were also designed to facilitate wall erection, particularly in off-site construction methods. The specimens consisted of symmetric double shear plane connections entailing two lateral members and one central member made of dimensional Chilean radiata pine lumber of 41 mm x 135 mm (2x6) graded as C16 according to NCh1198 (INN, 2014). To simulate the SW sheathing between a SW and a TSW, a layer of OSB was attached to each side of the central element (see the connection configuration in Figure 2.1). The screwed configuration has two pairs (one per shear plane) of four crossed screws ESCRFTZ 8.0X300 positioned in an X-pattern at a 45° angle, certified per ETA-13/0796 and manufactured by Simpson Strong-Tie. The slotted connection consisted of one SLOT 90 connector per shear plane certified per ETA-19/0167 and manufactured by Rothoblaas (see the details of the connection hardware in Figure 2.1). Each configuration comprised three or four specimens: one for monotonic testing and two or three for cyclic testing. A reaction steel frame was utilized to conduct the connection tests (Figure 2.2). The specimen was positioned between two heavy-duty steel beams, which transferred forces to the strong floor through four high-strength rods. Two lateral beams were installed to prevent excessive rotation of the lateral elements. A double-action cylinder with a force and displacement capacity of $\pm$ 600 kN and $\pm$ 100 mm, respectively, was employed to apply loading. This cylinder transferred the vertical load to the specimen through a load-transfer system comprised of two steel plates connected to the specimen with bolts. Several instruments were employed to monitor the vertical response (i.e., along the local x-axis of the connection) of the specimen (see Figure 2.18 for further details). The loading protocol followed the ASTM E564-06 (ASTM, 2006) standard for the monotonic tests and the ASTM E2126-19 (ASTM, 2019) standard for the cyclic tests. In the monotonic tests, the ultimate displacement (i.e., the maximum displacement at which the strength remains above 80% of the peak strength) was determined to calculate the reference displacement for the CUREE-Caltech (Krawinkler et al., 2001) cyclic testing protocol, following method C of ASTM E2126-19 (ASTM, 2019). The loading protocol was displacement-controlled until failure.

2.4.2. Full-scale assemblies

To evaluate the system effects (TSW, FDIA, and AXL), two full-scale specimens of 7.32 m length by 5.1 m width (one without a diaphragm and one with a diaphragm) were tested. These specimens are representative of ground-level strong wood-frame SW assemblies of a 7-story residential building designed according to the Chilean seismic design code NCh433 (INN, 2009). The specimens consisted of a non-planar T-shaped strong wood-frame SW aligned with a planar strong wood-frame SW. The web and flanges of the T-shaped SW assembly entailed one type A SW and two type B TSWs, respectively, as defined in Table 2.1. The isolated (planar) SW was a type B SW (see Table 2.1), similar to the flanges of the T-shaped SW. In order to assess the isolated effect of TSWs,

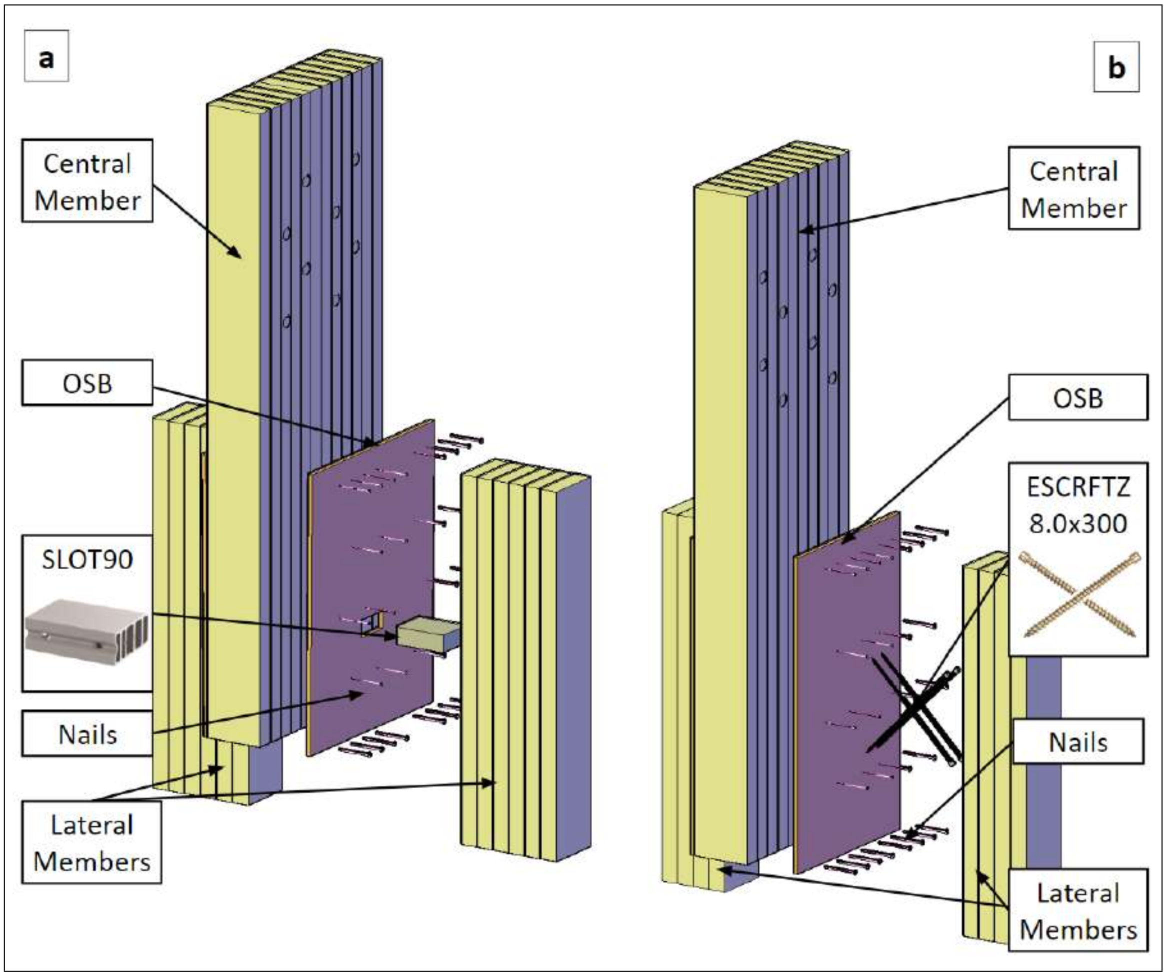

Figure 2.1. Specimen configurations: (a) slotted and (b) screwed connections.

the web of the T-shaped SW was connected to the planar SW by a pinned steel collector. The collector transferred in-plane forces and made possible comparisons between the response of the planar SW and that of the non-planar T-shaped SW. The specimen configuration is shown in Figures 2.3a and 2.5a, and the test layout is shown in Figure 2.4. In order to assess the FDIA and AXL effects together with the TSW effect, a representative diaphragm of a typical light wood-frame floor made up of dimensional lumber joists was added atop the walls. Figures 2.3b and 2.5b show that the diaphragm has a T shape, and that the characteristics of the diaphragm on top of the planar SW are different from that on top of the T-shaped SW. This results in the assembly of two types of diaphragms

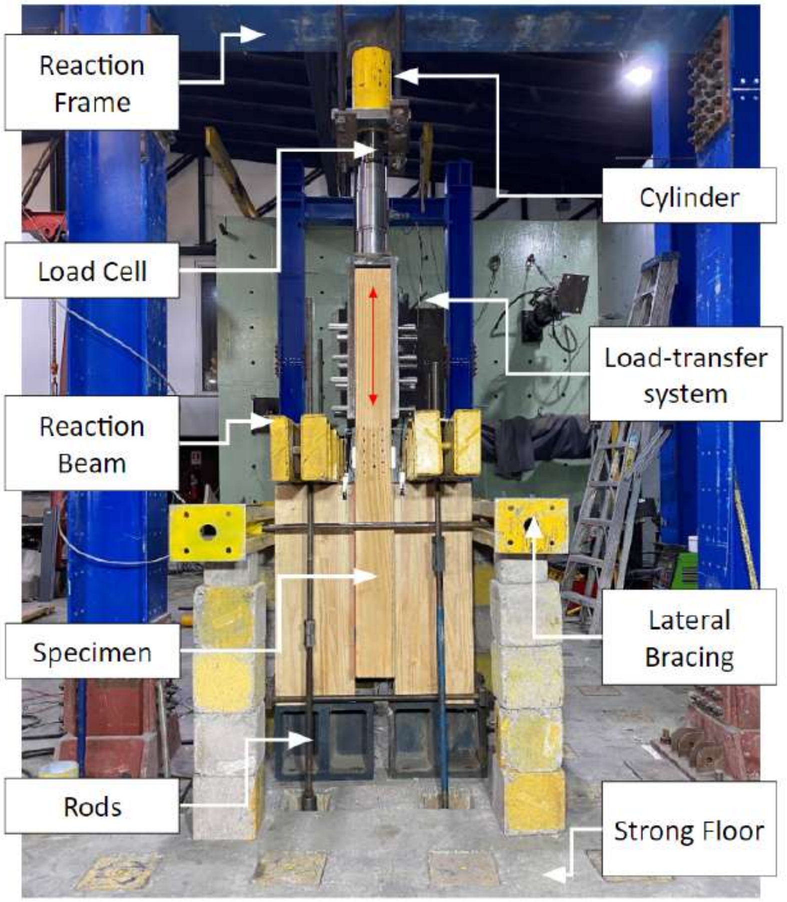

Figure 2.2. Connection setup for evaluating the vertical response (or local x-axis of the connection represented by the red arrow) of a SW-to-TSWs connection.

(type D_1 and type D_2), as listed in Table 2.2. The wall and diaphragm framing was constructed with 41 mm by 185 mm (2x8") C16 Chilean radiata pine dimensional lumber graded according to NCh1198 (INN, 2014) (the same wood of the connection tests). All SWs were 1:1 in aspect ratio (2440 mm width by 2481 mm height), sheathed at both sides with 11.1 mm thick APA-rated (APA, 2012) OSB panels. Double plates were nailed to the studs using ϕ3.0 mm x 80 mm smooth shank nails conforming to ASTM F1667 (ASTM, 2021). OSB sheathing layers were attached to the lower top plate and the upper bottom plate. According to the SDPWS (AWC, 2021), edge-nailing at the end studs should be uniformly distributed among the four framing members and spaced at a maximum of 300 mm. In order to transfer the lateral load to each specimen, a built-up collector beam of 205 mm by 207 mm (i.e., five members of 41 mm by 185 mm C16 Chilean radiata pine plus an 11.1 mm thick OSB layer on top and bottom) was mechanically attached to the top plate through 38 Simpson Strong-Tie SCDP221100 screws. Six SLOT90 connectors were employed to join the web to the flange in the T-shaped SW. The selection of the SLOT90 connector over the inclined screw type was based on its favorable performance and ease of installation, as demonstrated by the results obtained from the connection tests (presented later in Section 2.5.1.2). The diaphragm was sheathed on both sides with 15.1 mm thick APA-rated OSB (APA, 2012) panels. Perimeter beams were nailed to the internal beams using ϕ3.0 mm x 80 mm smooth shank nails as per ASTM F1667 (ASTM, 2021). The attachment of OSB panels to the wood frame followed the nailing requirements stated in section 2.4.2 of the SDPWS (AWC, 2021). The diaphragm was secured to the collector beams of the SW using two rows of Simpson Strong-Tie ESCR8.0x100 screws at 100 mm on center spacing.

Figure 2.3. General configuration of the tested full-scale assemblies to evaluate the impact of (a) TSW effect only; and (b) TSW effect + FDIA and AXL effects.

The tests were conducted using an L-shaped cantilever reaction wall, a strong floor, and a T-shaped reaction steel beam, following the ASTM E2126-19 (ASTM, 2019) guidelines (Figure 2.4). The specimens were secured to the reaction beam using 43 ϕ32 mm x 220 mm ASTM A193 Grade B7 anchor bolts to prevent sliding in the T-shaped SW. In

Table 2.1. Configuration of the SWs (see Figure 2.5)

Wall Type	OSB Sheathing		Overturning restraint system [c]		# of end-studs
	Sheathing nail[d]	Spacing edge/field	# of rods	Location	
A[a]	ϕ2.9x80	100/200	1	one-side	3
B[b]	ϕ2.9x80	100/200	2	both-sides	4

[a] Wall framing: 41mm x 185 mm (2x8) C16 Chilean radiata pine (INN, 2014) studs at 400mm o.c., (2) 41mm x 185 mm used as a central stud, left end-stud is formed by (4) 41mm x 185 mm studs mechanically joined and located symmetrically with respect to the rod and (5) 41mm x 185 mm studs mechanically joined are used as right end-studs for the SW-to-TSW connection.

[b] Wall framing: 41mm x 185 mm (2x8) C16 Chilean radiata pine (INN, 2014) studs at 400mm o.c., (2) 41mm x 185 mm used as a central stud, (4) 41mm x 185 mm studs mechanically joined and located symmetrically with respect to the rod are used as end-studs.

[c] Wall shear anchorage: ϕ32 mm x 220 mm ASTM A193 Grade B7 anchor bolts (14 and 15 for wall type A and B, respectively) with ϕ80 mm x 4.0 mm Grade A36 washers. Overturning restraint provided by ϕ38.1 mm ASTM A193 Grade B7 rods, bearing plate (MiTek BPW36-6), take-up device (MiTek CNX-12), and two Simpson Strong-Tie SDS25600 screws.

[d] Spiral nails (BSI, 2008) pneumatically driven to the frame with minimum end/edge distance of 20/40 mm, respectively.

Table 2.2. Configuration of the diaphragms (see Figure 2.5)

Diaphragm Type	Diaf. size (L by W)	OSB Sheathing	
		Sheathing nail[c]	Spacing (edge/edge/field)
D_1[a]	2441x2234	ϕ3.4x100	100/150/200
D_2[b]	2440x1120	ϕ3.4x100	100/150/200

[a] Diaphragm framing: 41mm x 185 mm (2x8) C16 Chilean radiata pine (INN, 2014) studs at 400mm o.c., (2) 41mm x 185 mm used as a central and perimeter beams, one end-beam formed by (4) 41mm x 185 mm studs mechanically joined.

[b] Diaphragm framing: 41mm x 185 mm (2x8) C16 Chilean radiata pine (INN, 2014) studs at 400mm o.c., (2) 41mm x 185 mm used as central and perimeter beams.

[c] Smooth shank nails (BSI, 2008) pneumatically driven to the frame with minimum end/edge distance of 20/40 mm, respectively.

the planar SW, cylinders reacting against a couple of L-shaped connectors were employed

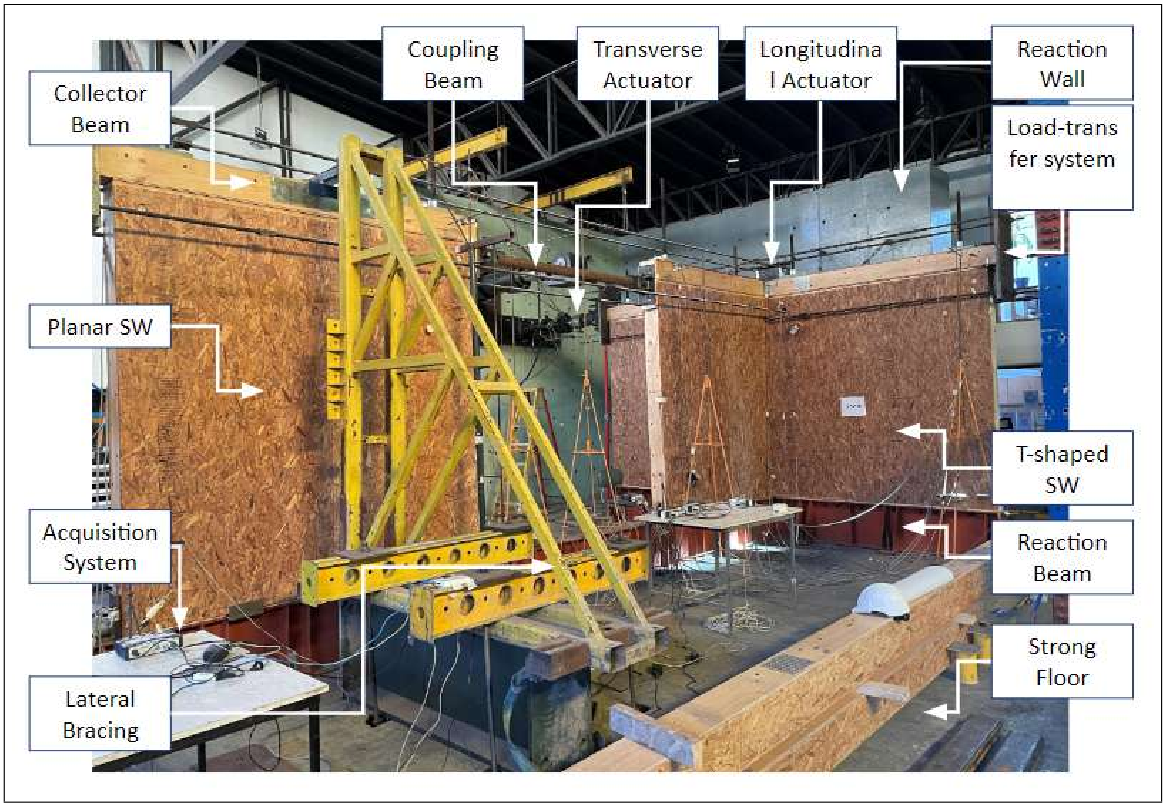

Figure 2.4. Test setup for evaluation of the TSW effect under bidirectional loading.

to prevent sliding and to measure the shear force (element 9 in Figure 2.20). The continuous rod system of the walls transferred forces to the top flange of the reaction beam through double hexagonal nuts. Out-of-plane support was provided to the planar SW in the specimen without diaphragm. This support was not necessary in the other specimen as the diaphragm prevented the out-of-plane instability of the planar SW. The most important installation and restraining details are shown in Figures 2.4 and 2.6.

The loading protocol for the cyclic test was defined based on the bidirectional hexagonal loading protocol of FEMA 461 (ATC, 2007). The objective displacement of each cycle was determined using the CUREE-Caltech (Krawinkler et al., 2001) cyclic testing protocol, following method C of ASTM E2126-19 (ASTM, 2019) (see Figure 2.19 of the supplementary material). The bidirectional protocol was conducted to capture the 3D response of the web and flanges of the T-shaped SW applying 100% and 50% of the target

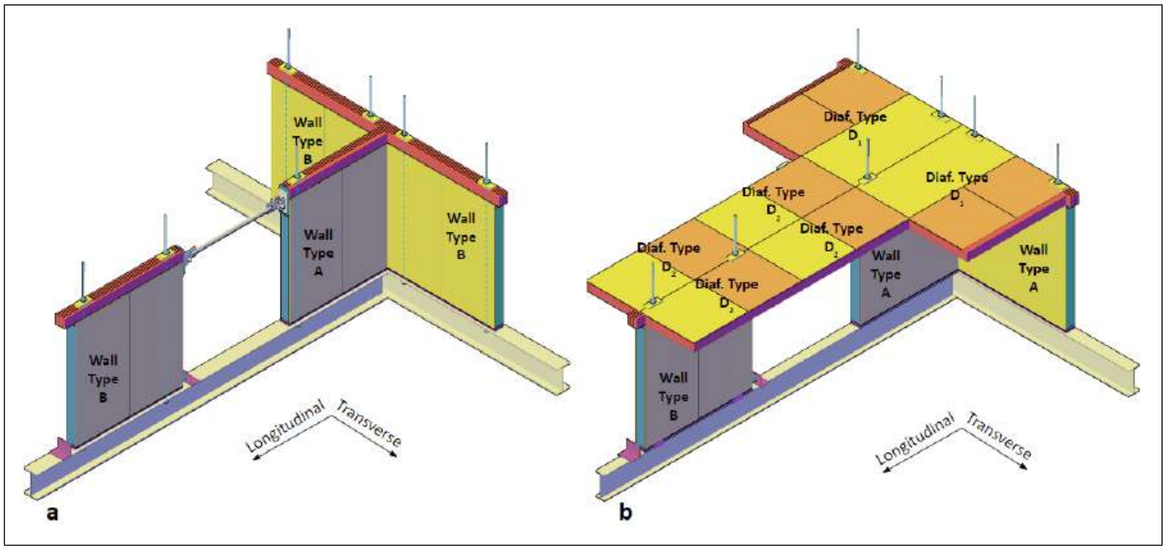

Figure 2.5. Test layouts of the SW assemblies: (a) with and (b) without diaphragm. The diaphragm was made up of two type D1 and four type D2 diaphragms according to Table 2.2.

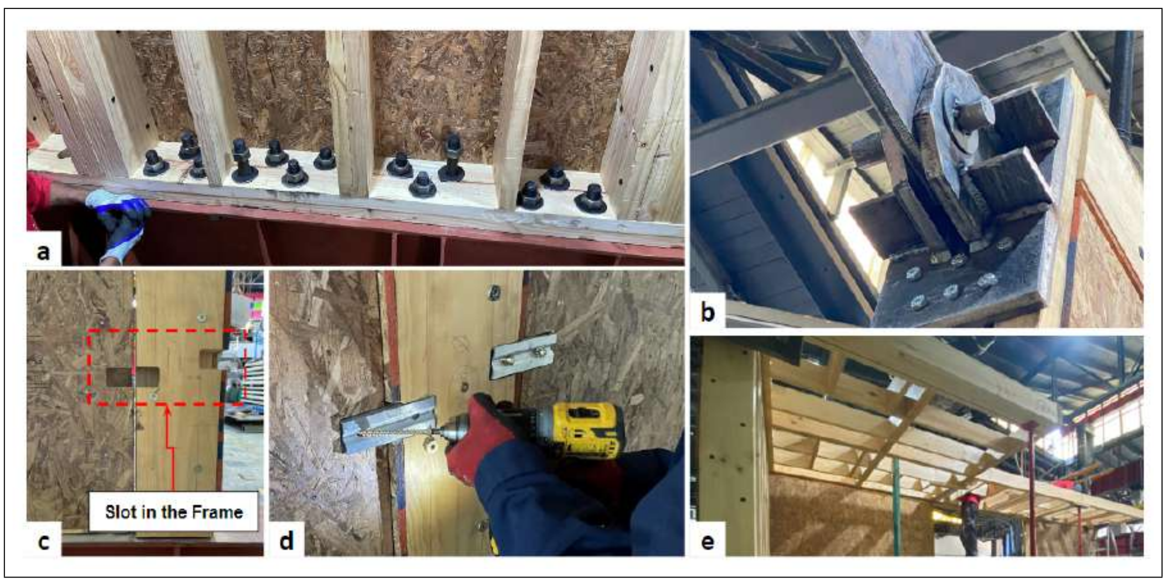

Figure 2.6. (a) sliding restraining system for wall types *A* and *B* in the T-shaped SW; (b) installation of the steel pinned-beam; (c) detail of slot in the frame for installing the SW-to-TSW connection; (d) installation of the *SLOT90* connector between web and flanges of the T-shaped SW; and (e) diaphragm attachment to the collector beam.

displacement in the longitudinal and transverse directions, respectively (directions are indicated in Figure 2.5). Hydraulic bidirectional actuators were employed to apply lateral load in the longitudinal (displacement capacity of the actuator equal to $\pm$200 mm) and transverse (displacement capacity of the actuator equal to $\pm$50 mm) directions, with a specific force capacity of +588kN/-294kN. Both actuators transferred the load to the specimen through the collector beam. The evaluation of the specimen with the diaphragm was split into two phases. In the first phase, an axial (gravity) load was applied to the specimen (by applying a tension force 85 $\pm$ 0.5 kN on the rods of the walls) to capture the combined FDIA and AXL effects. The applied tension force did not reach the expected gravitational load in a 7-story LFTB: it was the maximum load that the laboratory could apply and synchronize with the lateral protocol. The loading protocol continued until a maximum lateral deformation of 15 mm was reached, which was assumed not to damage the assembly based on previous test data on planar SWs (Guinez et al., 2019; Estrella, Malek, et al., 2021). In the second phase, the gravity load was removed and the bidirectional hexagonal protocol was applied without the AXL effect. Therefore, the first testing without a diaphragm plus the two-phase testing with a diaphragm allowed us to separately elucidate the relative influence of all three system effects, namely TSW, FDIA, and AXL. Instrumentation was designed to evaluate system effects, which included 41 displacement transducers (LVDTs), two load cells at the reaction cylinders (element 9 in Figure 2.20), and two load cells and displacement transducers (LVDTs) integrated into the actuator. Further details on the instrumentation are illustrated in Figure 2.20. The rod stress was computed based on measurements from strain gauges attached to the fully threaded rods. The uplift of the continuous rod system was measured using LVDTs at the lower edge of the specimens (as shown in element 5 of Figure 2.20).

2.5. Results and discussion

The failure mode, hysteresis shape, and eight relevant engineering parameters were determined from both the connection tests and the SW tests. The parameters are the followings: (1) elastic stiffness (K_e), calculated as the secant stiffness between 0% and 40% of maximum load F_{max}; (2) yield displacement (Δ_y); (3) yield force (F_y); (4) deformation capacity (Δ_u), defined as the displacement after peak strength at which the load dropped to F_u = 0.8 F_{max}; (5) ultimate force (F_u); (6) secant stiffness of cycle i ($k_{s,i}$); (7) dissipated energy of cycle i ($E_{H,i}$), which is the area under the load-displacement curve of cycle i; and (8) equivalent viscous damping (ζ_{eq}). The Equivalent Energy Elastic-Plastic (EEEP) method (G. C. Foliente, 1996), as outlined in ASTM E2126-19 (ASTM, 2019), was used to estimate the parameters. This study focused on displacement capacity rather than on ductility, as it is a more meaningful predictor of seismic performance. To examine the evolutionary trends, the investigation also analyzed secant stiffness, dissipated energy, and equivalent viscous damping in terms of load cycle or drift level. Additionally, the secant stiffness and strength at 0.2% ($K_{0.2\%}$, $F_{0.2\%}$) and 0.4% ($K_{0.4\%}$, $F_{0.4\%}$) drift levels (i.e., design drift levels) of the SW assemblies were calculated to assess how the specimens behave when subjected to the current (INN, 2009) and proposed (Estrella, Guindos, et al., 2021) drift design demands for LFTBs according to the NCh433 (INN, 2009) guidelines. To assess the response of the T-shaped SW under the combined longitudinal and transverse response, we employed the Square Root of the Sum of Squares (SRSS) combination. This approach allowed us to obtain representative quantities (i.e., force and displacement) for the combined directions, as commonly employed in concrete non-planar shear walls (Constantin, 2016; Kolozvari et al., 2021).

$$F_{SRSS} = \text{sign}(u_{LD})\sqrt{F_{LD}^2 + F_{TD}^2} \tag{2.1}$$

$$u_{SRSS} = \text{sign}(u_{LD})\sqrt{u_{LD}^2 + u_{TD}^2} \tag{2.2}$$

where F_{LD} and F_{TD} are the forces carried by the T-shaped SW in the longitudinal (LD) and transverse (TD) directions, respectively. Similarly, u_{LD} and u_{TD} denote the lateral displacements of the T-shaped SW in the longitudinal and transverse directions, respectively. In order to plot the hysteresis loops in a consistent manner, the SRSS values were multiplied by the sign of the u_{LD} displacement. The directions are indicated in Figure 2.21 of the supplementary material.

2.5.1. Connections

2.5.1.1. Failure mode

We assess the failure modes of the examined connections to characterize and compare the ductility of their behavior. Although the design process does not mandate a dissipative connection, the response of these connections has a significant influence on the non-planar SW behavior. Among the evaluated connection types, the slotted connection exhibited a more ductile failure mode characterized by wood stud crushing (label 3 in Figure 2.7) and local yielding in the SLOT 90 connector (label 4 in Figure 2.7). In contrast, the screwed connection exhibited a more brittle failure mode, attributed to screw bending, wood crushing, and tearing in the OSB sheathing layer (label 7 in Figure 2.7). The brittle failure of the screwed connections was influenced by withdrawal failure (label 9 in Figure 2.7), pull-through of screw heads (label 8 in Figure 2.7), tension failure, and pulling out of connected wood members (label 5 in Figure 2.7). Both connection types showed primary failure modes associated with the nailed OSB-to-wood frame connection, including excessive nail bending (label 1 in Figure 2.7) and nail pull-out resulting in sheathing detachment (label 2 in Figure 2.7). The sheathing detachment was more pronounced in the screwed connection due to higher lateral deformation (label 6 in Figure 2.7). Therefore, even when the SW-to-TSW connection might be intended to remain elastic, we preferred the slotted connection for the SW assembly tests because of its ductile failure and ease of installation.

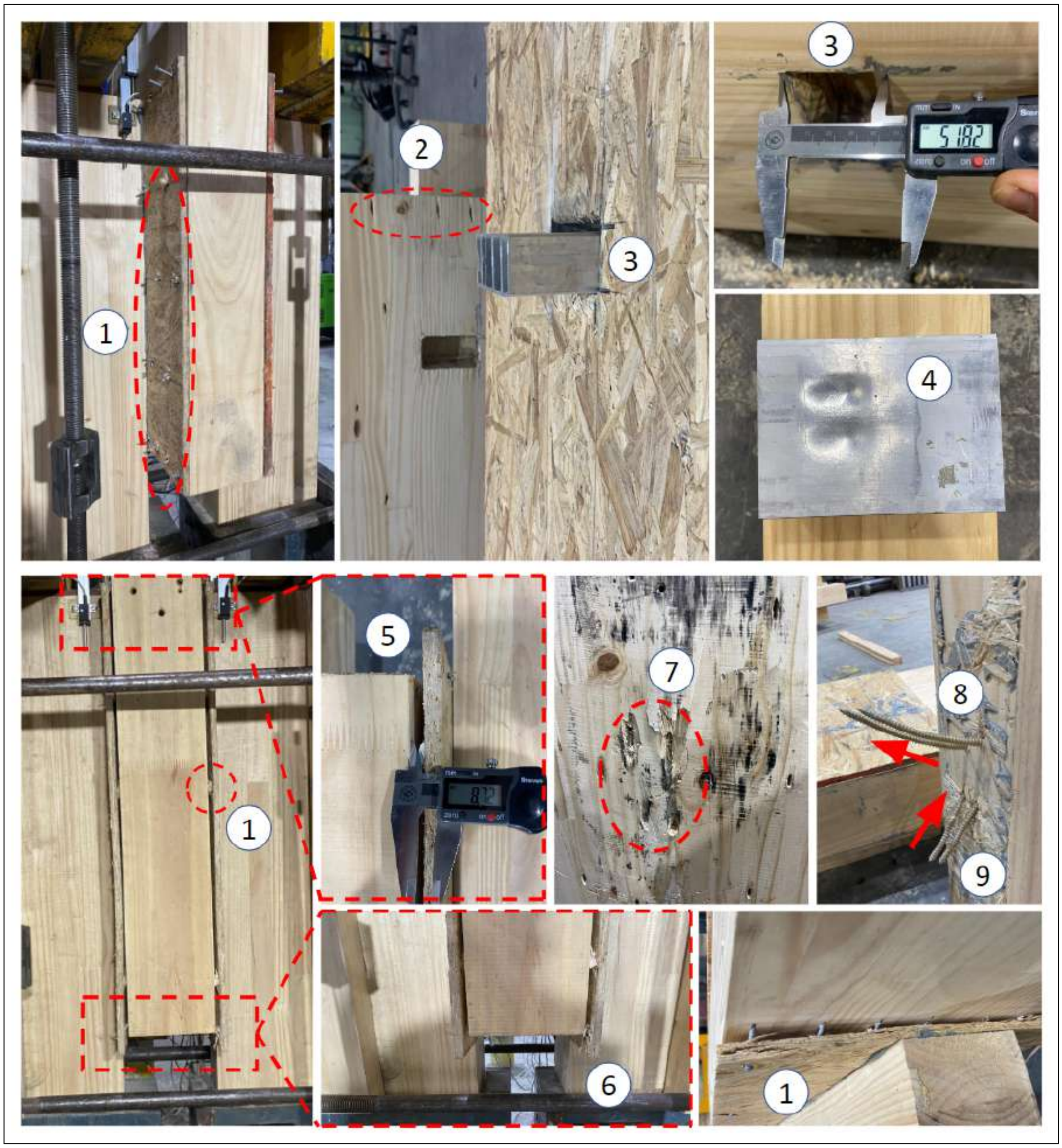

Figure 2.7. Failure modes of tested connections: (1) bending and (2) pulling out of the nailed connection. Slotted connection: (3) wood stud crushing and (4) local yielding in the connector. Screwed connection: (5) pulling out of the wood member; (6) excessive lateral deformation at the OSB sheathing; (7) screw bending, wood crushing, and tearing in the OSB; and (8) pull-through and (9) withdrawal of the screws.

2.5.1.2. Monotonic and cyclic response

Figure 2.8 shows the monotonic results of the connection tests in terms of the differential slip between wood frames (x-axis) and the force exerted by a single SLOT 90 connector or a group of four inclined ESCRFTZ 8.0X300 screws along a single shear plane (y-axis). Table 2.3 summarizes the relevant engineering parameters. To qualify as a suitable candidate for a SW-to-TSW connection, the vertical stiffness requirement is crucial (if the stiffness is not large enough there are no benefits from the TSW effect). Preliminary numerical models reported by the authors50 indicate that SW-to-TSW connection should possess a stiffness of at least 40% of that of the planar SW (in this case 1.6 kN/mm for assembly-level specimens). Additionally, the connection must demonstrate sufficient overstrength to remain within the linear-elastic range. These requirements are essential to ensure the effectiveness of the TSWs and maintain the desired coupled anchoring restriction. The peak strength of both connection types are similar to each other, surpassing the values reported in previous studies (van de Lindt, Pei, Pryor, et al., 2010; Perez et al., 2018; Gonzalez et al., 2020; Benedetti et al., 2022). Regarding the elastic stiffness, both connection types exhibit favorable characteristics to achieve coupling effects between perpendicular walls. Specifically, the stiffness of the screwed connections is approximately 300% higher than that of the slotted connections. However, in terms of deformation capacity, slotted connections outperformed screwed connections by 15%. Parallel-to-grain failure mode was observed in slotted connections, which contributes to their enhanced deformation capacity.

Table 2.3. Engineering parameters from monotonic connection-level test results

Connection Type	K_e kN/mm	Δ_y mm	F_y kN	Δ_u mm	F_u kN	F_{peak} kN
Screwed	156.0	0.59	92.4	6.74	84.5	105.7
Slotted	39.2	2.64	103.6	7.72	92.7	115.8

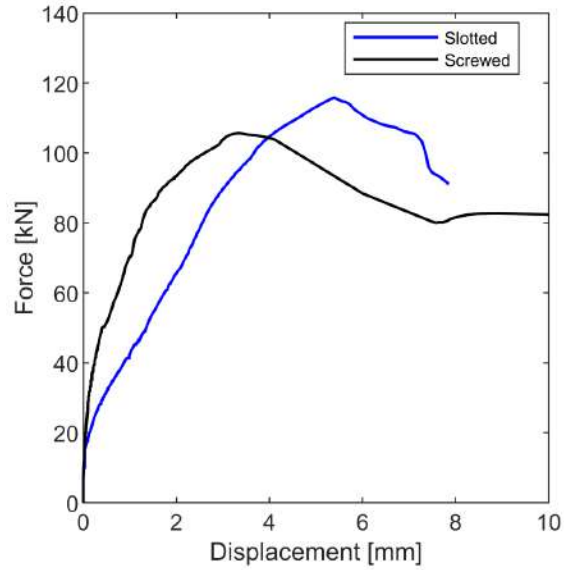

Figure 2.8. Monotonic test results from the evaluated connection types.

Figure 2.9 illustrates the cyclic force-displacement response of both connection types. The cyclic tests conducted on all connections revealed a pronounced pinching effect caused by wood frame crushing at the shear planes. Additionally, strength and secant stiffness degradation (Figures 2.9 and 2.10) was observed in all tests after repeated cycles. The screwed connections exhibited a sudden decrease in stiffness and strength after the peak strength (i.e., after cycle 30) attributed to the brittle withdrawal failure, which contrasts with the parallel-to-the-grain crushing observed in the slotted connection.

Figure 2.10 illustrates the evolution of cumulative energy dissipation and equivalent viscous damping over cycles. In the initial cycles, both connection types exhibit similar responses of these parameters. However, after cycle 30 the slotted connection demonstrated higher energy dissipation due to the induced failure mechanism (i.e., crushing parallel to the grain), whereas the screwed connection displayed higher values of equivalent viscous damping attributed to frictional effects after the failure of the screw-to-wood connection interface. These characteristics can be observed in Figure 2.9b at slips greater than $\pm$ 5 mm. Nevertheless, both connection types exhibit nearly identical equivalent viscous damping ratios of approximately 0.1. Results from monotonic and cyclic tests

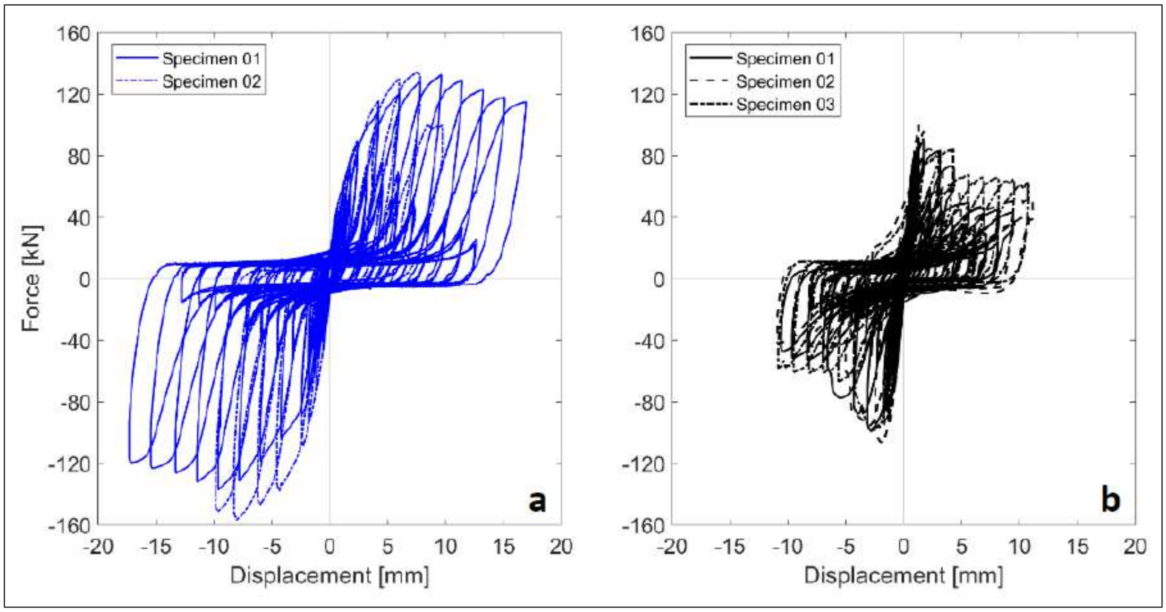

Figure 2.9. Cyclic response of: (a) slotted connections; and (b) screwed connections.

on the SW-to-TSW connections showed that both connection types have sufficient stiffness and strength to obtain benefits from the TSW effect. However, the slotted connection performed better under cyclic loading, displaying a smoother stiffness and strength degradation. Additionally, the slotted connections were easier to install than the screwed connections. Taken together, these results suggest that the slotted connection exhibits practical and behavioral advantages over the screwed connection, even though both meet the minimum requirements set by the authors (Valdivieso, Lopez-Garcia, et al., 2023).

2.5.2. SW assemblies

2.5.2.1. Failure mode

The wall specimens underwent comprehensive examinations to identify specific failure modes after each test. Three failure modes were observed in both assemblies (i.e., with and without the diaphragm): nail pull-out (label 3 in Figure 2.11); nail shear-off due to excessive fastener bending (label 5); and detachment (out-of-plane unsheathing) of the OSB panels from the wood-frame as a result of nail failure (labels 1 and 2). Nail failure

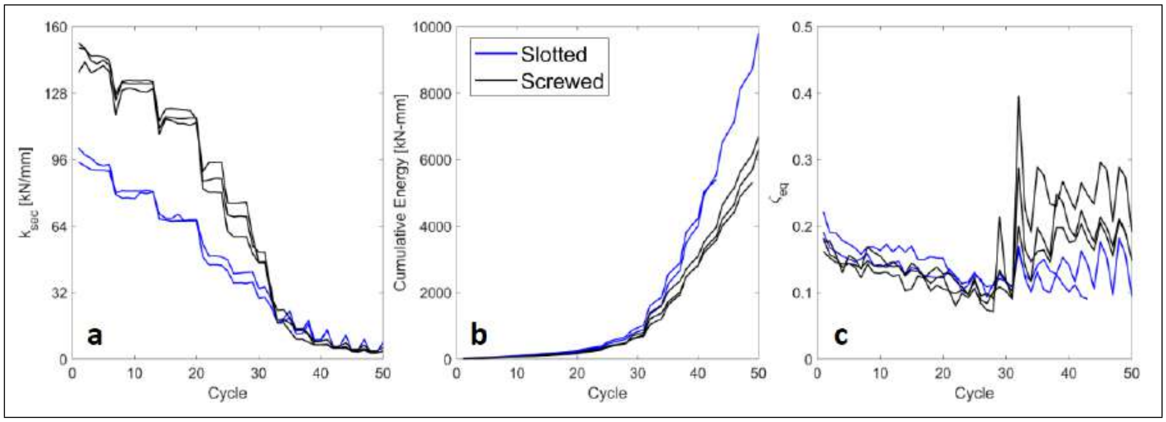

Figure 2.10. Connection level tests: evolution of: (a) secant stiffness; (b) cumulative dissipated energy; and (c) equivalent viscous damping.

was primarily initiated at the center studs and propagated toward the edge of the walls during the later stages of the loading protocol (see Figure 2.11a). This behavior is consistent with the findings of previous studies (Estrella, Malek, et al., 2021) on SWs with continuous rod systems because of the concentration of fasteners near the continuous rod, leading to failure at the interior sheathing edges. Furthermore, in the specimen with the diaphragm, two additional failure modes were observed: local embedding failure (crushing) in the OSB panels of the wall due to excessive stress concentration when in contact with the diaphragm (label 4 in Figure 2.11); and nail pull-out in the diaphragm (label 3). In the T-shaped SW, the presence of a concentrated load at the right side of the web (specifically, the right side of wall type A) resulted in the premature occurrence of failure modes labeled 1 to 3 and 5. At the flange of the T-shaped SW, only the failure modes labeled 3 and 5 were evident due to the relatively minor displacement demand. To avert early nail failure at the right side of the web wall of the T-shaped assembly, the results suggest that it is advisable to employ design criteria with a denser nail pattern. The wood frame exhibited moderate to low damage in all cases, with the central (interior) double stud experiencing the most damage. As expected, the continuous rod system remained undamaged throughout the tests, as it was designed to behave elastically even at peak strength.

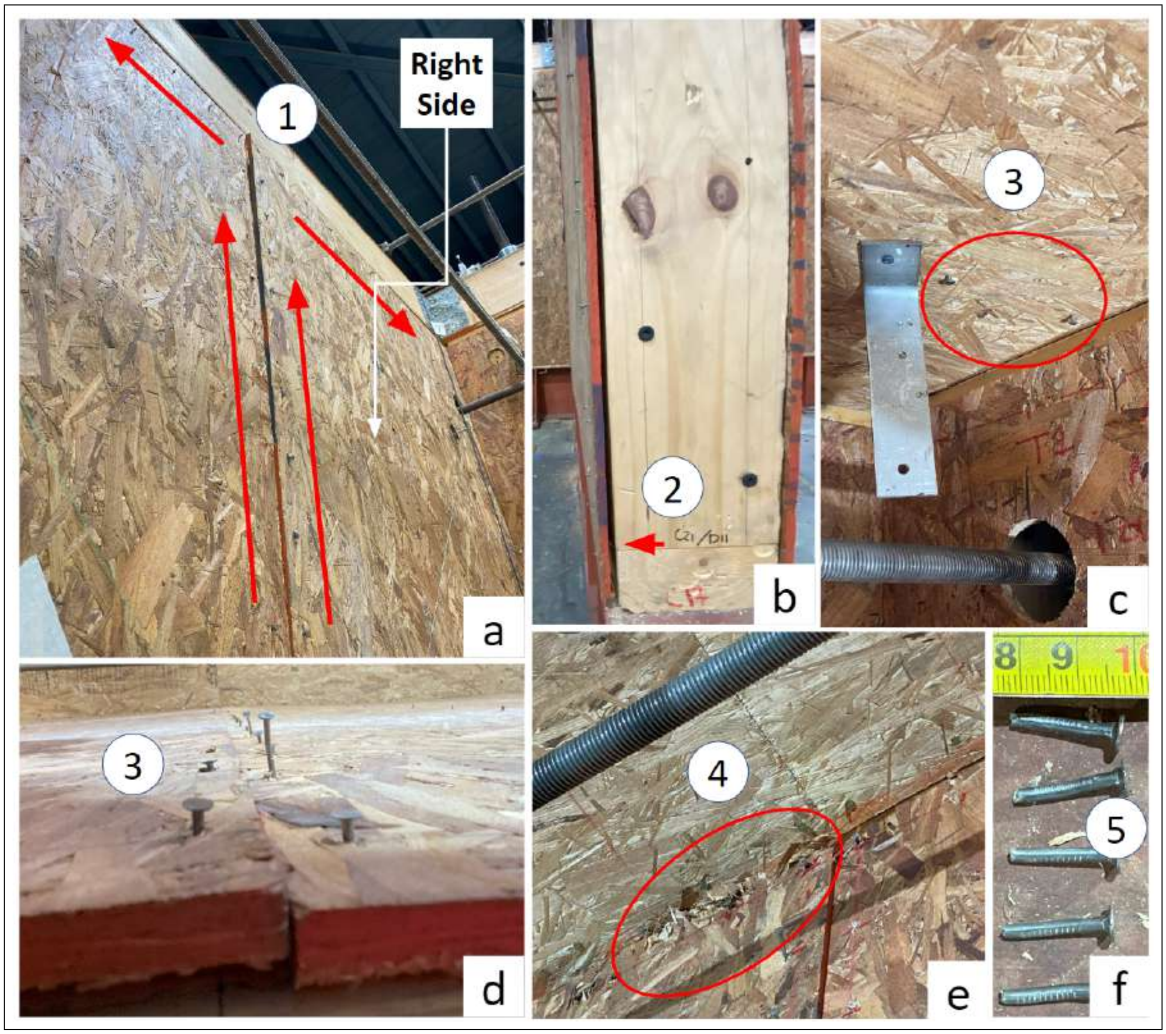

Figure 2.11. Failure modes of SW assemblies: (a) nail failure pattern (label 1) in the web of the T-shaped SW; (b) lateral view of the web wall of the T-shaped SW showing the detachment of the OSB sheathing panels (label 2); nail pull-out (label 3) in (c) diaphragm type D_1 and (d) SW assemblies; (e) zoomed view of the wall-to-diaphragm connection illustrating crushing in the OSB panels (label 4); and (f) nail shear-off (label 5).

2.5.2.2. Lateral cyclic response

Figure 2.12 presents a comparison between the backbone curves obtained from cyclic loading on the SW assemblies. The displacement reported refers to the effective displacement of the wall in relation to the reaction steel beam. The relevant engineering parameters derived from the backbone curves are summarized in Table 2.5 of the supplementary material. The T-shaped SW exhibited an asymmetric response in the longitudinal direction (labeled as T shape SW LD in Figure 2.12) and a symmetric response in the transverse direction (T shape SW TD), being thus consistent with the response of T-shaped concrete shear wall assemblies (Brueggen, 2009; Zhang & Li, 2016). The asymmetry in the longitudinal direction is attributed to the effect of the TSWs' out-of-plane stiffness and the SW-to-TSWs connection (i.e., web-to-flange connection). On the other hand, the symmetry in the transverse direction results from the symmetrical installation of the web walls relative to the flange. The TSW effect caused an increase of up to 19% in elastic stiffness and up to 98% in peak strength, and a decrease of 30% in deformation capacity relative to the planar SW. The reduced deformation capacity was attributed to the premature failure of the OSB-to-frame nailing due to stress concentration at the web-to-flange connection. At the NCh 433 (INN, 2009) design drift level, the influence of the TSWs on the longitudinal secant stiffness and strength of the T-shaped SW was more significant than at the elastic level defined according to ASTM E2126 (ASTM, 2019). In fact, an increase in the longitudinal secant stiffness (and strength) of up to 50% and 40% at 0.2% and 0.4% drift, respectively, were found when comparing the T shape SW LD to the Planar SW. Regarding the FDIA effect, the diaphragm tended to generate a more symmetric response of the T-shaped SW in the longitudinal direction (T shape SW LD + FDIA) compared to the case without diaphragm. Additionally, the average peak strength of the T-shaped SW increased by approximately 50% with respect to that of the planar SW (Planar SW + FDIA) (Figures 2.12a and 2.12b). The FDIA effect also led to an average increase of about 30% in deformation capacity compared to the planar SW. Moreover, when considering secant stiffness, the T-shaped SW with the diaphragm (T shape SW LD + FDIA) showed a 68% increase at 0.2% drift and a 28% increase at 0.4% drift compared to the T-shaped SW without the diaphragm (T shape SW LD). This signifies that the diaphragm not only enhances the symmetry of the T-shaped SW's response but also increases both its stiffness and strength, addressing the limitation of lower deformation capacity in the absence of a diaphragm. Consequently, the diaphragm's inclusion makes the T-shaped SW response more favorable and relatively symmetric, making it a more feasible option in practice. However, in the transverse direction (T shape SW TD + FDIA), the diaphragm's benefits were less pronounced, resulting in only an 8% increase in peak strength compared to the T-shaped SW without a diaphragm (T shape SW TD), making it less advantageous in this orientation. The combined effect of the diaphragm and axial load (FDIA + AXL) was found to have a significant influence on the response of the T-shaped SW (T shape SW LD + FDIA + AXL) in the longitudinal direction and on the response of the planar SW (Planar SW + FDIA + AXL). As lateral drift increases in the T-shaped SW with diaphragm and axial load, the rise in secant stiffness becomes more pronounced compared to cases without diaphragm and axial load. For instance, when comparing T shape SW LD + FDIA + AXL to T shape SW LD, there was an increase of up to 76% and 33% in longitudinal secant stiffness at 0.2% and 0.4% lateral drift, respectively. This phenomenon results from the increased out-of-plane deformation of the diaphragm's collector beam in the bay between the planar SW and T-shaped SW as lateral drift intensifies (refer to Figure 2.22 in the supplemental material). Additionally, the longitudinal elastic stiffness of the T shape SW LD + FDIA + AXL and the Planar SW + FDIA + AXL showed an increase of up to 162% and 66% with respect to that of the cases without diaphragm and axial load (T shape SW LD and Planar SW, respectively). The findings for the planar SW are consistent with previous research (Orellana et al., 2021) on the effect of axial load on planar strong wood-frame SW without diaphragm. The response of Planar SW + FDIA + AXL suggests that the diaphragm does not significantly affect the stiffness of planar SW when the AXL effect is considered. Similar results were also observed in numerical studies on planar CLT SWs (Tamagnone et al., 2020). However, in the case of the T-shaped SW, a comparison between the combined FDIA + AXL effect and the isolated FDIA effect indicates that the role of the diaphragm appears to be more relevant, highlighting the importance of considering the tridimensional behavior of non-planar shear walls when analyzing the impact of the diaphragm on the overall response. Considering the lack of prior experimental research on T-shaped SWs, it is crucial to elucidate their hysteretic behavior by examining secant stiffness, cumulative energy dissipation, and viscous damping ratio, while also conducting a comparative analysis with planar SWs. Figure 2.13 displays the hysteretic response in the longitudinal direction of both the T-shaped SW (T shape SW LD) and the planar SW. The cyclic response in the transverse direction of the T-shaped SW (T shape SW TD) is shown in Figure 2.23. Additionally, Figures 2.12c and 2.14 show the backbone curves and the cyclic response of the T-shaped SW at the combined longitudinal and transverse direction (T shape SW SRSS) as per Eqs. 2.1 and 2.2. The cyclic response of the T-shaped SW in the longitudinal direction (T shape SW LD) exhibited asymmetry, with a more pronounced strength degradation compared to that of the planar SW. This behavior can be attributed to the premature detachment of the OSB sheathing, specifically the failure of the nailed OSB-to-wood frame connection near the web-to-flange connection. Progressive degradation of secant stiffness was observed after the peak strength (Figure 2.15a). The presence of high redundancy in the specimens, owed to the nailed connections, led to significant drift levels with no brittle failures. Consequently, the hysteresis exhibited noticeable pinching due to the non-reversible crushing effect of the nails, as the lateral behavior of the specimens was governed by the response of the nailed connections. The hysteretic response in the SRSS direction shows higher asymmetry (Figure 2.14a). Most of the enclosed area of the loops is concentrated in the negative quadrant (identified in Figure 2.21 of the supplementary material). This can be attributed to the asymmetric configuration of the T-shaped SW, where a minor transverse contribution to strength is expected from the free side (left side) of the web. When evaluating the SRSS response of the T-shaped SW under only longitudinal displacement (labeled as T shape SW SRSS + FDIA + AXL in Figure 2.14b), a more similar loop shape between the positive and negative quadrants is observed which is consistent with the response of T-shaped concrete walls (Brueggen, 2009; Constantin, 2016; Zhang & Li, 2016; Kolozvari et al., 2021) under in-plane longitudinal load. Figure 2.15a depicts the evolution of the secant stiffness per meter of wall as a function of the lateral drift for both the T-shaped SW and the planar SW under different conditions. In all cases, there is a clear stiffness degradation as the lateral drift increases, resulting in a residual secant stiffness ranging from 0.15 kN/mm/m to 0.30 kN/mm/m. This behavior is influenced by frame-to-frame interaction and the remaining field nailed OSB-to-frame connections. Furthermore, the T-shaped SW maintains a higher secant stiffness compared to that of the planar SW across the entire range of lateral drift because of the TSW effect. Additionally, the presence of out-of-plane bending stiffness in the diaphragm (FDIA effect) results in a smoother degradation of the secant stiffness of both the T-shaped SW and the planar SW. In Figure 2.15b, the evolution of the cumulative dissipated energy per meter of wall as a function of the lateral drift is presented for both the T-shaped SW and the planar SW. Again, the out-of-plane bending stiffness produces a smoother increase in energy dissipation. Also, when the FDIA effect is considered, the T-shaped SW (T shape SW + FDIA - LD) dissipates more energy than the planar SW (Planar SW + FDIA), which illustrates the positive impact of the diaphragm on a non-planar SW. Figure 2.15c illustrates the evolution of equivalent viscous damping (ζ_{eq}) as a function of the lateral drift. The equivalent viscous damping (ζ_{eq}) of the T-shaped SW in the longitudinal direction (T shape SW - LD) is approximately 20% smaller than that of the planar SW without a diaphragm, despite similar energy dissipation (Figure 2.15). However, when the out-of-plane bending stiffness of the diaphragm (FDIA effect) is considered, the difference becomes almost negligible. Specifically, the ζ_{eq} of the T shape SW - LD is 35% smaller than that of the planar SW, while the ζ_{eq} of the T shape SW + FDIA - LD is almost 6% higher than that of the Planar SW + FDIA (see Figure 2.24 in the supplemental material). Moreover, in the transverse direction of the T-shaped SW, when the FDIA effect is considered the ζ_{eq} is up to 16% higher than when the FDIA effect is absent (see Figure 2.24 in the supplemental material). Clearly, the FDIA effect significantly modifies the longitudinal and transverse equivalent viscous damping response of non-planar SWs such as the T-shaped SW tested in this study.

2.5.2.3. Effect of system effects on the cyclic uplift response of the SW's overturning restraint system

To evaluate the role of system effects on the uplift, Figure 2.16 presents the stress-uplifting response of the left rod of the overturning restraint system for both the T-shaped SW and the planar SW. The response of the other rods is shown in Figure 2.25 (planar

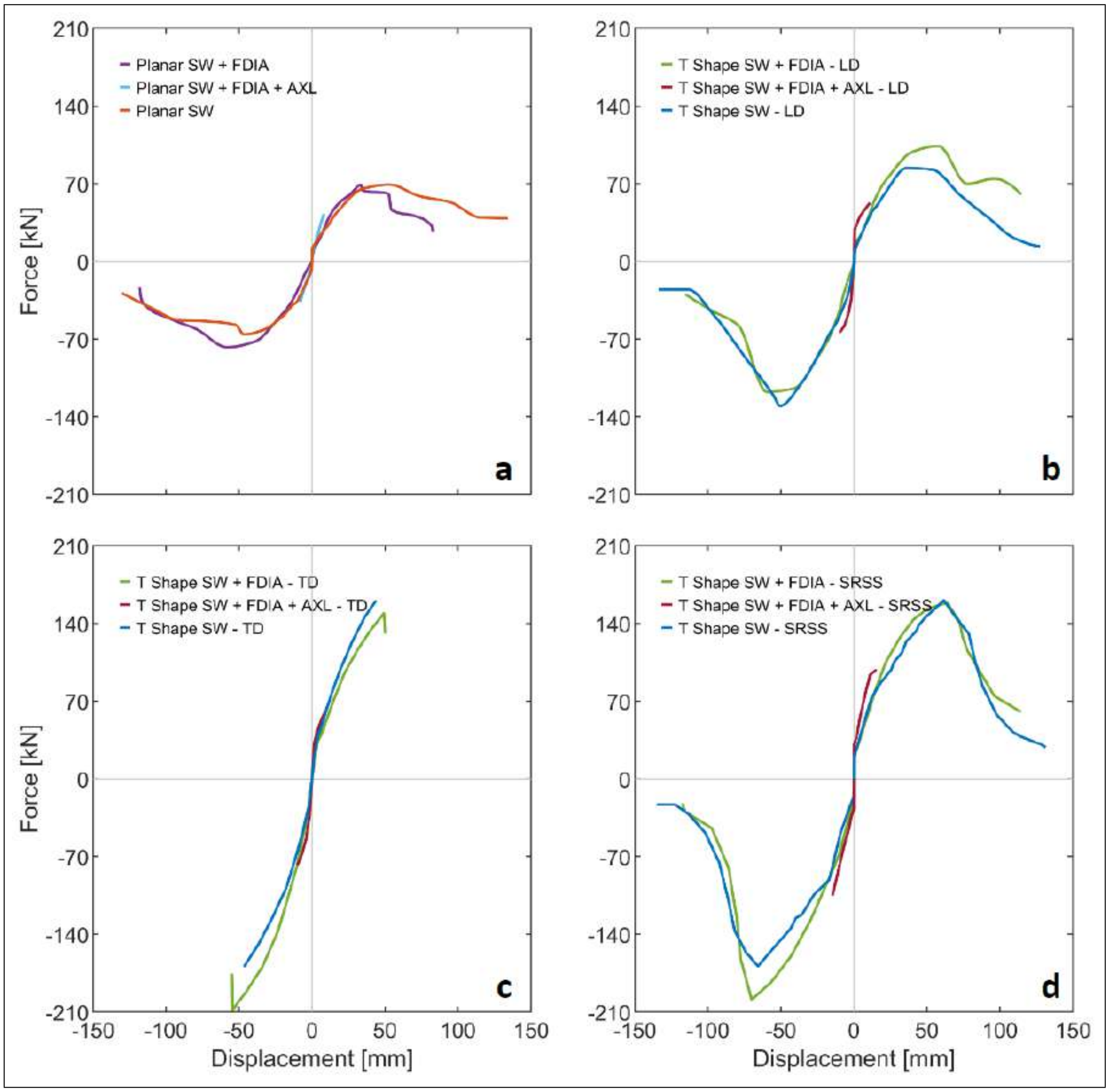

Figure 2.12. Backbone curves of (a) planar SW and T-Shape SW in the: (b) longitudinal direction (LD); (c) transverse direction; and (d) SRSS combination.

SW) and in Figures 2.26 and 2.27 (T-shaped SW) in the supplementary material. During the tests, the rods themselves responded perfectly elastically, with computed stresses about four times smaller than the nominal yield stress. However, hysteretic behavior was observed due to: (a) plastic deformation perpendicular to the grain; and (b) wood crushing under the compressive load activated by the continuous rod system. These effects

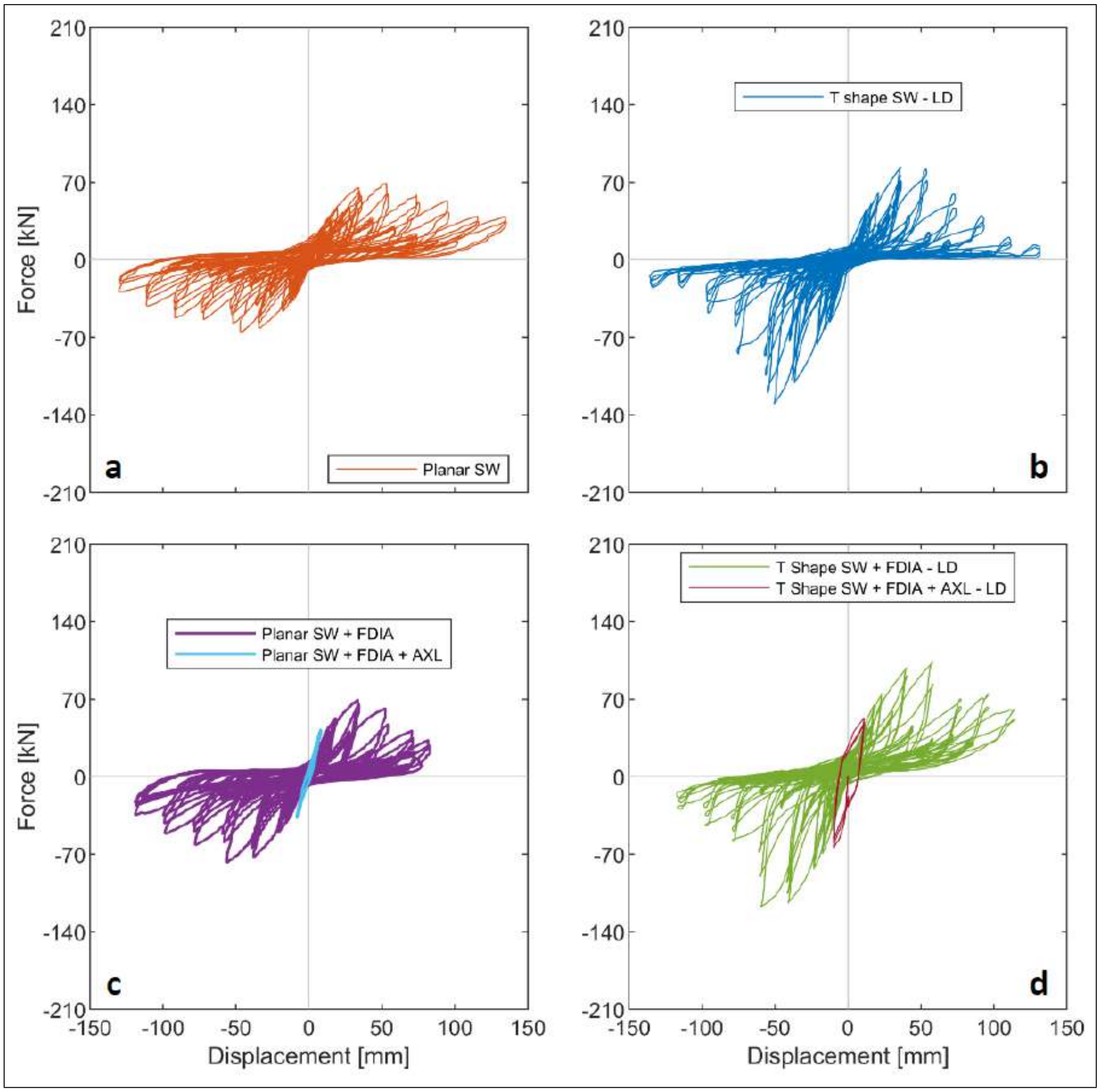

Figure 2.13. Cyclic response of (a) Planar SW and T-Shape SW in the: (b) longitudinal direction (LD); (c) transverse direction; and (d) SRSS combination.

were evident in the reaction zone on the bottom/top plate and the collector beam. Moreover, since the T-shaped SW specimens had a tridimensional response and underwent a hexagonal displacement protocol, the stress-uplifting curves exhibited a more hexagonal response (see Figures 2.16c and 2.26 and 2.27 in the supplementary material) rather than the linear response observed in the planar SW under in-plane loading protocols (Guinez

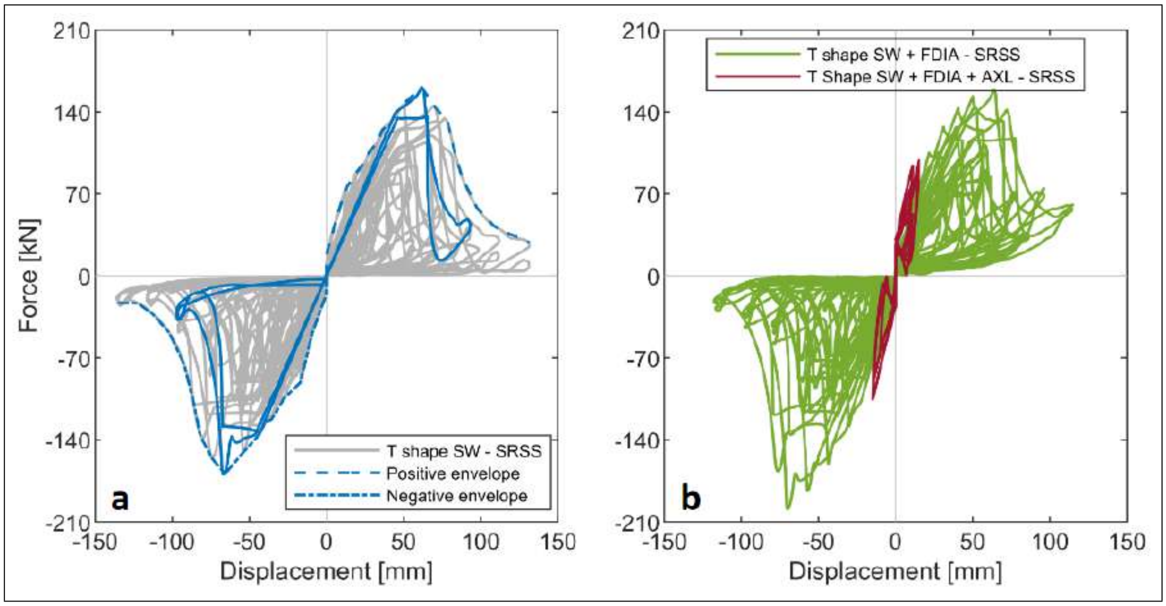

Figure 2.14. Backbone curves of (a) Planar SW and T-Shape SW in the: (b) longitudinal direction (LD), (c) transverse direction (TD), and, (d) SRSS combination.

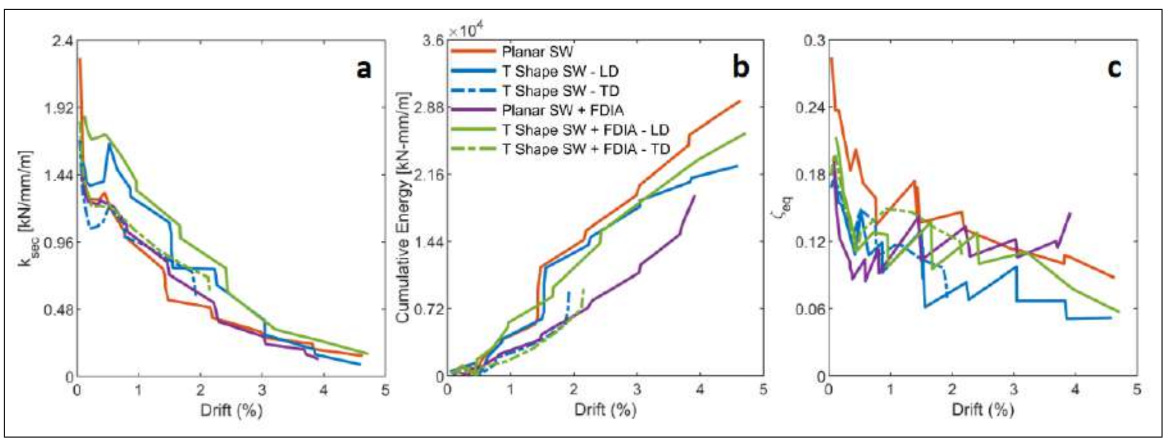

Figure 2.15. Comparisons between the (a) secant stiffness, (b) cumulative dissipated energy, and (c) equivalent viscous damping of the Planar SW and the T shape SW with different effects.

et al., 2019; Estrella, Malek, et al., 2021; Valdivieso, Guindos, et al., 2023). This bidirectional response is consistent with the expected behavior of overturning restraint systems in LFTBs under earthquake loading. Furthermore, as the compressive deformation under the bearing plate increased (see Figure 2.28 in the supplementary material), the rod also experienced some compressive stresses (illustrated in the negative y-axis of Figure 2.16). Additionally, tensile stresses were measured at the compressed corner of the wall (Figure 2.16, negative x-axis values). These tensile stresses could be attributed, at least in part, to the high levels of compressive plastic deformation at the bottom plate, which might have misaligned the kinematics of the system, causing the rod to experience some tension (Valdivieso, Guindos, et al., 2023). The maximum uplift at the corner of the T-shaped SW is approximately 35% smaller than that of the planar SW. This reduction is no doubt due to the TSW effect. Moreover, the combined TSW and FDIA effect on the T-shaped SW led to a decrease of up to 25% in maximum uplift with respect to that of the T-shaped SW without diaphragm. Similarly, the planar SW with the FDIA effect showed up to a 50% reduction in uplift compared to that of the planar SW without the FDIA effect. We therefore conclude that the FDIA effect significantly influences the kinematic response of the continuous rod system, with increasing out-of-plane bending deformation in the diaphragm collector as the lateral drift increases (see Figure 2.22 in the supplemental material). The out-of-plane bending deformation of the diaphragm, in turn, reduces the uplift in the wall, which is evident from the comparison between initial and final cycles in Figures 2.16b and 2.16d, and initial and final cycles in Figures 2.16a and 2.16c, respectively. Lastly, both the planar and the T-shaped SWs under the combined FDIA + AXL effect experienced smaller tensile stresses in the rod compared to those of the SWs without the AXL effect. These observations emphasize the significance of axial load in mitigating tensile demands in the continuous anchorage system and in reducing the contribution of racking deformation to the lateral displacement of the wall, highlighting the importance of considering the axial load at the design stage.

2.5.3. Potential impact of the findings of this study

A linear elastic analysis under lateral loading of the building model presented in Figure 2.17 was conducted to explore the impacts of the experimental findings of this investigation. The building was designed in such a way that approximately 70% of the shear walls are non-planar, which is consistent with typical building archetypes for residential LFTBs

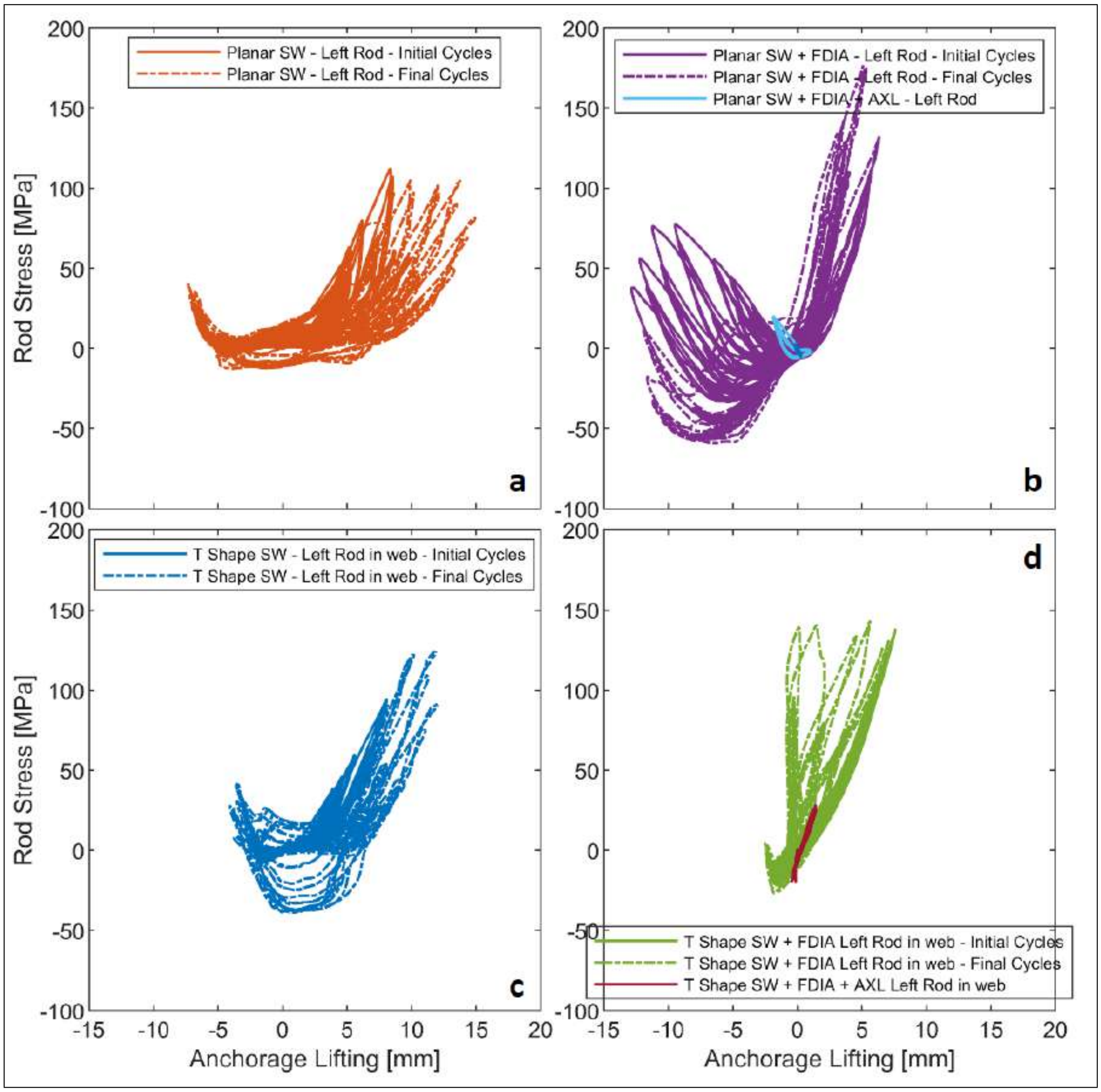

Figure 2.16. Cyclic response of the left anchorage of the Planar SW (a) without and (b) with the FDIA effect; the web in the T shape SW (c) without and (d) with the FDIA effect.

(Estrella, Guindos, et al., 2021). Because LFTBs are relatively flexible compared to concrete wall buildings, a large number of SWs are commonly required, especially when the number of stories is 6 or greater. Therefore, most SWs are not planar (isolated) but inevitably grouped in clusters of T-shaped, L-shaped, U-shaped, and X-shaped assemblies.

In this fictitious building, all clusters of SWs are T-shaped because the investigation focused on this type of non-planar SWs, but similar amounts of clusters are expected in real residential buildings. Additionally, to minimize the number of assumptions, the wall configurations *a* and *b* in Figure 2.17 had dimensions consistent with those tested and reported in Section 2.4.2 (see Figure 2.29).

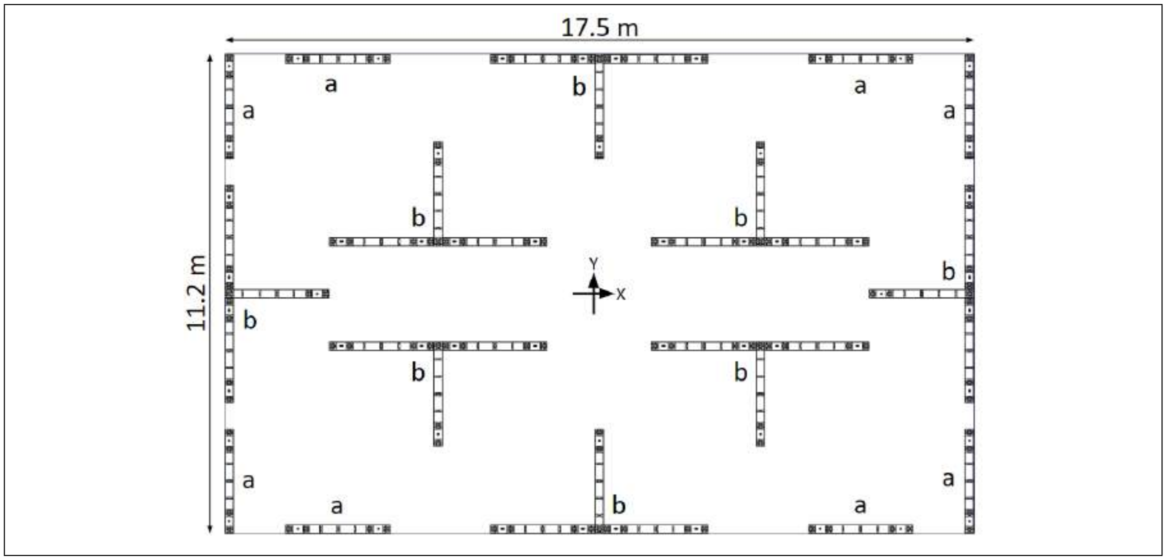

Figure 2.17. Layout of the representative LFTB story for evaluation of the TSW, FDIA, and AXL effects

To represent the in-plane stiffness of the SWs, an elastic macroelement (i.e., orthotropic shell element) was utilized, following the procedure outlined by S. Carcamo et al. (2018). The in-plane stiffness was calibrated considering the values of the elastic stiffness and the stiffness at the design drift level (i.e., 0.4%) reported in Section 2.4.2. A detailed numerical model was constructed to capture the out-of-plane stiffness of the SW in a cantilever layout. The wood frame elements were modeled using Euler-Bernoulli elastic frame elements with a nominal modulus of elasticity E = 7900 MPa according to NCh 1198 (INN, 2014). The OSB sheathing layer was represented using an elastic orthotropic shell element with shear modulus G = 1.3 GPa and modulus of elasticity E_S = 6560 MPa and E_W = 2470 MPa in the strong and weak directions, respectively (values obtained from the tests). Subsequently, the plate properties of the macroelement were adjusted based on the obtained numerical out-of-plane stiffness of the wall (EI_{OUT} = 135 kNm2/m, which is almost 100% higher than that reported for conventional SWs Winkel and Smith (2010)). The SW-to-TSW connection was modeled using a linear stiffness of 0.119 kN/mm/mm (i.e., 39.2 kN/m/330 mm = 0.119 kN/mm/mm) as measured in the tests, i.e., 39.2 kN/m, and considering the SLOT90 connectors spaced at 330 mm. Finally, the continuous rod systems were modeled using tensile-only link elements with a uniaxial elastic stiffness of 43.6 kN/mm, which was calculated using the design values provided by Simpson Strong-Tie (Simpson Strong-Tie, 2021). The wood-frame roof of the structure was modeled explicitly considering Euler-Bernoulli elastic frame elements with a nominal modulus of elasticity E = 7900 MPa according to NCh 1198 (INN, 2014). The structural details of the roof matched those outlined in Table 2.2. To focus solely on the FDIA effect and eliminate any in-plane roof deformation, we assumed that the roof's in-plane stiffness was infinite. Table 2.4 summarizes the lateral drift reduction (in the Y direction) with respect to that of a model that considers planar SWs only. Since the building incorporates symmetrically installed T-shaped SWs along the X direction, the reduction in lateral drift is about half of what is observed in the longitudinal direction of the tested T-shaped SW, owing to the TSW effect. We observed reduced uplift around individual T-shaped SWs when we focused solely on the TSW effect in our model. However, this reduction did not extend to the other SWs because we had not yet included beams in the model. Consequently, we overlooked the potential interactions between a specific T-shaped SW and the rest of the SWs. Considering the FDIA effect, there is a significant reduction in lateral drift (up to 37%) due to the out-of-plane bending stiffness of the collector beams of the diaphragms. This reduction is mainly attributed to the FDIA's role in decreasing the uplift of the walls (up to 67%). When the combined TSW + FDIA + AXL effect is considered, a reduction of up to 46% in lateral drift is observed. However, this value is smaller than what was expected based on the experimental results, possibly due to unaccounted friction effects not incorporated into the model. These friction effects might be significant when the AXL effect is considered, as previously reported by Orellana et al. (2021). The reduction of uplift in the continuous rod system is 100% relative to the uplift observed in planar SWs without any system effect, further explaining the significant reduction of the lateral drift. The evaluation of the TSW, FDIA, and AXL effects on the lateral drift reduction leads to the following findings: the FDIA and AXL effects are comparable, resulting in an additional mean reduction of 13% when comparing TSW + FDIA to TSW and TSW + FDIA + AXL to TSW + FDIA, respectively, excluding frictional effects. In contrast, the impact of the TSW effect varies based on the drift level, whether it is evaluated at the elastic level or the design drift level. Due to the variation in the TSW effect with different levels of drift, design provisions that consider the TSW effect should be in accordance with the chosen drift level for design as specified in the code.

Table 2.4. TSW, FDIA, and AXL effects on the response of the building model

Effect	Stiffness	Reduction [%]	
		Lateral Drift	Uplift of Walls
TSW	Elastic	10	-
	At 0.4% drift	20	17
TSW + FDIA	Elastic	20	50
	At 0.4% drift	37	67
TSW + FDIA+AXL	Elastic	37	100
	At 0.4% drift	46	100

2.6. Chapter Conclusions

This study investigated the system effects of transverse shear walls (TSW), out-of-plane bending stiffness of diaphragms (FDIA), and axial loading (AXL) on the lateral response of strong wood-frame shear walls (SWs) with details representative of those of mid-rise multistory light frame timber buildings located in high seismic zones. In this study, two SW-to-TSW connection type tests and three bidirectional assembly tests were carried out to explore these system effects separately and together and examine the implications for design. This study unveils significant findings in the context of wood-frame strong SW systems. It highlights that both slotted and screwed SW-to-TSW connections can effectively achieve the desired TSW effect, with a preference for slotted connections due to their ductile failure mode and ease of assembly. Furthermore, the study underscores the substantial benefits of T-shaped SWs because of the TSWs effect, significantly increasing lateral stiffness and strength compared to planar SWs. However, this enhancement comes at the expense of reduced deformation capacity, which is mitigated by the presence of FDIA and AXL effects. The FDIA has the effect of improving the symmetry in the hysteresis response, as well as the strength and stiffness of T-shaped SWs in the longitudinal direction, thereby, mitigating the issue of reduced deformation capacity, rendering T-shaped SWs a more practical choice for applications. The combined effects of FDIA + AXL significantly increased secant stiffness in T-shaped SWs in the longitudinal direction, with more substantial enhancement observed as lateral drift increased. Lastly, numerical analysis on a one-story light-frame timber building demonstrates significant reductions in lateral drift and uplift because of system effects, laying the groundwork for integrating these effects into future seismic design methods for light-frame timber buildings. It is imperative for practicing engineers to incorporate the effects of TSW, FDIA, and AXL into the design of light-frame timber buildings. This consideration is essential for mitigating the impact of conservative simplifications that currently result in significant underestimations of building stiffness, leading to underestimated seismic demands and an overestimation of the required stiffness for overturning restraint systems. These factors collectively influence structural efficiency throughout the design process. Furthermore, when designing non-planar wood-frame SWs, particular attention should be devoted to addressing the high-stress concentrations anticipated at the web-to-flange interaction. One effective strategy to mitigate this issue involves implementing a denser nail pattern in the web wall, thereby preventing premature failure modes at the OSB-to-wood frame nailed connection. Such comprehensive considerations and strategies are integral to optimizing the performance and safety of light-frame timber building structures.

2.7. Supplementary Material - Figures

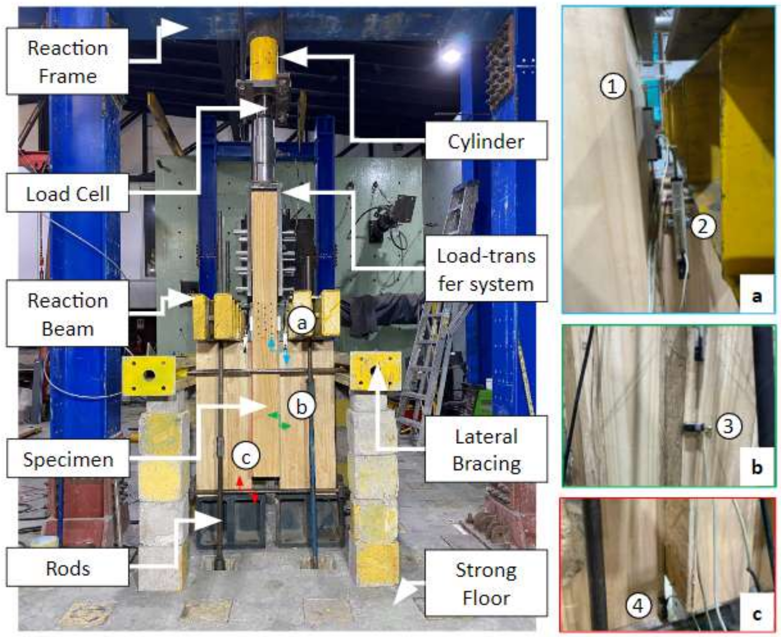

Figure 2.18. Connection setup including LVDTs (labeled as 1 to 4 in the figure) used to measure: (a) slip; (b) angle distortion between the central and the lateral elements; and (c) uplift between the specimen and the reaction steel beam. Specifically, two displacement transducers (LVDTs) were used to measure the OSB slip relative to the central element (labeled “1”). Additionally, four LVDTs were strategically positioned on each specimen (two per shear plane) to measure the total slip of the connection (labeled “2”). Two LVDTs (one per shear plane) were installed to monitor the detachment of the lateral element from the central element (labeled “3”). Furthermore, two LVDTs were employed to measure the specimen uplift relative to the strong floor (labeled “4”). The shear force between the end studs was measured using a double-effect load cell.

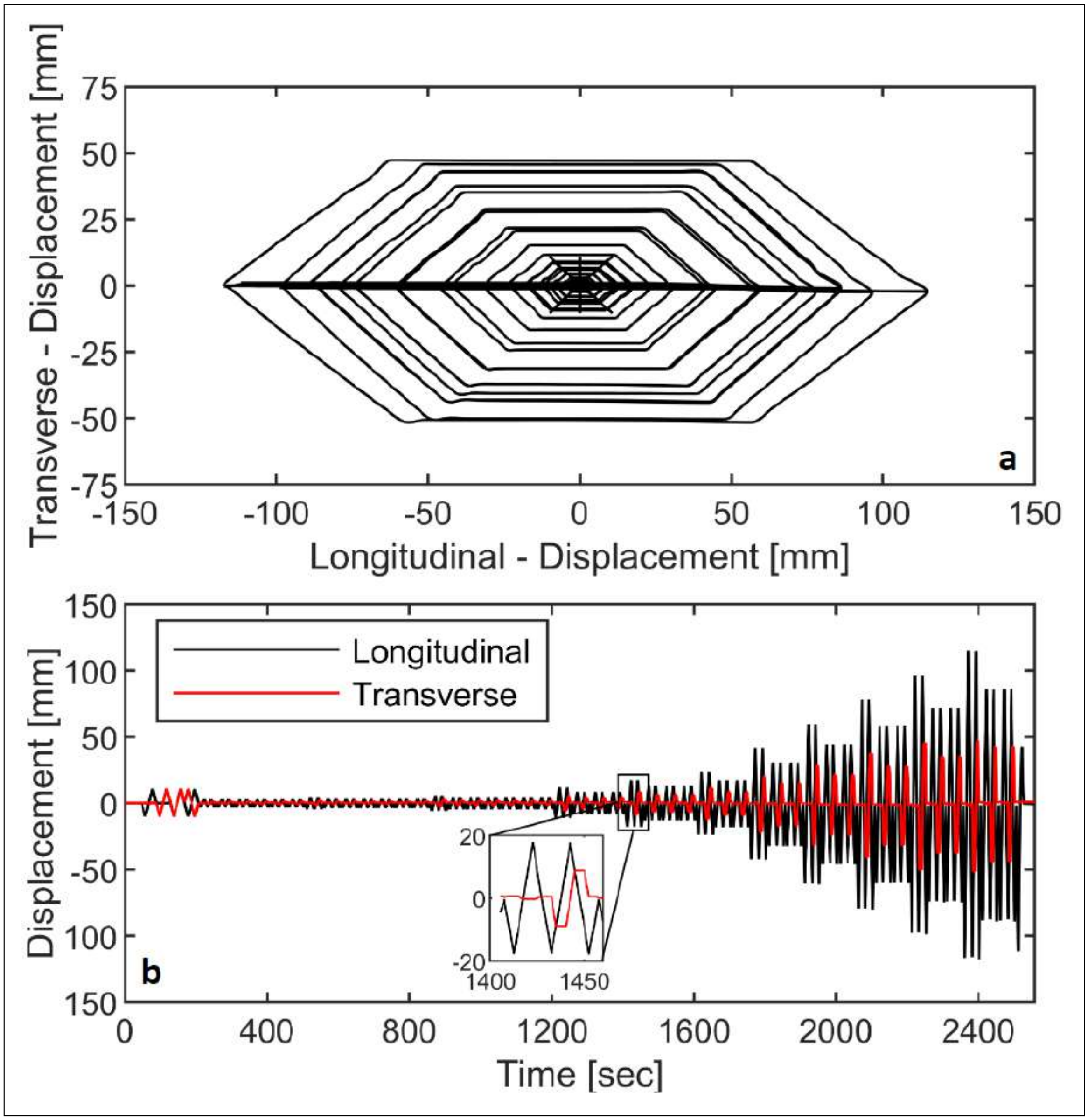

Figure 2.19. (a) Hexagonal testing protocol applied to the assembly-level specimen and (b) detail of the longitudinal and transverse displacement components of the hexagonal protocol.

Figure 2.20 illustrates the instrumentation used for capturing the evaluated system effects. These instruments measured lateral displacement and shear force along each axis (elements 1 and 2 in Figure 2.20). The slip between the wall and the steel reaction beam (elements 6 and 8 in Figure 2.20), the diagonal (shear) deformation (element 4 in Figure 2.20), and the uplift at the exterior edge of the wall (element 5 in Figure 2.20) were also recorded. Additionally, the out-of-plane displacement of the web of the T-shaped SW (element 10 in Figure 2.20), the relative displacement between the steel reaction beam and the strong floor (element 7 in Figure 2.20), and the compressive deformation under the bearing plate of the strong-rod system (element 3 in Figures 2.20) were measured. Furthermore, seven unidirectional strain gauges were attached to the rods of the continuous hold-down to measure tension (element 11 in Figure 2.20). In addition to the measuring layout described in the former paragraph, additional devices were used in the specimen with a diaphragm. In order to control the applied axial load on the structure, a load cell and a cylinder were employed (element 12 in Figure 2.20). Four LVDTs were used to monitor the out-of-plane deformation of the diaphragm span between the planar SW and the T-shaped SW. Furthermore, as the lateral bracing was eliminated for the evaluation of the FDIA and AXL effects, the out-of-plane displacement of the planar SW was monitored (element 13 in Figure 2.20).

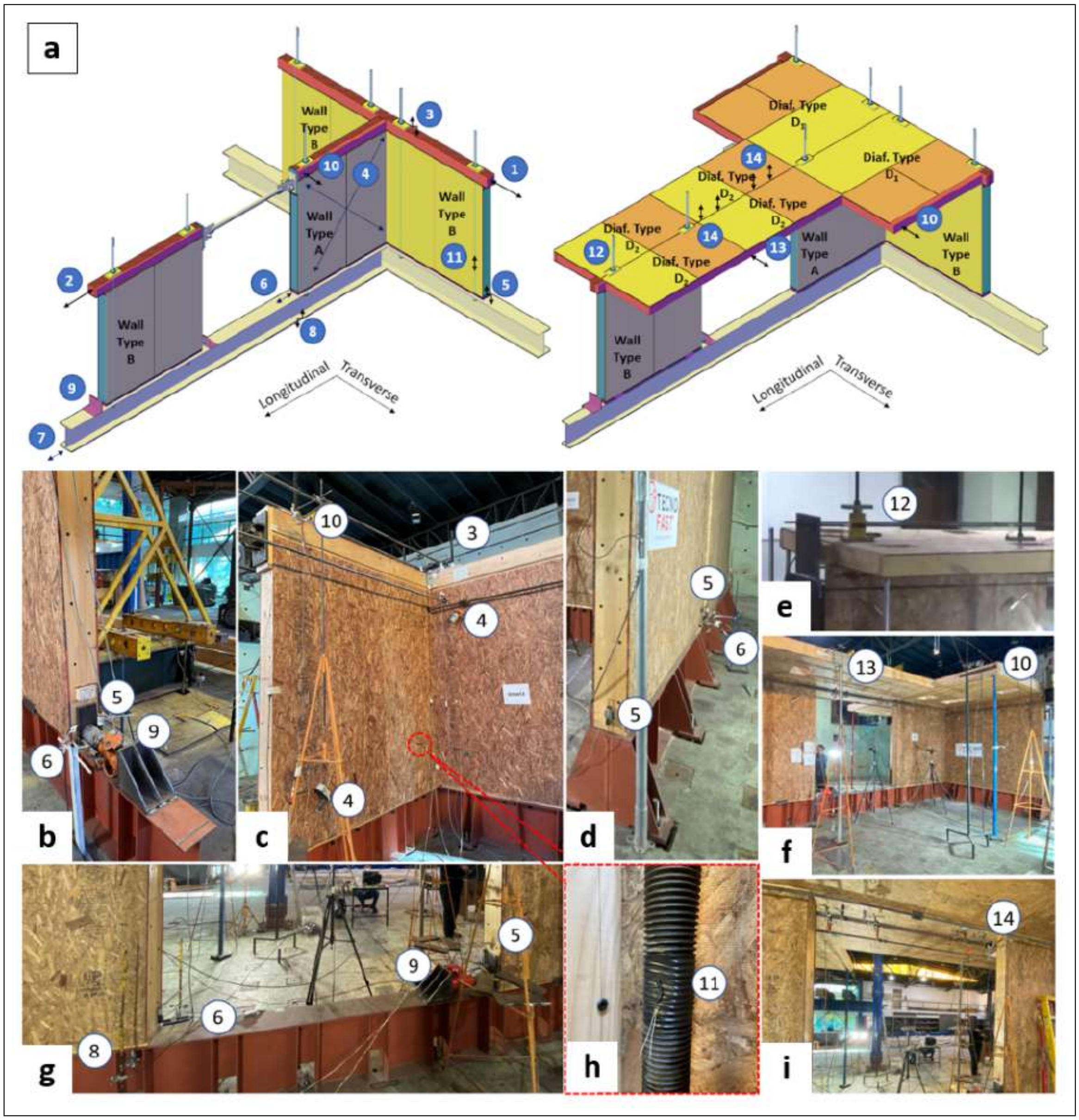

Figure 2.20. Test layouts of the SW assemblies including LVDTs and strain gauges (labeled 1 to 14 in the figure): (a) general layout with and without diaphragm. The diaphragm was made up of two type D_1 and four type D_2 diaphragms according to Table 2.2; (b) sliding restraint system and overturning measurement for the planar (isolated) SW. Zoomed views of instrumentation: (c) front view and (d) transverse view of the T-shaped SW assembly; (e) cylinder installation to control the axial (gravity) load on the SWs. Displacement tracking: (f) out-of-plane SW displacements measured at the diaphragm; (g) sliding and overturning displacement tracking at SWs; (h) strain gauge installation in a rod; and (i) measurement of out-of-plane diaphragm bending.

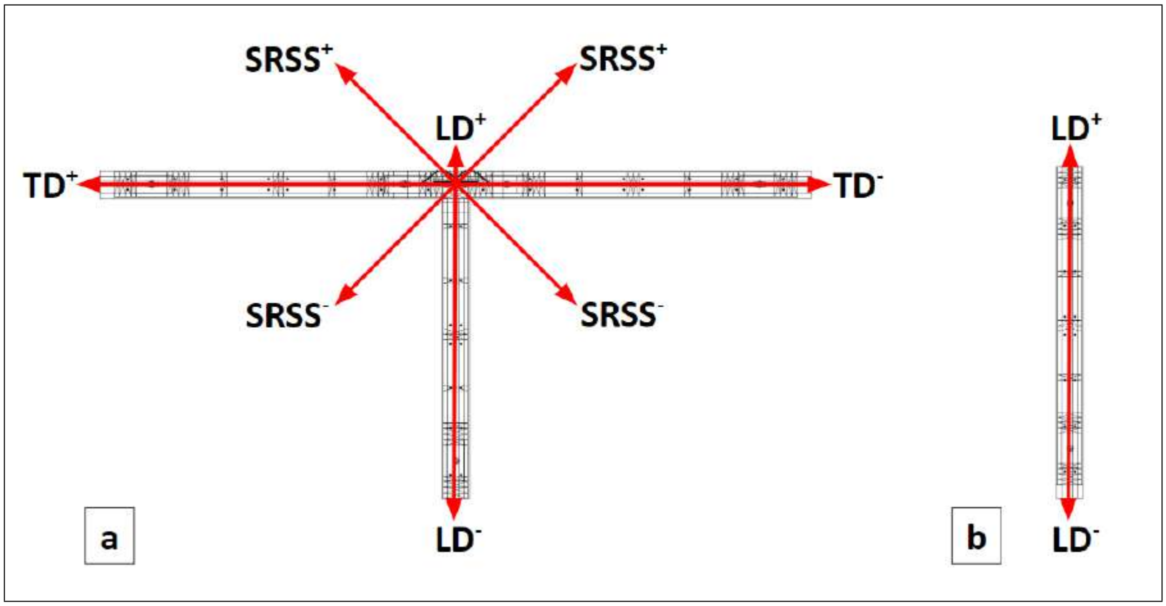

Figure 2.21. Identification of the analysis directions of the (a) T shape SW and (b) Planar SW. LD is the longitudinal direction, TD is the transverse direction, and, SRSS is the diagonal direction at 45 degrees.

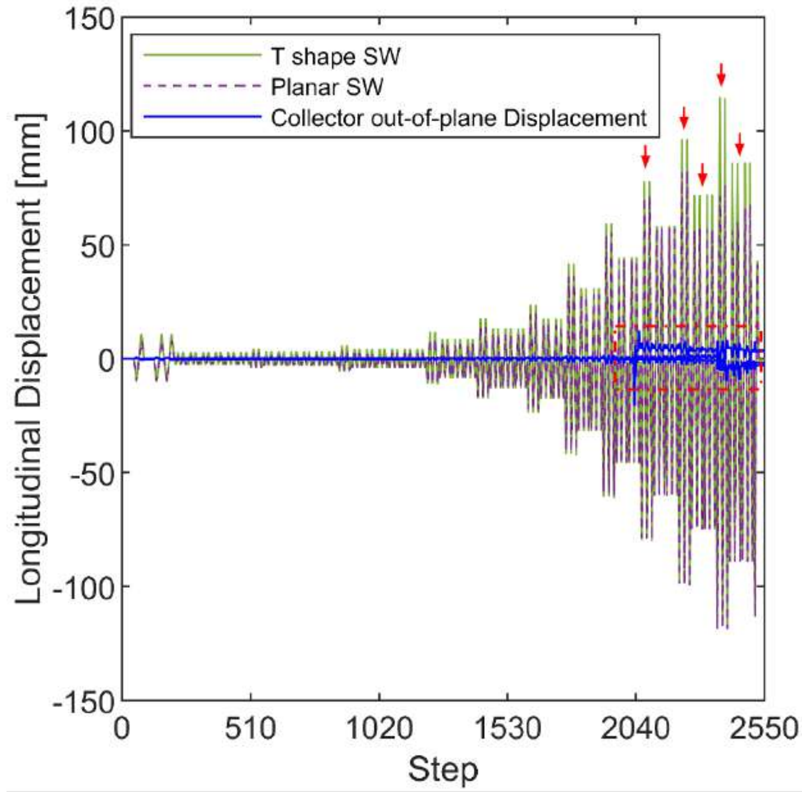

Figure 2.22. Evolution of the reduction in longitudinal lateral displacement of the Planar shear wall as the out-of-plane bending deformation of the diaphragm's collector occurs.

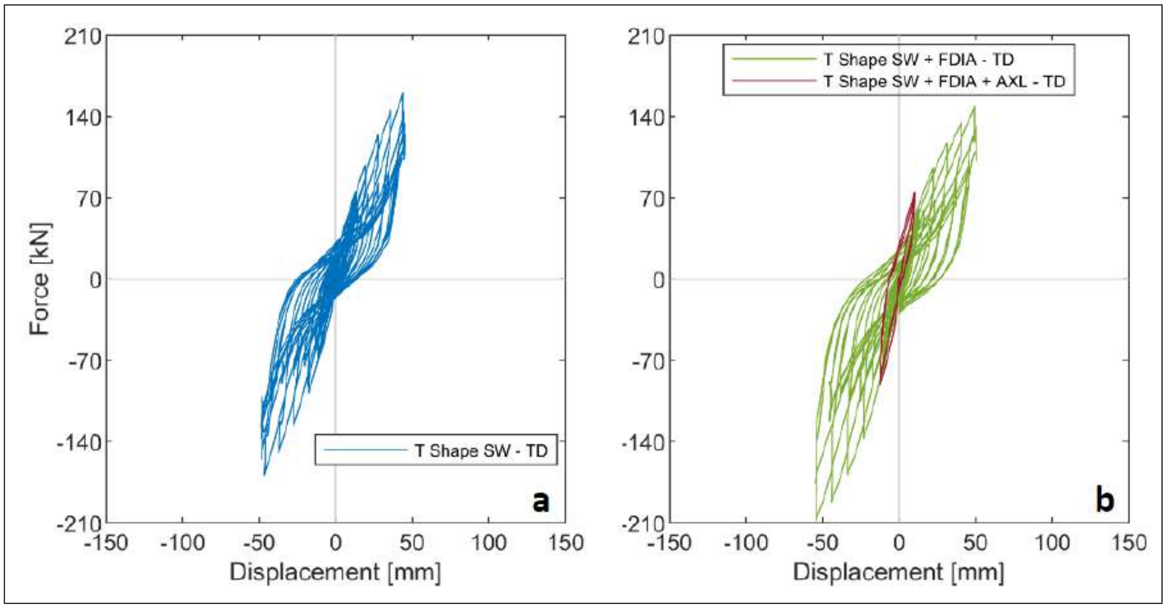

Figure 2.23. Cyclic response in the transverse direction of the T shape SW considering the effect of(a) TSWs and (b) FDIA + AXL.

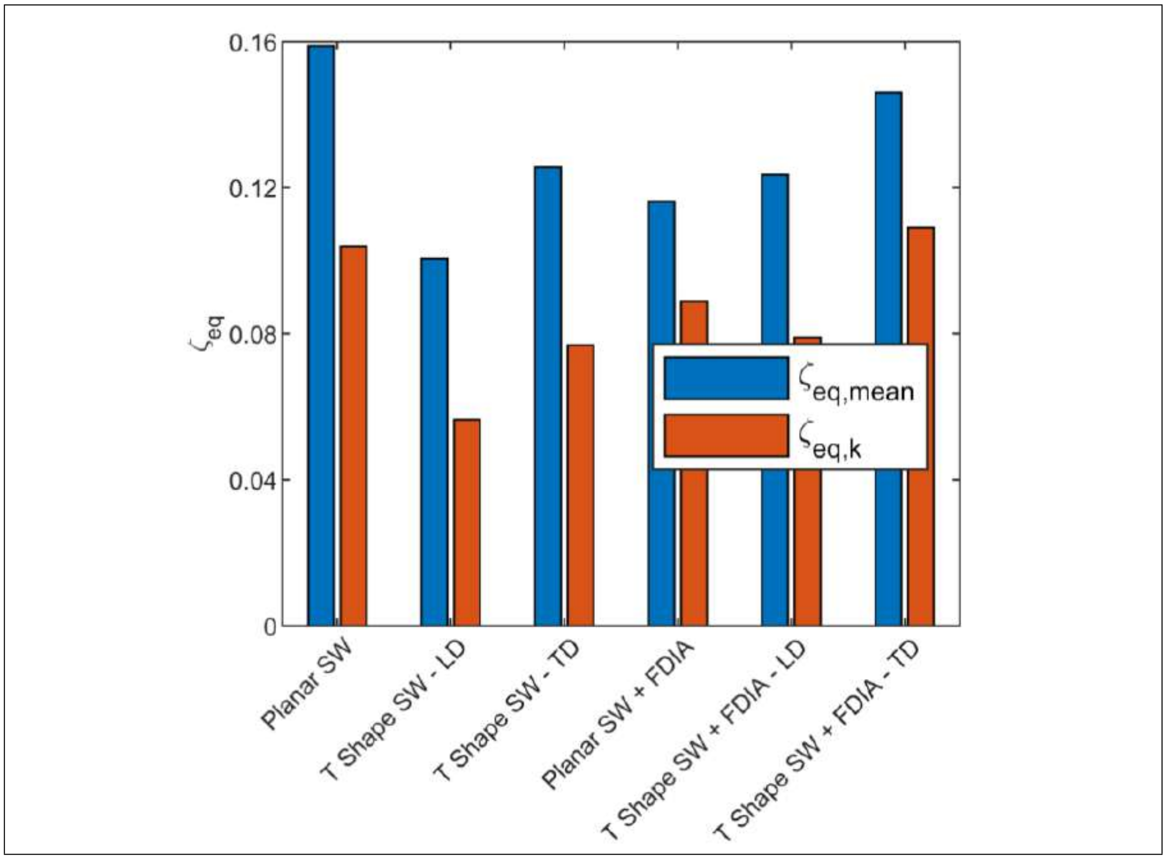

Figure 2.24. Cyclic response in the transverse direction of the T shape SW considering the effect of(a) TSWs and (b) FDIA + AXL.

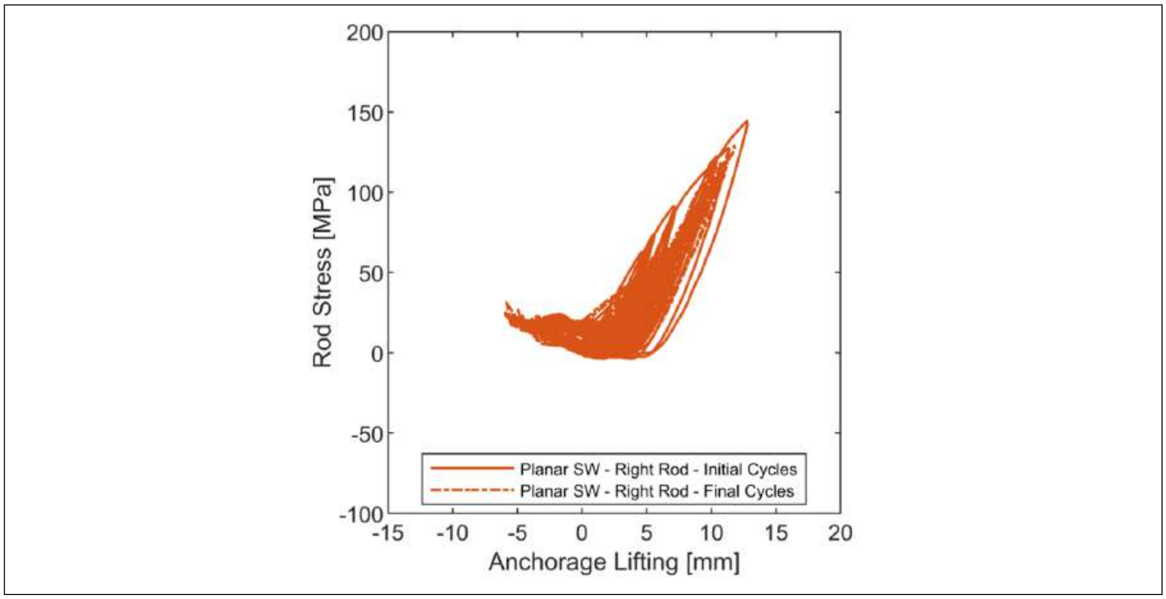

Figure 2.25. Cyclic response of right anchorage of the Planar SW.

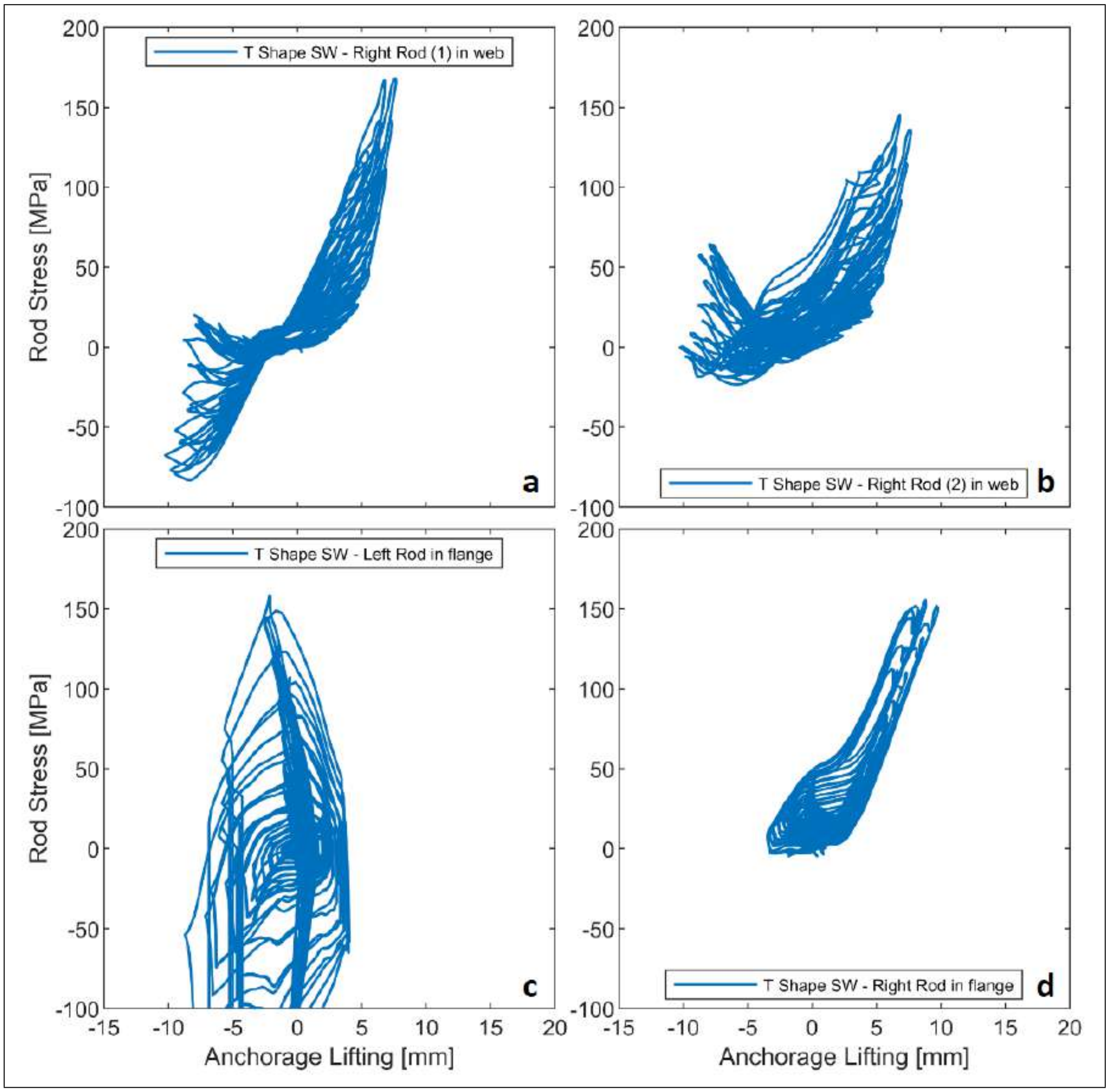

Figure 2.26. Cyclic response of the (a) first right anchorage in web, (b) second right anchorage in web, (c) left anchorage in flange, and, (d) right anchorage in flange of the T shape SW.

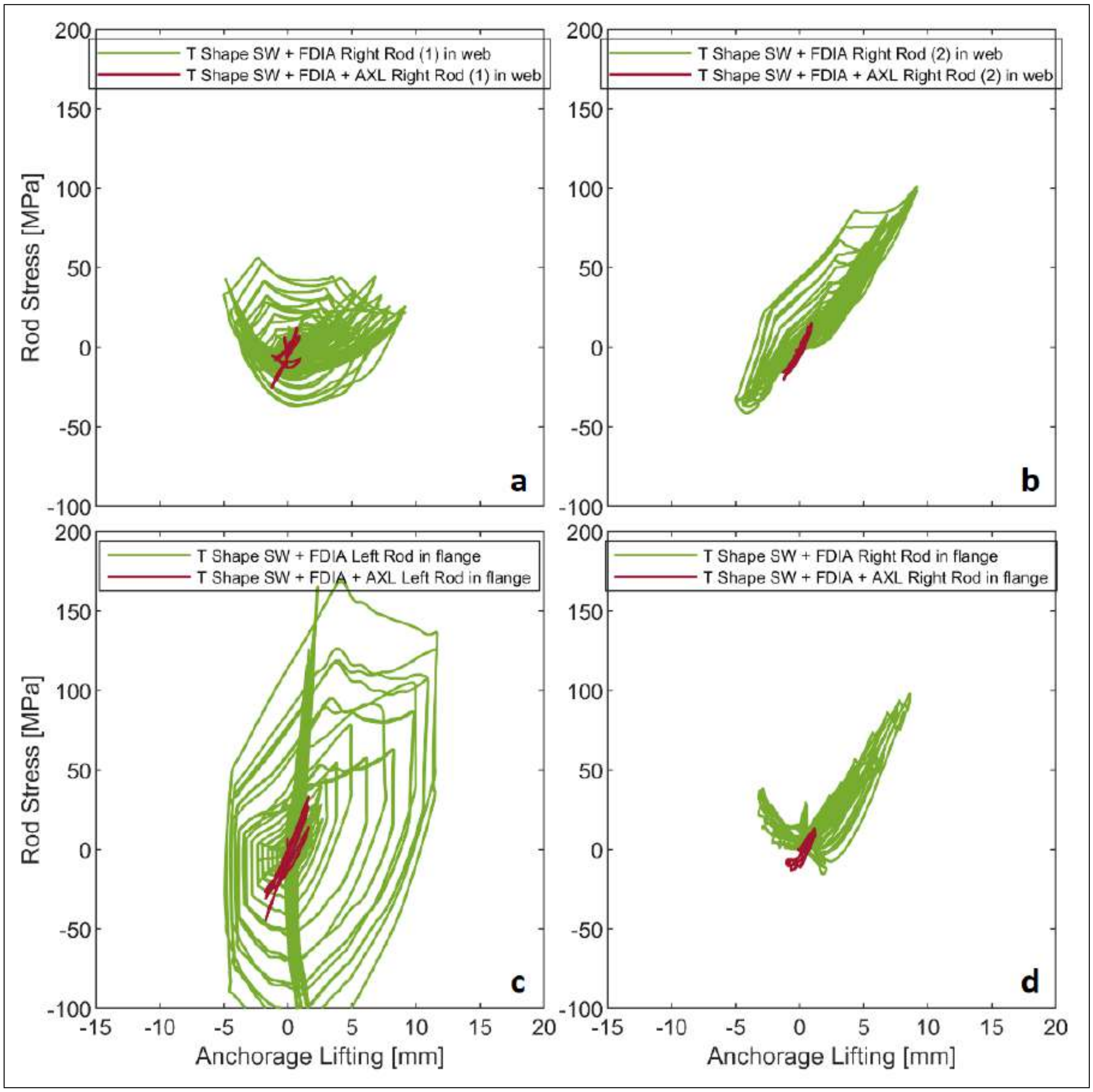

Figure 2.27. Cyclic response of the (a) first right anchorage in web, (b) second right anchorage in web, (c) left anchorage in flange, and, (d) right anchorage in flange of the T shape SW considering the out-of-plane bending stiffness of the diaphragm (FDIA effect).

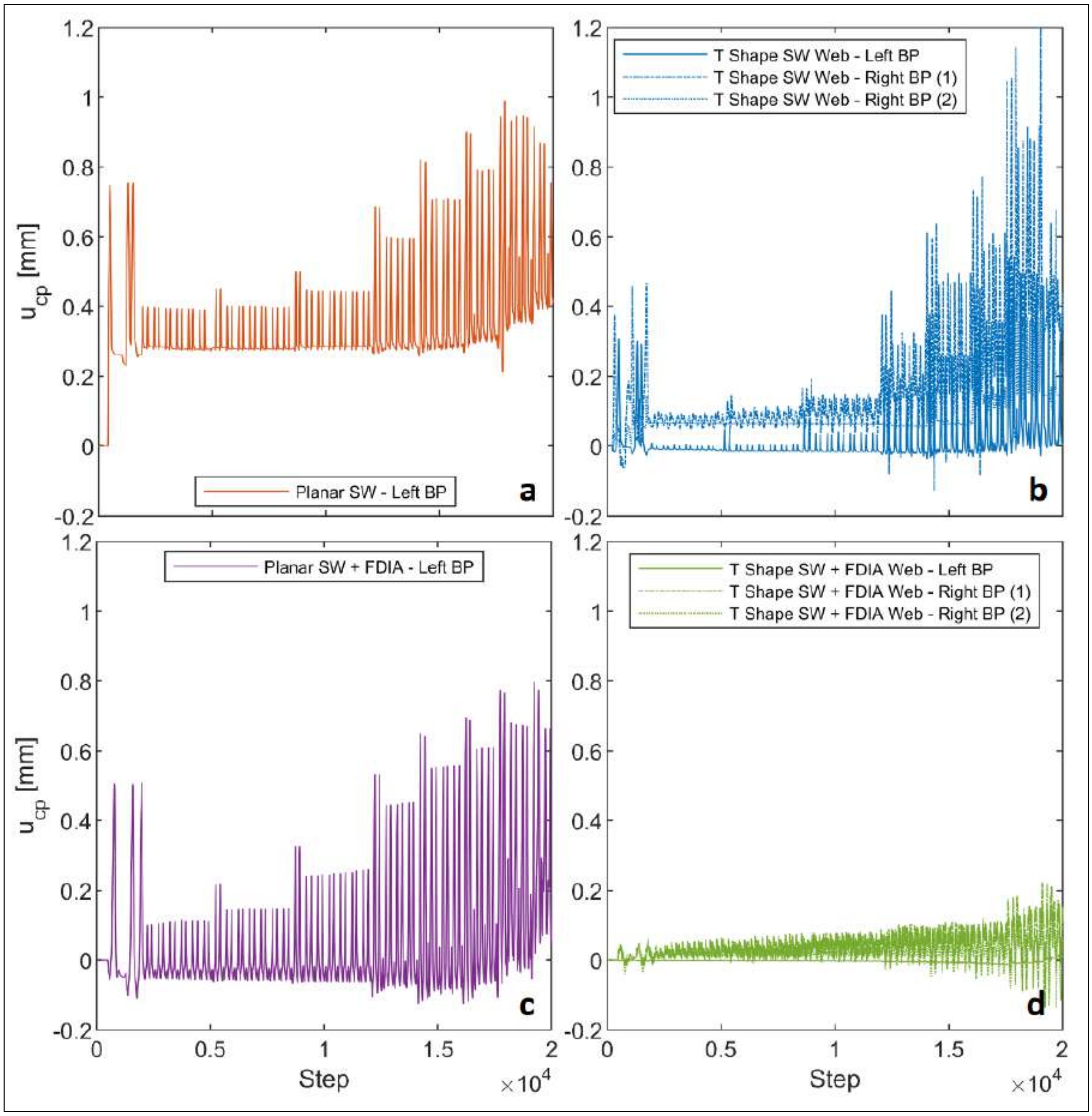

Figure 2.28. Evolution of the deformation under the bearing plate located on the collector beam at the location of the continuous rod system for (a) Planar SW and (b) T shape SW without diaphragm, and, (c) Planar SW and (d) T shape SW with diaphragm.

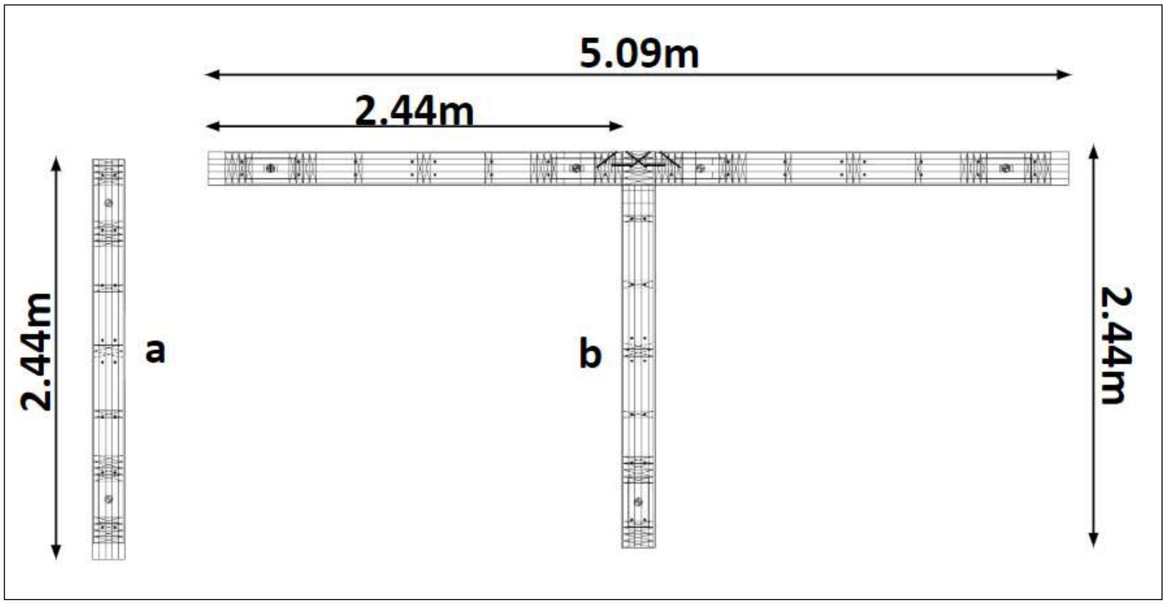

Figure 2.29. General dimension of wall type "a" and "b" used for the numerical model.

2.8. Supplementary Material - Tables

Table 2.5. Engineering parameters from backbone curves test results

Studied Effect	SW Conf.	$K_{0.2\%}$ kN/mm	$K_{0.4\%}$ kN/mm	K_e kN/mm	Δ_y mm	F_y kN	Δ_u mm	$F_{0.2\%}$ kN	$F_{0.4\%}$ kN	F_u kN	F_{peak} kN
	T shape SW LD+	4.85	3.87	4.05	18.9	76.3	68.6	24.1	38.4	67.3	84.1
	T shape SW LD -	6.75	5.00	4.83	22.7	109.4	64.3	33.5	49.7	104.2	130.2
	T shape SWmean LD	5.80	4.44	4.44	20.8	92.9	66.5	28.8	44.1	85.8	107.2
	T shape SW TD +	8.58	6.28	6.19	-	-	-	42.6	62.3	-	160.9
TSW	T shape SW TD -	8.26	6.54	6.41	-	-	-	41.0	64.9	-	169.5
	T shape SWmean TD	8.42	6.41	6.30	-	-	-	41.8	63.6	-	165.2
	T shape SW SRSS +	8.68	6.62	6.76	19.5	132.0	79.3	43.1	65.7	128.8	161.0
	T shape SW SRSS -	6.63	5.27	5.55	25.3	140.5	82.1	32.9	52.3	135.2	169.0
	T shape SWmean SRSS	7.66	5.95	6.16	22.4	136.3	80.7	38.0	59.0	132.0	165.0
	Planar SW+	4.44	3.09	3.58	17.1	61.3	88.0	22.0	30.6	55.3	69.1
-	Planar SW-	4.48	3.56	4.06	13.8	55.9	92.4	22.3	35.3	52.6	65.8
	Planar SWmean	4.46	3.33	3.82	15.5	58.6	90.2	22.2	33.0	54.0	67.5
	T shape SW LD +	4.90	4.02	4.00	21.8	87.1	95.2	24.3	39.9	83.1	103.9
	T shape SW LD-	4.11	4.46	4.45	24.1	106.9	63.0	20.4	44.2	94.1	117.6
	T shape SWmean LD	4.51	4.24	4.23	23.0	97.0	79.1	22.4	42.1	88.6	110.8
	T shape SW TD +	7.40	5.27	5.05	-	-	-	36.7	52.3	-	149.1
TSW+FDIA	T shape SW TD -	9.16	7.70	7.42	-	-	-	45.5	76.4	-	208.4
	T shape SWmean TD	8.28	6.49	6.24	-	-	-	41.1	64.4	-	178.8
	T shape SW SRSS +	10.54	6.27	5.92	24.4	144.2	74.6	52.3	62.2	127.0	158.8
	T shape SW SRSS -	8.65	6.78	5.83	28.7	167.4	78.0	42.9	67.3	159.3	199.1
	T shape SWmean SRSS	9.60	6.53	5.88	26.6	155.8	76.3	47.6	64.8	143.2	179.0
	Planar SW+	3.95	3.52	3.63	16.8	60.9	53.4	19.6	34.9	55.2	69.0
FDIA	Planar SW-	2.33	2.63	2.65	26.2	69.5	77.9	11.6	26.1	61.9	77.4
	Planar SWmean	3.14	3.08	3.14	21.5	65.2	65.7	15.6	30.5	58.6	73.2
	T shape SW LD +	8.54	5.15	9.15	-	-	-	42.4	51.1	-	-
	T shape SW LD-	10.60	6.48	12.66	-	-	-	52.6	64.3	-	-
	T shape SWmean LD	9.57	5.82	10.91	-	-	-	47.5	57.7	-	-
	T shape SW TD +	10.34	7.30	8.65	-	-	-	51.3	72.4	-	-
TSW+FDIA+AXL	T shape SW TD -	10.89	8.06	7.84	-	-	-	54.0	80.0	-	-
	T shape SWmean TD	10.62	7.68	8.25	-	-	-	52.7	76.2	-	-
	T shape SW SRSS +	12.20	9.01	11.63	-	-	-	60.6	89.4	-	-
	T shape SW SRSS -	10.57	7.86	7.80	-	-	-	52.4	78.0	-	-
	T shape SWmean SRSS	11.39	8.44	9.72	-	-	-	56.5	83.7	-	-
	Planar SW+	5.87	4.18	5.95	-	-	-	29.1	41.5	-	-
FDIA+AXL	Planar SW-	4.50	4.35	4.58	-	-	-	22.3	43.2	-	-
	Planar SWmean	5.19	4.27	5.27	-	-	-	25.7	42.4	-	-

3. CHAPTER 3 - SHAKE TABLE TESTING FOR SYSTEM EFFECTS ANALYSIS IN A 1:2 SCALE THREE-STORY LIGHT FRAME TIMBER BUILDING

3.1. Introduction

The seismic vulnerability of Light-Frame Timber Buildings (LFTBs) is of significant concern, particularly in earthquake-prone regions. Events like the 1994 Northridge Earthquake, which caused extensive damage and loss of life in some kinds of LFTBs, underscore the need for a deeper understanding of the seismic behavior of these structures (Filiatrault et al., 2001, 2002; van de Lindt, 2008; van de Lindt, Pei, Pryor, et al., 2010; van de Lindt, Pei, Liu, & Filiatrault, 2010; van de Lindt et al., 2011). Recently, there has been increasing interest in mid-rise (i.e., up to 7 stories) timber buildings to address housing shortages in many parts of the world. This interest has been supported by public authorities, academia, and the industry, especially in seismic-risk areas like Chile. Moreover, the structural configuration of such residential buildings in Chile is different from structural configurations found in other countries. The key difference is the typical floor plan pattern of Chilean buildings, referred to in the literature as "fish-bone" pattern (Ugalde & Lopez-Garcia, 2020), where non-planar strong wood-frame shear walls and floor/roof diaphragms are used as both lateral and gravitational load-resisting systems. However, existing design methods, such as the analytical model presented in the Special Design Provisions for Wind and Seismic (AWC, 2021), often rely on simplified approaches that neglect the interactions between structural components in these configurations. These design simplifications lead to underestimated building stiffness, which in turn leads to stronger structural components to satisfy story drift requirements. As a result, further research is needed to understand the seismic response of LFTBs. Shake table testing has proven to be a highly effective method to evaluate the seismic performance of full-scale wood frame buildings, as evidenced by extensive previous research (Ceccotti, 2008; Ceccotti et al., 2013; Casagrande et al., 2016; Filiatrault et al., 2001; Fiorino et al., 2017; Isoda et al., 2021; Tomasi et al., 2015; van de Lindt, 2008; van de Lindt, Pei, Pryor, et al., 2010; van de Lindt, Pei, Liu, & Filiatrault, 2010; van de Lindt et al., 2011;

Ventura et al., 2023; Quizanga et al., 2024). Historically, much of this research focused on the response of LFTBs with different shear wall sheathing materials, mirroring standard construction practices in North America and Europe (Ceccotti, 2008; Ceccotti et al., 2013; Casagrande et al., 2016; Filiatrault et al., 2001, 2002, 2010; Fiorino et al., 2017; van de Lindt & Liu, 2007; van de Lindt, 2008; van de Lindt, Pei, Pryor, et al., 2010; van de Lindt, Pei, Liu, & Filiatrault, 2010; van de Lindt et al., 2011; Ventura et al., 2023). However, in recent studies the focus shifted towards a deeper understanding of the interaction between structural components in realistic building configurations including those found in other parts of the world (Ceccotti, 2008; Ceccotti et al., 2013; E. M. Ruggeri et al., 2023; Sartori et al., 2012; Tomasi et al., 2015; Valdivieso, Guindos, et al., 2023; Valdivieso, Lopez-Garcia, et al., 2023). The concept of ”system effects” in building structures, often referred to as the ”box effect” (Ceccotti et al., 2013), plays a crucial role in understanding how various structural elements interact with each other within a building (Martin et al., 2011; Valdivieso, Lopez-Garcia, et al., 2023). In this paper, we use “system effects” to refer to: a) the effect of the transverse shear walls on non-planar shear walls; b) the influence of the out-of-plane bending stiffness of diaphragms; and c) the effect of gravity loading on structural components. Tomasi et al. (2015) emphasized the essential need to incorporate these system effects into the seismic design of LFTBs. They showed that the behavior of individual structural walls can be significantly altered by their connections to and interactions with other elements. Isoda et al. (2021)’s experimental work Benedetti et al. (2022)’s numerical studies likewise demonstrated that tests on isolated planar shear walls fail to replicate the system effects observed in actual building configurations. In component-level research, Valdivieso, Lopez-Garcia, et al. (2023) carried out experimental studies on the behavior of non-planar T-shaped shear walls, designed assuming that they are part of a 7-story building that complies with the Chilean seismic design standard NCh 433 (INN, 2009). This latter investigation revealed significant differences between the stiffness, peak strength, and deformation capacity of non-planar T-shaped shear walls and those of planar shear walls. The findings emphasize the critical role of boundary shear walls, also known as system effect, in the response of non-planar wood-frame shear walls. Likewise, Orellana et al. (2021) studied the effects of high gravitational forces on the cyclic response of wood-frame shear walls, noting improvements in stiffness, peak strength, damping ratio, and ductility. These improvements in engineering parameters were attributed to changes in OSB-to-wood frame connections and framing interactions, including an unknown frictional effect. Their numerical analysis of mid-rise LFTBs showed a 6.7% decrease in the fundamental period when the gravity load effect is considered, underscoring the significant impact of the gravity load on the dynamic properties of LFTBs. Various numerical and analytical models have been developed to simulate the seismic response of mid-rise LFTBs (Folz & Filiatrault, 2004a; Pei & van de Lindt, 2009, 2011; W. Pang & Hassanzadeh Shirazi, 2013; Tomasi et al., 2015; AWC, 2021), but they often struggle to accurately represent system effects due to interconnected elements. It is crucial to overcome these challenges to improve the accuracy of analytical predictions (van de Lindt, Pei, Pryor, et al., 2010; Benedetti et al., 2022): current state-of-the-art models (Pei and van de Lindt (2009); W. Pang and Hassanzadeh Shirazi (2013) have been shown to accurately capture the behavior of low-rise LFTBs with smaller footprints only (i.e., limited interaction between components) (Pan et al., 2021). This paper emphasizes the importance of exploring system effects in LFTBs to improve the assessment of their seismic lateral response. We do so by leveraging data from shaking table experiments and numerical modeling to illustrate how interactions among structural components are critical to refine seismic design methods, especially in areas that are prone to earthquakes.

3.2. Method

3.2.1. Specimen

The test specimen is a 3-story LFTB representative of a residential building designed in compliance with the Chilean seismic design standards (INN, 2009). Due to the limitations of shake table testing equipment available in Chile, the specimen was constructed at a 1:2 scale, with its structural elements being half the size of those in an actual building.

However, the OSB sheathing and the wood frame could not be scaled due to market limitations. To address this issue, the spacing of the nailed connections was increased to reduce the lateral stiffness and strength of the shear walls, thereby compensating for the scaling limitation. The footprint of the test specimen is 1960 mm by 2760 mm and features an L- and U-shaped non-planar shear walls, along with a planar wall (Figure 3.1-b). The lateral resisting system consists of light-frame timber diaphragms and shear walls anchored with hold-downs, constructed using a platform system approach (detailed in Tables 3.1 and 3.2). To provide effective interaction between longitudinal and transverse shear walls of the non-planar L-shaped and U-shaped walls, the W_1-to-W_2 perpendicular connections were designed to have a local x-axis stiffness that is at least 40% of the in-plane stiffness of wall W_1 (Valdivieso, Lopez-Garcia, et al., 2023). To achieve this stiffness, we used 4 timber screws ESCRFTZ 8.0 mm x 300 mm, installed at a 45º angle, for this purpose.

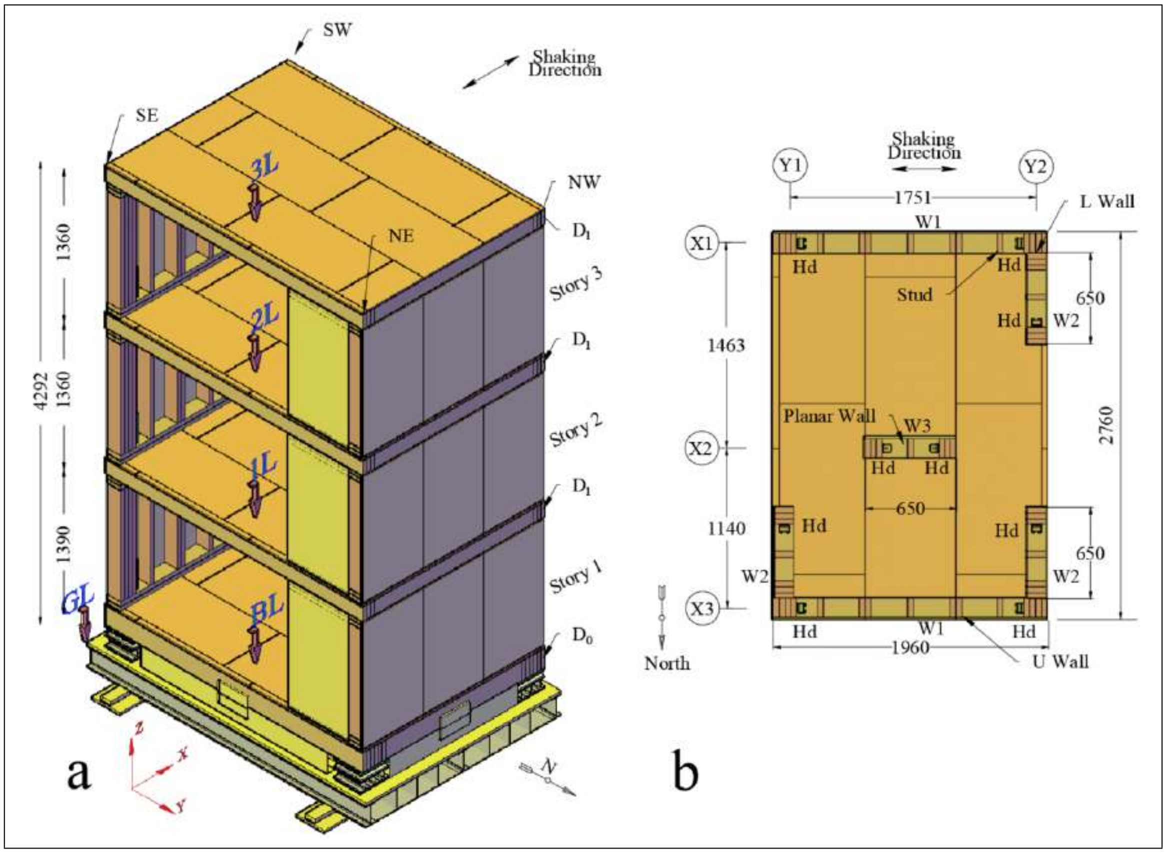

Figure 3.1. (a) Isometric view and (b) top-down layout of each story. See notation in Tables 1 and 2. All dimensions are in millimeters.

Table 3.1. Wall-type configuration by story (see Figure 3.1). All dimensions are in millimeters.

Wall Type	OSB Sheathing[c]		Hold-down (Hd)[d]			# of end-studs
	Sheathing nail[e]	Spacing edge/field	Type	Rod Diameter [in]	Location	
		150/300	HDQ8-SDS3	7/8		
W_1[a]	ϕ2.9x80	200/400	HTT5	5/8	both-sides	4
		200/400	HTT4	5/8		
		100/200	HDQ8-SDS3	7/8		
W_2[b]	ϕ2.9x80	150/300	HTT5	5/8	one-side	3
		200/400	HTT4	5/8		
		150/300	HDQ8-SDS3	7/8		
W_3[b]	ϕ2.9x80	200/400	HTT5	5/8	both-sides	3
		200/400	HDI	5/8		

[a] Wall framing: 41mm x 138 mm (2x6) C16 Chilean radiata pine as per NCh 1198 (INN, 2014) studs at 315 mm to 325 mm o.c., (2) 41mm x 138 mm used as an intermediate stud (at the joint of OSB panels), end-studs are formed by (4) 41mm x 138 mm studs mechanically joined and located at the edge of the walls.

[b] Wall framing: 41mm x 138 mm (2x6) C16 Chilean radiata pine as per NCh 1198 (INN, 2014) studs at 315mm o.c., end-studs are formed by (3) 41mm x 138 mm studs mechanically joined and located at the edge of the walls.

[c] A single 11.1 mm thick layer of OSB sheathing is installed on one side of the shear walls by APA (2012).

[d] Wall shear anchorage: Simpson Strong-Tie SDWS19600 at 100 mm o.c. Overturning restraint provided by Simpson Strong-Tie hold-downs attached to the end-studs using SDS25312 or SD10112 screws as per manufacturer recommendations.

[e] Spiral nails, as per EN14592:2008+A1:2012 (BSI, 2008), pneumatically driven to the frame with minimum end/edge distance of 20/40 mm, respectively.

Table 3.2. Configuration of the diaphragms (see Figure 3.1). All dimensions are in millimeters.

Diaphragm Type	Diaph. size (L by W)	Plywood Sheathing[c]	
		Sheathing nail[d]	Spacing (edge/edge/field)
D_0[a]	2760x1960	ϕ3.0x80	150/150/300
D_1[b]	2760x1960	ϕ3.0x80	150/150/300

[a] Diaphragm framing: 41mm x 185 mm (2x8) C16 Chilean radiata pine (INN, 2014) beams at 300mm o.c., (3) 41mm x 185 mm used as a central beam, (4) 41mm x 185 mm as perimeter beams, end-beams formed by (6) 41mm x 185 mm beams mechanically joined.

[b] Diaphragm framing: 41mm x 138 mm (2x6) C16 Chilean radiata pine (INN, 2014) studs at 300mm o.c., (3) 41mm x 138 mm used as central and perimeter beams.

[c] A 15.0 mm thick layer of plywood sheathing is applied to one side of each diaphragm type.

[d] Smooth shank nails, as per EN14592:2008+A1:2012 (BSI, 2008), pneumatically driven to the frame with minimum end/edge distance of 20/40 mm, respectively.

3.2.2. Test Setup

The test setup and instrumentation are shown in Figures 3.2 and 3.10. The unidirectional Anco shake table moves along the direction indicated by an arrow in Figures 3.1 and 3.2, features a dynamic actuator capable of generating $\pm$ 1.0 g acceleration, 0.45 m/s velocity, and up to 15 Hz frequency, supporting a maximum payload of 40 kN. To handle a larger payload, a steel table extension capable of supporting up to 200 kN was added to the shake table. This extension sits on low-friction sliders that are placed directly on the reaction slab, which slightly reduces the load capacity of the actuator by 10% due to friction. The specimen was tested under two conditions: base isolated and fixed-base. Initially, four isolators were placed between the D0 diaphragm of the specimen and the shake table extension. For the fixed-base tests, RHS 200 x 150/8.5 steel beams were added to connect the outer edge of the D_0 diaphragm to the shake table extension, simulating a strip foundation typical of such buildings. This paper reports the results of the fixed-base test configuration only. See Quizanga et al. (2024) for results of the base isolated test configuration. Concrete cubes with dimensions of 200 mm and 150 mm, as depicted in Figure 3.10, were used as additional masses to represent loads in an occupied building. Masses of 1449.30 kg were added at the first floor and at the second floor, and a 1843.20 kg mass was added at the third floor. The total weight of the specimen was then 17.5 kN (self-weight) + 46.5 kN (added masses) = 64.5 kN. Due to the physical size of the test specimen it was not possible to monitor all the structural elements of the specimen. Rather, the instrumentation plan focused on obtaining comprehensive data at the first floor of the specimen to specifically track the hysteretic response of the shear walls and the uplift response of the hold-downs, which provide insight into system effects. Instrumentation details, as per Figure 3.2 and Table 3.3, are: (A) Analog uniaxial accelerometers with a range of $\pm$ 4.0 g were installed on all floors of the specimen and on the shake table extension; (A_V) Wireless triaxial accelerometers of the G-Link-200-8g type (Lord Microstrain) were employed to measure vertical accelerations with a range of $\pm$ 8.0 g; (A_{Ch}) Wired uniaxial accelerometers of the ES-U2 type (Kinemetrics) with a range of $\pm$ 0.5 g for ambient vibrations and $\pm$ 2.0 g for strong motion inputs (i.e., seismic events); (d) LVDTs measuring shear deformations at the first-story walls with measurement ranges from $\pm$ 50 mm to $\pm$ 100 mm; (v) LVDTs measuring uplift of the walls (all stories) with measurement ranges of + 40 mm and -10 mm; (s) LVDTs measuring relative slip of the wall-to-wall perpendicular connection at the first-story walls with measurement ranges of $\pm$ 25 mm; (sg) Strain gauges to record the hold-down anchor bar responses installed at the base of the walls of all stories of the specimen; and (Δ) 1D laser transducers with a range of $\pm$ 150 mm measuring the absolute displacement of each story with respect to the reaction slab. To evaluate the out-of-plane bending behavior of the floor diaphragms, A_V accelerometers were employed (vertical direction only). A PC-based system was utilized to control the test and capture data at a frequency ranging from 300 Hz to 400 Hz.

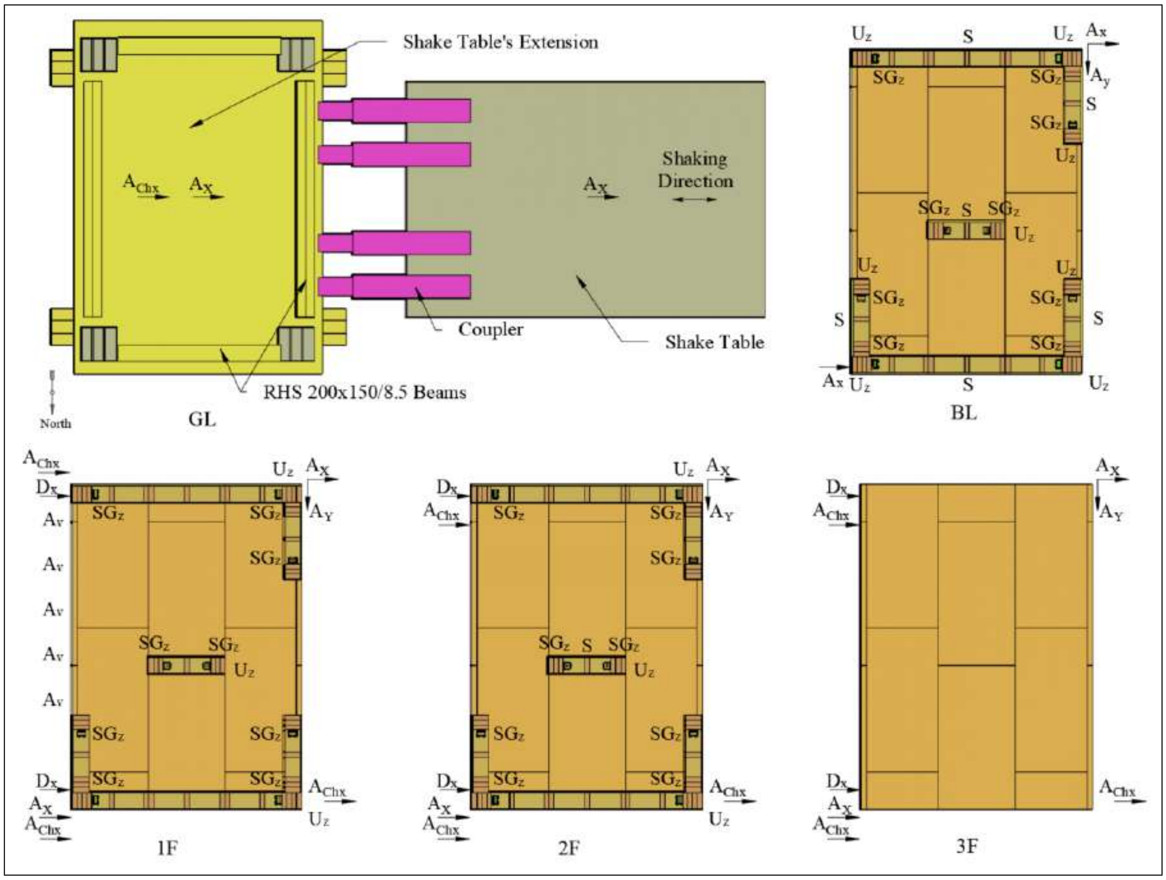

Figure 3.2. Test setup and instrumentation details (see Table 3).

3.2.3. Testing sequence

The input signals for the shake table tests were carefully chosen to evaluate system effects given the capabilities of the shake table. Table 4 outlines the sequence of these signals along with the scale factors (SFs), specifying the Peak Ground Acceleration (PGA), Peak Ground Velocity (PGV), and Peak Ground Displacement (PGD) as measured at the steel table extension. Our goal was to induce significant damage to the specimen. However, during the most intense sequences (i.e., *T15-MAULE-SF0.33*, *T16-CUREE-SF0.25*, *T17-CUREE-SF0.33*), the shake table extension platform experienced overturning, due to the slenderness of the specimen. This overturning prevented us from subjecting the specimen to higher seismic demands. Interestingly, this overturning phenomenon was generated by the base moment reaction generated by the specimen. In this study, we focused on

Table 3.3. Instrumentation Detail

Measurement	Location	Type	Range	Qty
Absolute acceleration (A)	Each floor	Uniaxial accelerometer	$\pm$ 4.0 g	14
Absolute acceleration (A_{ch})	Each floor	Uniaxial accelerometer	$\pm$ 0.5 g to $\pm$ 2.0 g	10
Diagonal shear wall drift (S)	1st-floor shear walls	LVDT	$\pm$ 50 mm to $\pm$ 100 mm	7
Shear wall end stud uplift (U)	Selected shear walls	LVDT	+ 40 mm (uplift) -10 mm (comp.)	15
Hold-down strain (SG)	In all hold-down's rod	Strain gauges	-	27
Absolute displacements (D)	Building exterior	1D laser potentiometer	$\pm$ 150 mm	6
Connection slip	Wall-to-wall perp. connection	LVDT	$\pm$ 25 mm	3
Out of plane diaphragm bending deformation (A_V)	2nd-floor	3D wireless accelerometer	$\pm$ 8.0 g	9

examining system effects, as opposed to evaluating seismic performance. Therefore, the key tests involved the application of a dynamic CUREE protocol, scaled as per Table 3.4 and adjusted by ASTM E2126 (ASTM, 2019) following the guidelines of Uang and Gatto (2003), as well as tests where the input signal was an actual seismic record. The range of accelerations of the applied signals closely mirrors the acceleration range specified in the unreduced (i.e., R = 1.0) seismic acceleration spectrum of NCh 433 (INN, 2009) considering seismic zone 3 and soil type C (Figure 3.3-a). This consistency ensures that our testing conditions are representative of Chilean seismic scenarios.

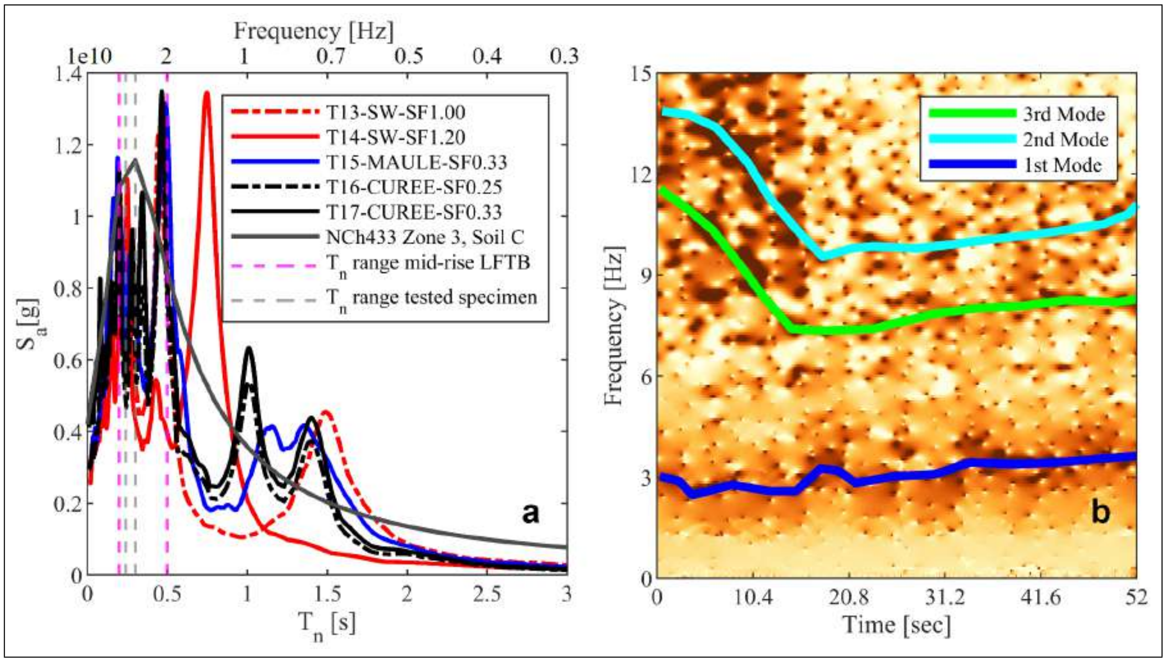

Figure 3.3. (a) Acceleration response spectra (damping ratio of 5%) of the most intense signals used in this study. The typical structural first mode periods characteristic of LFTBs and tested specimens can be observed. (b) Changes in the identified natural frequencies overtime during the *T15-MAULE-SF0.33* seismic event.

Table 3.4. Signal sequence

ID	Input	SF	Period [s]	PGA [g]	PGV [mm/s]	PGD [mm]
T1-WN-SF1.00	White Noise	1.00	-	0.05	54.8	178.2
T2-WN-SF2.00	White Noise	2.00	-	0.17	134.7	49.0
T3-WN-SF3.00	White Noise	3.00	-	0.28	216.8	218.0
T4-SW-SF1.00	Sine Wave	1.00	0.75	0.33	277.6	276.1
T5-SW-SF0.50	Sine Wave	0.50	1.50	0.16	137.7	248.8
T6-SW-SF0.80	Sine Wave	0.80	1.50	0.24	236.3	341.6
T7-WN-SF1.00	White Noise	1.00	-	0.05	48.5	11.9
T8-WN-SF2.00	White Noise	2.00	-	0.19	146.7	70.0
T9-WN-SF3.00	White Noise	3.00	-	0.26	204.9	196.7
T10-SW-SF1.00	Sine Wave	1.00	0.75	0.33	292.1	438.4
T11-SW-SF0.50	Sine Wave	0.50	1.50	0.16	151.5	291.5
T12-SW-SF0.80	Sine Wave	0.80	1.50	0.25	270.4	887.2
T13-SW-SF1.00	Sine Wave	1.00	1.50	0.30	325.3	1128.6
T14-SW-SF1.20	Sine Wave	1.20	0.75	0.26	294.7	123.5
T15-MAULE-SF0.33	Maule, Chile, 2010	0.33	-	0.30	246.0	1028.0
T16-CUREE-SF0.25	CUREE Wave	0.25	0.21/0.35/1.02/1.40	0.29	247.0	123.5
T17-CUREE-SF0.33	CUREE Wave	0.33	0.21/0.35/1.02/1.40	0.40	280.8	1017.8

3.3. Numerical Models

To compare the experimental response of the specimen with that obtained from current analytical tools, two numerical models were developed. *Model A*, developed in the M-CASHEW software (W. Pang & Hassanzadeh Shirazi, 2013; Estrella et al., 2020), is representative of current non-linear numerical modeling of shear walls (i.e, no system effects are considered). This model was used primarily to estimate the relationship between story drift ratios and several response quantities of interest (described later). Model B implements the SDPWS (AWC, 2021) analytical model, enhanced by Lopez et al. (2023), that considers the linear lateral response of longitudinal shear walls only (i.e., oriented along the shake table direction) with their respective hold-downs and coupled with an in-plane diaphragm at each floor. Additionally, variants of *Model B* were analyzed to evaluate system effects not accounted for in the SDPWS (AWC, 2021) model (see Figure 3.12). These modifications include: a) deactivation (i.e., high uplift stiffness) of hold-downs to mimic gravity load effects (Bna), b) consideration of the out-of-plane bending stiffness of the diaphragms (DIA), and c) inclusion of the in-plane response of the transverse shear walls (i.e., perpendicular to the shaking direction) (+TSW). The modifications on *Model B* led to the development of *Model Bna* (*Model B* with deactivated hold-downs), *Model B-DIA* and *Model Bna-DIA* (incorporating the diaphragm effect with and without activated hold-downs), and *Model B-DIA+TSW* and *Model Bna-DIA+TSW* (adding both diaphragm and transverse shear wall effects, with hold-down variants). In *Model B-DIA+TSW* and *Model Bna-DIA+TSW*, the out-of-plane bending stiffness of transverse shear walls (i.e., W_2) was not taken into account. Therefore, we focus on coupling the in-plane stiffness of transverse shear walls through the wood frame of the diaphragm. These models were used primarily to estimate natural frequencies and hold-down uplifts. In *Model A*, wood-frame elements with a modulus of elasticity of 7900 MPa were simulated using Euler-Bernoulli frame elements with a corotational transformation. OSB sheathing was modeled using a 5-DOF shear rectangular element with a shear modulus of 1.3 GPa. Wall connections were modeled with 3-DOF link elements with various constitutive models. These included pinned connections for frame interactions and a bilinear model for the hold-down and the wall-to-foundation connections. The MSTEW hysteretic model (Folz & Filiatrault, 2004b), calibrated with experimental data from (Valdivieso, Guindos, et al., 2023), was used for the sheathing-to-frame connections (see Table 3.6). The analysis was of displacement-controlled type, adhering to specific convergence criteria with incremental displacements at the top of the wall model. In *Model B*, each wall is modeled by three springs: one related to the shear response and two associated with the uplift response of the hold-downs (Lopez et al., 2023). Given the scaled nature of the shear walls of the specimen, the apparent shear stiffness was calculated based on the monotonic response obtained from *Model A*, following the procedure indicated in Valdivieso, Guindos, et al. (2023) and SDPWS (AWC, 2021) (see Table 3.7). In the time history analysis under the *T11-SW-SF0.50* input (see Table 3.4) a modal damping of 2% was assigned to all the modes of the structure as per J. R. Jayamon et al. (2018). The input of test *T11-SW-SF0.50* was selected to obtain the response of the numerical model considering the reduced (by R = 6.5) design spectrum as per NCh 433 (INN, 2009).

3.4. Results

Before each seismic test, white noise signals were used to evaluate the dynamic properties of the specimen using system identification techniques. After each seismic test, the specimen was inspected for potential damage. Overall, the structure exhibited only minor damage, even after the most intense seismic sequences (specifically, tests *T15-MAULE-SF0.33*, *T16-CUREE-SF0.25* and *T17-CUREE-SF0.33*). The observed damage included some permanent shear deformation in the OSB sheathing of the north W_1 shear wall at the first story and slight loosening of the nuts of the conventional hold-downs at the first and third stories. A detailed depiction of the observed damage is provided in Figure 3.11. The subsequent sections describe the dynamic response of the specimen. The shear forces were calculated as the cumulative value of the product of the absolute acceleration data measured at each floor level and their corresponding floor masses.

3.4.1. System identification

Table 3.5 summarizes the dynamic properties identified from the response to white noise signals *T1-WN-SF1.00* and *T2-WN-SF2.00* with more detail presented in Table 3.8. Analysis of the results using the ERA-DC algorithm (Juang et al., 1988) (see Figure 3.13), shows that, as the PGA increases, the identified frequencies decrease (indicating a more flexible structure) and the modal damping at the first three lateral modes increase. These trends are primarily due to lateral deformations in the structure. One of the most important observed phenomena is the rocking of the shear walls, which triggers a highly nonlinear response due to uplift in the hold-downs. Additionally, shear deformations in the nailed OSB-to-wood frame connections further contribute to nonlinearities that begin to appear at low levels of lateral deformations. Both phenomena increase the flexibility of the building and the level of damping. The observed damping ratios in the first four modes significantly exceed the typical 2%-5% range commonly assumed for wooden structures, a finding also reported by J. R. Jayamon et al. (2018). This discrepancy is likely due to: a) system effects that mitigate uplift at the hold-downs; and b) the influence of frictional forces at low-intensity inputs. Figure 3.3-b showcases the Short-Time-Transfer-Function or STTF (Hernandez et al., 2021), calculated from the ratio of acceleration measurements at the third floor to those at the base of the building during the *T15-MAULE-SF0.33* shake table test. This figure reveals significant fluctuations in the natural frequencies during the seismic event, especially during the strong motion phase (0-18 sec). As a result, the natural frequencies presented in Table 3.5 are best regarded as average values spanning the duration of the seismic event. This interpretation supports further the observation that the average frequencies identified are consistent with the natural frequency range illustrated in Figure 3.3-b. The conspicuous nonlinearity observed is linked to the inelastic response induced by inter-story rocking and the consequent reduction of the secant stiffness, as elucidated in Figure 3.8. Table 3.5 also compares the experimentally-obtained frequencies and those predicted by *Model B* and by *Model B-DIA+TSW*. The experimental frequencies are higher than those predicted by *Model B*, suggesting that the actual structure is significantly stiffer than the analytical model as per SDPWS (AWC, 2021). A more accurate prediction of mode shapes and frequencies was achieved by considering the combined effects of the transverse shear walls, the out-of-plane bending stiffness of the diaphragms, and with/without deactivation of hold-downs due to gravity load action (i.e., *Model B-DIA+TSW* and *Model Bna-DIA+TSW*). Conversely, the incorporation of the out-of-plane bending stiffness of the diaphragms into planar shear wall models had a negligible impact, which is consistent with Tamagnone et al. (2020). Nevertheless, the influence of the out-of-plane stiffness of the diaphragms becomes markedly significant in a three-dimensional context, particularly when there is interaction with non-planar shear walls (see Table 3.9).

Table 3.5. Identified (experiment) and predicted (model) dynamic properties

	Identified				Predicted	
Mode	T1-WN-SF1.00		T2-WN-SF2.00		B	B-DIA+TSW
	Frequency [Hz]	Damping Ratio [%]	Frequency [Hz]	Damping Ratio [%]	Frequency [Hz]	
1	4.2	6.5	3.7	10.0	2.1	3.7
2	8.4	6.5	7.6	7.5	6.1	6.9
3	13.0	6.7	11.2	11.0	9.6	8.5

3.4.2. Lateral response

The time history response of the building indicates that there was almost no torsional effect under most of the inputs (see Figure 3.14), which allows a direct comparison between the response of the U-shaped wall and that of the L-shaped wall. In the subsequent figures, the responses to all the signals described in Table 3.4 are shown together. Figure 3.4-a illustrates the peak story drifts, which remain below 0.70% and follow a typical pattern encountered in buildings dominated by rocking mechanisms (i.e., higher drift at upper stories). The measured peak story drift is smaller than the expected 0.85% drift demand from the displacement spectrum as per NCh 433 (INN, 2009). These smaller-than-expected values can be attributed to: a) gravitational forces, which induce friction effects;

b) three-dimensional coupling, stemming from the transverse response of non-planar shear walls and the out-of-plane bending stiffness of the diaphragms (which increase the natural frequencies); and c) the relatively high level of damping.

Figure 3.4-b illustrates the Peak Floor Accelerations (PFAs). There is a pronounced whip effect at the third floor, where the PFA is 250% of the PGA. The PFA values recorded at this floor are nearly equivalent to those of the unreduced design spectrum (ranging from 1.0 g to 1.6 g) as outlined in NCh 433 (INN, 2009) and Figure 3.3-a. Such a phenomenon is typical in very stiff structures. Therefore, it becomes crucial to appropriately account for system effects on predicting building stiffness, as they can significantly amplify the whip effect at the upper floor levels (particularly at the roof level) because of higher non-predicted lateral stiffness on lower stories.

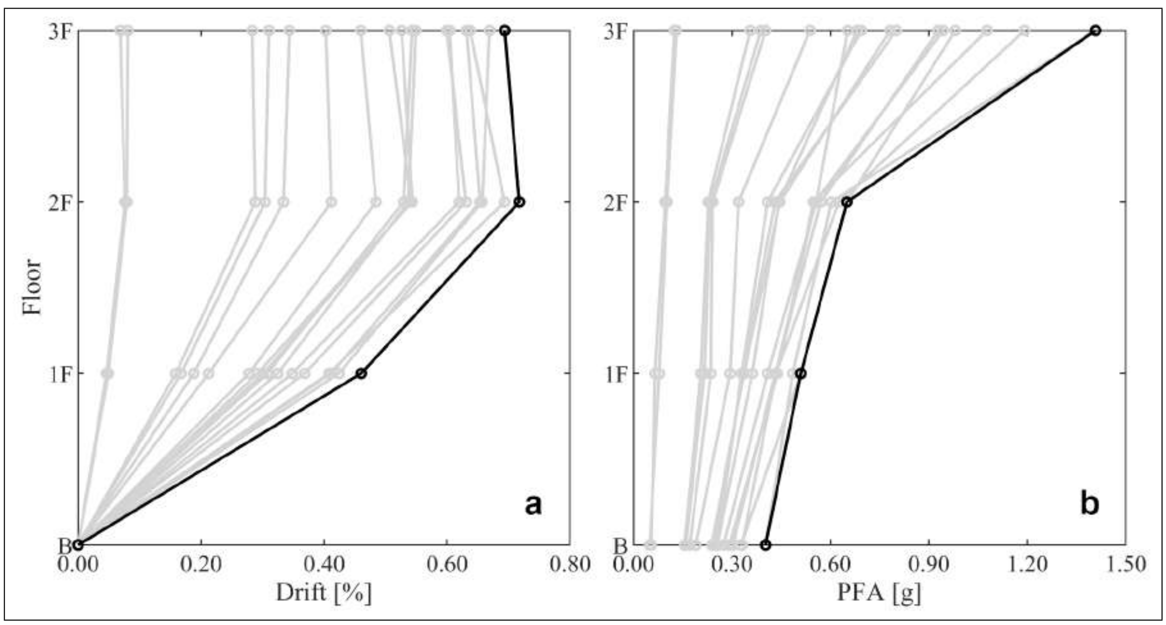

Figure 3.4. (a) Peak story drift ratios and (b) peak floor accelerations.

3.4.2.1. Strength

Figure 3.5 shows the global and story-specific hysteretic response of the building, as derived from all testing sequences. The overall hysteretic behavior of the building (Figure 3.5-a) displays a predominantly frictional response (Orellana et al., 2021), achieving significant strength levels at small drift demands. Notably, a story-level analysis (Figure 3.5-b) reveals that at a 0.2% drift ratio, the design drift limit as per NCh 433 (INN, 2009) which controls the design of multi-story LFTBs, the measured strength of the first story is approximately 2.3 times greater than the predictions of *Model A*, which considers planar shear walls only. This disparity between measured and predicted strengths was also found at the other stories and also at other drift ratios (Table 3.10), which suggests that the behavior of the structure is greatly influenced by the transverse shear walls and the out-of-plane bending stiffness of the diaphragms. When we compared the measured strength of the second story with that of the third story, we observed that at the design drift level (i.e., 0.2%), the strength we measured at the second story was almost 60% higher than what we measured on the third floor. This difference in strength (as well as in stiffness and damping ratio) stems from the role of gravity load in influencing the lateral response of light-frame shear walls, as reported by Orellana et al. (2021). However, as the story drift increases, the experimental results tend to become more similar to the predictions of *Model A*. This last observation means that either the influence of system effects diminishes at large story drifts or the numerical models overestimate the response. For a comprehensive analysis, Table 3.10 in the supplementary material provides detailed information on story strength and story secant stiffness at various story drift levels.

3.4.2.2. Uplift responses of hold-downs

System effects also influence the uplift response of hold-downs, as depicted in the time histories presented in Figure 3.6 and the hysteretic responses shown in Figure 3.15. The strain measurements from strain gauges were used to calculate the stresses on hold-downs reported in Figure 3.15. At the first and second stories, the uplift responses of the

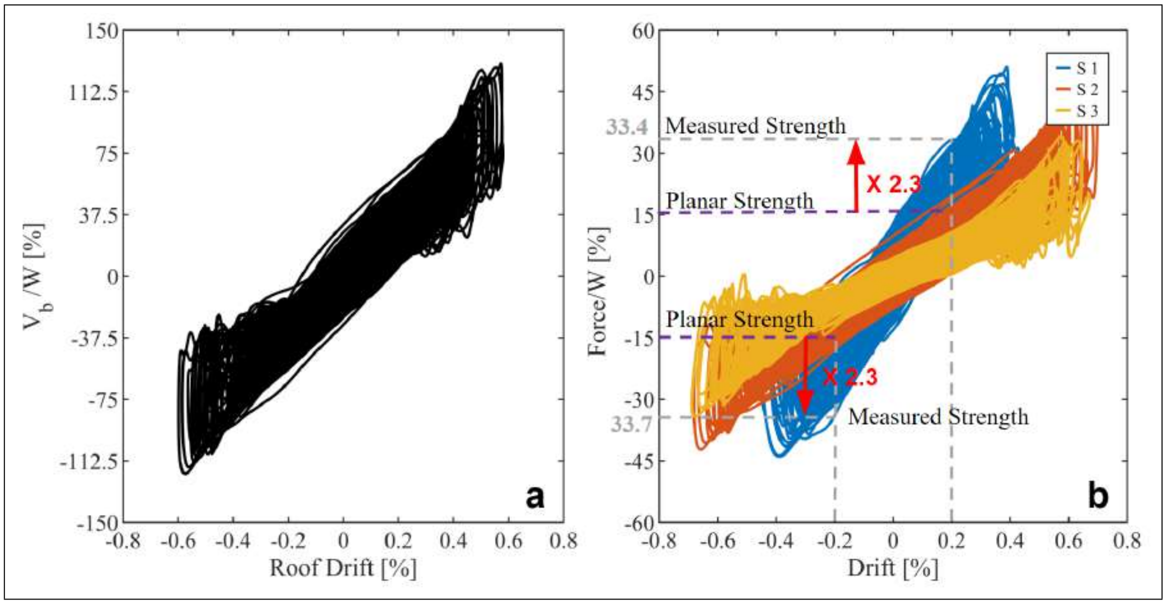

Figure 3.5. Hysteretic Response: (a) entire building, and (b) individual stories.

non-planar and planar shear walls are almost identical to each other due to the significant impact of the out-of-plane bending stiffness of the diaphragms and the gravity load (Figure 3.6-a). However, at the third story, where the gravity load is minimal compared to that on the other stories, the hold-down uplift is smaller at the non-planar shear walls. We attribute this uplift difference to the role of the transverse shear walls in reducing uplift (Figure 3.6-b). Therefore, these results demonstrate that the L- and U-shaped non-planar shear walls, despite not being constructed monolithically as in reinforced concrete, are in fact behaving as effective L and U wall sections. A comparison between U-shaped walls and L-shaped walls indicates that the influence of the transverse wall on the hold-down uplift is greater at the U-shaped walls. The negative uplift shown in Figure 3.6 is attributed to the compressive deformation perpendicular to the bottom/upper plates of the shear walls, as well as to installation and manufacturing misalignments of the specimen's wood frame. The non-planar shear walls typically exhibit minimal uplift (less than 0.3mm) at story drift levels smaller than 0.15% (Figure 3.7). However, the relationship between the uplift and the story drift depends on the story and the gravity load. For example, at the first story, the uplift remains essentially constant at story drifts greater than 0.1%, whereas, at the third story, the uplift increases monotonically with increasing story drifts. Interestingly, the uplift response at the second story, as a function of the story drift, lies somewhere in between those at the first and third stories, illustrating again the influence of the gravity load on the uplift response. A comparison between the uplift response of hold-downs obtained from numerical *Model B* (which reflects SDPWS, AWC (2021), predictions) and the response in the shake table test reveals that the numerical models tend to overpredict the uplift response (Figures 3.16-a and 3.17-a). This observation is consistent with the already described analytical underestimation of the building stiffness. Such discrepancies are again attributed to the system effects explored in this study. These effects not only increase the lateral stiffness (especially the rocking component of the stiffness) of non-planar shear walls with respect to that predicted by the SDPWS (AWC, 2021) analytical model (i.e., *Model B*) but also reduce the uplift response of hold-downs to almost negligible levels at low levels of story drift (Figures 3.16-b and 3.17-b).

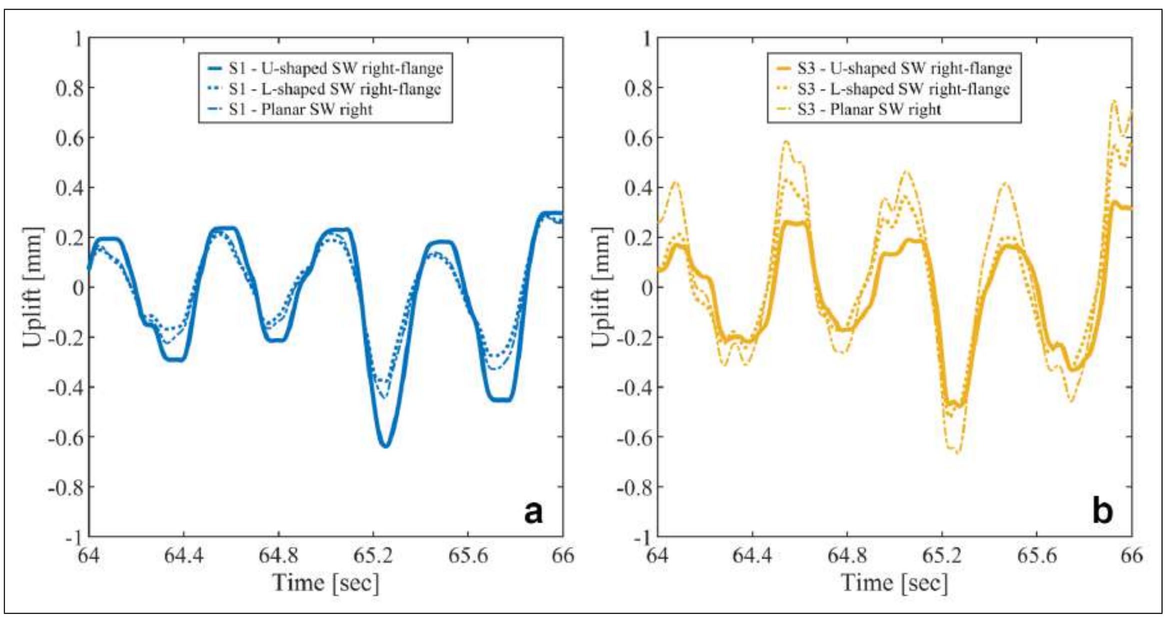

Figure 3.6. Test *T17-CUREE-SF0.33*: uplift strong motion phase time history response of hold-downs at the U-shaped wall, the L-shaped wall, and the planar shear walls at (a) the first and (b) the third story.

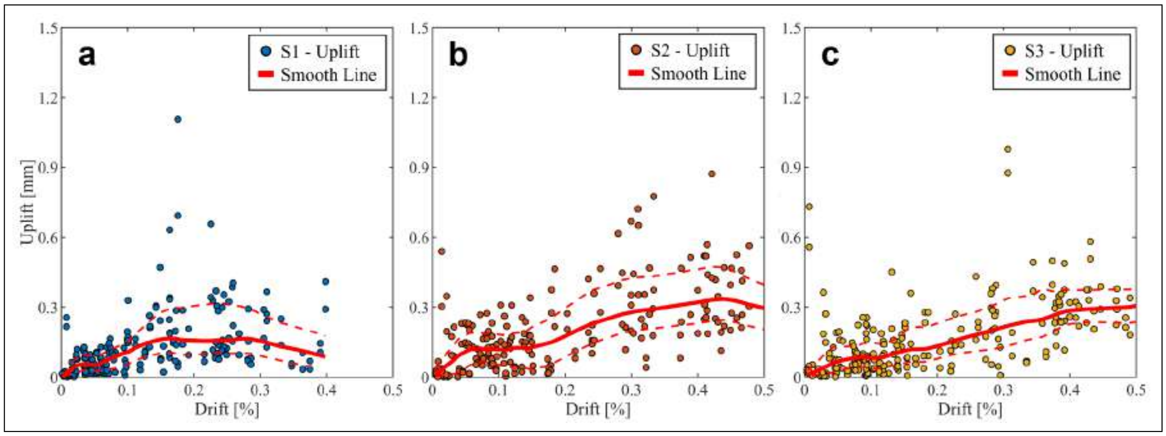

Figure 3.7. Uplift response at the non-planar shear walls versus story drift:(a) first story, (b) second story, and (c) third story.

3.4.2.3. Secant Stiffness and Damping Ratio

To investigate the influence of the level of lateral deformation on system effects, we also explored the relationship between the story drift and two relevant quantities (secant lateral stiffness and equivalent viscous damping), as shown in Figure 3.8. The secant stiffness for each hysteresis loop is determined by dividing the change in force observed at the peak positive and negative displacements of the loop by the change in peak displacement of the loop. The equivalent viscous damping is calculated by comparing the energy dissipation within a hysteresis loop (i.e., the area enclosed by the loop) to the maximum loop's elastic strain energy calculated using the secant stiffness.

At the first story, the experimental secant stiffness at the design story drift level (i.e., 0.2%) is 1.7 to 2.0 times greater than the stiffness predicted by the SDPWS (AWC, 2021) analytical model (which is based on a cantilever beam model for planar shear walls). This significant discrepancy between experimental and analytical stiffness is also observed at higher story drift levels. The comparison between experimental and analytical (i.e., *Model A*) secant stiffness at different story drift levels reveals that system effects tend to decrease as the story drift increases (Table 3.10). This observation is consistent with what has been reported in previous studies on T-shaped shear walls (e.g., Valdivieso, Lopez-Garcia, et al. (2023)). Furthermore, despite the measured drift demands falling below the drift range

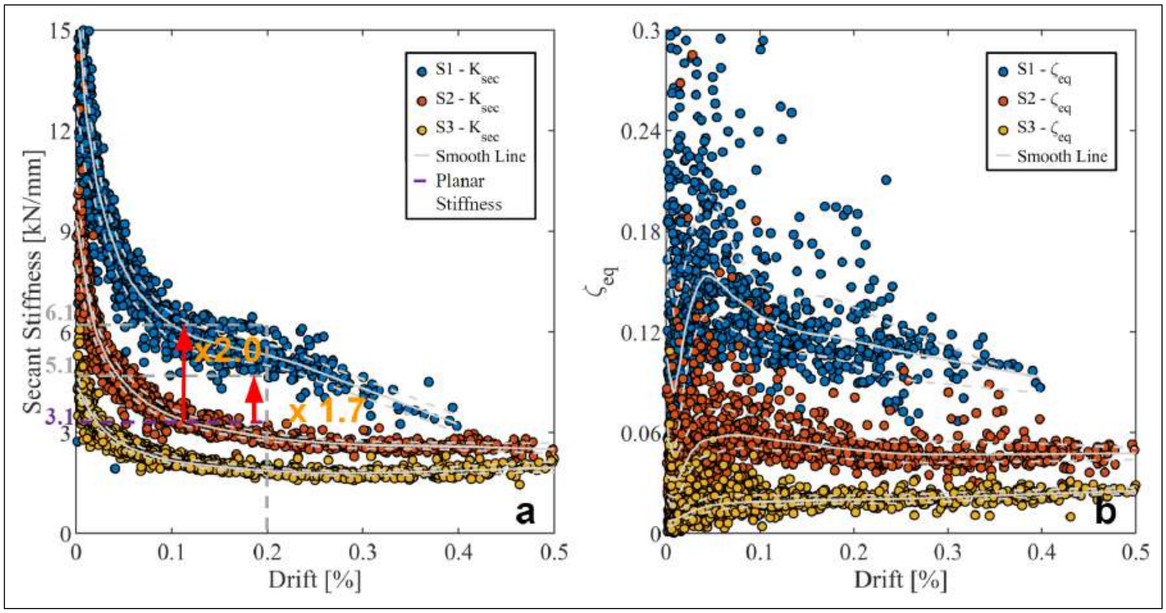

Figure 3.8. (a) Story secant stiffness vs. story drift ratio and (b) equivalent story damping ratio vs. story drift ratio.

(i.e., 0.6% to 0.8%) at which permanent deformation occurs in the OSB-to-wood frame nailed connection (Valdivieso, Lopez-Garcia, et al., 2023), Figure 3.8 exhibits a highly non-linear response of the secant stiffness as a function of the story drift, primarily due to the uplift response of the hold-downs (see the relationship between the uplift activation of the hold-downs and the story's secant stiffness in Figure 3.9-a). The secant stiffness levels recover after each test as shown by the multiples dots at each drift level in Figure 3.8-a. Although the shear walls at the second and third stories are identical to each other, they differ in the applied gravity load. As shown in Figure 3.8, the secant stiffness and the damping ratio are greater at the second story, demonstrating the substantial impact of the gravity load on system effects due to the transverse shear walls and the out-of-plane bending stiffness of the diaphragms. There is a clear relationship between the uplift activation of the hold-downs and the level of damping ratio (Figure 3.9). The third story damping ratio increases monotonically with increasing story drift, but the first story and second story damping ratios increase with increasing uplifts, then remain essentially constant (i.e., a plateau), and then decrease as the uplift increases further. This phenomenon is explained by the initial influence of frictional forces due to the gravitational loads at the lower stories of the structure. As the structure experiences increased drift, the impact of these frictional forces begins to decrease. This transition in force dynamics ultimately leads to a state where the damping effects come into play, particularly noticeable through mechanisms such as uplift at the hold-downs and the shear deformation that occurs at the OSB-to-wood frame connections. Finally, it was determined that the damping matrix of the structure is essentially proportional to the stiffness matrix rather than to both the mass and stiffness matrices (Quizanga et al., 2024).

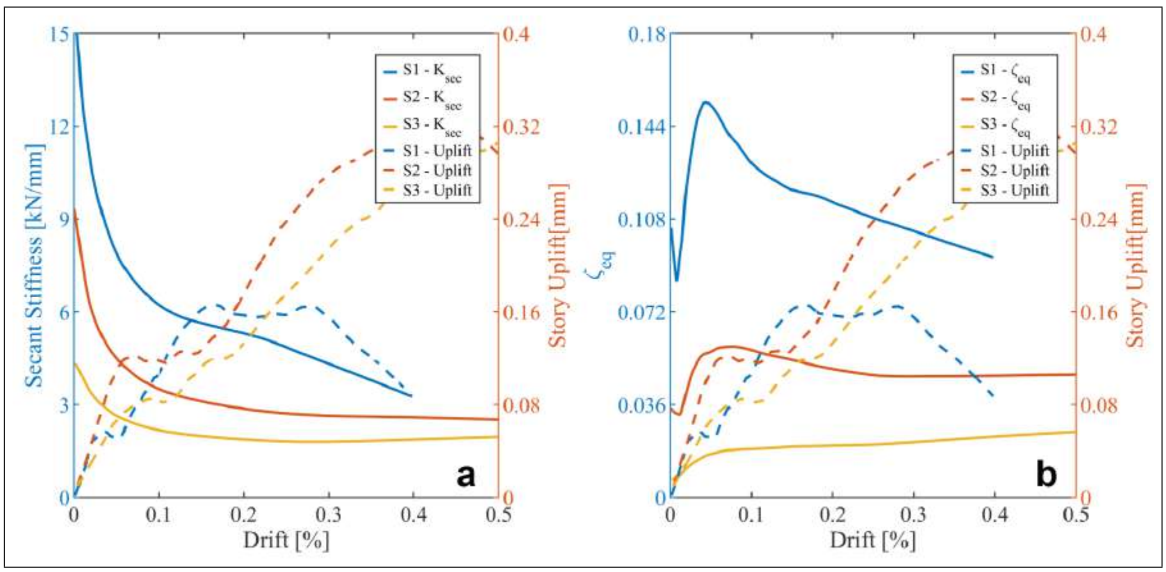

Figure 3.9. (a) Story secant stiffness and uplift of the shear walls vs. story drift ratio, as well as (b) story damping ratio and uplift of the shear walls vs. story drift ratio.

3.5. Practical Implications

LFTBs experience early, recoverable stiffness degradation due to rocking influenced by hold-downs. This characteristic leads to a pronounced non-linear behavior when subjected to earthquake forces. Consequently, design approaches that consider the curvature of shear walls may offer a viable approach to accurately address the building response, as suggested by Isoda et al. (2021). Until further research is available, we advise engineers to design LFTBs using numerical models that account for the in-plane response of both transverse and longitudinal shear walls and the out-of-plane bending stiffness of the diaphragms due to their significant effect on stiffness. We also advise that dynamic properties and seismic forces be calculated without taking into account the overturning restraint system (i.e., the hold-downs). Since the building frequency is highly influenced by the level of seismic intensity, research is needed on the intensity-dependent behavior of the overturning restraint system. Meanwhile, existing models that take into account the overturning restraint system are recommended for design lateral drift checks because they can be adapted for incorporating system effects as was illustrated in this paper. The influence of the gravity load on the design of the overturning restraint system is critical for precise detailing. In LFTBs, prevention of degraded lateral stiffness and potential loosening of nuts in overturning restraint devices due to repeated seismic activity require a proactive approach. Regular reassessment of structural integrity after significant earthquakes is advised, along with the establishment of inspection protocols after major seismic events. These protocols should specifically focus on easily accessible areas to examine critical components like overturning restraint systems, ensuring safety and reliability. The findings of this research on system effects could be extended to other structural systems such as CLT shear wall buildings. CLT shear walls and diaphragms have greater out-of-plane bending stiffness than their light-frame timber counterparts. Hence, consideration of the interaction between diaphragm effects and gravity loads is vital for the adequate design of buildings with non-planar CLT shear walls. Additionally, understanding the kinematic response of shear walls made of multiple CLT panels is essential, as diaphragms can alter the kinematic response and the energy dissipation mechanism.

3.6. Chapter Conclusions

In this study, system effects on Light Frame Timber Buildings (LFTBs), especially on those featuring non-planar shear walls, are experimentally evaluated by subjecting a 1:2 scale 3-story LFTB specimen to shake table tests. Results of this study highlights the considerable benefits of component interactions in LFTBs subjected to lateral loads.

They emphasize the crucial role played by transverse shear walls, the out-of-plane bending stiffness of the diaphragm, and the gravity load. These factors significantly influence the uplift response of hold-downs, the lateral secant stiffness, and the damping ratio. Notably, these system effects substantially reduce story drift demands and enhance both the lateral stiffness and the damping ratio with respect to what is predicted by the SDPWS (AWC, 2021) analytical model and by current non-linear models that account for planar shear walls only. Additionally, this study discovered a specific influence of system effects on the uplift response of hold-downs, i.e., the flanges of the non-planar shear walls, together with the out-of-plane bending stiffness of the diaphragm, also contribute to the uplift stiffness in the in-plane lateral response of the wall. The findings herein findings indicate that gravity loads amplify the system effects due to the transverse shear walls and the out-of-plane bending stiffness of the diaphragms. Proper incorporation of these system effects into current analytical and non-linear numerical models can lead to safer and more efficient design of LFTBs, particularly in regions prone to seismic activity. Consequently, there is a pressing need for continued research aimed at creating analytical and numerical models that can accurately forecast these system effects on LFTBs.

3.7. Supplementary Material - Figures

Figure 3.10. Shake Table Test Setup: (a) additional mass on the third floor; (b) additional mass on the first and second floors; (c) accelerometer placement at each story and the wood restraint system to secure the additional mass; (d) front view of the test specimen; (e) side view of the specimen and the reference blue steel frame used to track the lateral displacement at each story; and (f) detailed view of the system employed to measure the lateral displacement of the specimen.

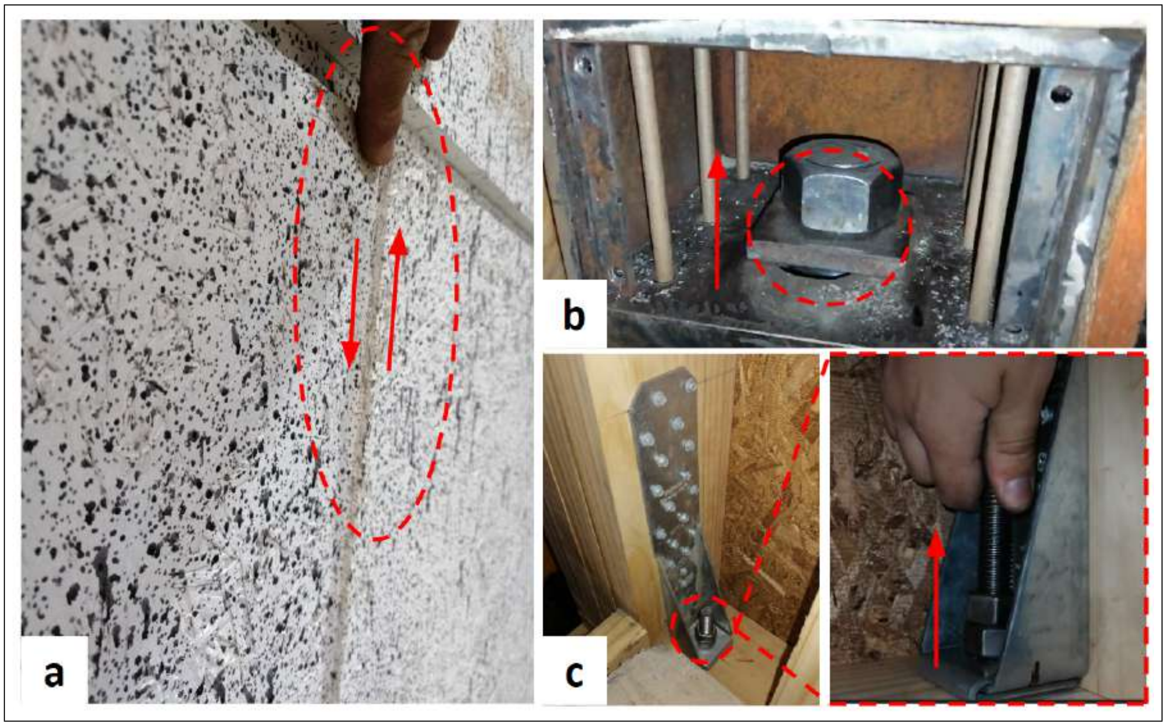

Figure 3.11. Examples of Damage: (a) Residual shear deformation observed in the first story W1 shear wall; (b) Slight loosening of the nut of the first story conventional hold-down; and (c) Similar loosening detected at the third story hold-down.

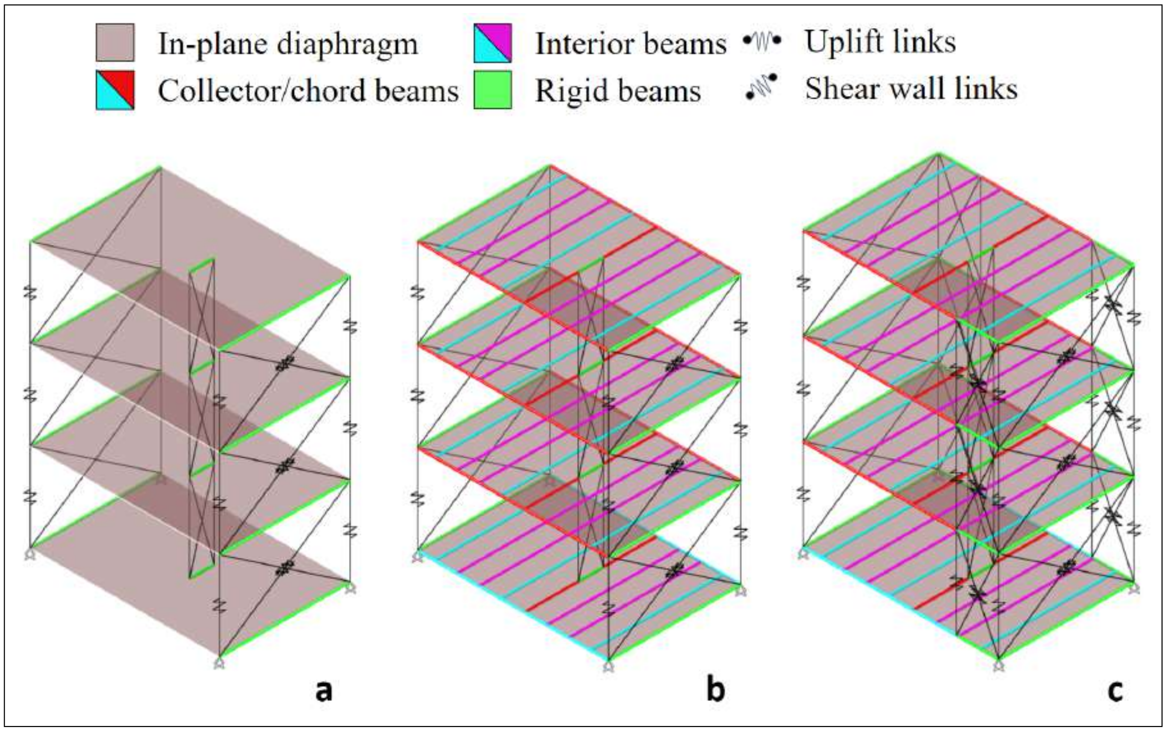

Figure 3.12. Isometric view of the building in (a) Model B and Model Bna; (b) Model B-DIA and Model Bna-DIA; and (c) Model B-DIA+TSW and Model Bna-DIA+TSW.

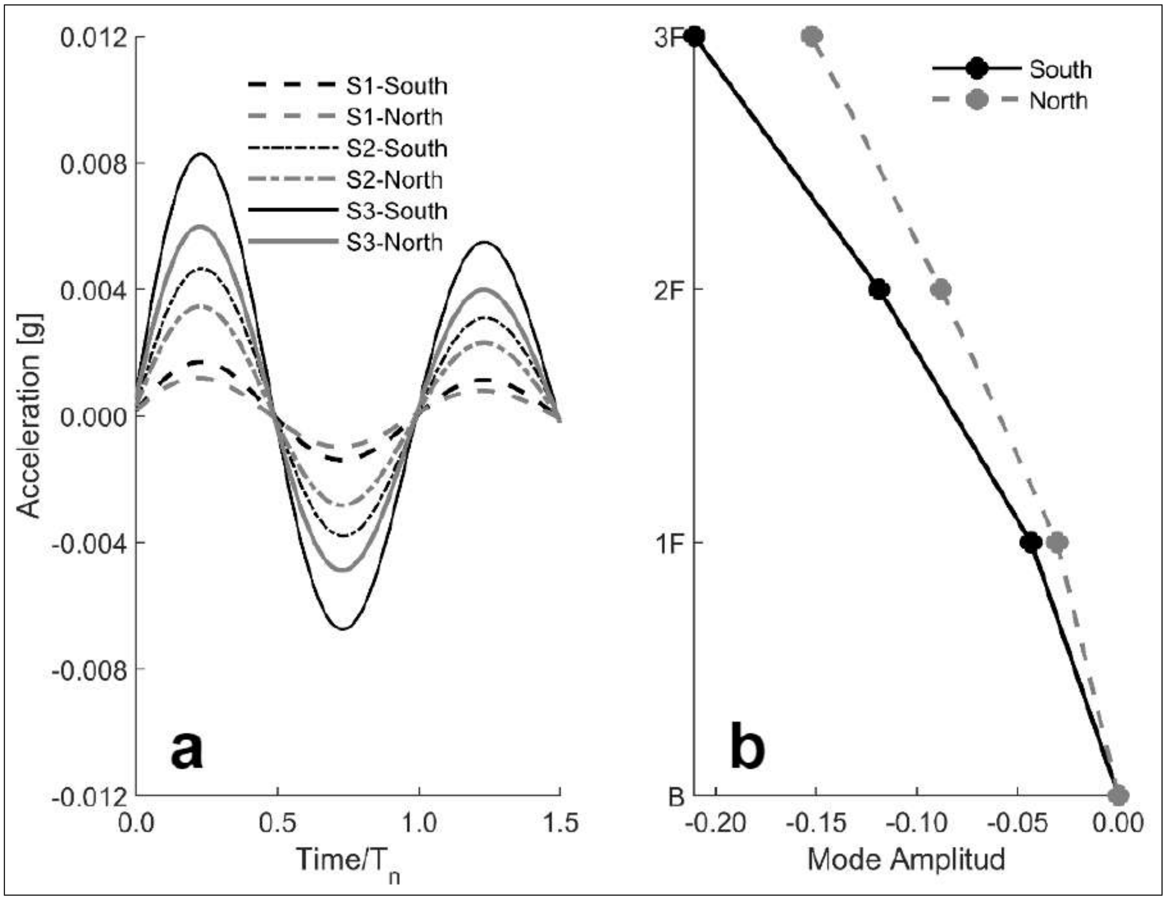

Figure 3.13. Test WN-0.05g (*T1-WN-SF1.00*) (a) response to impulsive loading, and (b) first mode shape (determined using the ERA-DC algorithm as per Juang et al. (1988)).

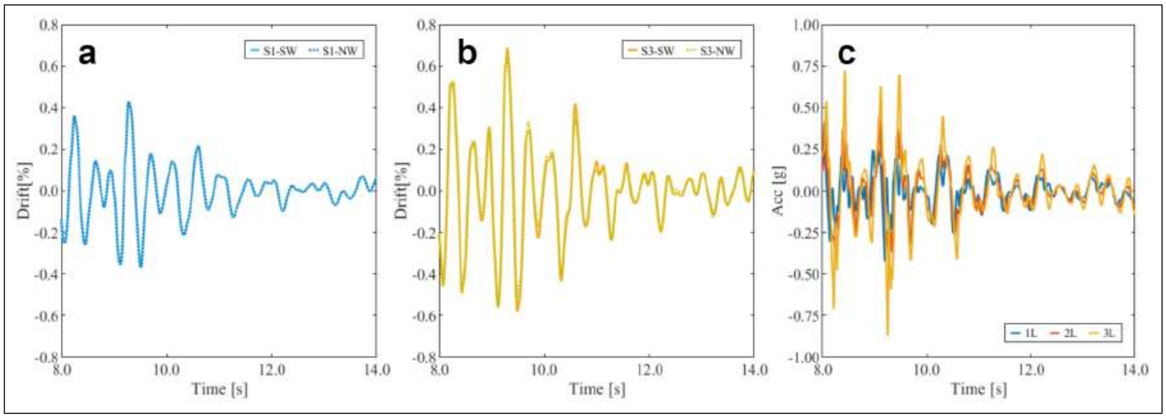

Figure 3.14. Test *T17-CUREE-SF0.33*: (a) first story drift, (b) third story drift, and (c) floor accelerations during the strong motion phase.

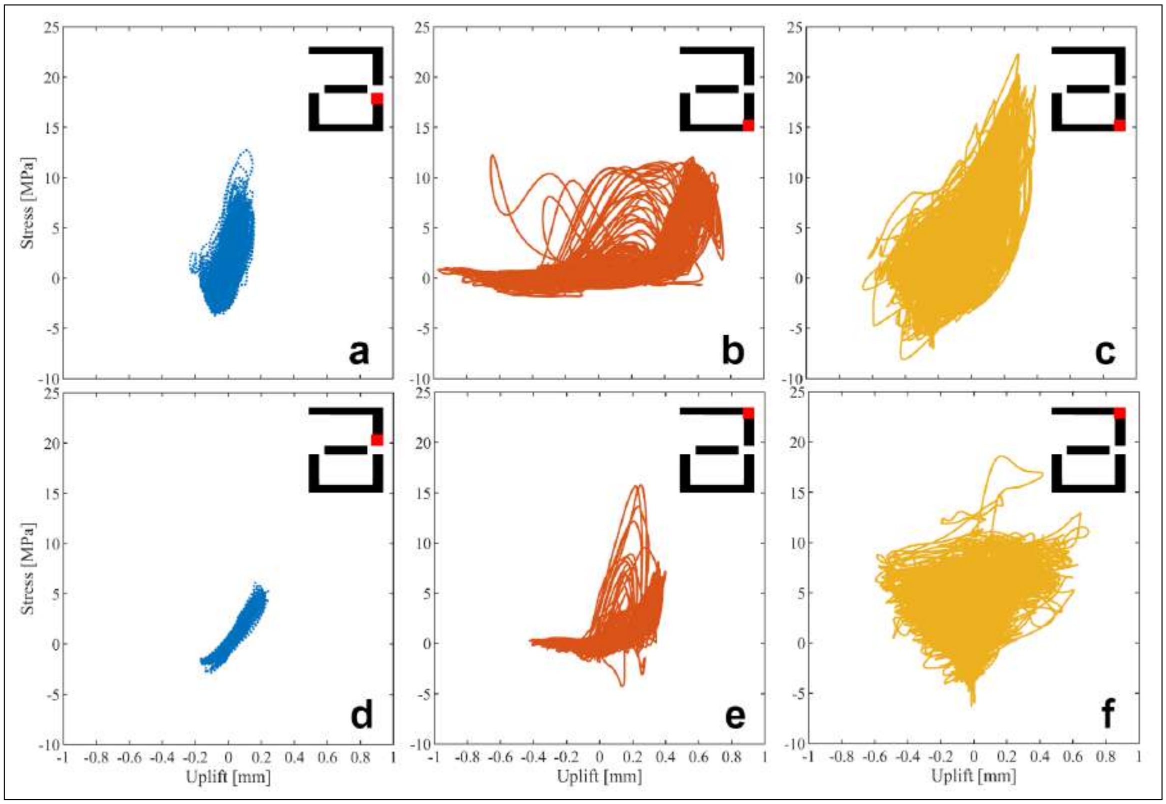

Figure 3.15. Hysteretic response of hold-down devices in the U-shaped shear wall at (a) the first story's perpendicular wall W2, and at wall W1 in (b) the second and (c) the third story of the building. Additionally, the hysteretic response of hold-down devices in the L-shaped shear wall at (d) the first story's perpendicular wall W2, and at wall W1 in (e) the second and (f) the third story of the building.

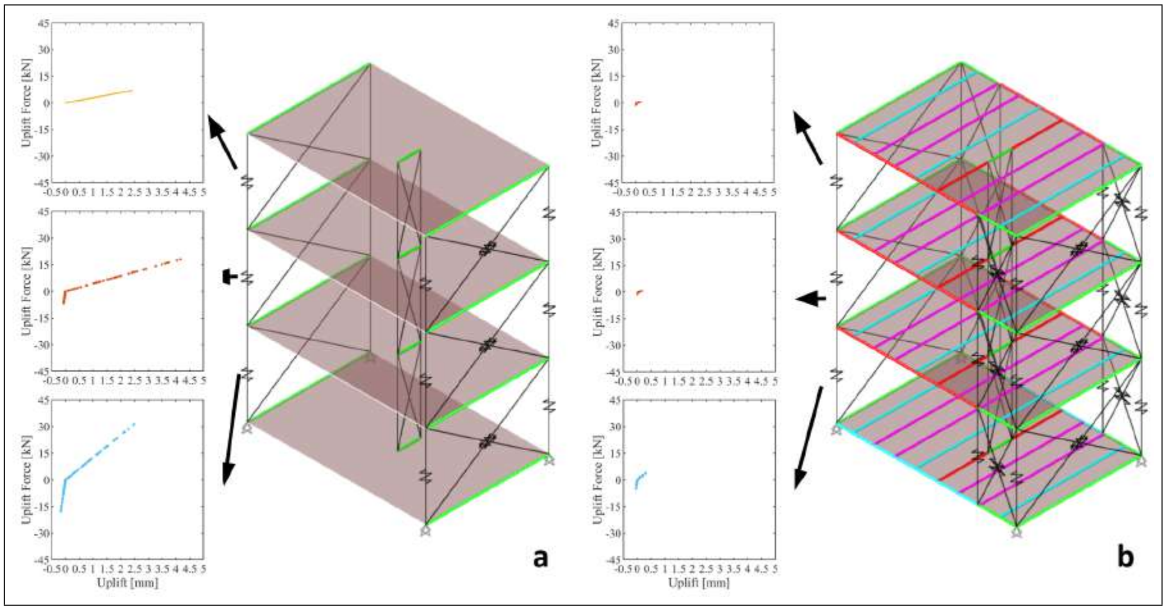

Figure 3.16. Response of hold-down devices at the L-shaped shear wall obtained from (a) *Model B* and (b) *Model B-DIA+TSW* (input equal to that of test *T11-SW-SF0.50*).

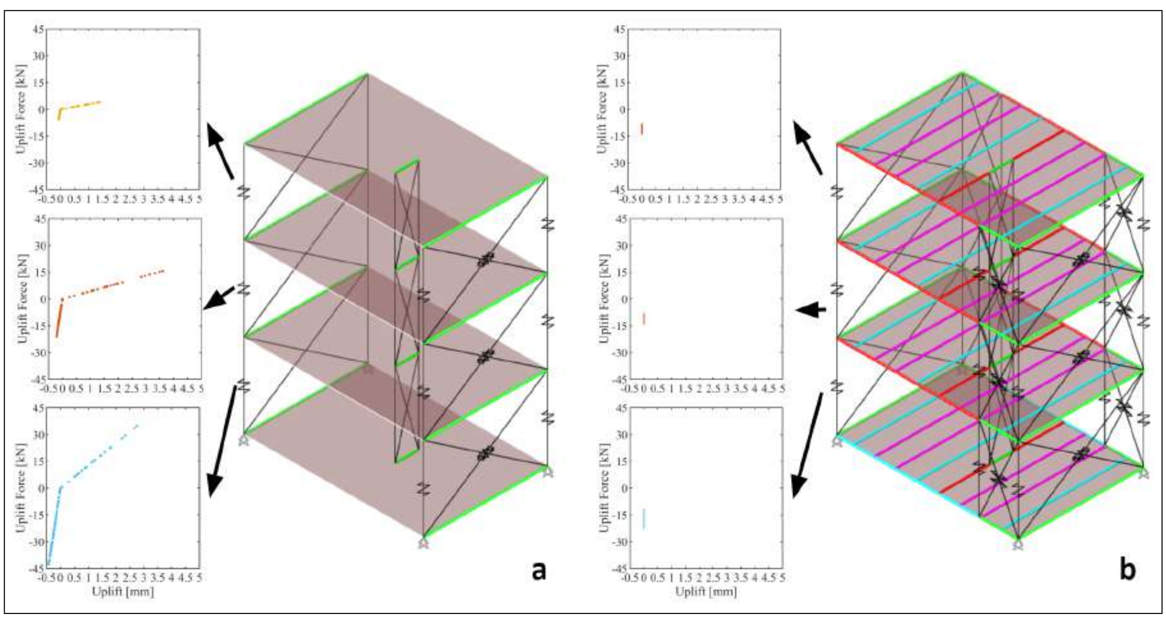

Figure 3.17. Response of hold-down devices at the L-shaped shear wall obtained from (a) *Model Bna* and (b) *Model Bna-DIA+TSW* (input equal to that of test *T11-SW-SF0.50*).

3.8. Supplementary Material - Tables

Table 3.6. MSTEW modeling parameters[a] for *Model A*

Test Group	K_0 kN/mm	r_1	r_2	r_3	r_4	F_0 kN	F_I kN	Δ_u mm	α	β	F_u kN
Nailed OSB-to-wood frame connection[b]	0.904	0.055	-0.060	1.274	0.004	0.864	0.104	9.178	0.764	1.219	1.321

[a] K_0 is the initial stiffness of the hysteretic curve, r_1 to r_4 are dimensionless parameters that represent stiffness ratios at different parts of the curve, F_0 and F_I are strength parameters of the hysteretic curve (Folz & Filiatrault, 2004b), and Δ_u is the displacement at peak load. Parameters α ($\alpha > 0$) and β ($\beta > 0$) control the stiffness degradation and energy degradation, respectively.

[b] Taken from Valdivieso, Guindos, et al. (2023) and as per Table 3.1 sheathing nail

Table 3.7. Input variables for numerical *Model B*

Wall Type	Story	G_a[a] [kN/mm]	Uplift Stiffness[b] [kN/mm]	K_{lat}[c] [kN/mm]	$K_{lat,na}$[d] [kN/mm]
	1	0.901	12.6	1.379	1.450
W_1	2	0.683	4.4	0.987	1.099
	3	0.659	2.9	0.659	1.061
	1	0.832	12.6	0.376	0.445
W_2	2	0.594	4.4	0.231	0.318
	3	0.438	2.9	0.165	0.235
	1	0.780	12.6	0.356	0.417
W_3	2	0.511	4.4	0.206	0.274
	3	0.438	2.9	0.165	0.235

[a] Apparent shear stiffness, determined from nail slip and panel shear deformation, was calculated following the methods outlined in SDPWS (AWC, 2021) and as per the approach described by Valdivieso, Guindos, et al. (2023).

[b] The stiffness for overturning restraint system's uplift at the first story was calculated using the hold-down stiffness values provided in the Simpson Strong-Tie catalog. For the second and third stories, the uplift stiffness was computed by summing the series of stiffness values from both the Simpson Strong-Tie catalog for the hold-downs (one at each story) and the axial stiffness of the rod employed for transmitting tension forces between stories.

[c] Lateral secant stiffness calculated as per SDPWS (AWC, 2021) cantilever beam analytical model for shear walls.

[d] Lateral secant stiffness calculated as per SDPWS (AWC, 2021) cantilever beam analytical model for shear walls assuming that the overturning restraint system uplift stiffness is not activated.

Table 3.8. Identified (experiment) dynamic properties at different inputs' amplitude

Mode	Identified T1-WN-SF1.00 Frequency [Hz]	T1-WN-SF1.00 Damping Ratio [%]	T2-WN-SF2.00 Frequency [Hz]	T2-WN-SF2.00 Damping Ratio [%]	T3-WN-SF3.00 Frequency [Hz]	T3-WN-SF3.00 Damping Ratio [%]
1	4.2	6.5	3.7	10.0	3.3	12.5
2	8.4	6.5	7.6	7.5	6.8	8.0
3	13.0	6.7	11.2	11.0	10.2	7.8
4	19.4	16.4	15.6	13.5	14.9	12.9

Table 3.9. Identified numerical frequencies

Mode	Frequency [Hz] Model Type B	Bna	B-DIA	Bna-DIA	B-DIA+TSW	Bna-DIA+TSW
1	2.1	2.3	2.1	2.4	3.7	4.4
2	6.1	6.8	6.1	6.7	6.9	10.2
3	9.6	9.8	9.4	9.6	8.5	14.4

Table 3.10. Comparison of secant stiffness and peak strength at different drift

Story		Secant Stiffness[a,b] [kN/mm]					Mean Peak Strength/Weight[c] [%]				
		Drift [%]									
		0.1	0.2	0.3	0.4	0.5	0.1	0.2	0.3	0.4	0.5
1	Measured	[7.5,4.7]	[6.1,4.7]	[4.7,4.2]	[3.8,3.2]	-	23.5	33.6	42.4	47.5	-
	Model A	4.2	4.0	3.9	3.7	3.6	8.0	15.0	22.0	28.0	33.0
	Model B	-	3.1	-	-	-	-	-	-	-	-
2	Measured	[4.1 ,3.5]	[3.3,2.7]	[3.1 ,2.6]	[2.9,2.6]	[2.8,2.5]	13.9	18.9	24.6	29.7	34.3
	Model A	3.3	3.0	2.9	2.8	2.6	6.0	12.0	16.0	21.0	25.0
	Model B	-	2.2	-	-	-	-	-	-	-	-
3	Measured	[2.5,2.2]	[2.1 ,1.8]	[1.9,1.7]	[2.1,1.7]	[2.3,2.1]	8.1	12.0	15.1	21.4	26.8
	Model A	3.1	2.9	2.8	2.7	2.5	5.0	11.0	16.0	20.0	24.0
	Model B	-	2.0	-	-	-	-	-	-	-	-

[a] Reported measured stiffness as [maximum, minimum] values as per Figure 3.8.

[b] For numerical models *Model A* and *Model B*, the story secant stiffness was determined by adding the in-plane stiffness of the shear walls that are parallel to the shaking direction.

[c] For numerical model *Model A*, the story mean peak strength relative to the specimen weight was calculated by aggregating the mean peak strengths, each divided by the specimen weight, of the shear walls that are parallel to the shaking direction.

4. CHAPTER 4 - EXPERIMENTAL INVESTIGATION OF MULTI-LAYERED STRONG WOOD-FRAME SHEAR WALLS WITH NONSTRUCTURAL TYPE X GYPSUM WALLBOARD LAYERS UNDER CYCLIC LOAD

4.1. Introduction

Light Frame Timber Building (LFTB) is one of the structural systems currently evaluated by the Chilean construction industry, public authorities, and academia to enhance the sustainability of the Chilean building inventory. Since Chile is subjected to strong earthquakes, it is essential to provide LFTBs with enhanced levels of lateral stiffness and strength. Equally important is the prevention of excessive levels of nonstructural damage, as significant costs of damage repairs (i.e.,gypsum wallboard replacement) after earthquake events have been reported (Kircher et al., 1997). In Chile, wood-frame shear walls usually have a strong structural configuration, consisting of 41 mm × 185 mm (2×8) framing members, sturdy end studs (typically comprising 4 or more members), conventional or continuous hold-down devices, wood structural panels (WSPs) -typically OSB on both sides- and closely spaced nails for attachment of sheathing to wood-frame members (Estrella et al., 2020). On the other hand, the nonstructural sheathing customarily consists of one or two layers of Type X gypsum wallboard (GWB) at both sides, fastened to the framing with screws or staples through the OSB. These features cast multi-layered strong shear walls (MLSSWs), as exemplified in Fig. 4.1, whose characteristics have neither been thoroughly investigated nor explicitly considered by design codes or mechanical models. More precisely, although previous investigations have reported a distinct behavior for these types of strong walls (i.e., more prevalence of the rocking effect Guinez et al. (2019); Estrella et al. (2020); Estrella, Malek, et al. (2021), the influence of the nonstructural finishes is rather unknown, and no adequate modeling procedures are currently available. The structural effect of the GWB has been mainly studied in conventional light-frame shear walls (the term conventional was introduced by Estrella et al. (2020)), hence a brief summary of the experimental testing of conventional walls with nonstructural finishes is presented next.

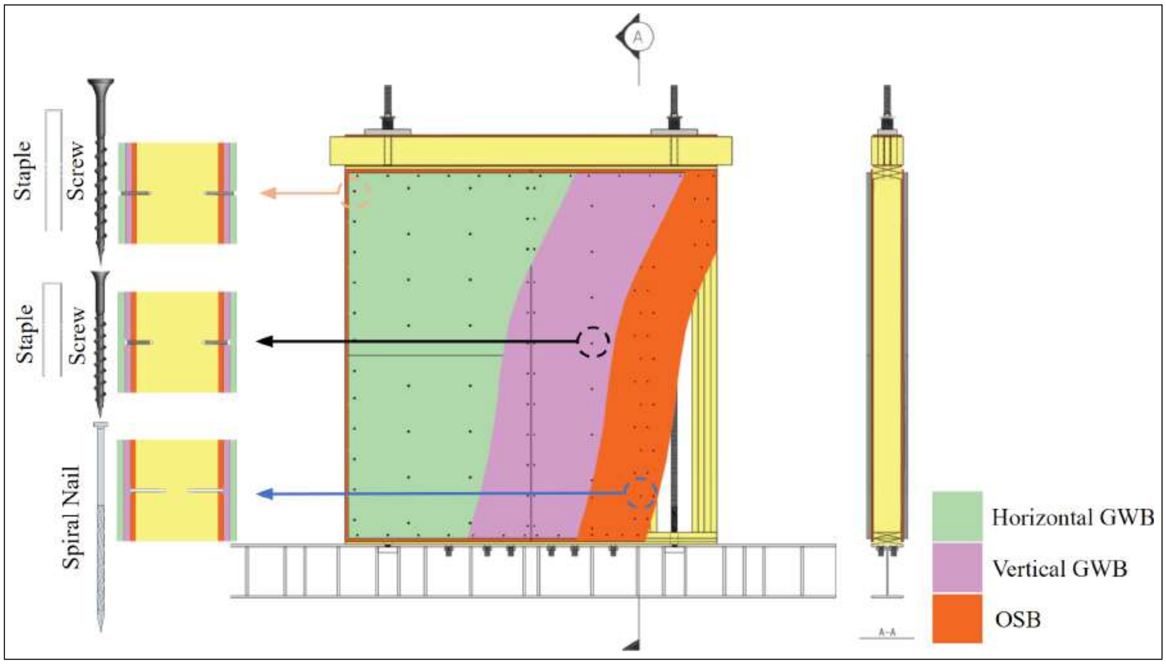

Figure 4.1. Typical Chilean MLSSW configuration

4.1.1. Experimental evaluation of the effect of nonstructural GWB finish layers

GWB is the most common interior wall sheathing material for fire protection used in residential construction (Wolfe, 1983). Due to the brittle nature of its core material and its supposedly low stiffness and strength relative to that of wood-based panel materials, the structural contribution of GWB to the lateral response of light-frame buildings is rarely recognized (Wolfe, 1983). For this reason, manufacturers have focused on the characterization of GWB for acoustic and fire protection purposes rather than on the mechanical properties that influence the lateral response of a shear wall, such as the shear modulus (Cramer et al., 2003; Rahmanian, 2011; Group, 2022). However, previous research has evaluated the contribution of different finish layers to the lateral response of different configurations of shear walls. Wolfe (1983) set the basis for the racking resistance of wood-frame shear walls sheathed with GWB on one side with typical details for housing purposes. The experimental campaign found that GWB has a potential contribution to the racking resistance of light-frame walls and its performance is orientation-dependent, i.e., walls sheathed with horizontal GWB panels were 40% stronger than walls sheathed with the panels oriented vertically (this is the reason why the external paper layer that confined the gypsum core is horizontally oriented). Filiatrault et al. (2002) evaluated the influence of wall finishes materials (i.e., exterior stucco and interior GWB layer) on a two-story wood-frame house. Test results revealed that the installation of wall finishes substantially increased the structure's lateral stiffness and reduced its seismic displacement response compared to the case with bare shear walls (i.e., when only OSB sheathing is considered without gypsum wallboard). The study motivated further studies to quantify the long-term effect of finish materials on wood-frame houses and to evaluate the possible incorporation of such effect into seismic design procedures. Uang and Gatto (2003) evaluated experimentally the effect of the GWB finish layer on the lateral response of wood-frame shear walls. They found a 12% and 60% increase in lateral strength and stiffness, respectively, but also a 31% reduction in deformation capacity due to significant strength degradation. Moreover, GWB impacted the failure mode of the shear walls, by limiting the twisting in the stud caused by the eccentricity due to sheathing placed at only one side. Kharrazi et al. (2002) pointed out that non-structural materials such as stucco and GWB played a major role in reducing earthquake damage, which should be recognized in the design process. Therefore, T. W. White and Ventura (2007); T. White and Ventura (2007) proposed seismic design parameters for up to two-story light-frame timber houses in Canada, where GWB is considered as an interior sheathing material of the wall acting in parallel with the OSB installed on opposite sides of the frame. However, this study was constrained by the amount of GWB participation in the lateral response of a structure. Filiatrault et al. (2010) evaluated the effect of GWB on a full-scale two-story wood-frame townhouse. A reduction of up to 9% of the fundamental period was found because of a 21% of increase in the lateral stiffness of shear walls, which was attributed to the incorporation of GWB in the interior side. Also, contrary to other findings (Uang & Gatto, 2003), when the finish layer was incorporated the lateral stiffness degradation was smaller than that of bare shear walls. The study highlighted the need to develop a seismic design method that takes into account the effect of wall finishes materials. Chen et al. (2016) evaluated experimentally the effect of double-layer vertically oriented Type X GWB on the lateral behavior of light-frame timber shear walls. As evaluated in previous research (Kharrazi et al., 2002; Uang & Gatto, 2003; T. W. White & Ventura, 2007; T. White & Ventura, 2007; Filiatrault et al., 2010), OSB and GWB were installed on opposite sides of the frame. When two GWB layers were used, the base GWB layer tended to behave like a single large panel increasing the strength by 29% and decreasing the deformation capacity by 25% compared with the case where one GWB layer was installed. The finding was important in the context of fire protection of mid-rise buildings, where two GWB layers are typically required. Even though the aforementioned research results were promising, the experimental evaluation of the MLSSW configuration typically used for mid-rise buildings in highly seismic-prone areas was not considered. In this context, a first approach was given by Goodall and Gupta (2011). They looked for improvements in the performance of GWB in wood-frame shear walls, motivated by the fact that the configuration typically used for houses (i.e., OSB and GWB panels installed on opposite sides of the frame) tended to trigger substantial damage to the GWB mainly because of the different lateral stiffness of OSB and GWB. A promising solution was to install the GWB at the top of a shear wall sheathed on both sides with OSB, which resulted in improvement of the GWB performance (i.e., reduction of earthquake damage) due to minimization of the difference in lateral stiffness between both sides of the wall. However, the effect of the finish layer on the lateral behavior of the shear wall (which is of great interest for MLSSWs and mid-rise LFTBs) was not quantified. As part of the NEESwood project, van de Lindt, Pei, Pryor, et al. (2010) evaluated experimentally the seismic response of a full-scale six-story LFTB at the world's largest shake table in Miki, Japan. The rocking restraint system was a continuous rod system (i.e., anchoring tie-down system, ATS) (Tyrell, 2007) typically used in SSWs and MLSSWs. However, since a case with bare shear walls was not considered in the test program, the contribution of the nonstructural finish layer was considered through the estimation of nonstructural damage and as part of the seismic mass rather than through its effect on the lateral response. Recently, Line et al. (2021) evaluated experimentally the contribution of Type X GWB to the racking strength of wood-frame shear walls with representative multi-story details (i.e., the racking restraint system was a continuous rod system Tyrell (2007)). GWB and OSB were installed on opposite sides of the frame, as in previous research (Kharrazi et al., 2002; Uang & Gatto, 2003; T. W. White & Ventura, 2007; T. White & Ventura, 2007; Filiatrault et al., 2010). Results showed that Type X GWB increased the peak strength by 3% and the initial stiffness by 11% when shear walls were tested cyclically and monotonically, respectively, compared to bare shear walls. Contrary to previous research, the study reinforced the traditional practice that ignores the contribution of GWB in the seismic design of LFTBs. Even though most research has focused on typical GWB, several studies have looked for a gypsum-based board with improved performance (Reyes et al., 2010; Dinehart & Blasetti, 2012; Seim et al., 2016; Casagrande et al., 2016). Solutions such as viscoelastic (VE) GWB and gypsum fiberboard (GFB) were demonstrated to behave similarly to a properly detailed OSB or plywood sheathing. Swensen et al. (2016) proposed a different approach by replacing the typical GWB-to-frame joint with adhesive, achieving increases of three and two times in stiffness and strength, respectively, compared to the conventional screwed solution. Finally, J. R. Jayamon et al. (2018) pointed out the importance of the experimental quantification of damping effects of nonstructural components used in LFTBs, since some previous studies (Filiatrault et al., 2002) reported increments of up to 35% in system damping due to the addition of wall finishes (i.e., exterior stucco and interior GWB). In summary, even though several studies have demonstrated the benefits of nonstructural finish GWB layers, the experimental evaluations have been limited to wall assemblies that are different from those typically used in mid-rise LFTBs located in highly seismic-prone areas (i.e., MLSSWs). Hence, it becomes important to quantify experimentally and/or numerically the effect of GWB layers in strong shear wall assemblies, particularly in the context of the development of tall timber buildings in seismic areas. In this paper, the contribution of finish Type X GWB layers to the lateral response of strong timber shear walls (SSWs) is evaluated through reverse cyclic tests on 2.44 m x 2.44 m full-scale MLSSWs and comparisons with previous findings on bare shear walls (Guinez et al., 2019; Estrella, Malek, et al., 2021). Findings are generalized in terms of quantification of parameters necessary for structural design and evaluation of the analytical model presented in the Special Design Provisions for Wind and Seismic (SDPWS) standard (AWC, 2021). Finally, a simplified numerical model was developed based on the hysteretic response of the connection-level assemblies (i.e., nailed OSB-to-frame and screwed multilayer Type X GWB+OSB-to-frame) of the layers that are part of the walls, which are then combined to represent the hysteretic response of MLSSWs.

4.2. Experimental Program

An experimental program was developed to characterize the behavior of multi-layered sheathing-to-frame connections and full-scale shear walls under monotonic and/or cyclic loading. All the full-scale MLSSW shear walls have the same configuration (see subsection 4.2.2) because the test results will be used to develop empirical damage fragility curves of MLSSWs. The resulting fragility curves will be published in another paper.

4.2.1. Connection-level

4.2.1.1. Test Specimens

Three different configurations of multi-layered sheathing-to-frame connections were assembled considering the typical fasteners used for attaching OSB and Type X GWB to wood frames. As shown in Figure 4.2, the connection-level specimen consisted of a frame of 41 mm x 185 mm (2x8) dimensional Chilean radiata pine lumber mechanically graded as C16 according to NCh1198 (INN, 2014) and attached to different sheathing materials and fastener types (see Table 4.1).

4.2.1.2. Test set-up

A reaction steel frame was used to perform the connection-level tests. As shown in Figure 4.3, the reaction steel frame is anchored to a concrete floor. A heavy-duty steel beam is installed on the frame at a suitable location to accommodate the specimen, which

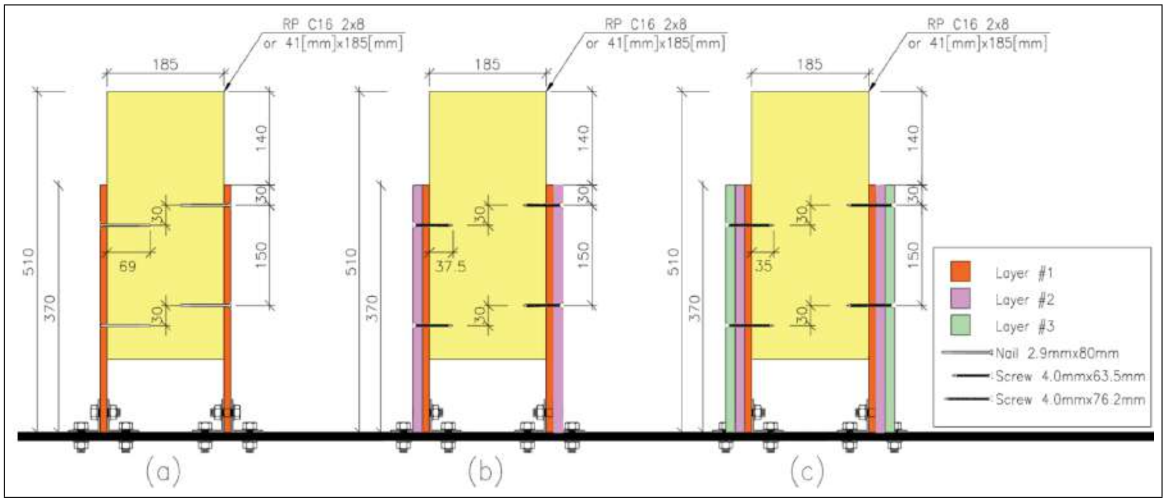

Figure 4.2. Multi-layered connection specimen for: (a) Connection A, (b) Connection B, and, (c) Connection C. All dimensions in millimeters

Table 4.1. Summary of the connection-level specimens [a]

Test Group	n[b]	Layer # 1	Layer # 2	Layer # 3	Fastener Type	p[g]
A	4	11.1, OSB	-	-	Nail[c,f] ϕ 2.9x80	69.0
B	4	11.1, OSB	15, Type X GWB	-	Screw[d,f] ϕ 4.0x63.5	37.5
C	4	11.1, OSB	15, Type X GWB	15, Type X GWB	Screw[e,f] ϕ 4.0x76.2	35.0

[a] all dimensions in millimeters
[b] one and three specimens for monotonic and cyclic tests, respectively
[c] OSB sheathing layer attached to frame with pneumatically driven wire coil spiral nails (80 x 2.9 x 6.5 mm) according to EN14592:2008+A1:2012 (BSI, 2008)
[d] Type X GWB sheathing first layer attached to frame through the OSB with type “W” screws (63.5 x 4.0 x 8.0 mm)
[e] Type X GWB sheathing second layer attached to frame through the 1st Type X GWB and OSB with type “W” screws (76.2 x 4.0 x 8.0 mm)
[f] geometry of nails and screws are specified as length x root diameter x head diameter
[g] penetration of the nail or screw in the wood-frame

is attached to the heavy-steel beam through bolted L-shape elements (Figure 4.3). The load was applied by a double-action cylinder of $\pm$86 kN and $\pm$75 mm of force and displacement capacity, respectively, which transfers the vertical load to the specimen through a load-transfer system that consists of two L-shape elements welded to a steel plate and attached to the specimen through bolts. As shown in Figure 4.3, all specimens were instrumented with two displacement transducers (LVDTs) and one double-effect load cell to capture the slip and shear force between the frame and sheathing multi-layers.

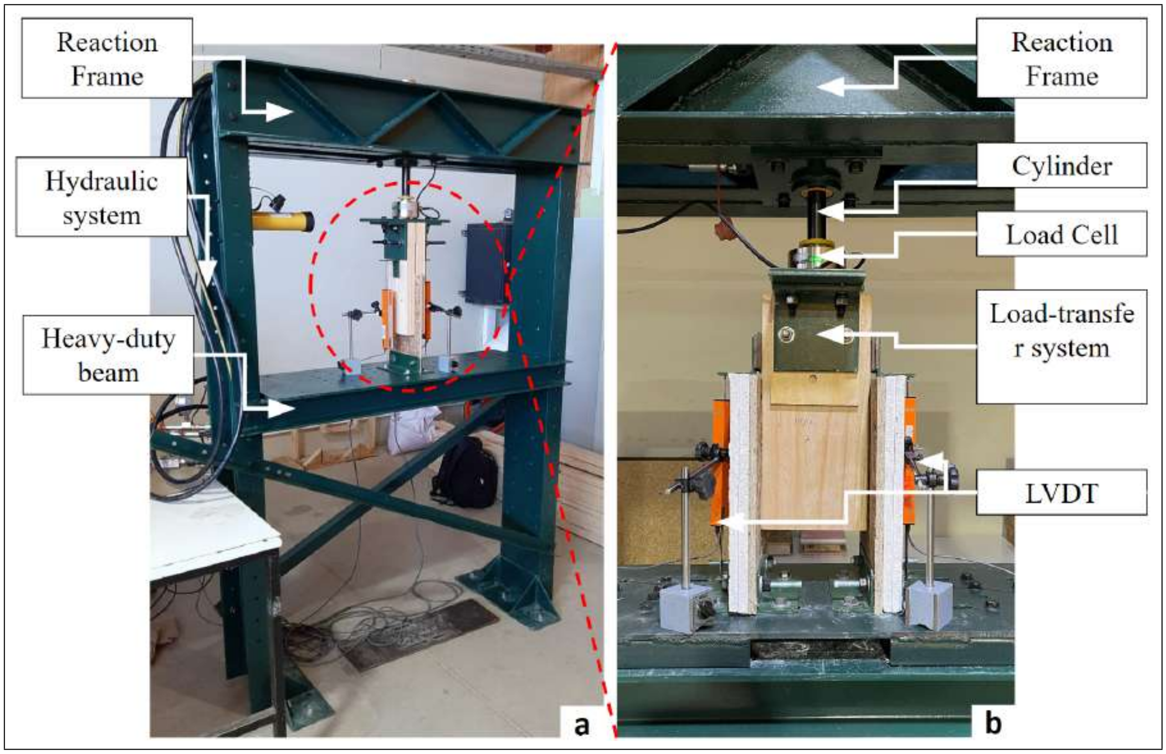

Figure 4.3. Connection-level test set-up: (a) general view of the reaction steel frame and (b) detailed view of the specimen set-up

4.2.1.3. Test protocol

The loading protocol was established according to ASTM E564-06 (ASTM, 2006) and ASTM E2126-19 (ASTM, 2006) for the monotonic and cyclic tests, respectively. The ultimate displacement observed in the monotonic test (i.e., the maximum displacement at which the strength has not yet dropped below 80% of the peak strength) was used to compute the reference displacement for the simplified CUREE-Caltech cyclic testing protocol (Krawinkler et al., 2001) according to method C of ASTM E2126-19 (ASTM, 2006). The loading protocol was displacement-controlled and applied until failure of the specimen.

4.2.2. Assembly-level (shear wall)

4.2.2.1. Test Specimens

Specimens are representative of typical ground-level walls of a 7-story building designed per the Chilean seismic design code NCh433 (INN, 2009) (see Figure 4.4). Four of them are MLSSWs, whereas the remaining one (i.e., the control wall) is a bare strong shear wall. Details of the test specimens are summarized in Table 4.2. Double plates at the top and bottom of the wall were nailed to the studs with ϕ3.0 mm x 80 mm smooth shank nails that conform to ASTM F1667 (ASTM, 2021). All framing elements were 41 mm x 185 mm (2x8) C16 Chilean RP dimensional lumber, with a nominal modulus of elasticity E = 7900 MPa according to NCh1198 (INN, 2014). The walls were sheathed on both sides with 11.1 mm thick APA-rated OSB panels (APA, 2012) with G = 1307.5 MPa (measured in previous studies Estrella, Malek, et al. (2021)), and pneumatically driven to the frame with ϕ2.9 mm x 80 mm spiral nails. OSB sheathing layers were installed at both sides of the specimens and attached to the lower top plate and to the upper bottom plate as illustrated in Figure 4.4. According to the SDPWS (AWC, 2021), edge-nailing at the end studs should be uniformly distributed among the four framing members and spaced at a maximum of 300 mm. The walls of the MLSSWs specimens were sheathed on both sides with two layers of 15 mm thick Type X GWB panels (Group, 2022) with a measured G = 1177.9 MPa according to the ASTM D3044-16 (ASTM, 2016) prescriptions. The first Type X GWB layer was vertically oriented and attached to the frame through the OSB with ϕ4.0 mm x 63.5 mm (i.e., Nº 8 x 2-½") screws, whereas the second Type X GWB layer was horizontally oriented and attached to the frame through the first Type X GWB layer and OSB with ϕ4.0 mm x 76.2 mm (i.e., Nº 8 x 3") screws. In order to transfer the lateral load to each specimen, a built-up collector beam of 205 mm x 207 mm (i.e., five members of 41 mm x 185 mm C16 RP plus an 11.1 mm thick OSB layer on top and bottom) was mechanically attached to the top plate through 38 Simpson Strong-Tie's SCDP221100 screws.

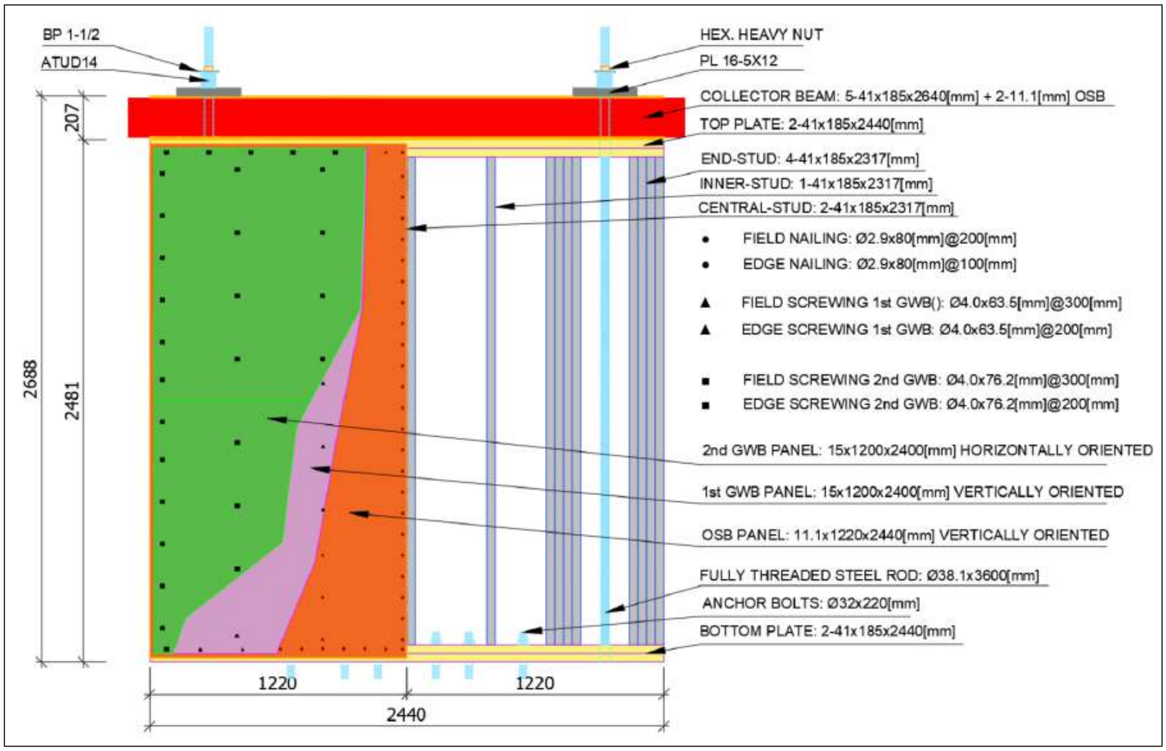

Figure 4.4. Configuration and components of the MLSSW specimens

Table 4.2. Experimental design of the assembly-level specimens[a,b]

Test Group	n	Wall size (L by H)	Wood Structural Panel (WSP)			Gypsum Wallboard (GWB)		
			Thickness	Sheathing Nails[c]	Spacing edge/field	Thickness and Type	Wallboard screws[d]	Spacing edge/field
CT-100-38	1	2440x2481	11.1	ϕ 2.9x80	100/200	None	-	-
MLSSW	4	2440x2481	11.1	ϕ 2.9x80	100/200	(2) - 15, Type X	ϕ 4.0x63.5 ϕ 4.0x76.2	200/300

[a] Wall framing consisted of 41mm x 185 mm (2x8) C16 Chilean RP studs at 400mm o.c.

[b] Wall shear anchorage consisted of ϕ 32 mm x 220 mm ASTM A193 Grade B7 anchor bolts.

[c] Nails installed considering a minimum of 20/40 mm of end/edge distance respectively.

[d] ϕ 4.0 x 63.5 and ϕ 4.0 x 76.2 screws for the first and second Type X GWB respectively.

4.2.2.2. Test set-up

A cantilever reaction wall, a strong floor, and a reaction steel beam were used to perform the assembly-level tests following ASTM E2126-19 (ASTM, 2019) prescriptions. As shown in Figure 4.5, the MLSSW specimens were attached to the reaction beam through a rod-to-steel beam connector (i.e. Simpson Strong-Tie ATS-SBC10H connector) and 14 ϕ32 mm x 220 mm ASTM A193 Grade B7 anchor bolts to prevent overturning and sliding, respectively. The lateral load was applied by a hydraulic bidirectional actuator of $\pm$245 kN and $\pm$ 250 mm of force and displacement capacity, respectively, which transfers the lateral load to the specimen through the collector beam (see Figures 4.4 and 4.5). As illustrated in Figures 4.5 and 4.6(a), the actuator is supported by two slings attached to the reaction wall to prevent possible influence of the vertical loading on the response of the specimen. Out-of-plane support was provided in such a way that in-plane displacements were not affected. As shown in Figure 4.6, all specimens were instrumented with thirteen displacement transducers (LVDTs), one laser displacement transducer, and one load cell and displacement transducers (LVDT) incorporated into the actuator to capture the lateral displacement and shear force along the axis of the collector beam (element 15 in Fig. 4.6), the slip of the wall with respect to the steel reaction beam, the diagonal (shear) deformation (element 5 and 6 in Fig. 4.6), uplift in the exterior edge of the wall (element 2 in Fig. 4.6), the relative displacement between the multiple layers of the wall (element 11 for OSB-to-1st Type X GWB and element 13 for 1st Type X GWB-to-2nd Type X GWB in Fig 4.6, respectively), the relative displacement of the steel reaction beam with respect to the strong floor (elements 7 to 9 in Fig. 4.6), and the compressive deformation under the bearing plate of the strong-rod system (elements 12 and 14 in Fig. 4.6). To measure the tension in the rods of the continuous hold-down, two unidirectional strain-gauges were attached to the rods (elements 3 and 4 in Fig. 4.6).

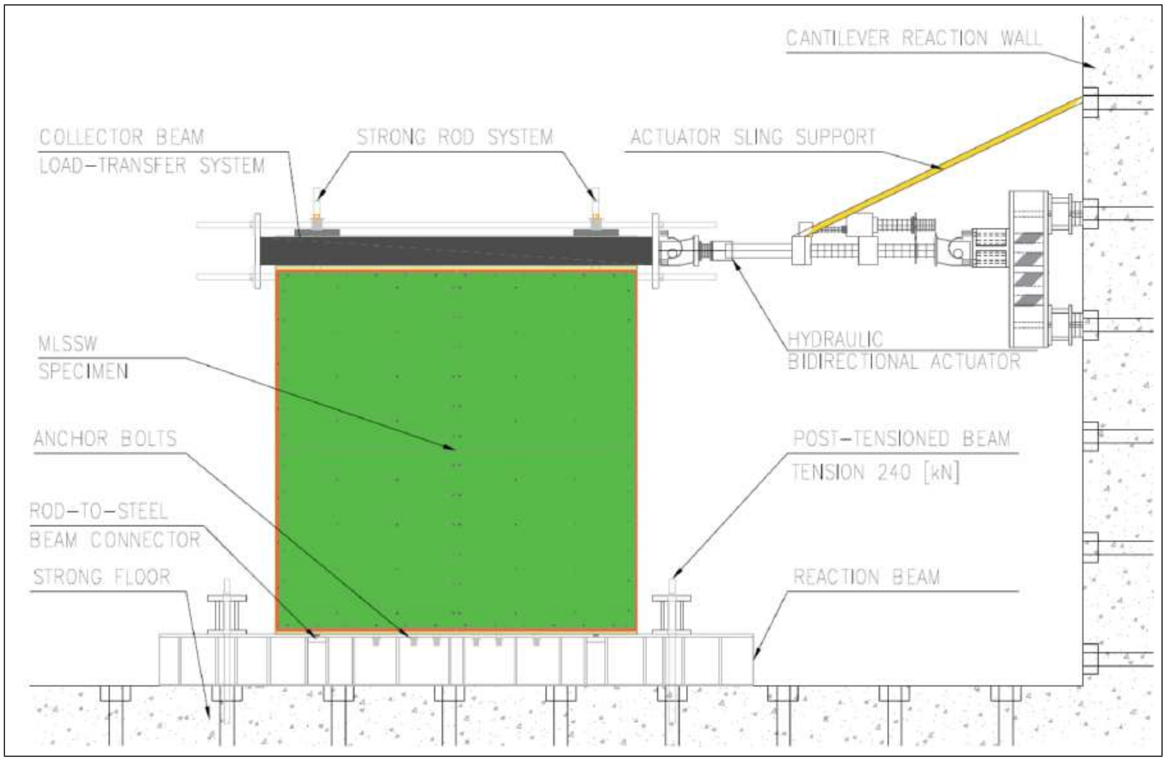

Figure 4.5. Front view of the test set-up for assembly-level specimens.

4.2.2.3. Test protocol

In order to characterize the in-plane cyclic behavior of MLSSWs, the CUREE-Caltech cyclic testing protocol proposed by Krawinkler et al. (2001) was applied. The reference displacement was based either on: a) previous monotonic tests conducted by Guinez et al. (2019) on bare shear walls of comparable MLSSW features for the case of conventional hold-downs; or b) the shear walls investigated by Estrella, Malek, et al. (2021) for the case of continuous rod hold-down anchorages. The maximum limit for the reference displacement Δ = 61 mm was set for the MLSSW specimens (i.e. 0.025 times the wall height) as established in method C (i.e. the simplified CUREE-Caltech protocol) of ASTM E2126-19 (ASTM, 2019). The loading protocol was displacement-controlled and applied until the specimens reached a safe minimum capacity after the peak strength.

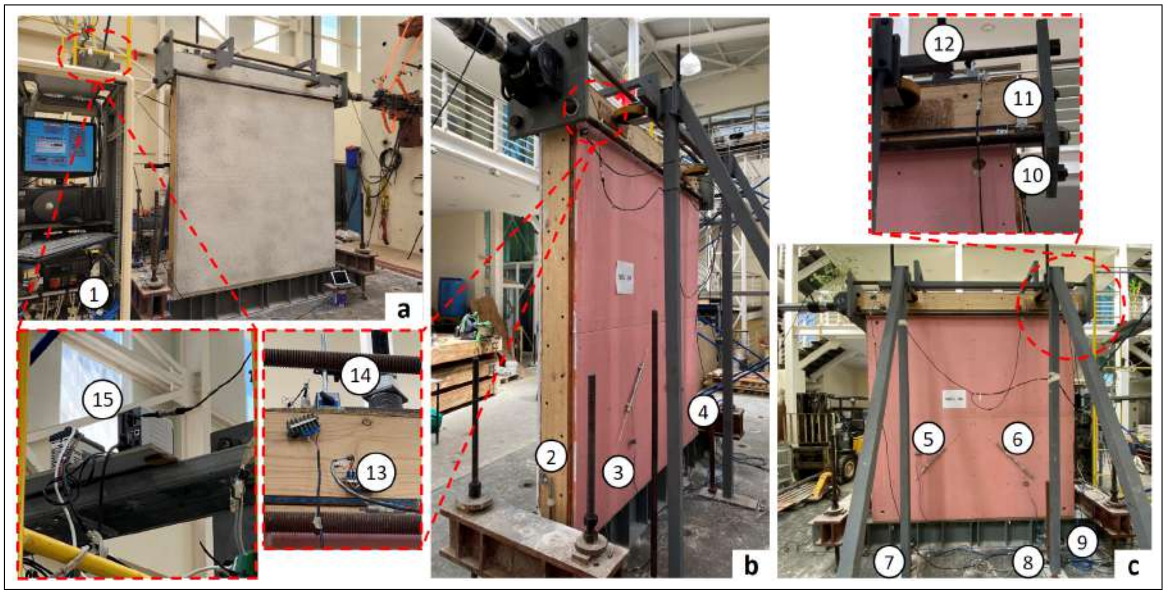

Figure 4.6. Test set-up, (a) overall front view where DIC was applied, (b) lateral view, (c) overall back view where transducers were installed.

4.3. Results and discussion

Failure mode, hysteresis shape, and eight engineering parameters were established for connection-level and assembly-level test results: (1) elastic stiffness (K_e); (2) yield displacement (Δ_y); (3) yield force (F_y); (4) ultimate displacement (Δ_u); (5) ultimate force (F_u); (6) ductility (μ); (7) energy dissipation ($E_{H,i}$), and (8) equivalent viscous damping (ζ_{eq}). Moreover, the lateral behavior of MLSSWs is compared with that of bare SSWs reported in previous test campaigns (Estrella, Malek, et al., 2021) and that of a bare assembly used in this study as reference (i.e., the same MLSSW configuration but without Type X GWB panels). Finally, findings on MLSSWs are generalized. Nominal shear capacity (v_{SDPWS}) and an apparent shear wall shear stiffness (G_a) for the studied MLSSW specimens are proposed, and the suitability of the design guidelines provided by the Special Design Provisions for Wind and Seismic (SDPWS) North American standard (AWC, 2021) are evaluated.

4.3.1. Connection-level

4.3.1.1. Failure mode

The specimens were inspected after each cyclic test in order to evaluate typical failure modes (see Figure 4.7). On the nailed OSB-to-frame connection (i.e., test group A) two failure modes were identified: (1) excessive bend in the nail leading to shearing-off of the fastener; and (2) pull out or pull-through of the nail from the OSB-to-frame joint, leading to detachment of the OSB. In both cases, crushing in the wood and OSB panel and fiber tear in the OSB panel were observed. These failure modes were consistent with those identified by other researchers (J. D. Dolan & Madsen, 1992; Fonseca et al., 2002; Sartori & Tomasi, 2013; Seim et al., 2016; Estrella et al., 2020). On the screwed one layer Type X GWB+OSB-to-frame connection (i.e., test group B) two failure modes were identified: (3) excessive bend in the screw leading to shearing-off of the fastener; and (4) pull-through of the screw from the one layer Type X GWB+OSB-to-frame joint, leading to detachment of the GWB and OSB sheathing. In both cases, crushing in the wood and panels and tearing in OSB and GWB panels were likewise observed. These failure modes were also consistent with those identified by other researchers (Swensen et al., 2016). On the screwed two layers of type X GWB+OSB-to-frame connection (i.e., test group C), one failure mode was identified: (5) excessive bend in the screw leading to shearing-off of the fastener. Wood crushing and tearing in OSB and Type X GWB panels were observed. These failure modes were again consistent with those reported by other researchers (Fonseca et al., 2002; Swensen et al., 2016).

4.3.1.2. Monotonic force-displacement response

The monotonic force-displacement test response for all the tested groups is presented in Figure 4.8, in which the reported displacement is the differential slip between the wood frame and the multi-layer sheathing, and the force is that taken by only one fastener along a single shear plane. In specimens with two Type X GWB, two screws are needed (one

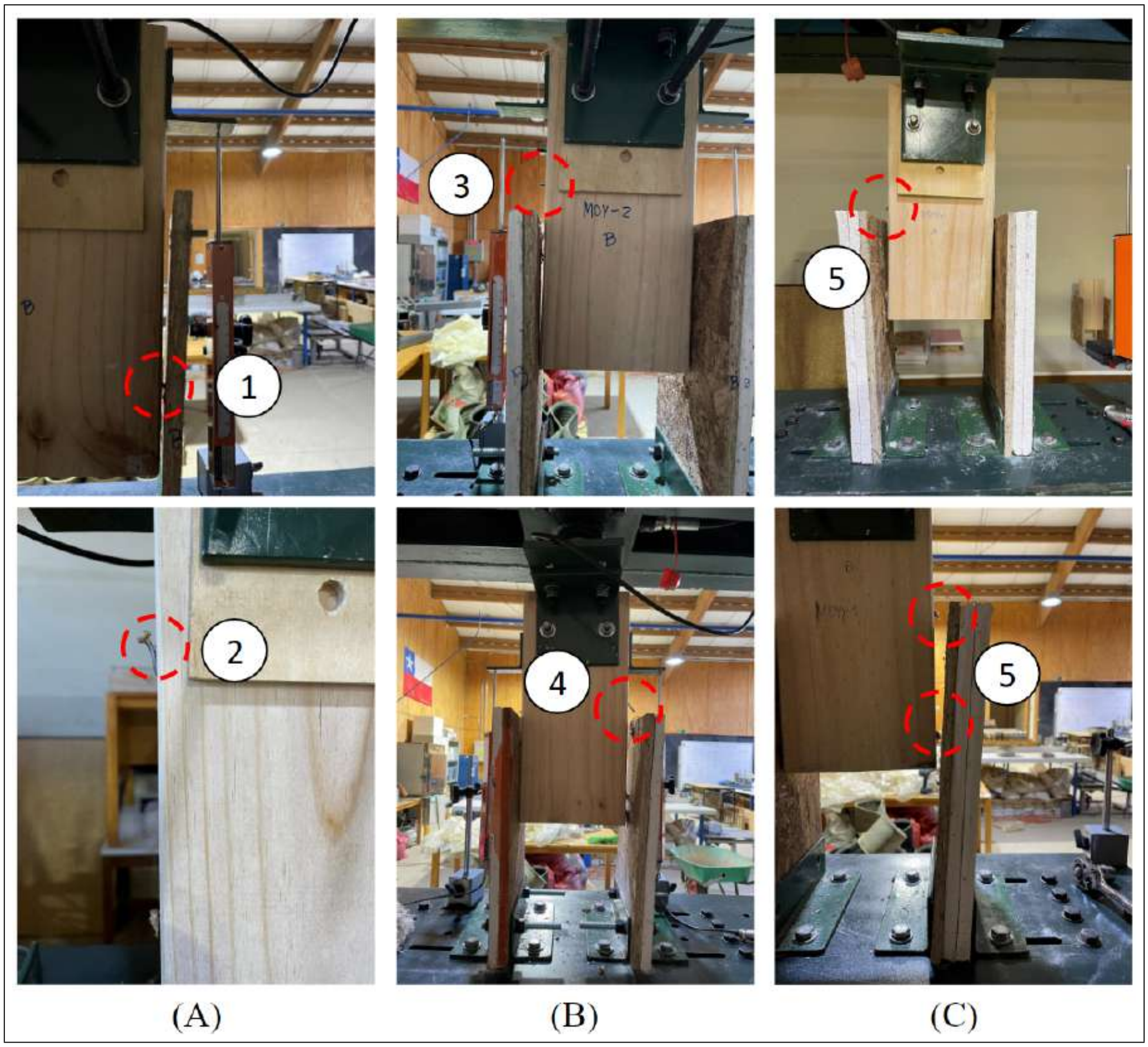

Figure 4.7. Failure modes identified in connection-level test: (A) nailed OSB-to-frame, (B) screwed one layer Type X GWB+OSB-to-frame, and (C) screwed two layers Type X GWB+OSB-to-frame.

for each GWB), but results reported in this section refer to either one nail (for bare connections) or one screw, regardless of the number of Type X GWB. This makes possible a direct evaluation of the use of only one fastener in different configurations. Six engineering parameters are summarized in Table 4.3, where the Equivalent Energy Elastic-Plastic (EEEP) (G. C. Foliente, 1996) approach was used to estimate the parameters according to ASTM E2126-19 (ASTM, 2019). Monotonic test results indicate that connections A

(OSB+nail) and B (OSB+Type X GWB+screw) exhibited almost the same elastic stiffness, even though connection B has multiple layers of sheathing. In contrast, connection C (OSB+(2)Type X GWB+screw) was about twice stiffer than connections A and B. Results for connections A and C were consistent with the analytical stiffness expressions reported in (EN, 2004). However, connection B exhibits smaller stiffness than the analytical prediction, attributable to installation defects that tend to leave a gap between the sheathing layer and the wood-frame due to difficulties in screwing throughout the finish layers. Regarding capacity (strength), the screwed connections B and C exhibited stronger capacity than the nailed connection A. The screwed connection takes advantage of the axial capacity of the fastener, whereas the nailed connection is easily pulled out. From a ductility point of view, connection A performs better than all other GWB-sheathed connections. Ductilities of connections B and C were expected because screws are typically less ductile than nails and the reinforcing effect of the Type X GWB produced a more prominent strength degradation and a reduction of the inelastic ultimate displacements. However, the behavior of connection C are similar to the one reported in concrete-to-wood hybrid connections (Carrero et al., 2020) in terms of elastic stiffness (i.e. elastic stiffness is almost double of the test group B), but the peak strength and the ultimate displacement are similar to the ones of connections B. That is why the ductility of connections C is 80% higher than that of connection B. Likewise, it was found that even when all connections showed comparable yielding displacements of about 1-2 mm, the ultimate displacement of the bare connection A was about twice larger than that of the other connections, indicating that GWB-sheathed connections can clearly undergo lesser inelastic displacements.

Table 4.3. Engineering parameters from monotonic connection-level test results

Test Group	K_e kN/mm	Δ_y mm	F_y kN	Δ_u mm	F_u kN	μ
A	0.904	1.870	1.690	31.510	1.527	16.849
B	0.903	2.150	1.940	17.049	1.830	7.931
C	1.892	1.010	1.911	14.389	1.847	14.247

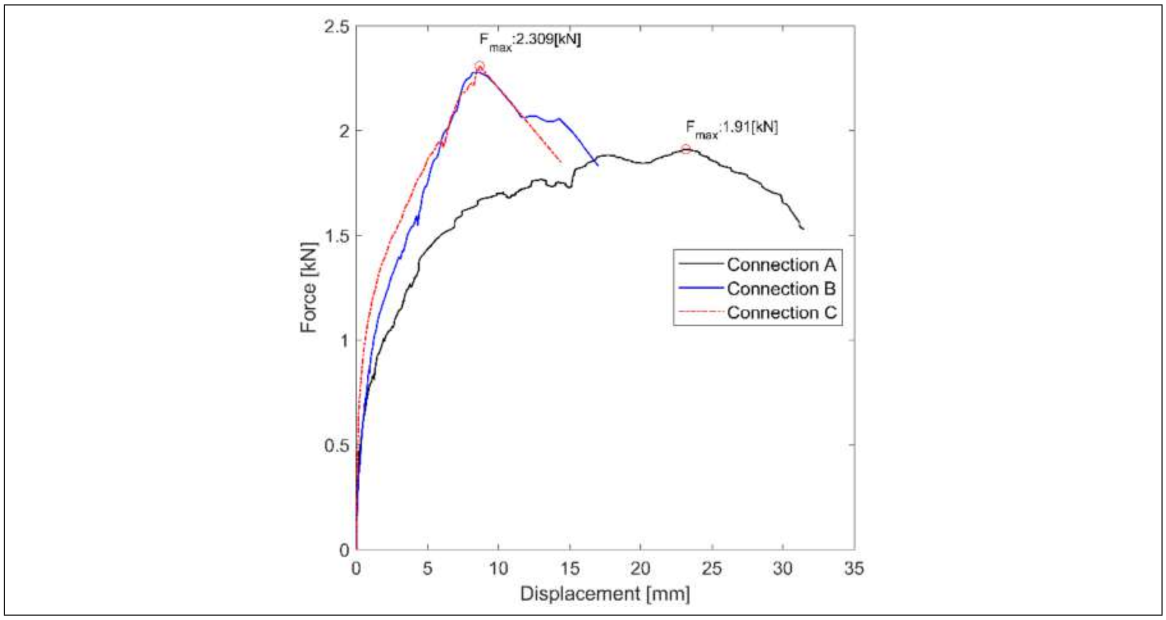

Figure 4.8. Monotonic test results for connection-level tests.

4.3.1.3. Cyclic force-displacement response

The cyclic force-displacement test response for all the tested connections is presented in Figures 4.9 and 4.10. Again, results are expressed in terms of differential slip per fastener/shear plane. Cyclic test results for all tested connections depict a strong pinching effect due to wood frame and OSB crushing at the shear planes. Moreover, an abrupt strength degradation after repeated cycles at the same target displacement was found in all tests. A markedly asymmetric hysteretic response was found for bare OSB connections (group A), which was not consistent with previous findings (J. D. Dolan & Madsen, 1992; Fonseca et al., 2002; Sartori & Tomasi, 2013; Seim et al., 2016; Estrella et al., 2020). This asymmetric response could be attributed to: (1) the threaded portion of the nail is located at its end rather than distributed along the whole length (as in previously reported tests Estrella et al. (2020)), which would affect the rope effect in the connection (Sartori & Tomasi, 2013); and/or (2) an installation effect (i.e., the use of a pneumatic nail gun). This asymmetric response behavior of full-scale MLSSWs should be analyzed with more detail in the future. Apart from the response asymmetry, cyclic test results were consistent with monotonic test results: larger strength and stiffness of screwed connections, and a significantly larger ultimate displacement capacity of nailed connections.

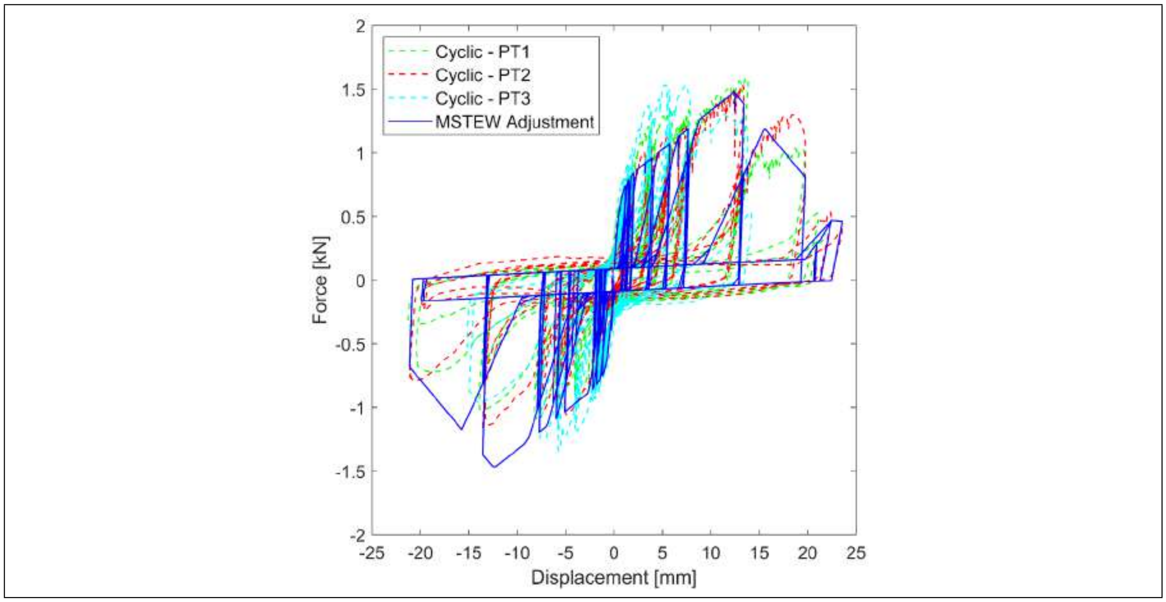

Figure 4.9. Force-displacement response of Connection A (i.e., nailed OSB-to-frame)

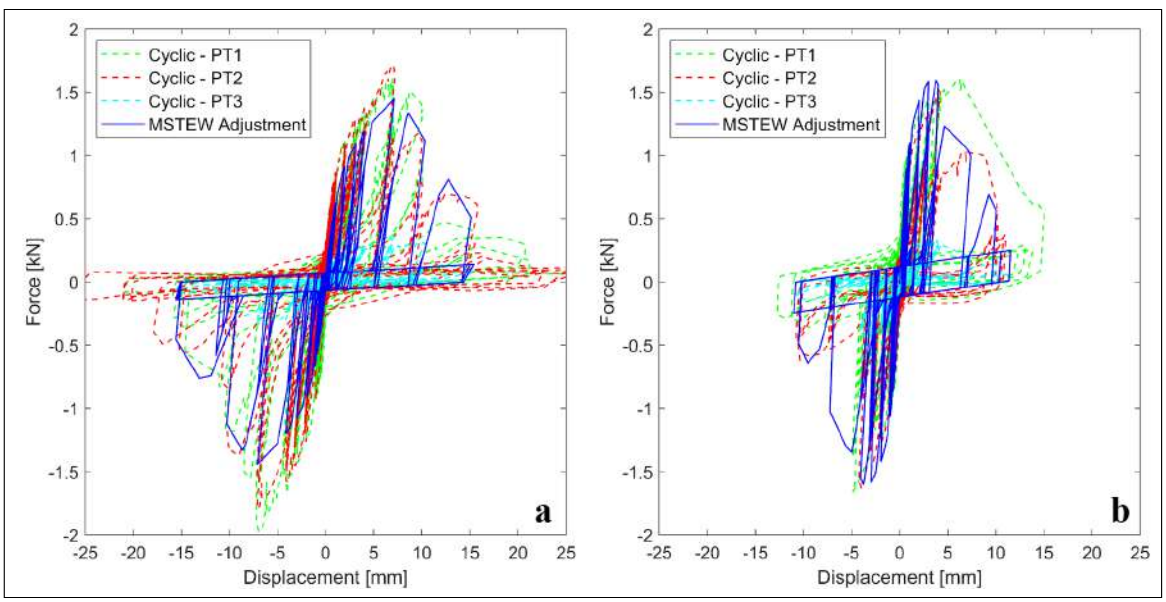

Figure 4.10. Force-displacement response of Connections (a) B (i.e., screwed one layer Type X GWB+OSB-to-frame), and (b) C (i.e., screwed two layers Type X GWB+OSB-to-frame).

4.3.1.4. MSTEW hysteretic model

The experimental force-displacement behavior of sheathing-to-framing connections was highly nonlinear under monotonic loading and exhibited pinched hysteresis with strength and stiffness degradation under cyclic loading. These results are consistent with those reported by other researchers (J. D. Dolan & Madsen, 1992). The MSTEW model is capable of phenomenologically capturing such behavior, which is attributed to wood crushing (framing and sheathing) and yielding of the fastener (Folz & Filiatrault, 2004b). The MSTEW model was adopted in this research, even though it accounts for symmetric responses only. The equation that describes the backbone curve of the monotonic and cyclic behavior, as well as the hysteretic loop shape, can be found in (Folz & Filiatrault, 2004b). The MSTEW modeling parameters for each test group were calibrated with the MSTEWfit tool that is part of the MATLAB M-CASHEW software (W. Pang & Hassan-zadeh Shirazi, 2013). A good agreement with test results was found. Errors in cumulative energy dissipation (calculated as the area enclosed by hysteresis cycles) were smaller than 5% in most cases. All calibration results are summarized in Table 4.4.

Table 4.4. MSTEW modeling parameters [a]

Test Group	K_0 kN/mm	r_1	r_2	r_3	r_4	F_0 kN	F_I kN	Δ_u mm	α	β	F_u kN
A	1.050	0.020	-0.101	1.189	0.004	0.850	0.090	13.800	0.750	1.100	1.480
B	0.905	0.085	-0.140	1.010	0.005	0.899	0.068	7.500	0.450	1.200	1.410
C	1.892	0.050	-0.087	1.25	0.006	1.322	0.120	3.500	0.750	1.250	1.570

[a] K_0 is the initial stiffness of the hysteretic curve, r_1 to r_4 are dimensionless parameters that represent stiffness ratios at different parts of the curve, F_0 and F_I are strength parameters of the hysteretic curve (Folz & Filiatrault, 2004b), and Δ_u is the displacement at peak load. Parameters α ($\alpha > 0$) and β ($\beta > 0$) control the stiffness degradation and energy degradation, respectively.

4.3.1.5. Evolution of secant stiffness

The evolution of the secant stiffness with test cycles is illustrated in Figure 4.11. The secant stiffness (k_sec) was calculated as:

$$k_{sec,i} = \frac{F_i^+ - F_i^-}{\delta_i^+ - \delta_i^-} \tag{4.1}$$

where $k_{sec,i}$ is the secant stiffness at cycle i, F_i^+, F_i^- are the peak forces and δ_i^+, δ_i^- are their corresponding displacements, respectively. Multilayer sheathing-to-frame screwed connections (i.e., test groups B and D) showed higher peak strength and secant stiffness than nailed connections (i.e., test group A). In general, these results are consistent with the findings of other researchers, as screwed connections typically show considerably more hardening than nailed connections (Carrero et al., 2020). Moreover, as also found in monotonic test results, connection C exhibited almost twice the secant stiffness of connection B up to cycle 10, even though the screws have the same root diameter and penetration length in the wood frame. The authors attribute these results to the fact that the double Type X GWB layers in test group C essentially behave as a concrete layer in a hybrid connection. According to test results reported by Carrero et al. (2020), the European design code (EN, 2004) accurately predicts the stiffness and strength of hybrid connections. In that code, a factor of 2.0 over the wood-based stiffness equation is used to predict the elastic stiffness of connections with a concrete layer. The 2.0 factor is consistent with the results reported in Figure 4.8. From cycle 20, connections B and C show almost the same secant stiffness, mainly because the secant stiffness is controlled by yielding of the screws and by crushing of the sheathing layers.

4.3.1.6. Dissipated energy and equivalent viscous damping

The evolution of the cumulative dissipated energy and the equivalent viscous damping is presented in Figure 4.12. The cumulative dissipated energy was computed as the area enclosed by the hysteresis cycle. The equivalent viscous damping (ζ_{eq}) was computed to

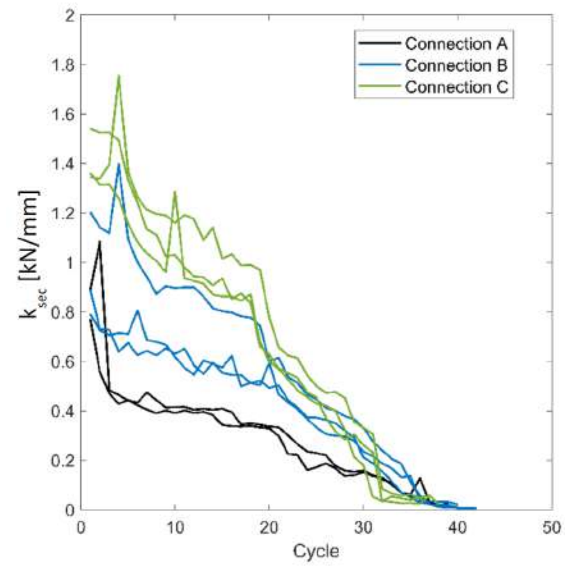

Figure 4.11. Connection-level tests: evolution of secant stiffness

quantify the capacity of the connection to dissipate energy under cyclic loading. For a given cycle i, ζ_{eq} was calculated as follows:

$$\zeta_{eq,i} = \frac{E_{H,i}}{\pi \left(F_i^+ \delta_i^+ + F_i^- \delta_i^- \right)} \tag{4.2}$$

where $E_{H,i}$ is the dissipated energy during cycle i, computed as the area enclosed by the hysteresis loop. Test group A showed higher levels of cumulative dissipated energy, followed by test groups B and C (i.e., screwed connections). Most of the multilayer connections showed steady values of damping ratio up to cycle 30, where an increment was observed. Comparison between mean and characteristic ζ_{eq} values are presented in Figure 4.13. The characteristic value was set equal to the 10th percentile of the ζ_{eq} values at all cycles and all specimens of each test group. In the case of test group A, mean and characteristic ζ_{eq} values are $\approx$ 15% and $\approx$ 10%, respectively. These values are consistent with those reported by previous researchers (Sartori & Tomasi, 2013; Seim et al., 2016). The mean ζ_{eq} values of test groups B and C were roughly 9% smaller and 1.5% larger than that of test group A, respectively. The characteristic ζ_{eq} values of test groups B and C were

47% and 18% smaller than that of test group A, respectively. The difference in results between connections B and C is attributable to the initial difference in stiffness (i.e., up to cycle 10), which is consistent with results of hybrid connections reported in (Carrero et al., 2020). However, from cycle 20, results of connections B and C exhibit a similar trend, which is attributed to yielding screws and crushing in wood and sheathing layers. However, given the large dispersion observed in test results, further research is recommended to confirm the findings presented in this paper.

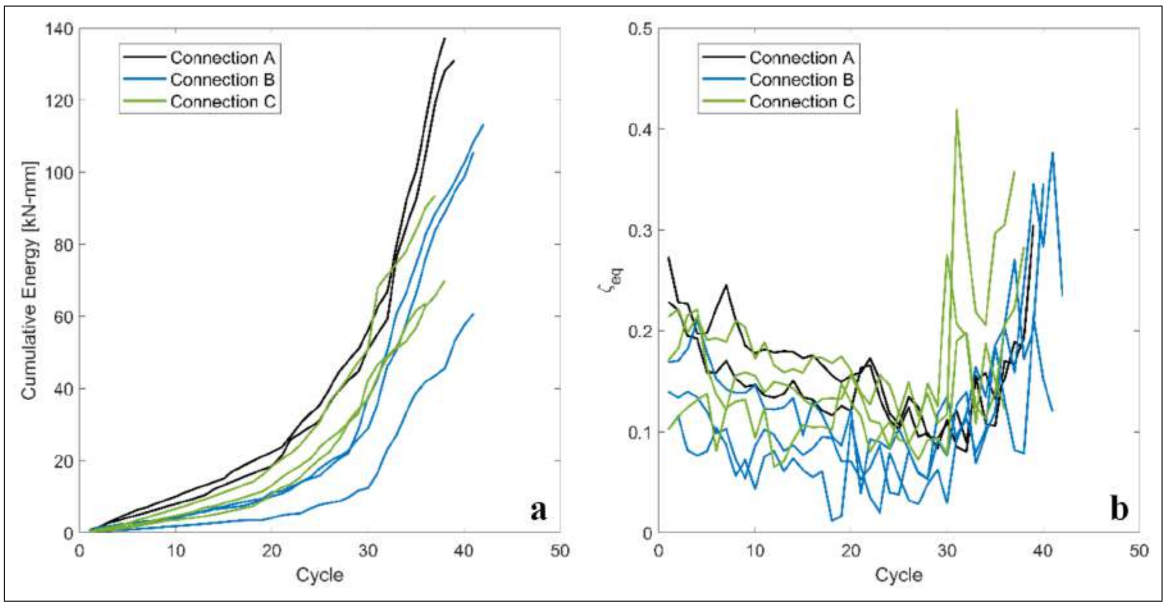

Figure 4.12. Connection-level tests: evolution of (a) cumulative dissipated energy, and (b) equivalent viscous damping

4.3.2. Assembly-level

4.3.2.1. Failure mode

The wall specimens were inspected after each test in order to evaluate typical failure modes. In all four specimens (all of them had a 2-Type X GWB screwed configuration, as detailed in Section 4.2.2.1) five failure modes were identified: (i) pulling out of the nails and screws (see labels 4 and 6 in Figure 4.14); (ii) pulling out of the nail and screw heads through the OSB or Type X GWB panels (see label 7 in Figure 4.14); (iii) shear-off of nails

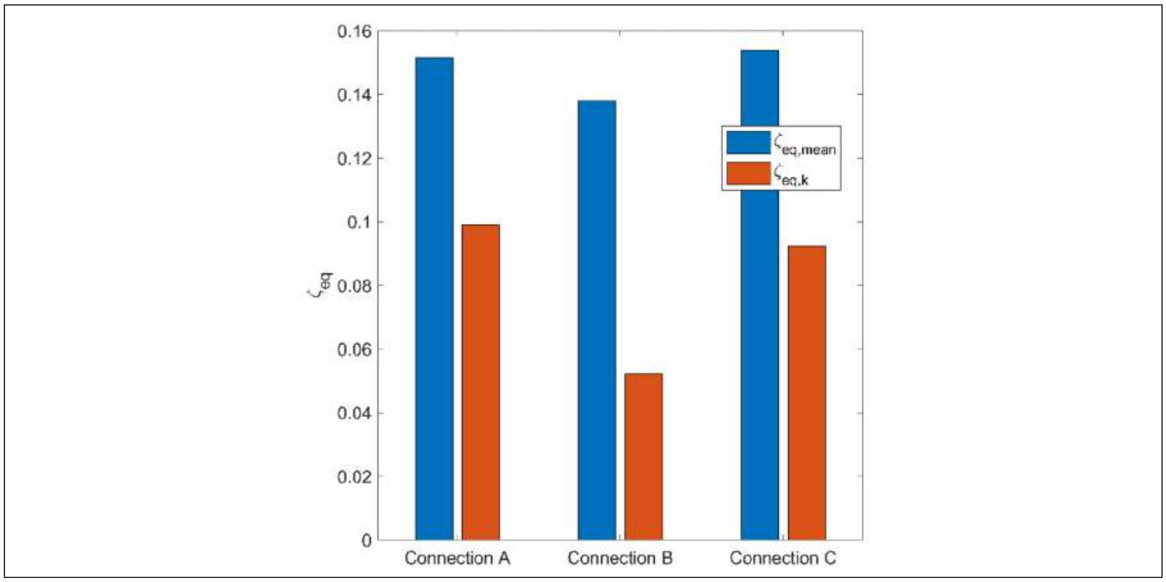

Figure 4.13. Connection-level tests: comparisons between mean and characteristic equivalent viscous damping

and screws due to excessive fastener bending (see labels 2, 3, 6 and 10 in Figure 4.14); (iv) local embedding failure (crushing) in the OSB and Type X GWB panels attributable to an excessive stress concentration around the fastener (see labels 5 and 9 in Figure 4.14); and, (v) detachment (out-of-plane unsheathing) of the OSB and GWB panels (see label 8 in Figure 4.14) from the wood-frame because of failure of the fasteners (i.e. nails and screws). In all cases, excessive and moderate crushing in the wood and in the OSB and Type X GWB panels were observed. The fasteners failure typically followed the patterns illustrated in label 1 of Figure 4.14. It initiated at the center studs of the walls and propagated to the edge of the walls at the final stages of the loading protocol. This phenomenon is consistent with findings of previous researchers for continuous rod hold-downs (Estrella, Malek, et al., 2021), and can be explained by the concentration of fasteners in end studs around the continuous rod, which typically initiates failure at interior sheathing edges. It is remarkable that double shear failure (i.e. shear-off failure of screws located at the central double stud because of the presence of two shear planes in the interaction between the 2nd and 1st layer of Type X GWB and the 1st layer of Type X GWB and OSB layer), pull-out, and pull-through of fasteners, along with local embedding of sheathing, were found as failure modes. However, there was no evidence of shear Type X GWB failure, and apparently, there was no reduction of the shear wall racking deformation capacity. Typically, the failure of non-structural finishes has been a cornerstone in restraining the design inter-story drift limit because it is commonly thought that it has much less deformation capacity and is more brittle than OSB. In MLSSWs, however, there was neither evidence of GWB failure nor shortening of the deformation capacity. This behavior is attributed to the fact that OSB sheathing offers protection to GWB (Goodall & Gupta, 2011), preventing brittle failure modes if OSB and GWB are located on both sides of the frame (i.e., the GWB always has a protective OSB layer beneath). In fact, as reported by Line et al. (2021), when shear walls are sheathed only with GWB layers or with both GWB and OSB layers but installed at opposites sides of the frame, typical failure modes include screws head pull through the panels (to the point where the GWB eventually detached from the wood framing) or fatigue fracture of the screws around the perimeter of the panel, which leads to a brittle failure of the wall. Even though these failure modes were presented in MLSSW after reaching the peak load, they do not affect the deformation capacity of the wall leading to more ductile behavior. Moreover, failure of the nails and detachment of the OSB occurred only at the ultimate stages of the loading protocol because of the minimal reinforcing effect of the GWB after the general failure of the GWB-screwed connections. The wood frame showed moderate to low damage in all cases. Damage was concentrated mainly on the double central (interior) stud of the specimens and its connection to the top and bottom double plate, and was not as excessive as observed in previous tests on specimens with denser nailing patterns of 50 mm (Estrella, Malek, et al., 2021). At the final stages of the loading protocol, detachment between the end studs located at the edge of the specimen and the bottom double plate was observed due to failure of the nailed OSB-to-bottom plate connection. As expected, the rocking restraint system showed no damage in all the wall tests (it was designed to behave elastically even at the peak strength of the MLSSW specimens). The top-bearing steel plates were not damaged, as no crushing into the OSB of the collector beam was observed. This was also attributable to the overstrength factor used to design the specimens, which led to predominant nail and screw ductile failures.

Figure 4.14. Main failure modes observed in MLSSW specimens: (1) nail and screw failure pattern; (2) and (3) failure of the screwed Type X GWB+OSB-to-wood frame connection (in orange) for the 2nd layer and 1st layer, respectively; (4) and (6) pulling out of screws and nails; (5) and (9) local failure of the Type X GWB panels and OSB, respectively; (7) pulling through of nails and screws;(8) sheathing layers detachment from the wood-frames; and, (10) double shear failure of the screws.

4.3.2.2. Cyclic force-displacement response

The hysteretic curves of the four MLSSW specimens (CT-MLSSW-0i, all comprising 2 screwed Type X GWB) and the control wall (CT-100-38, only with bare OSB without any GWB sheathing) are shown in Figures 4.15 and 4.16, respectively. The reported displacement is the effective displacement of the wall measured at the collector axis where the actuator was located. Effective displacement is the measured lateral displacement at the collector of the wall minus the displacement measured at the specimen-to-reaction beam relative to the reaction beam-to-strong floor. The overall shape of the hysteresis loops was consistent with that reported in previous research (Pei & van de Lindt, 2009; Guinez et al., 2019; Estrella, Malek, et al., 2021). The MLSSW specimens showed elastic response up to a drift of about 1.0%, and then a nonlinear response was observed, attributable to the multilayer sheathing-to-wood frame connection. After the specimens reached the peak strength, progressive and smooth strength and stiffness degradation was found. As expected, high redundancy was evident in the specimens because of the multiple screwed and nailed connections at multiple layers, resulting in high drift levels with no brittle failures. Hence, as the lateral behavior of the MLSSWs was governed by the connection-level response, the MLSSW hysteresis was markedly pinched because of the non-reversible crushing effect of the fasteners (i.e., nails and screws) over the wood-frame components, which leads to a gap between the wood and the fasteners.

4.3.2.3. Continuous rod system response

The stress-uplifting response of the overturning restraint system at the right rod of the selected MLSSW specimens is presented in Figure 4.17. The rod stress was computed based on measurements by strain gauges attached to the fully threaded rods. The continuous rod system lifting was measured via LVDTs at the lower edge of the specimens, as described in section 4.2.2.2. Even though the rods behaved perfectly elastic during the tests (the computed stress on the rods was about 3 times smaller than the nominal yielding

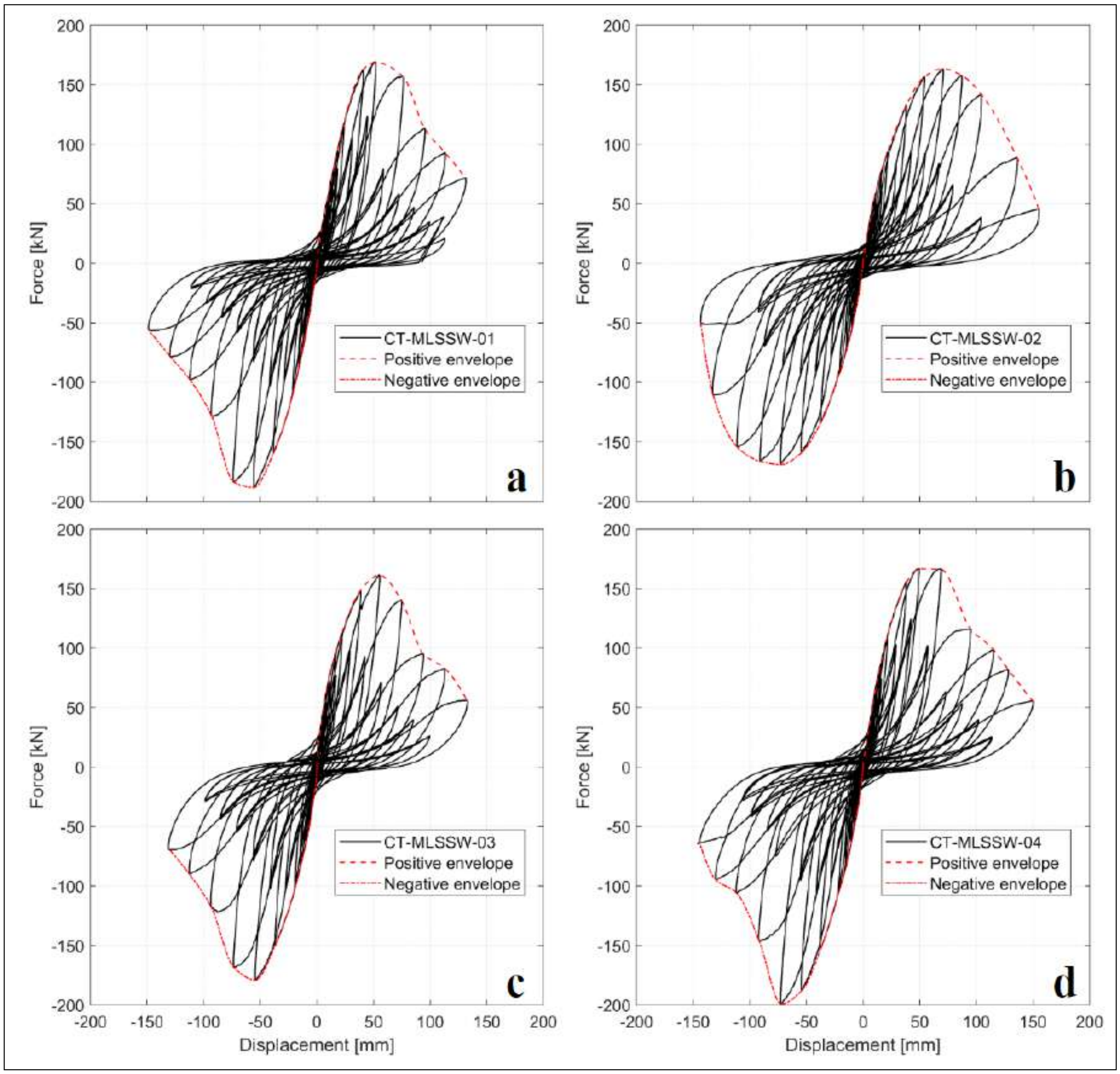

Figure 4.15. Force-displacement cyclic response of MLSSW specimens: (a) MLSSW-01, (b) MLSSW-02, (c) MLSSW-03, and (d) MLSSW-04.

stress), the curves showed a slight hysteresis attributable to the plastic deformation perpendicular to the grain and wood crushing under the compressive load generated by the activation of the continuous rod system. These effects became visible at the reaction zone on the bottom/top plate and collector beam (see Figure 4.17). These results are consistent with those reported in previous research (Estrella, Malek, et al., 2021) for bare strong walls with 50 mm nail spacing rather than the 100 mm used in the MLSSW specimens tested in

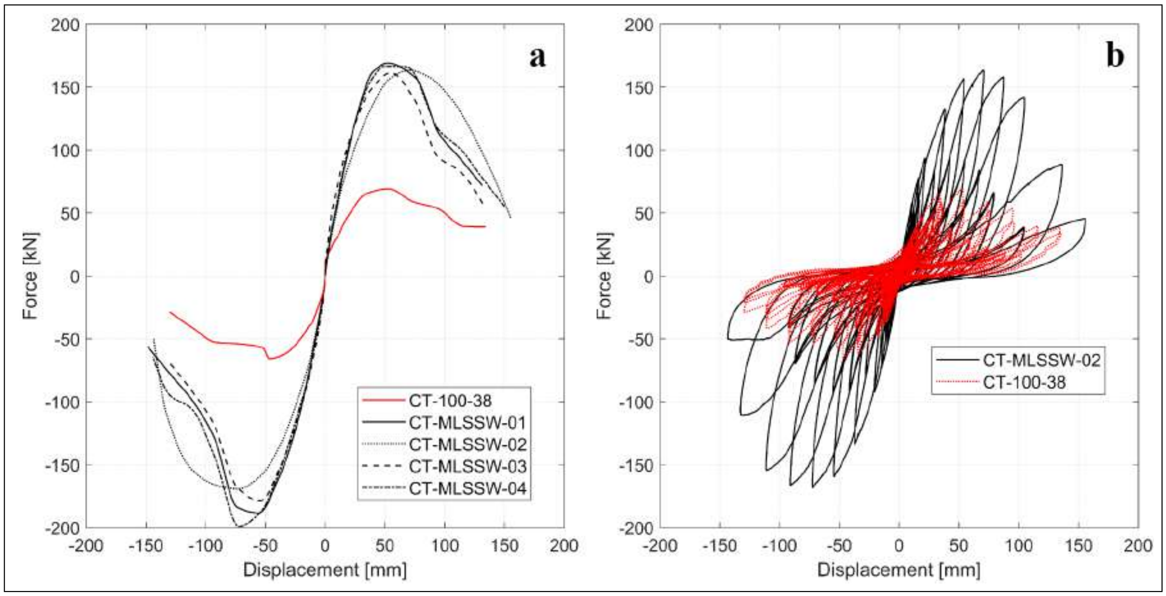

Figure 4.16. Comparison between (a) backbone curves of all tested specimens, and (b) force-displacement hysteretic response of MLSSW sample CT-MLSSW-02 and control wall (i.e., bare strong shear wall) CT-100-38.

this study. High-stress levels were evident at the rod in some MLSSW specimens. Furthermore, tensile stresses were measured at the compressed corner of the wall (Figure 4.17, negative x-axis values). This behavior could be attributable in part to the high levels of compressive plastic deformation at the bottom plate, which could misalign the kinematics of the system causing the rod to take some tension. Finally, a slight clearance of about 5 mm was found in the anchoring system, which may arise from the initial misalignment of the components of the shear wall and/or the testing apparatus. In addition, wood plastic embedment/crushing of top and bottom plates may also lead to additional tolerances of the anchoring during the loading process (Figure 4.17). Regardless of the cause, a short plateau is evident at the center of the stress-uplift curves, generating U-shaped curves.

4.3.2.4. Analysis of the engineering parameters of the MLSSW

The engineering parameters of the shear walls' backbone curves were estimated according to the Equivalent Energy Elastic-Plastic (EEEP) approach (G. C. Foliente, 1996) per ASTM E2126-19 (ASTM, 2019). Values of the secondary stiffness factor r_1 (Koliou

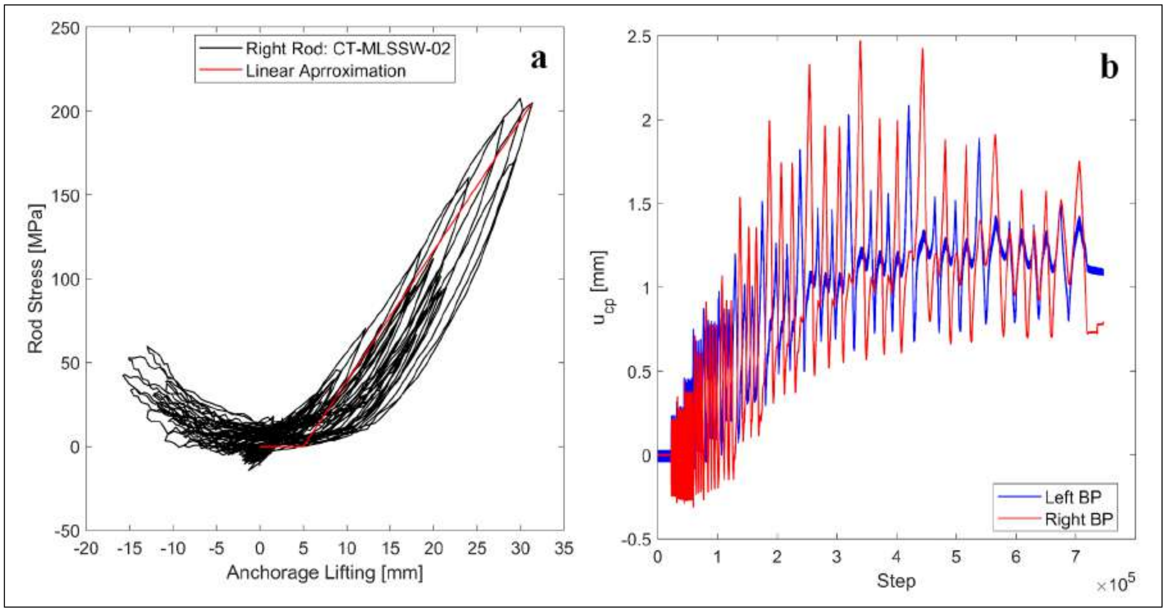

Figure 4.17. Specimen CT-MLSSW-02: (a) anchorage response; (b) deformation under the bearing plate located on the collector beam at the location of the continuous rod system.

et al., 2018) and the degradation stiffness factor r_2 (also called post-yield stiffness factor J. Jayamon et al. (2016)) were calculated considering the MSTEW constitutive model (Folz & Filiatrault, 2004b) and the generalized force-deformation relation proposed for ASCE 41 by Koliou et al. (2018). The resulting values are summarized in Table 4.5. The parameters of the with-GWB sheathed shear walls (MLSSW, labeled as MLSSW-0i) are presented along with the parameters of the control wall without GWB sheathing (labeled as CT-nail spacing in mm-rod diameter in mm), and the parameters of two additional bare shear walls reported in the literature (Estrella, Malek, et al., 2021). All the shear walls tested in this research had a panel edge nail spacing of 100 mm and an anchoring rod of 38 mm in diameter, whereas the comparison walls extracted from the literature (Estrella, Malek, et al., 2021) were similar but unsheathed with GWB and with a) a nail spacing of 100 mm and a rod of 44 mm (CT-100-44); and b) a nail spacing of 50 mm and a rod of 44 mm (CT-50-44). To enhance the visibility of the asymmetric response of the tested walls, positive, negative, and mean backbone responses are reported. Moreover, statistical parameters (i.e., mean, standard deviation, and coefficient of variation) for the MLSSWs studied in this research are also presented. The highest dispersions are that of ductility and yield displacement, with up to 20% variations with respect to the mean. This dispersion is reasonable, due not only to the inherent variability of timber structures but also to the significant influence of the shape of the response curve on the determination of yield displacement and ductility.

4.3.2.5. Strength

The MLSSW specimens showed a mean peak strength of 174.5 kN, which is up to 160% higher (i.e., almost 3 times) than the peak strength (67.5 kN) observed in the equivalent bare strong shear wall specimen (CT-100-38), see Table 4.5. According to previous test results (Estrella, Malek, et al., 2021), bare strong shear walls with characteristics similar to those of the walls tested in the present study (i.e., OSB panel thickness of 11.1 mm and nail spacing of 100 mm, but with steel rod bar diameter of 44 mm) presented a peak strength of 89.67 kN, which is almost 50% lower than that of the MLSSWs. Finally, MLSSW peak strength is approximately 39% higher than that of bare shear walls with a similar configuration but with a 50 mm nail spacing pattern (125.6 kN), which is the minimum nail spacing reported in SDPWS (AWC, 2021). These surprising results confirm that double sheathing and screwing Type X GWB in timber shear walls can make an enormous structural difference, as it may have an even stronger influence than denser nailing patterns or stronger anchorages (these two parameters are currently among the most important design parameters to increase the capacity of timber shear walls). This enormous increase is thought to be generated not only by the "parallel spring" action of the screws but also because of the axial strength of the screws and their axial sheathing fixing may also reinforce and benefit the nailed OSB-to-wood frame connection, which is believed to control the strength of bare shear walls. This is related to the fact that in MLSSWs the evident pulling-out of OSB-to-wood frame connections took place at the final stage of the testing protocol, whereas in the CT-100-38 specimen the same phenomenon started right after the peak strength was reached.

Table 4.5. Engineering parameters from cyclic MLSSW and control wall test results

Test Group	K_e [kN/mm]	Δ_y [mm]	F_y [kN]	Δ_u [mm]	F_u [kN]	F_{peak} [kN]	μ	r_1	r_2
MLSSW-01+	5.531	28.407	157.120	86.586	135.138	168.985	3.048	0.200	-0.237
MLSSW-01-	5.600	30.616	171.463	86.975	150.740	188.426	2.841	0.200	-0.277
MLSSW-01$_{mean}$	5.455	29.512	164.292	86.781	142.939	178.705	2.945	0.200	-0.257
MLSSW-02+	5.177	38.350	147.771	112.825	130.670	163.338	3.980	0.100	-0.254
MLSSW-02-	5.152	29.832	153.682	123.611	135.386	169.232	4.144	0.100	-0.250
MLSSW-02$_{mean}$	5.165	34.091	150.727	118.218	133.028	166.285	4.062	0.100	-0.252
MLSSW-03+	7.631	18.639	142.233	79.755	129.067	161.333	4.279	0.100	-0.182
MLSSW-03-	6.175	25.786	159.215	84.972	143.134	178.917	3.295	0.100	-0.252
MLSSW-03$_{mean}$	6.903	22.213	150.724	82.364	136.101	170.125	3.787	0.100	-0.217
MLSSW-04+	5.909	25.988	153.573	87.915	133.269	166.587	3.383	0.079	-0.201
MLSSW-04-	5.660	30.936	175.113	86.315	159.135	198.919	2.790	0.105	-0.366
MLSSW-04$_{mean}$	5.785	28.462	164.343	87.115	146.202	182.753	3.087	0.092	-0.284
MLSSW$_{mean}$	5.854	28.569	157.521	93.619	139.567	174.467	3.470	0.123	-0.252
MLSSW$_{std}$	0.795	5.607	11.123	15.652	10.601	13.247	0.591	0.048	-0.055
MLSSW$_{CV(\%)}$	13.6	19.6	7.1	16.7	7.6	7.6	17.0	39.1	21.8
CT-100-38[a]+	3.582	17.120	61.320	88.045	55.277	69.097	5.143	0.100	-0.109
CT-100-38[a]-	4.060	13.757	55.861	92.375	52.650	65.812	6.715	0.100	-0.093
CT-100-38$^{a}_{mean}$	3.821	15.439	58.591	90.210	53.964	67.455	5.929	0.100	-0.101
CT-100-44[b]	4.004	19.785	79.219	81.910	71.736	89.670	4.140	0.122	-0.154
CT-50-44[b]	5.622	21.790	122.503	137.710	100.504	125.63	6.320	0.104	-0.075

[a] CT-NP-AD: CT = cyclic test; NP = nail spacing pattern (i.e., 100 = 100[mm]); AD = anchorage diameter (i.e., 38 = 38[mm])

[b] Results from reference Estrella, Malek, et al. (2021), 1:1 aspect ratio strong shear wall with continuous hold-down similar to that used in this research.

4.3.2.6. Stiffness

The elastic stiffness for the MLSSWs, CT-100-38 and other research specimens is reported in Table 4.5. By elastic stiffness, we refer to the secant stiffness measured at 40% of the peak load, according to the following expression:

$$K_e = \frac{0.4P_{peak}}{\delta_{0.4P_{peak}}} \tag{4.3}$$

where P_{peak} and $\delta_{0.4P_{peak}}$ are the peak load and displacement measured at the 40% of the peak load, respectively, obtained from the backbone curves of the cyclic test. MLSSW specimens show a mean elastic stiffness of 5.854 kN/mm, which is up to 53% higher than the elastic stiffness observed in the control specimen CT-100-38 (3.821 kN/mm). According to previous experimental studies (Estrella, Malek, et al., 2021), the CT-100-44 specimen shows an elastic stiffness 32% smaller (4.004 kN/mm) than that obtained in MLSSWs. Moreover, MLSSW specimens are approximately 4% stiffer than specimen CT-50-44 (5.622 kN/mm). The evolution of the secant stiffness (defined in section 4.3.1.5) as a function of the lateral drift is presented in Figure 4.18. All specimens show a clear stiffness degradation as the lateral drift increases, presenting a residual stiffness between 0.5 kN/mm to 1.5 kN/mm. At 0.1% to 4% lateral drift the MLSSWs exhibit the highest levels of secant stiffness, and the degradation is linear rather than quadratic as observed in bare shear walls. At lateral drifts higher than 4% specimen CT-50-44 (Estrella, Malek, et al., 2021) presents a behavior similar to that of the MLSSWs. Finally, at lateral drifts smaller than 0.1%, specimens CT-50-44, CT-100-44 and CT-100-38 present a secant stiffness that is 4% higher, and 6.5% and 99% smaller than that of the MLSSWs, respectively. These results confirm that the actual elastic and secant stiffness of MLSSWs are greater than those based on the assumption of bare shear wall.

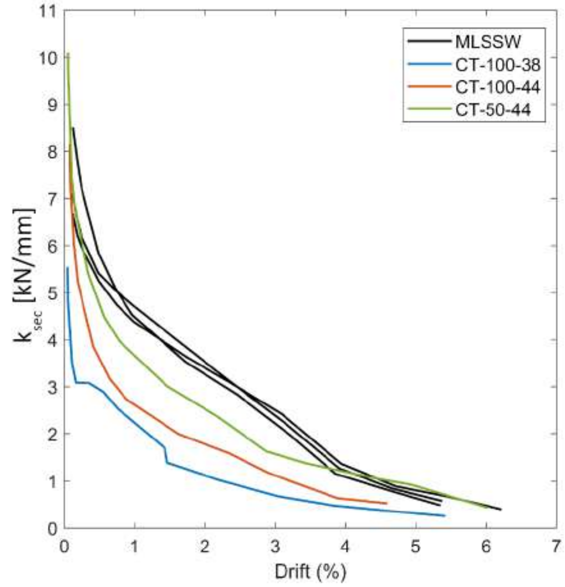

Figure 4.18. Secant stiffness degradation as a function of the lateral drift.

4.3.2.7. Ductility

In bare wood-frame strong shear walls the ductility is governed mainly by the nailed sheathing-to-frame connection. MLSSWs, on the other hand, have multiple sheathing-to-frame connections and each of these has a different ductility level, hence the overall ductility of MLSSWs depends on the combined effect of all connections. Values of ductility μ are reported in Table 4.5. They were computed according to ASTM E2126 (ASTM, 2019) as the ratio of ultimate to yield displacement: $\mu = \frac{\Delta_u}{\Delta_y}$. MLSSW specimens show a mean ductility of 3.47, which is 42%, 16%, and 45% smaller than the observed ductility in the control specimen CT-100-38 (5.929) and the previously tested (Estrella, Malek, et al., 2021) specimens CT-100-44 (4.144) and CT-50-44 (6.32). This reduction in ductility could be attributed to the screwed 1st/2nd layer GWB+OSB-to-frame connection, which contributes mainly to stiffness and strength rather than to deformation capacity because screws tend to fail first as the lateral drift of the MLSSW increases. In other words, the screwed connections themselves are less ductile than the nailed connections. However, once the screwed connections fail in MLSSWs, a rapid failure of the nails is expected as they are unable to take all the load previously taken by the screws. Therefore, the ductility of the screws (rather than that of the nails) is thought to govern the MLSSW ductility as was reported by previous researchers (Guinez et al., 2019; Estrella, Malek, et al., 2021), the nail spacing in OSB-to-frame connection controls the ductility of bare shear wall. Also, larger ductilities in bare shear walls could be attributable to larger steel rod diameters in specimens CT-100-44 and CT-50-44.

4.3.2.8. Energy dissipated and equivalent viscous damping

In order to evaluate the suitability of MLSSWs under seismic loading, it is necessary to quantify the dissipated energy in order to realistically estimate the performance of the system and its capability to dissipate energy induced by earthquakes. As previously mentioned, the behavior of wood-frame shear walls is controlled by the connections, which are the main source of energy dissipation. Other components of the system (i.e., the continuous rod system and the wood-frame) are design-protected to behave essentially elastic. The cumulative dissipated energy of the wall specimens is quantified according to the prescription described in 4.3.1.6. The evolution of the cumulative dissipated energy as a function of the lateral drift is presented in Figure 4.19. Specimen CT-50-44 (Estrella, Malek, et al., 2021) is the one with the highest level of dissipated energy. This specimen is the one with the greatest number of nailed connections, which are characterized by high ductility and energy dissipation capability. MLSSWs, on the other hand, are controlled by the elastic portion of the screwed connection. For drifts of up to 0.8%, there is no significant difference among MLSSW, CT-100-38 and CT-100-44 (Estrella, Malek, et al., 2021) specimens. However, for drifts between 0.8% to 4% MLSSWs exhibit an increment in dissipated energy that is comparable to that observed in specimen CT-50-44 (Estrella, Malek, et al., 2021), which is attributable to the effect of multiple sheathing layers. For example, at a 4% lateral drift MLSSW specimens show an increment of 109% and 66%, and a decrease of 6.6% with respect to specimens CT-100-38, CT-100-44 (Estrella, Malek, et al., 2021) and CT-50-44 (Estrella, Malek, et al., 2021), respectively. Finally, at drifts larger than 4% specimen CT–50-44 (Estrella, Malek, et al., 2021) dissipates as much energy as the MLSSWs because CT-50-44 has higher levels of redundancy in the nailed OSB-to-frame connections (which are still effective at large lateral drifts), whereas in MLSSWs the screwed one/two layer Type X GWB+OSB-to-frame connections have already failed at 4% lateral drift, leaving the nailed connections as the main source of energy dissipation. In conclusion, at lateral drifts smaller than 2%, the evaluated shear walls dissipate essentially the same amount of energy, but at larger displacements, MLSSWs dissipate about twice the energy dissipated by an equivalent bare shear wall, even though they are less ductile. Therefore, Type X GWBs layers and the interaction of the screws with the Type X GWB and OSB layers leads to a 100% increment not only in strength but also in energy dissipation. This is an important finding because fewer MLSSWs at a given story may not compromise the energy dissipation capacity (n MLSSWs should dissipate as much energy as 2n equivalent bare shear walls). However, there is still unclear how much of this extra dissipated energy comes from Type X GWB layers and/or from the screwed connections interacting with the Type X GWB and OSB layers. In order to quantify the capacity of MLSSW specimens to dissipate energy under cyclic loading, a commonly used indicator is the equivalent viscous damping ratio (ζ_{eq}). Section 4.3.1.6. describes the expression to calculate ζ_{eq}, which was used to compute the values shown in Figure 4.19. MLSSWs exhibit smaller values of ζ_{eq} (less than 0.1) at drifts smaller than 0.5%, and an increment to steady values at drifts higher than 0.5% (ζ_{eq} values between 0.10 to 0.15). In specimens CT-100-38, CT-100-44 (Estrella, Malek, et al., 2021), and CT-50-44 (Estrella, Malek, et al., 2021), on the other hand, ζ_{eq} is higher at drifts smaller than 0.1% (from 0.17 to almost 0.4) and drops to steady values at drifts larger than 0.5% (values between 0.10 and 0.15) (Estrella, Malek, et al., 2021). Even the mean (ζ_{eq}, mean = 9.5%) and characteristic ($\zeta_{eq,k}$ = 8%) values for MLSSWs are higher than those reported in previous studies (Casagrande et al., 2016) for walls where the OSB and GWB panels are installed at opposite sides of the frame. The latter are smaller than those for the CT-100-38 specimen and for strong shear walls with continuous hold-down reported in previous studies (Estrella, Malek, et al., 2021). In fact, reported values observed in MLSSWs are similar to those obtained in strong shear walls with conventional hold-down, as reported in (Guinez et al., 2019).

This is explained by the fact that even though MLSSWs exhibit a higher level of cumulative dissipated energy there is a more important increment in strength with respect to the CT-100-38 control specimen.

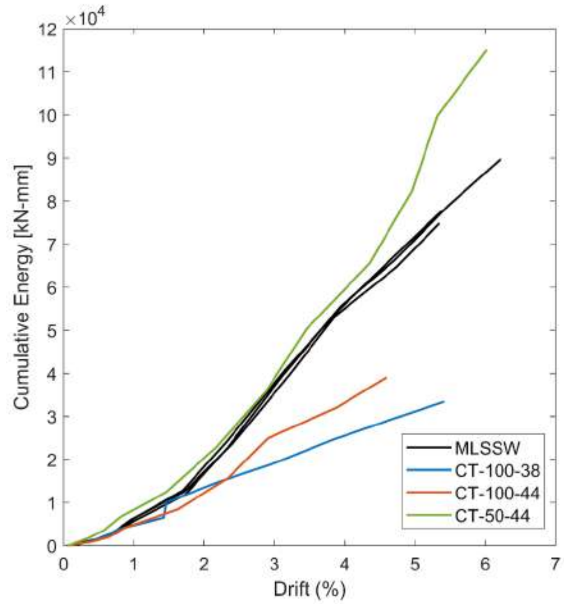

Figure 4.19. Energy dissipated as a function of the lateral drift.

4.3.2.9. Generalization of results and potential design implications

Per the Special Design Provisions for Wind and Seismic (SDPWS) standard (AWC, 2021), the nominal unit shear strength (v_{SDPWS}) and apparent shear wall shear stiffness (G_a) are deduced from assembly-level test results. The isolated cantilever analytical model proposed in SDPWS (AWC, 2021) to estimate the lateral stiffness/displacement of MLSSWs is analyzed in the following subsections to evaluate its applicability.

4.3.2.10. Nominal strength

According to Table 4.5, the mean and standard deviation of the peak strength of the 1:1 aspect ratio MLSSWs are 174.467 kN and 13.247 kN, respectively. Then, the characteristic value of the peak strength is computed (=143.34 kN), which is associated with the

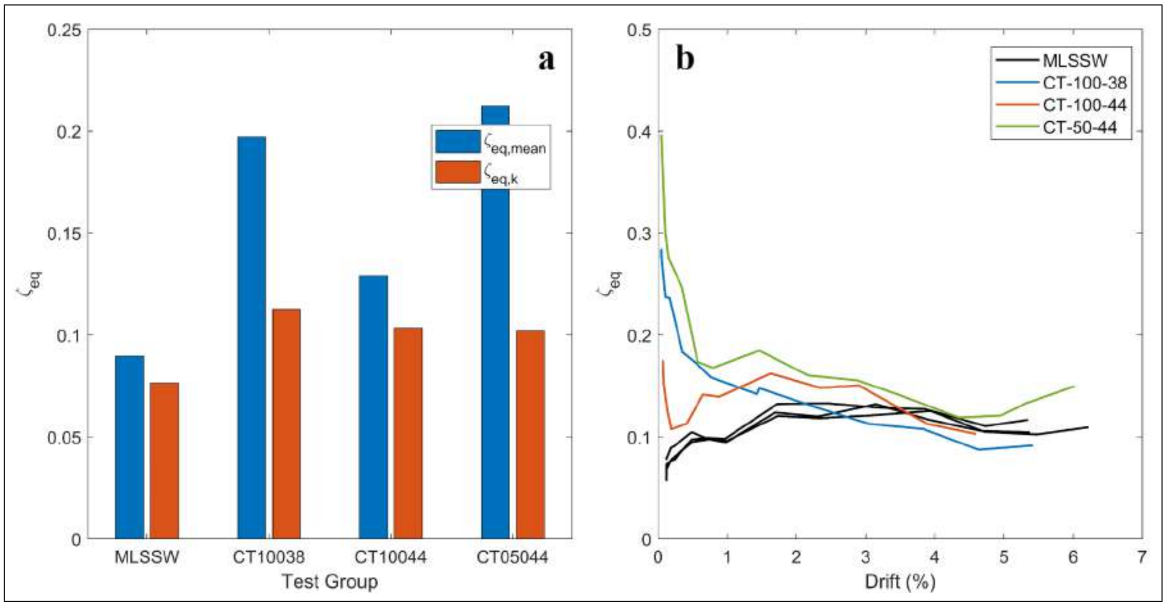

Figure 4.20. (a) Mean and characteristic values of the equivalent viscous damping, and (b) evolution of the equivalent viscous damping as a function of the lateral drift.

5th percentile of the cyclic assembly-level test results. The characteristic shear strength per unit of length of the MLSSW is v_{MLSSW} = 0.059 kN/mm (MLSSW is sheathed at both sides). The nominal strength of the MLSSW is set equal to the estimated 5th percentile value of the peak load of the fully-reversed cyclic testing. This value is compared with SDPWS values for bare shear walls. Moreover, as MLSSW specimens have spiral shank nails, comparisons are made with SDPWS values valid for similar nail diameters. For shear walls sheathed with 11.1 mm thick OSB at both sides and 100 mm panel edge nail spacing (i.e. 8d common nail), SDWPS reports 0.01414 kN/mm x 2 = 0.028 kN/mm, which is 53% smaller than the nominal capacity of an equivalent MLSSW. According to Lam et al. (1997), an increment of 13.5% in the peak strength is due to spiral nails in the MLSSW instead of smooth shank nails.

4.3.2.11. Apparent shear wall shear stiffness

For the definition of the apparent shear wall shear stiffness (G_a), Section 8 of the ASTM E564-06 standard (ASTM, 2006) was considered. In order to account only for the shear displacement of the panels and the slip in the multilayer sheathing-to-frame connection, it is necessary to eliminate other sources of flexibility (i.e., anchorage uplifting, wood-frame bending, and compression perpendicular to the grain at the bottom plate) from test results. The following expression from ASTM E564-06 (ASTM, 2006) should therefore be considered:

$$\Delta_{int} = \Delta_{lat} - \Delta_{bend} - \Delta_{slip} - (\Delta_{up} - \Delta_{down}) \frac{h_{wall}}{L_{wall}} \tag{4.4}$$

where Δ_{int} is the shear deformation, Δ_{bend} is the bending deflection of the end-studs, Δ_{slip} is the slip between the specimen and reaction beam, Δ_{up} is the uplift at the tensioned lower edge corner of the wall, Δ_{down} is the vertical displacement at the lower edge corner of the wall under compression, h_{wall} is the height of the wall, and L_{wall} is the length of the wall. This pure shear deformation can then be used to compute the apparent modulus according to the characteristic peak force (considered as nominal in this paper) developed in 4.3.2.10and wall dimensions as:

$$G_{a,i} = \frac{0.5F_{peak,k}}{\Delta_{int,i}} \frac{h_{wall}}{L_{wall}} \tag{4.5}$$

Results for the apparent shear wall shear stiffness for each assembly-level specimen are summarized in Table 4.6. The mean value of the apparent shear wall shear stiffness in 1:1 aspect ratio MLSSWs is 49.1 kN/mm. For shear walls sheathed with 11.1 mm thick OSB at both sides and 100 mm panel edge nail spacing (i.e. based on smooth shank nail), SDWPS reports 3.9 kN/mm x 2 = 7.8 kN/mm, which is 84% less than that of the equivalent MLSSW. According to Lam et al. (1997), a 44% decrease in the shear stiffness of the wall is due to spiral nails in the MLSSW instead of smooth shank nails, which suggests that the shear stiffness of the MLSSW could potentially be even greater.

]Applicability of the SDPWS analytical model

Table 4.6. Apparent shear modulus for each assembly-level specimen

Test Group	$0.5F_{peak,k}$ [kN]	Δ_{lat} [mm]	Δ_{slip} [mm]	Δ_{up} [mm]	Δ_{down} [mm]	Δ_{int} [mm]	G_a [kN/mm]
MLSSW-01	71.715	13.194	0.554	7.394	-3.492	1.541	47.327
MLSSW-02	71.715	16.194	1.952	8.420	-4.259	1.321	55.215
MLSSW-03	71.715	12.333	1.543	5.390	-3.279	1.946	37.475
MLSSW-04	71.715	13.588	1.644	6.732	-3.711	1.296	56.267
MLSSW$_{mean}$	71.715	13.827	1.423	6.984	-3.686	1.526	49.071
MLSSW$_{std}$	0.000	1.662	0.605	1.269	0.421	0.301	8.699
MLSSW$_{CV(\%)}$	0.0	12.0	42.5	18.2	11.4	19.7	18.2

The SDPWS procedure estimates the lateral deflection of shear walls (δ_{SW}) based on an isolated cantilever model which accounts for bending and shear deflection, fastener deformation, and anchorage uplift as computed by the following equation:

$$\delta_{SW} = \frac{2}{3}\frac{vh_{wall}^3}{AEL_{wall}} + \frac{vh_{wall}}{G_a} + \frac{h_{wall}}{L_{wall}}\Delta_a \tag{4.6}$$

where v is the unit shear force induced by the design load, A is the area of the end studs, E is the elasticity modulus of end posts, and Δ_a is the vertical deformation of the wall continuous rod system and compression deformation. Considering the mean value of the apparent shear modulus presented in Table 4.6, the SDPWS analytical model underpredicts the shear deformation obtained from the assembly-level tests by 2.6%. This is consistent with results reported by previous researchers for bare shear walls (Guinez et al., 2019; Estrella, Malek, et al., 2021), i.e., other studies on walls without GWB also found the same tendency to underpredict the shear wall lateral drifts. However, as the values presented in this research are specific for MLSSWs, the SDPWS analytical model turned out to be more accurate than in previous research (Estrella et al., 2020), which used the values tabulated in SDPWS (AWC, 2021) as a point of comparison instead of developing specific design parameters for the tested samples. Having said that, a difference of -22.6% was found between the experimental and analytical total lateral deflection. The accuracy of the SDPWS analytical model lies in the capability to predict the vertical deformation of the wall overturning anchorage system (i.e., up to -24% of accuracy on the rocking component) since this is the most important contributor to the underestimation of the lateral deflection of an MLSSW. Also, the experimental results showed that up to 5 mm of such difference could be explained by installation tolerances, as presented in Figure 4.17.

4.4. Numerical Model

A simplified numerical model to represent the behavior of MLSSW specimens is presented in this research. To represent the behavior of bare shear walls (numerical model A), the efficient numerical model guidelines presented by Estrella et al. (2020) were implemented in the MATLAB M-CASHEW software (W. Pang & Hassanzadeh Shirazi, 2013). In the case of MLSSWs, two different approaches were used: (i) numerical model B, which considers the effects of sheathing multiple Type X GWB layers as a reinforcement of the OSB sheathing layer (i.e. multilayered 1st/2nd Type X GWB+OSB-to-frame connections modified the kinematic of the OSB layer and reinforce the response of the OSB-to-frame nailed connection); and, (ii) numerical model C, which considers the behavior of multiple layers as parallel springs, as presented in previous research (Folz & Filiatrault, 2004a; van de Lindt & Liu, 2007; van de Lindt, Pei, Liu, & Filiatrault, 2010; Asiz et al., 2011) to represent the contribution of Type X GWB and OSB when they are installed on opposites sides of the frame. Wood frame elements with a nominal modulus of elasticity E = 7900 MPa according to NCh 1198 (INN, 2014) were modeled using Euler-Bernoulli elastic frame elements with corotational transformation. For the OSB and Type X GWB sheathing layer, 5-DOFs shear rectangular elements were used in order to capture rigid body motion and in-plane angular shear deformation. Shear moduli G = 1.3 GPa and 1.18 GPa were considered for OSB and Type X GWB sheathing layers, respectively. 3-DOFs link elements were employed to represent the different connections in MLSSWs: (i) pinned connections were considered to represent the frame-to-frame interaction; (ii) for the sheathing-to-frame connection, the MSTEW hysteretic model (Folz & Filiatrault, 2004b) was employed at the X and Y directions and rotation was allowed (the parameters of the MSTEW model for each type of multilayer connection were presented previously in Table 4.4); (iii) to represent the continuous rod system that connects the foundation to the top plate, the vertical DOF of the link was calibrated based on a linear approximation of the response presented in Figure 4.17 (i.e. positive and negative responses controlled by the tension of the anchorage system and compression of wood member to the foundation, respectively) and zero stiffness springs were defined at the horizontal and rotational DOFs; (iv) the link elements that represent the sliding anchorage system have infinite stiffness in the horizontal direction, only compression was allowed along the vertical direction, and rotation was considered as a zero stiffness spring. A displacement-controlled analysis was performed employing the $l_{\text{inf}} - norm$ test on lateral displacement DOF increments as convergence criteria (W. Pang & Hassanzadeh Shirazi, 2013), with 50 iterations per step and a residual tolerance equal to 0.001 kN. Monotonic and cyclic analyses were carried out by applying 0.5 mm displacement increments at the top of the wall model. The monotonic response of the numerical models A to C and the backbone curves from cyclic test results are presented in Figure 4.21. Numerical model A showed good agreement with the CT-100-38 test results in terms of stiffness and strength, which is consistent with previous findings (W. Pang & Hassanzadeh Shirazi, 2013; Estrella et al., 2020; Estrella, Malek, et al., 2021). Regarding MLSSWs, numerical model B is the one that presents the highest accuracy in terms of stiffness, peak strength, and ultimate displacement. Numerical model C, on the other hand, overpredicts the initial stiffness, mainly because in such model the multiple layers act independently (i.e., modeled as parallel springs) rather than together as a system. Comparisons between the cyclic response predicted by numerical model B and test results are presented in Figure 4.22. The numerical model was able to predict the stiffness and strength degradation as well as the pinching effect in MLSSWs with a high level of accuracy in most cases. However, as the connection-level tests evaluated separately the behavior of each fastener (i.e. nails were tested with no screws surrounding them) there is still room for improvement in predicting the peak strength and the asymmetric shape of the hysteresis response observed in most of the MLSSW tests.

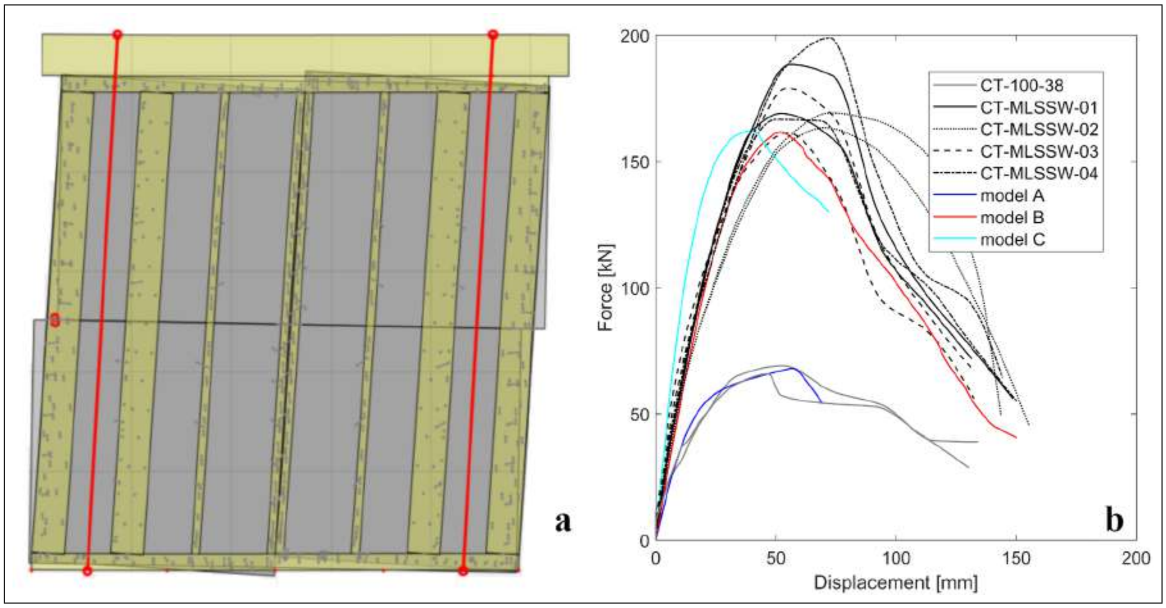

Figure 4.21. (a) numerical model, (b) comparison between analytical and experimental force-displacement relationships

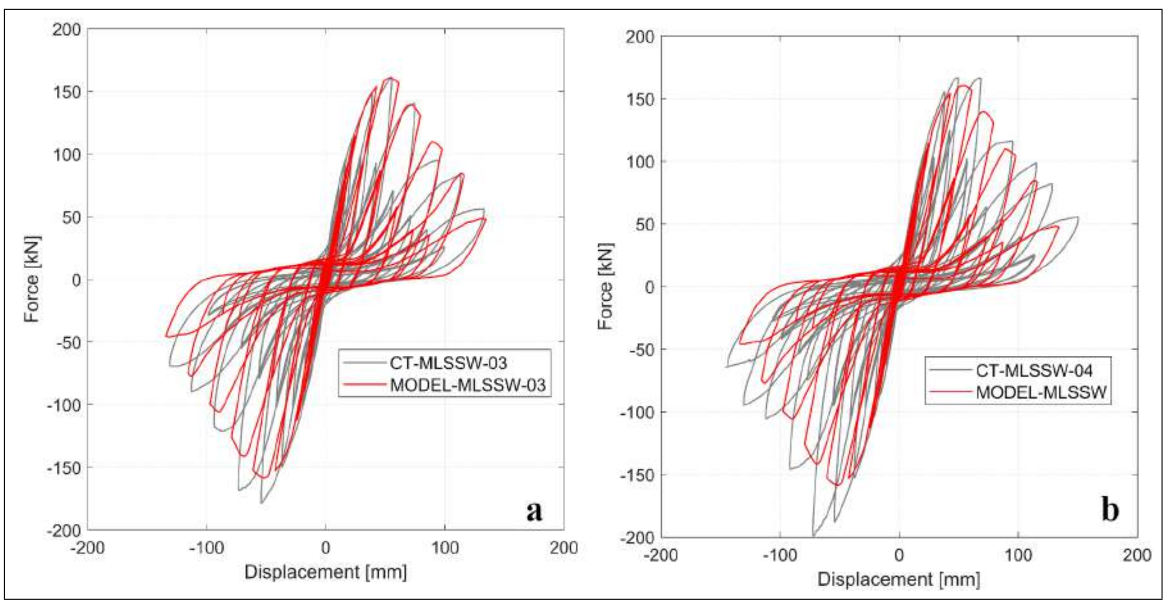

Figure 4.22. Cyclic response: comparison between analytical (model B) and experimental results

4.5. Chapter Conclusions

In this investigation, the influence of finishes (i.e., Type X GWB) on the cyclic lateral response of strong shear walls (MLSSW) was analyzed. Initially, it was thought that such influence would be essentially irrelevant due to the inherent strength and stiffness of strong shear walls. However, results clearly indicate that there is a surprising contribution of finishes, which mostly increased all relevant engineering parameters except ductility. Further, results were very consistent and predictable, which supports the argument of including the structural contribution of finishes in common design practice, as long as they cover structural wooden boards such as OSB. The main findings of this investigation can be summarized as follows:

- Multi-layered (including Type X GWB) connection-level tests depict that a screwed connection has higher strength and stiffness than a nailed connection. The equivalent viscous damping tends to be similar in all the evaluated connection-level systems. However, the nailed connection has a larger ultimate displacement capacity than a screwed connection, especially under reversed cyclic loading. However, because of the limited number of connection-level specimens tested, further experimental research is needed to validate the results presented in this paper.
- The overall cyclic lateral response of MLSSWs showed pinched hysteresis with strength and stiffness degradation, especially after reaching the peak strength. The response of MLSSWs was essentially elastic up to a lateral drift of 1.0%. In general, the cyclic response of MLSSWs was similar to that of equivalent bare strong shear walls with continuous hold-downs.
- MLSSWs exhibited a great increase in lateral strength (i.e. up to 160%) and stiffness (i.e. up to 53%), while keeping deformation capacity, with respect to both the control bare shear wall tested in this study and similar bare shear walls tested in previous studies.

- A hysteretic response was found in the overturning anchorage system of the MLSSW. Such hysteretic response is due to the deformation perpendicular to the grain under the bearing plate and top/bottom plate, and also to some initial adjustment of the system. The response is comparable to that also observed in equivalent bare strong shear walls.
- Mean ductility of the MLSSW specimens was between 16% to 42% smaller than that of bare shear walls with continuous hold-down. However, the energy dissipated is comparable to that observed in previous studies on bare shear walls.
- The analytical model presented in SDPWS (AWC, 2021) to calculate the lateral deflection of shear walls underestimated the uplift (overturning) by 26%, but the shear deflection was underpredicted by only 5.6%. Further research is needed to better understand the vertical deflection component, but results obtained in this investigation suggest that the underprediction may arise from the plastic compression of the top and bottom plates of the shear wall.
- Current numerical models for bare shear walls showed good accuracy in predicting the strength and stiffness of MLSSWs. Moreover, the pinching and the strength/stiffness degradation were accurately captured. However, there is still room for improvement in the prediction of the asymmetric response and the peak strength of MLSSWs.

Based on these findings, and also considering the stability of the results and the consistency of the analytical models, this investigation supports the argument of considering the influence of screwed Type X GWB finishes on the lateral response of MLSSWs when such finishes cover OSB or another equivalent wooden structural boards (thus reinforced against shear brittle failure). Consideration of Type X GWB finishes and the fastener used to attach them in MLSSWs can make a substantial difference in achieving cost-effective structural designs in highly seismic countries. For instance, consideration of such finishes would make it possible to comply with the no-damage requirement at a 0.2% lateral drift specified in the Chilean seismic design code for residential and office buildings. The authors of this paper, however, recommend further research to understand how much strength in MLSSW is contributed by the Type X GWB and by the interaction of screws with the OSB layer. Moreover, it is important to improve the understanding of finishes covering structural timber boards in shear wall configurations and aspect ratios different from the ones reported here. With such research, it would be possible to realistically evaluate damage fragility functions and damage stages in the context of performance-based earthquake engineering (PBEE), as well as to accurately characterize the corresponding seismic design parameters (such as the response reduction factor).

5. CHAPTER 5 - REINFORCEMENT EFFECTS AND PARAMETRIC STUDY OF THE LATERAL RESPONSE OF MULTI-LAYERED WOOD-FRAME SHEAR WALLS: AN EXPERIMENTAL AND NUMERICAL INVESTIGATION

5.1. Introduction

Light Frame Timber Buildings (LFTBs) have been extensively used in North America and Europe, with growing applications in Latin America and other parts of the world. The characteristics of the walls vary depending on the application, but generally include both wood structural panels and nonstructural sheathing. Of interest here are strong shear walls (SSWs) (Estrella et al., 2020), which consist of generally 4 or more 2 x 8 framing members, strong hold-downs, wood structural panels - typically oriented strand board (OSB) on both sides - and closely spaced edge and field nailing patterns (Guinez et al., 2019; Estrella et al., 2020; Estrella, Malek, et al., 2021). The nonstructural sheathing for fire protection customarily consists of one or two-ply Type X gypsum wallboard (GWB) at both sides. The Type X GWB layers are installed either vertically or horizontally, depending on the specific engineering detail. These finish layers are fastened to the framing with screws or staples through the OSB, as shown in Fig.5.1. Here, we adopt the term multi-layered strong shear walls (MLSSWs) to refer to SSWs with additional finish layers installed atop OSB on both sides. SSWs are distinguished from conventional shear walls where OSB sheathing is only present on one side. Also, in conventional shear walls, OSB and GWB are installed on opposite sides of the wood frame (Estrella et al., 2020). SSWs are needed where seismic loading is high, and are found with various characteristics, especially in multi-story buildings where conventional shear walls are inadequate. The seismic performance of these walls depends on the complex, combined contribution of the structural components, the overturning anchorage system, and the nonstructural components. Seismic damage to these systems can lead to high repair costs, especially associated with GWB replacement. Yet, traditionally, the contribution of finish layers, such as Type X GWB, has been conservatively ignored. Compared to conventional walls, the performance of MLSSWs cannot be solely attributed to additional layers and fasteners, prompting further investigation into what we refer to as the “reinforcement effect”, i.e., the fact that the deeply screwed Type X GWB may also prevent nails from pulling out during hysteresis cycles. However, previous work (Valdivieso, Guindos, et al., 2023) has been limited in the scope of configurations considered, such that there is a lack of knowledge regarding the contribution of nonstructural finish layers to the lateral response of wood-frame shear walls that have finish layers applied atop OSB sheathing layers. The significance of this reinforcement effect transcends specific construction scenarios and applies broadly to enhance the structural performance and integrity of such wood-frame shear wall systems. This paper evaluates the contribution of Type X GWB finish layers to the lateral response of MLSSWs (see Fig. 5.1). The reinforcement effect of screws and Type X GWB layers on the response of nailed connections is evaluated experimentally at the connection level and numerically at the assembly level. The effects of the aspect ratio, the number of Type X GWB layers, the type of multi-layered fastener (i.e., screws or staples), and the type of overturning anchorage system (i.e., conventional hold-down or continuous rod system) on the response of the MLSSW is evaluated through a parametric numerical analysis. The numerical models are developed based on the experimental hysteretic response of the connection-level assemblies of the layers that form part of the walls.

5.1.1. Previous Research

5.1.1.1. Experimental evaluations of the effect of nonstructural GWB finish layers.

Previous research has evaluated the contribution of different finishing layers to the lateral response of shear walls where the OSB and GWB are installed at opposites sides of the wood frame – this is the typical configuration in low-rise to mid-rise structures in countries with a tradition of LFTBs (e.g., North America, Europe, and Oceania). In general, these past test results revealed that the installation of wall finishes substantially increased the structure's lateral stiffness and dramatically reduced the displacement demand compared to the case with bare shear walls, i.e., when only OSB sheathing is considered without GWB finish layers (Wolfe, 1983; Filiatrault et al., 2002; Kharrazi et al., 2002; Uang &

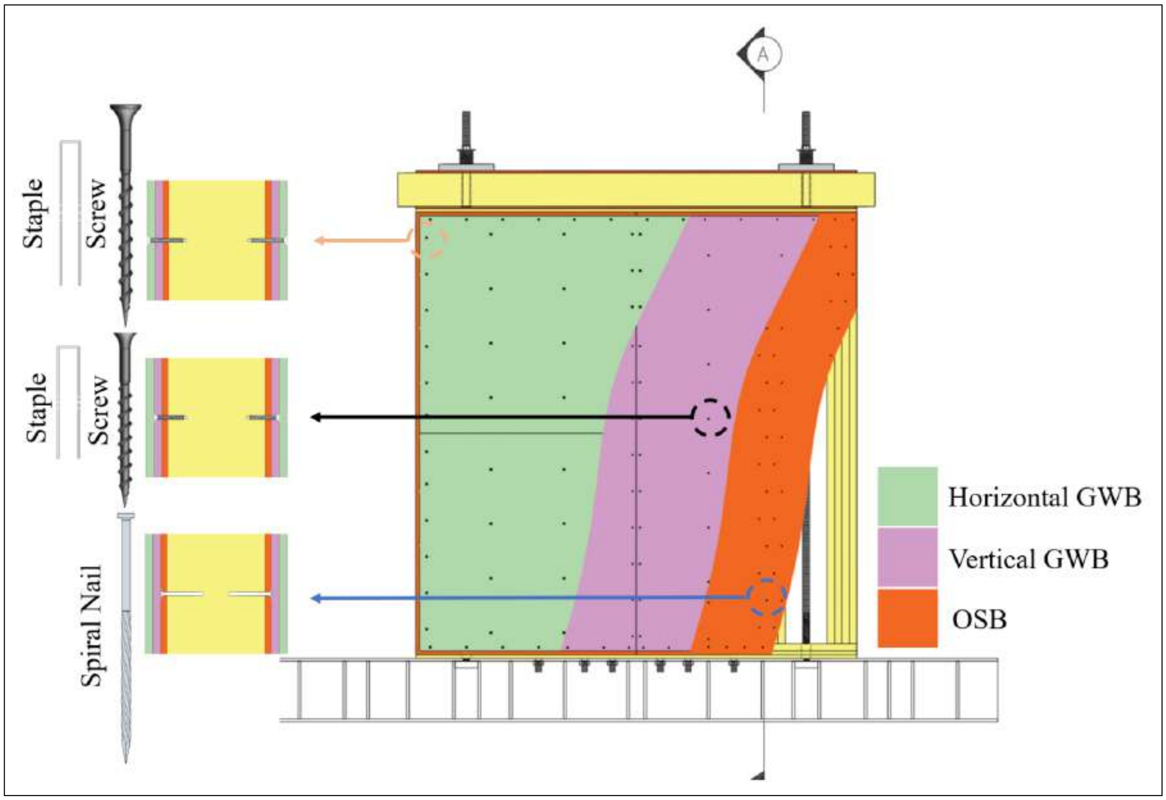

Figure 5.1. Configuration of a MLSSW with multiple finish layers of GWB.

Gatto, 2003; van de Lindt & Liu, 2007; T. W. White & Ventura, 2007; T. White & Ventura, 2007; Filiatrault et al., 2010). For example, Uang and Gatto (2003) evaluated the effect of the GWB finishing layer on the lateral response of wood-frame shear walls experimentally, finding a 12% and 60% increase in lateral strength and stiffness, respectively. However, the finish layer contributed to a 31% reduction in the deformation capacity. The influence of the orientation of the GWB finish layers is also significant. The strength of shear walls sheathed with horizontal GWB panels is 40% greater than that of shear walls with vertical panels. This strength enhancement is due to the horizontal alignment of the external paper layer surrounding the gypsum core, as identified by Wolfe (1983). As a result of differences in stiffness, strength, and deformation capacity of OSB and GWB sheathing layers there can be a damage concentration in the GWB layer (Asiz et al., 2011) contributing to high repair costs after an earthquake (Kircher et al., 1997). In this context, (Goodall & Gupta, 2011) evaluated approaches to improve the performance of GWB in wood-frame shear walls. In particular, installing the GWB layers on the top of a shear wall sheathed on both sides with OSB resulted in improvement of the GWB performance, i.e., lesser seismic damage because the differential lateral stiffness between both sides of the wall was reduced. However, the quantification of the reinforcement effect of GWB finish layers on the lateral response of the walls was not addressed. Building on this work, (Valdivieso, Guindos, et al., 2023) studied experimentally the effect of nonstructural Type X GWB finish layers on the cyclic lateral response of SSWs. The specimens consider a 1:1 aspect ratio (i.e., 2440mm x 2440mm) MLSSW with a continuous rod system as an anchorage system and with two layers of Type X GWB attached to the frame through the OSB sheathing with screwed connections on both sides. Results showed increases of 53% and 160% in elastic stiffness and strength, respectively, due to the contribution of the Type X GWB finish layers, without excessive damage on the finish layers. The authors postulated that such increases may arise from the high embedment strength of the GWB and that the deeply screwed GWB may prevent nails from pulling out during hysteresis cycles.

5.1.1.2. Numerical evaluation of the effect of nonstructural GWB finish layers.

Folz and Filiatrault (2004a) simulated numerically the first shake table test of a two-story wood-frame house that considers nonstructural components on walls (Filiatrault et al., 2002), using the Seismic Analysis of Woodframe Structures (SAWS) constitutive model (Folz & Filiatrault, 2004b). A parallel spring was incorporated into the model to represent the effect of the GWB layer of the wall, which was calibrated from full-scale wall test results (Uang & Gatto, 2003). Similarly, based on previous experimental research (Wolfe, 1983; Uang & Gatto, 2003; van de Lindt & Liu, 2007) evaluated the effect of finish layers on the allowable seismic mass within a one-story house numerically, again using SAWS. The structural and finish layers effects were considered by adding parallel springs representing OSB, GWB, and stucco. Up to 35% greater allowable base shear was found when GWB was included. However, the study recognized a lack of confidence in the ability to model the lateral response of wood-frame nonstructural elements mechanistically.

Subsequently, van de Lindt, Pei, Liu, and Filiatrault (2010) simulated a three-dimensional shake table test (Filiatrault et al., 2002) using the SapWood software (Pei & van de Lindt, 2009). The Evolutionary Parameter Hysteretic Model (EPHM) (W. C. Pang et al., 2007) was used for representing OSB sheathed walls and the SAWS constitutive models was used for representing the GWB finish layer, calibrated from full-scale wall test results. Good agreement was found between the SapWood model and the experimental shake-table test result for the design earthquake. However, the model could not represent the structure's response under the maximum considered earthquake. The first study on the contribution of the finish layer on a mid-rise LFTB was presented in Asiz et al. (2011). Asiz et al. (2011) numerically simulated a 5-story and a 6-story LFTBs, comparing the response of the building considering bare shear walls (sheathed on one side only with OSB) and shear walls sheathed on opposite sides with OSB and GWB. In the design of the buildings, the contribution of the GWB finish layer was ignored. Models were created in SapWood, where the effect of GWB and OSB was considered as parallel springs since the panels were located on opposite sides of the frame. The analysis led to stiffer buildings with up to 30% reduction in story drift demands compared to building models without considering GWB finish layers effect. Moreover, results showed that damage concentrated first in the GWB layer due to the installation detail of the sheathing (i.e., OSB and GWB on opposite sides). Recently, Valdivieso, Guindos, et al. (2023) evaluated numerically the behavior of an experimentally tested MLSSW, showing that the general rule of parallel spring does not apply to MLSSWs since the finished layers act as a reinforcement to pulling out the OSB nailing, rather than only working in parallel to it. In fact, the parallel spring approaches tend to overestimate the stiffness of the wall, even if the maximum strength is well predicted. Regarding this subject, Bahmani and van de Lindt (2016) and Chen et al. (2016) assessed the effectiveness of the direct combination rule (parallel springs) through comparisons with the FEMA P807 (Federal Emergency Management Agency, 2012) combination rule. Both studies concurred that the FEMA P807 rule leads to a more conservative approach. Nonetheless, they did not consider the potential impact of the reinforcement effect on the response of MLSSWs. Valdivieso, Guindos, et al. (2023) presented an approach in which nails and multi-layered connections work together, demonstrating good accuracy in the prediction of the hysteretic response of MLSSWs under lateral load. Moreover, the proposed numerical model permits reproduction of the response of an assembly-level MLSSW from connection-level tests (i.e., testing nailed, screwed, or stapled connection) allowing for virtual testing of different MLSSW configurations as real-scale tests are expensive and time-consuming (Estrella et al., 2020). This was a step forward in the numerical representation of the effect of finish layers as previous studies calibrated the effect of GWB layers in conventional shear walls from full-scale test results.

5.2. Experimental Program

The first step of this work was an experimental program developed to characterize the lateral behavior of the multi-layered sheathing-to-frame connections under monotonic and cyclic loading ("connection-level tests") and to evaluate the reinforcement effect of the multi-layers on the lateral response of the sheathing-to-frame fastener.

5.2.1. Experimental Program

5.2.1.1. Test Specimens

As reported in Table 5.1, four different configurations of multi-layered sheathing-to-frame connections were assembled to capture the isolated response of typical fasteners used for attaching Type X GWB through the OSB to the wood framing (*OSB(1)GWB-Sc* or *-St* and *OSB(2)-GWB-Sc* or *-St*). In order to facilitate comparison, a reference specimen was also constructed to represent the nailed OSB-to-wood frame connection (*OSB-N*). Another three specimens were assembled where the connectors were installed to represent the real condition of the connection in a MLSSW to capture the reinforcement effect (*rOSB-N*, *rOSB(1)GWB-Sc*, and, *rOSB(2)GWB-N/Sc*). Two reference specimens were constructed without the finish layers (*rOSB-N/Sc*, *rOSB-N/Sc-g*). These specimens served as a baseline for assessing the reinforcement effect. The test groups are labeled as sheathing layers-fastener type, where *N* is nail, *Sc* is screw, and *St* is staple. An "*r*" is added to the label for test groups that evaluate the reinforcement effect. A "*g*" is added to the label for test groups with a gap between the head of the screws and the sheathing, i.e., the screws were not fully screwed so that their heads are not pushing the sheathing against the framing. The gap aims to distinguish the lateral and axial stiffness and strength contribution of the screws from the reinforcing effect. All specimens used framing consisting of 41 mm x 185 mm (2x8) dimensional Chilean radiata pine (RP) lumber mechanically graded as C16 according to NCh1198 (INN, 2014) and attached to different sheathing materials. Fig. 5.2 illustrates the connection-level specimens and Table 5.1 the details of the layouts. More detailed illustrations of connection-level configurations are presented in Figs. 5.13 and 5.14 of the supplemental material.

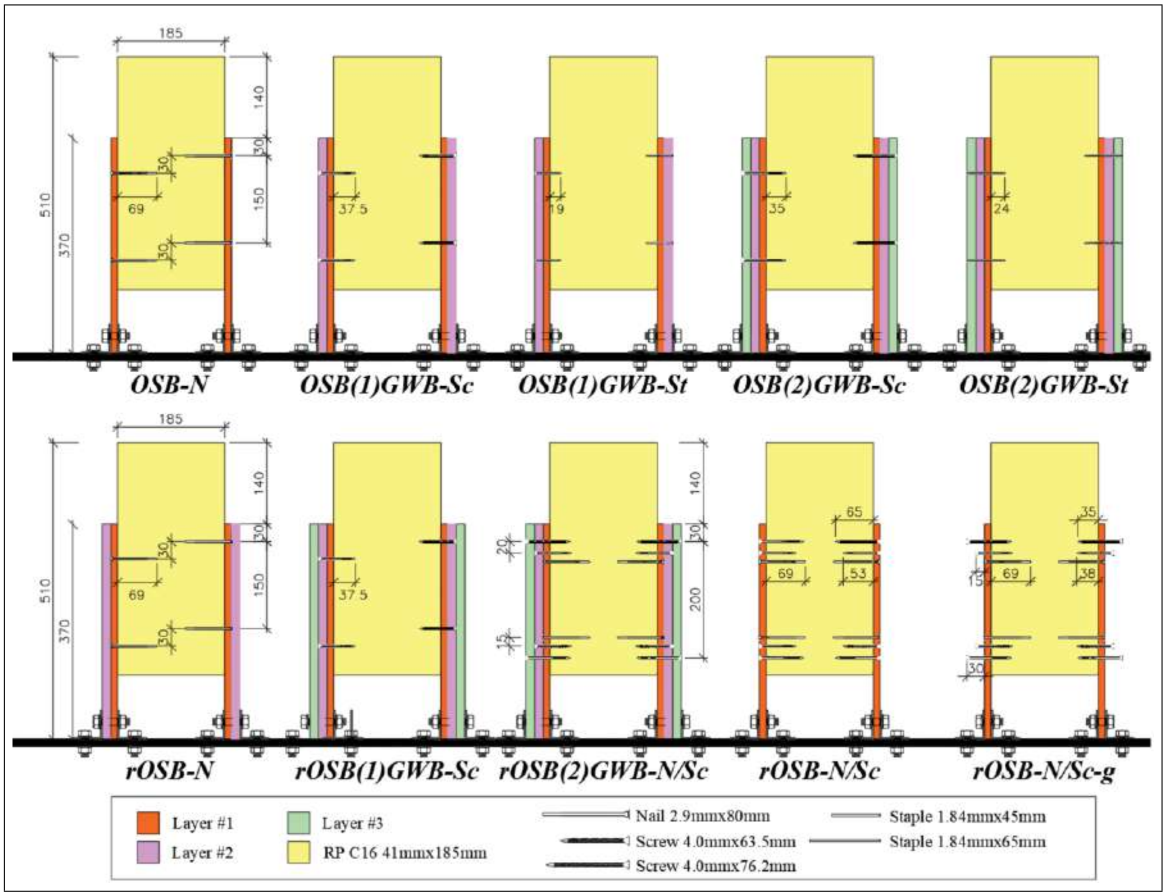

Figure 5.2. Multi-layered connection specimens. All dimensions in millimeters (1 mm = 0.039 in).

Table 5.1. Summary of the connection-level specimens[a]. Refer to Fig. 5.2 for an illustration of test groups

Test Group	n[b]	Layer # 1	Layer # 2[c]	Layer # 3[c]	Fastener Type	p[i]
OSB-N	4	11.1, OSB	NA	NA	Nail[d,g] ϕ2.9x80	69.0
OSB(1)GWB-Sc	4	11.1, OSB	15, Type X GWB	NA	Screw[e,g,h] ϕ4.0x63.5	37.5
OSB(1)GWB-St	4	11.1, OSB	15, Type X GWB	NA	Staple[f,h] ϕ1.84x45.0	19.0
OSB(2)GWB-Sc	4	11.1, OSB	15, Type X GWB	15, Type X GWB	Screw[e,g,h] ϕ4.0x76.2	35.0
OSB(2)GWB-St	3	11.1, OSB	15, Type X GWB	15, Type X GWB	Staple[f,h] ϕ1.84x65.0	24.0
rOSB-N	4	11.1, OSB	15, Type X GWB	NA	Nail[d,g] ϕ2.9x80	69.0
rOSB(1)GWB-Sc	3	11.1, OSB	15, Type X GWB	15, Type X GWB	Screw[e,g,h] ϕ4.0x63.5	37.5
					Nail[d,g] ϕ2.9x80	69.0
rOSB(2)GWB-N/Sc	4	11.1, OSB	15, Type X GWB	15, Type X GWB	Screw[e,g,h] ϕ4.0x63.5	37.5
					Screw[e,g,h] ϕ4.0x76.2	35.0
					Nail[d,g] ϕ2.9x80	69.0
rOSB-N/Sc	2	11.1, OSB	NA	NA	Screw[e,g,h] ϕ4.0x63.5	52.5
					Screw[e,g,h] ϕ4.0x76.2	65.0
					Nail[d,g] ϕ2.9x80	69.0
rOSB-N/Sc-g	2	11.1, OSB	NA	NA	Screw[e,g,h] ϕ4.0x63.5	37.5
					Screw[e,g,h] ϕ4.0x76.2	35.0

[a] All dimensions in millimeters. (1 mm = 0.039 in).

[b] Number of specimens (sample size). Of n, 1 was tested monotonically and n-1 were tested cyclically.

[c] Specimens were constructed using 15 mm thick Type X GWB, in compliance with the requirements of the Chilean fire standard NCh 935/1 (INN, 1997) and consistent with approved fire application solutions available in Chile.

[d] OSB sheathing layer attached to frame with pneumatically driven wire coil spiral nails (80 x 2.9 x 6.5 mm) according to EN14592:2008+A1:2012 (BSI, 2008).

[e] Type X GWB sheathing first layer attached to frame through the OSB with type "W" screws (63.5 x 4.0 x 8.0 mm). Type X GWB sheathing second layer attached to frame through the 1st Type X GWB and OSB with type "W" screws (76.2 x 4.0 x 8.0 mm).

[f] Type X GWB sheathing first layer attached to frame through the OSB with a staple (Bea 180/45 NK HZ). Type X GWB sheathing second layer attached to frame through the 1st Type X GWB and OSB with a staple (Bea 180/65 NK HZ). Staples according to ETA-15/0860.

[g] Geometry of nails and screws are specified as length x root diameter x head diameter.

[h] Fastener geometry was chosen based on the types of screws and staples available in the Chilean market, and the length of the fasteners was selected to meet the specifications of Eurocode 5 Part 1-2 (EN, 2004).

[i] Penetration of the nail, screw, and/or staple in the wood frame.

5.2.1.2. Test setup

A reaction steel frame was used to perform the connection-level tests. The load was applied by a cylinder of $\pm$ 86 kN and $\pm$ 75 mm on force and displacement capacity, respectively, which transfers the vertical load to the specimen through a load-transfer system. All specimens were instrumented with two displacement transducers (LVDTs) and one double-effect load cell to capture the slip and shear force between the frame and sheathing multi-layers, as illustrated in Figure 5.15. Valdivieso, Guindos, et al. (2023) provides further details of the connection-level test setup.

5.2.1.3. Test protocol

The loading protocol was established according to ASTM E564-06 (ASTM, 2006) and ASTM E2126-19 (ASTM, 2019) for the monotonic and cyclic tests, respectively. The ultimate displacement observed in the monotonic test (i.e., the maximum displacement at which the strength of the specimen has not yet dropped below 80% of the peak strength) was used to compute the reference displacement for the simplified CUREE-Caltech cyclic testing protocol (Krawinkler et al., 2001) according to method C of ASTM E2126-19 (ASTM, 2019). The loading protocol was displacement-controlled and applied until failure of the specimen, defined as the complete detachment of the multi-layered sheathing from the wood-frame.

5.3. Experimental program findings

Hysteresis shape and eight engineering parameters were established for connection-level tests: (1) elastic stiffness (K_e), calculated as the secant stiffness between zero and 40% of maximum load Fmax; (2) yield displacement (Δ_y); (3) yield force (F_y); (4) displacement capacity (Δ_u), defined as the displacement after post-peak load where the load dropped to F_u = 0.8 F_{peak}; (5) ultimate force (F_u); (6) secant stiffness of cycle i ($k_{sec,i}$); (7) the energy dissipation ($E_{H,i}$, which is the area under the load-displacement curve of cycle i; and (8) equivalent viscous damping (ζ_{eq}). The Equivalent Energy Elastic-Plastic (EEEP) (G. C. Foliente, 1996) approach was used to estimate the parameters according to ASTM E2126-19 (ASTM, 2019). We focus on reporting displacement capacity instead of the normalized quantity ductility, as it is a more meaningful predictor of seismic performance. We examine secant stiffness, energy dissipation, and equivalent viscous damping in relation to the cycle or lateral drift to assess the trends such that hysteretic model parameters can be developed to represent the cyclic test data in numerical models. Results from test groups *OSB-N*, *OSB(1)GWB-Sc*, and *OSB(2)GWB-Sc* were previously reported in Valdivieso, Guindos, et al. (2023) and are used here for comparison purposes.

5.3.1. Lateral characterization of multi-layered sheathing-to-frame connections

5.3.1.1. Monotonic force-displacement response

Fig. 5.3 presents the monotonic force-displacement test response for all the tested groups. The reported displacement is the differential slip between the wood frame and the multi-layer sheathing, and the force is that taken by only one fastener along a single shear plane. The seven key engineering parameters are summarized in Table 5.6. Failure modes of nailed, screwed, and stapled connections are illustrated in Figs. 5.16 and 5.17 of the supplemental material. Multi-layered sheathing-to-frame connections predominantly exhibited failure due to fastener shearing, together with wood crushing and tearing in the GWB and/or OSB layers. Monotonic test results show that all test groups exhibited almost the same elastic stiffness, despite the differences in sheathing layers and fastener type, except for *OSB(2)GWB-Sc* and *OSB(2)GWB-St*. We attribute this difference in elastic stiffness to the change in the boundary conditions of the fastener caused by the thicker sheathing on one side of the shear plane in the case of test group *OSB(2)GWB-Sc*; this caused a fixed condition and shear failure rather than plastic hinge formation in the fastener (Carrero et al., 2020; Valdivieso, Guindos, et al., 2023). In contrast, test group *OSB(2)GWB-St* was 40% less stiff than test groups *OSB-N*, *OSB(1)GWB-Sc*, and *OSB(1)GWB-St*, and its elastic stiffness was smaller than the analytical prediction. We attribute this smaller-than-expected stiffness to installation defects; with longer staple and greater thickness of the sheathing layers, the staple legs are more likely to be splayed. Regarding strength, screwed connections (i.e., test groups *OSB(1)GWB-Sc*, and *OSB(2)GWB-Sc*) presented higher peak strength compared to other test groups mainly because of the higher withdrawal strength of the threaded screw fasteners (Valdivieso, Guindos, et al., 2023). The strength difference between test groups *OSB(1)GWB-St* and *OSB(2)GWB-St* is due to the higher staple embedment length presented in *OSB(2)GWB-St*. From a deformation capacity point of view, the nailed cases, i.e., *OSB-N*, perform better than all other Type X GWB-sheathed connections. Test groups *OSB(1)GWB-St* and *OSB(2)GWB-St* exhibit 65% and 47% smaller deformation capacity than test group *OSB-N*. As with strength, the almost null withdrawal strength of staples limits the deformation capacity of test groups *OSB(1)GWB-St* and *OSB(2)GWB-St*.

5.3.1.2. Cyclic force-displacement response and hysteretic model parameters

As an illustration of the results, the cyclic force-displacement responses for the test groups *OSB(1)GWB-St* and *OSB(2)GWB-St* are presented in Fig. 5.4. All test groups show a strong pinching effect due to the wood frame and sheathing layers crushing at the shear planes (as found previously in J. D. Dolan and Madsen (1992)). Moreover, abrupt strength and stiffness degradation was observed in repeated cycles, which is consistent with results of screwed test groups reported in(Valdivieso, Guindos, et al., 2023). The result trends in the cyclic response among test groups were consistent with those found for the monotonic tests in terms of peak strength and deformation capacity. Regarding secant stiffness, test groups with screwed connections, i.e., *OSB(1)GWB-Sc* and *OSB(2)GWB-Sc*, had the highest secant stiffness (see Fig. 5.18 of the supplemental material). These screwed connections test groups also showed higher secant stiffness than those with stapled connections (i.e., *OSB(1)GWB-St* and *OSB(2)GWB-St*). However, stapled connections showed smoother degradation in stiffness because the two different legs of the staples do not necessarily pull out together, whereas abrupt drops in stiffness were

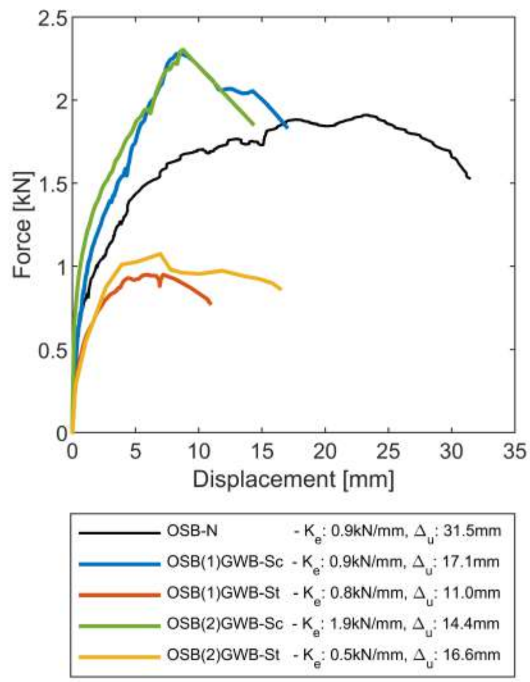

Figure 5.3. Monotonic test results of connection-level test groups. (1 mm = 0.039 in; 1 kN = 224.8 lbf)

found in screwed connections. Therefore, the secant stiffness (and capacity) of staples are solely determined by their lateral behavior, with no consideration for axial characteristics of the fastener (i.e., withdrawal and pull-through). The nailed connection (i.e., *OSB-N*) had a small secant stiffness (similar to test group *OSB(2)GWB-St*). Tested stapled connections also showed higher variability among repetitions (COV of 29% and 42% in test groups *OSB(1)GWB-St* and *OSB(2)GWB-St*, respectively, versus 4% in test group *OSB-N* when comparing the secant stiffness parameter at the tenth cycle), which is important as well as the mean trends. *OSB-N* showed the highest levels of cumulative dissipated energy followed by screwed connections and stapled connections, as illustrated in Fig. 5.5. One of the samples of test group *OSB(2)GWB-St* showed elevated levels of dissipated energy compared to the other specimen and test groups, evidencing again higher variability in stapled connections. Most of the test groups showed steady values of damping ratio up to cycle 30, beyond which damping increased (see Fig. 5.5 and Fig. 5.19 in the supplemental material). The mean and characteristic ζ_{eq} values were around 0.14 and 0.09, respectively, for all test groups except for *OSB(2)GWB-St*. The results support the idea that in all test groups crushing in wood and sheathing layers and the yielding of the fasteners control the energy-based parameters. For inclusion in the numerical models, this cyclic response is represented by the MSTEW hysteretic model, defined in Folz and Filiatrault (2004b). The MSTEW model is capable of phenomenologically capturing the behavior attributed to the crushing of wood (framing and sheathing) along with the yielding of the connector (Folz & Filiatrault, 2004b), although it accounts only for a symmetric response (see Fig. 5.20of the supplemental material). The MSTEW modeling parameters for each test group provided in Table 5.7 of the supplemental material were calibrated with the MSTEWfit tool which is part of the MATLAB M-CASHEW software (W. Pang & Hassanzadeh Shirazi, 2013). The fitted model, with examples provided in Fig. 5.4, showed good agreement with the test results, with errors in the cumulative energy dissipation (calculated as the area enclosed by hysteresis cycles) smaller than 5%. The single exception was test group *OSB(2)GWB-St* where there was high variability between specimens. As a conservative approximation, the MSTEW parameters for test group *OSB(2)GWB-St* were adjusted to the data with the smaller peak strength (i.e., Specimen 01 in Fig. 5.4b). For more information on the MSTEW fitting, please refer to Valdivieso et al. (2022).

5.3.2. Lateral characterization of multi-layered sheathing-to-frame connections for evaluating the reinforcement effect

5.3.2.1. Failure mode

The specimens were inspected after each cyclic test to evaluate typical failure modes and compare them with those reported in isolated nailed and screwed connections. In test groups *rOSB-N* and *rOSB(1)GWB-Sc*, there is a dominant ductile failure mode compared to test groups *OSB-N* and *OSB(1)GWB-Sc* (see also Valdivieso, Guindos, et al. (2023)). We attribute this ductile failure to the reinforcement effect of screws and Type X GWB

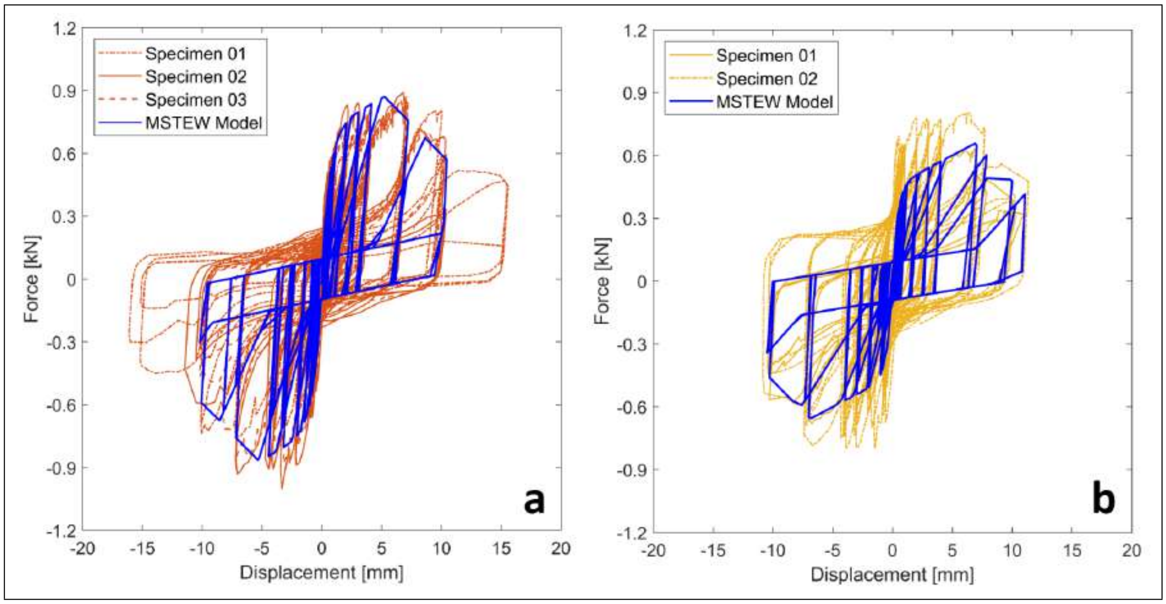

Figure 5.4. Force-displacement response of connection-level test groups (a) *OSB(1)GWB-St* and (b) *OSB(2)GWB-St*. (1 mm = 0.039 in; 1 kN = 224.8 lbf)

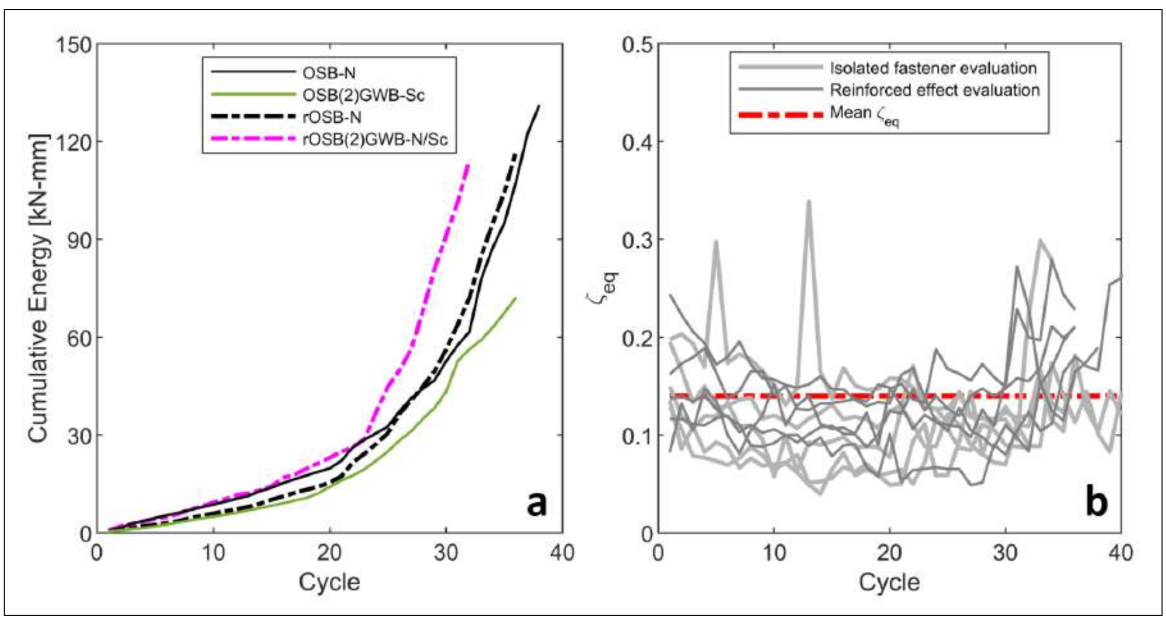

Figure 5.5. Evolution of (a) mean cumulative dissipated energy, and, (b) mean equivalent viscous damping for connection-level test groups. (1kN-mm =0.738 lbf-ft)

layers that prevent nails from pulling out and enhance the fatigue resistance and ductility of nails at large displacements. The presence of Type X GWB finish layers in multi-layered connections with multiple fasteners induces a different failure mode. This is observed when a nail and two screws work together (i.e., test group *rOSB(2)GWB-N/Sc*). The two layers of Type X GWB play a significant role, leading to shearing-off of the screws while preventing shear failure of the nail. This effect is attributed to the fixed nature caused by the thicker sheathing on one side of the shear plane (Carrero et al., 2020). When no finish layers are considered, as shown by test group *rOSB-N/Sc* or *rOSB-N/Sc-g*, neither screws nor nails fail in shear, and the fasteners develop plastic hinges. The introduction of a gap in test group *rOSB-N/Sc-g* does not result in any change in the failure mode compared to test group *rOSB-N/Sc*. Fig. 5.21 of the supplemental material illustrates the failure modes of test groups *rOSB(2)GWB-N/Sc*, *rOSB-N/Sc*, and *rOSB-N/Sc-g*.

5.3.2.2. Monotonic force-displacement response

The monotonic force-displacement test response for all the tested groups is presented in Fig. 5.6. In this figure, the force is that taken by one shear plane/fastener for test groups *rOSB-N* and *rOSB(1)GWB-Sc*, and by one shear plane/group of fasteners (i.e., 1 nail + 2 screws) for test groups *rOSB(2)GWB-N/Sc*, *rOSB-N/Sc*, and, *rOSB-N/Sc-g* (see Fig. 5.2). Table 5.8 summarizes seven engineering parameters developed from the EEEP. Monotonic test results depict that the main effect on the response of test groups *rOSB-N* and *rOSB(1)GWB-Sc* compared to test groups *OSB-N* and *OSB(1)GWB-Sc* is an increase of 82% in the deformation capacity. The test group with multiple layers of Type X GWB and one nail and two screws (*rOSB(2)GWB-N/Sc*) has the highest peak strength, elastic stiffness, and deformation capacity. These increases demonstrate that the response of multi-layered connections is controlled not only by the extra fasteners (i.e., screws for attaching finish layers), but also by the reinforcement effect of the Type X GWB finish layers (i.e., comparing *rOSB(2)GWB-N/Sc* vs *rOSB-N/Sc* and *rOSB-N/Sc-g*). When comparing the monotonic response of multi-layered connections and multiple fasteners, both with and without finish layers (i.e., test group *rOSB(2)GWB-N/Sc* vs *rOSB-N/Sc-g*), the presence of screw heads plays a significant role in enhancing the overall axial (i.e., pull-through) stiffness and capacity of the screws. This improvement in performance contributes to the system's enhanced ability to prevent nail pullout. Test group *rOSB(2)GWB-N/Sc* is also stronger than test group *OSB(2)GWB-N/Sc-sum*. The latter is determined from the summation of the results from test groups *OSB-N*, *OSB(1)GWB-Sc*, and *OSB(2)GWB-Sc* described in section 5.3.2. This difference is attributable to the reinforcement effect of screws and Type X GWB layers (including frictional effects of the component interactions) and the effects of surrounding fasteners that redistribute the load when one of them fails or yields. The reinforcement effect of screws and Type X GWB has an important role in increasing the deformation capacity of the connections, which explains the non-brittle behavior of MLSSWs when Type X GWB is applied on both sides.

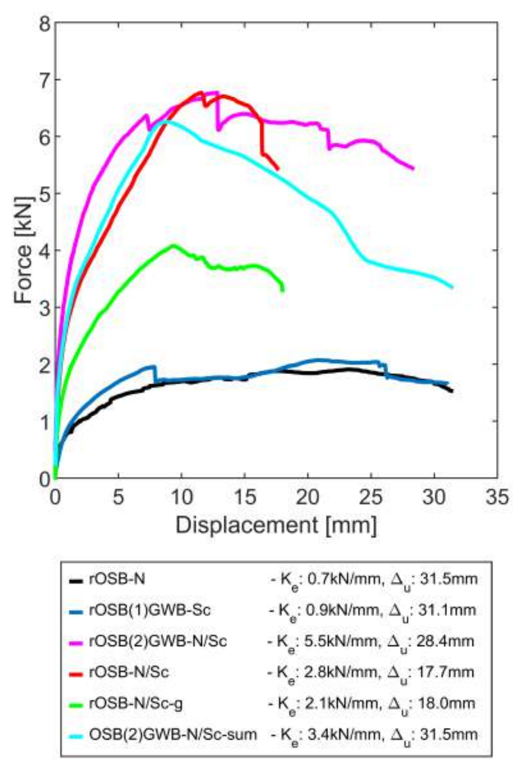

Figure 5.6. Monotonic test results of connection-level test groups to evaluate the reinforcement effect. (1 mm = 0.039 in; 1 kN = 224.8 lbf)

5.3.2.3. Cyclic force-displacement response and hysteretic model parameters

The cyclic force-displacement responses for the test groups investigating the reinforcement effect and the ones used as reference are presented in Figs. 5.7 and 5.8. The trends in the cyclic response of test groups *rOSB-N* and *rOSB(1)GWB-Sc* (see Fig. 5.7) were consistent with those found for the monotonic tests for strength, stiffness, and deformation capacity. Additionally, the reinforcement effect of finish layers leads to a more symmetrical cyclic response in the nailed OSB-to-wood frame connection. This can be observed by comparing the response of test group *OSB-N* to that of test group *rOSB-N*, where the presence of finish layers prevents nail pullout. In the cyclic response of test groups with multiple fasteners with/without finish layers (i.e., *rOSB(2)GWB-N/Sc*, *rOSB-N/Sc*, and *rOSB-N/Sc-g*) a different trend was found compared to that of the monotonic test. The cyclic response of test group *rOSB(2)GWB-N/Sc* is between that of test groups *rOSB-N/Sc* and *rOSB-N/Sc-g* in terms of peak strength (see Fig. 5.8), secant stiffness (see Fig. 5.18 in the supplemental material), energy dissipation, and damping ratio (see Figs. 5.5 and 5.19 in the supplemental material). Comparing the cyclic response of test group *rOSB(2)GWB-N/Sc* to that of *rOSB-N/Sc-g* reveals that the lateral behavior of MLSSWs is influenced not only by the additional fasteners on the OSB sheathing layer but also by the reinforcement effect resulting from screws and Type X GWB finish layers, which prevent nail pullout in the OSB-to-sheathing connection. Specifically, test group *rOSB(2)GWB-N/Sc* exhibits a higher deformation capacity and a 40% greater peak strength compared to test group *rOSB-N/Sc-g*. Moreover, results from test group *rOSB-N/Sc* indicate that the response of MLSSWs differs from that of a bare SSW with the same number of fasteners. The multi-layered connection *rOSB(2)GWB-N/Sc* demonstrates a 12.6% lower peak strength, but a higher deformation capacity when compared to test group *rOSB-N/Sc* (representing a bare wall with additional fasteners). The reinforcement effect of screws and Type X GWB has also a positive effect in that the energy dissipation of the connection is increased (see Fig. 5.5a). When the OSB is initially nailed and subsequently secured with Type X GWB and screws, nailing energy dissipation is preserved instead of relying solely on screw energy dissipation. Moreover, this combined approach results in an overall increase in dissipation by harnessing both nail and screw mechanisms. The dissipation attributed to screws might predominantly arise from axial mechanisms (i.e., withdrawal and pull-through), thus explaining the coexistence of lateral dissipation due to nails and axial dissipation due to screws.

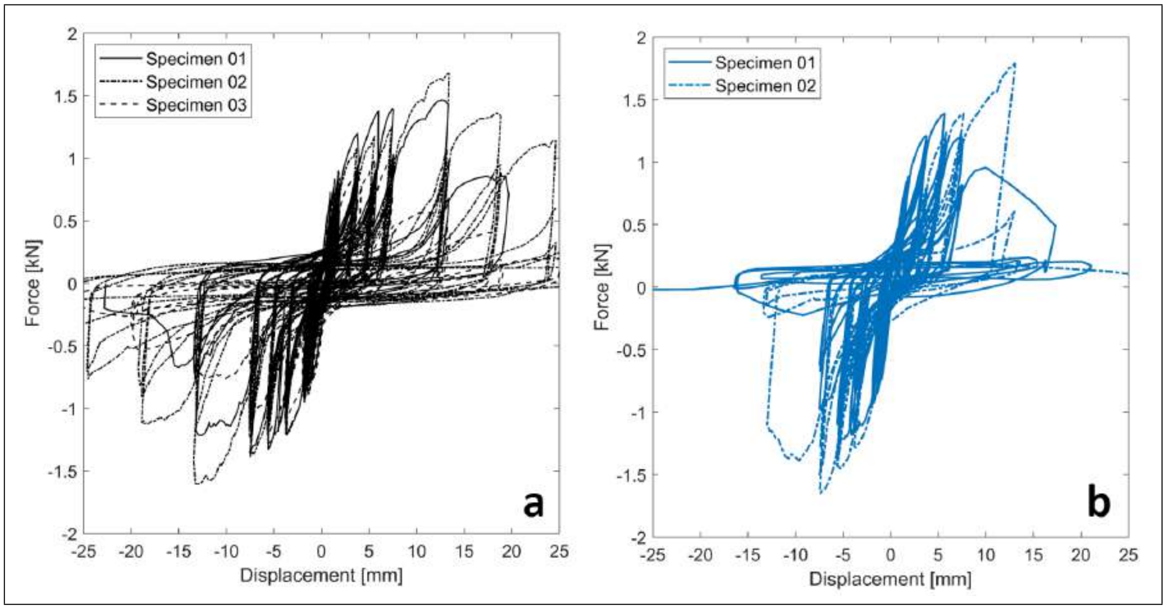

Figure 5.7. Force-displacement response of connection-level test groups: (a) *rOSB-N*; and (b) *rOSB(1)GWB-Sc*. (1 mm = 0.039 in; 1 kN = 224.8 lbf)

5.4. Numerical Simmulations

The MLSSW and bare SSW test results reported in Valdivieso, Guindos, et al. (2023) were numerically represented using the M-CASHEW software (W. Pang & Hassanzadeh Shirazi, 2013), leveraging connection-level test results from the "Experimental Program" section 5.2. The numerical simulations aim to: (a) assess the significance of incorporating the reinforcement effect of screws and Type X GWB layers in creating a more precise numerical model for MLSSWs (section 5.4.1), and (b) to extend the understanding of the performance to configurations of MLSSWs not experimentally evaluated through a parametric analysis as per Table 5.9 (section 5.4.2).

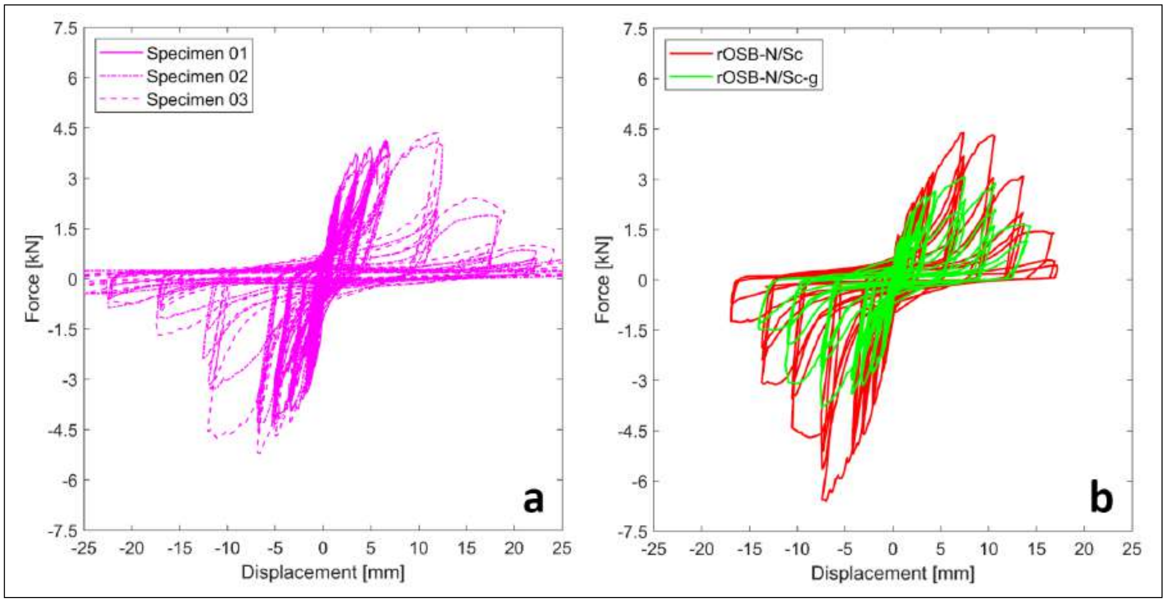

Figure 5.8. Force-displacement response of connection-level test groups: (a) *rOSB(2)GWB-N/Sc*; and (b) *rOSB-N/Sc* and *rOSB-N/Sc-g*. (1 mm = 0.039 in; 1 kN = 224.8 lbf)

5.4.1. Model description and verification

The models developed follow the numerical model guidelines presented by Estrella et al. (2020) on bare SSWs and previous work on MLSSWs (Valdivieso, Guindos, et al., 2023). To evaluate the implications of the reinforcement effect of screws and Type X GWB finish layers at the connection level on the lateral response of MLSSWs, three cases were studied and described in Table 5.2. These are SSWm for bare SSW, and MLSSWm and rMLSSWm for MLSSWs without and with the consideration of the reinforcement effect on the response of sheathing-to-frame connections, respectively. The calibrated MSTEW models from data reported in the “Lateral characterization of section 5.3.1 were used for the development of numerical models representing the sheathing-to-frame connections. Results from data reported in the section 5.3.2 were used in model rMLSSWm for calibrating the MSTEW models only in the circled sheathing-to-frame connections illustrated in Fig. 5.9. These circled connections are more likely to experience the reinforcement effect of screws and Type X GWB finish layers. At these locations, the screws used for attaching the Type X GWB finish layers are installed sufficiently distant (up to 30 mm away) from the nail used for the OSB-to-wood-frame connection. The analyses were carried out considering a displacement-controlled analysis employing the $l_{\inf} - norm$ test on displacement DOF increments as convergence criteria (W. Pang & Hassanzadeh Shirazi, 2013), with 50 iterations per step and a residual tolerance equal to 0.001 kN. The analyses were performed by applying 0.5 mm displacement increments at the top of the wall model. Fig. 5.10 shows the monotonic response of the numerical models. The reported displacement is the effective displacement of the wall measured at the top of the wall. Table 5.3 summarizes the engineering parameters of the shear walls' monotonic curves, which were estimated according to EEEP. An increase of 10%, 23%, and 26% in elastic stiffness, peak load, and deformation capacity, respectively, was found for model rMLSSWm compared to the values predicted by model MLSSWm (the one used in Valdivieso, Guindos, et al. (2023)). These results confirm the importance of the reinforcement effect in the lateral behavior of MLSSWs, as this effect strongly influences these key engineering parameters. Moreover, an increase of 55%, 130%, and 12% in the elastic stiffness, peak load, and deformation capacity, respectively, was found for rMLSSWm compared to SSWm. The cyclic responses and failure modes predicted by the numerical models were validated against the available test data on full-scale 1:1 aspect ratio MLSSW (*tO2G-244-10-r3.8-Sc* in Table 5.10 in the supplemental material) and SSW (*tOSB-244-10-r3.8-Sc* in Table 5.10 in the supplemental material) (Valdivieso, Guindos, et al., 2023). The experimental setup and failure modes of the full-scale shear walls tested by Valdivieso, Guindos, et al. (2023) are shown in Figures 5.22 and 5.23. Figure 5.23 highlights that failure modes in the MLSSW primarily occur at the connections of the OSB and GWB sheathing layers, which are key to energy dissipation in MLSSWs (Valdivieso, Guindos, et al., 2023). Consequently, the approach adopted to develop the analytical model (i.e., detailed modeling of the inelastic response of the connections while assuming linear behavior of the sheathing and the wood frames) accurately reflects the failure modes observed in the tests. Comparisons between the cyclic response predicted by the numerical model MLSSWm and the test results of MLSSWs are presented in Fig. 5.24a of the supplemental material. The numerical models were able to predict the stiffness and strength degradation as well as the pinching effect in MLSSWs and bare SSWs with a high level of accuracy as reported in Estrella et al. (2020) and Valdivieso, Guindos, et al. (2023), making it suitable for the parametric analysis of the section 5.4.2. However, the initial very large secant stiffness and equivalent viscous damping (i.e., for lateral drifts smaller than 0.1%) reported in test results from Valdivieso, Guindos, et al. (2023) were not captured by the numerical model (see Fig. 5.12, and Figs. 5.30 and 5.32 in the supplemental material) due to the model neglecting the friction and contact forces between the elements of the walls.

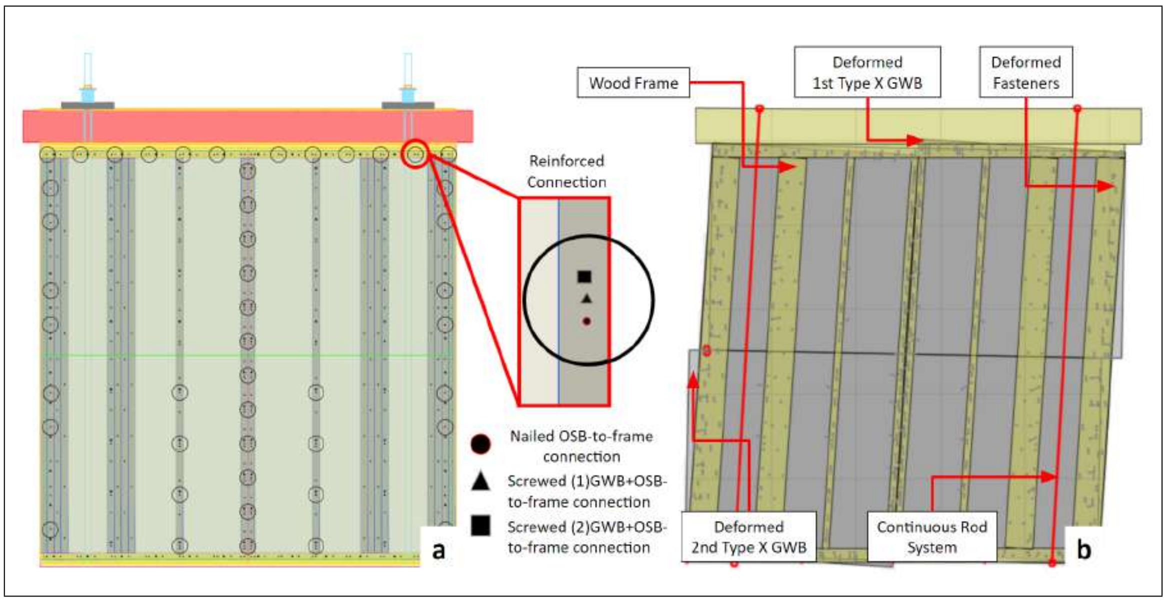

Figure 5.9. (a) Position of the reinforced connections (circled) in the numerically evaluated MLSSW from Valdivieso, Guindos, et al. (2023). (b) Deformed shape of the numerical model used to represent the MLSSW.

Table 5.2. Summary of the numerical models[a,b,c]. Symbols correspond to Fig. 5.9.

Model	Connection-level test group used for the MSTEW model calibration[d]			
	OSB ●	1st Type X GWB ▲	2nd Type X GWB ■	Multilayer Sheathing-to-Wood Frame Connection (Circled in Fig. 5.9)
SSWm	OSB-N	-	-	-
MLSSWm	OSB-N	OSB(1)GWB-Sc	OSB(2)GWB-Sc	OSB-N ● OSB(1)GWB-Sc ▲ OSB(2)GWB-Sc ■
rMLSSWm	rOSB-N	rOSB(1)GWB-Sc	OSB(2)GWB-Sc	rOSB(2)GWB-N/Sc

[a] Wood frame elements were modeled using Euler-Bernoulli elastic frame elements with a nominal modulus of elasticity E = 7900 MPa (1156 ksi) and corotational transformation. Pinned connections facilitated frame-to-frame interaction.

[b] The OSB and Type X GWB sheathing layers were modeled by 5-DOF shear rectangular elements with shear modulus G = 1.3 GPa (189 ksi) and 1.18 GPa (172 ksi), respectively.

[c] The overturning restraint system and the wall-to-foundation connection were modeled by a 3-DOF link element with a bilinear constitutive model in the vertical DOF. The tensile stiffness was set equal to the uplift stiffness of the continuous rod system and considered null for the wall-to-foundation connection. The compressive response of both the continuous rod system and the wall-to-foundation connection was set equal to the compressive response of wood members against the foundation

[d] 3-DOF link element for the sheathing-to-frame connection. MSTEW hysteretic model from the Section 5.2 in the X and Y directions and free rotation.

Table 5.3. Engineering parameters from monotonic assembly-level MLSSW numerical models. (1 mm = 0.039 in; 1 kN = 224.8 lbf)

Model	K_e [kN/mm]	Δ_y [mm]	F_y [kN]	Δ_u [mm]	F_u [kN]	F_{peak} [kN]
SSWm	3.52	31.0	109.0	160.0	97.1	121.3
MLSSWm	4.99	45.9	228.7	142.2	198.7	248.4
rMLSSWm	5.47	46.6	254.8	178.7	223.3	279.1

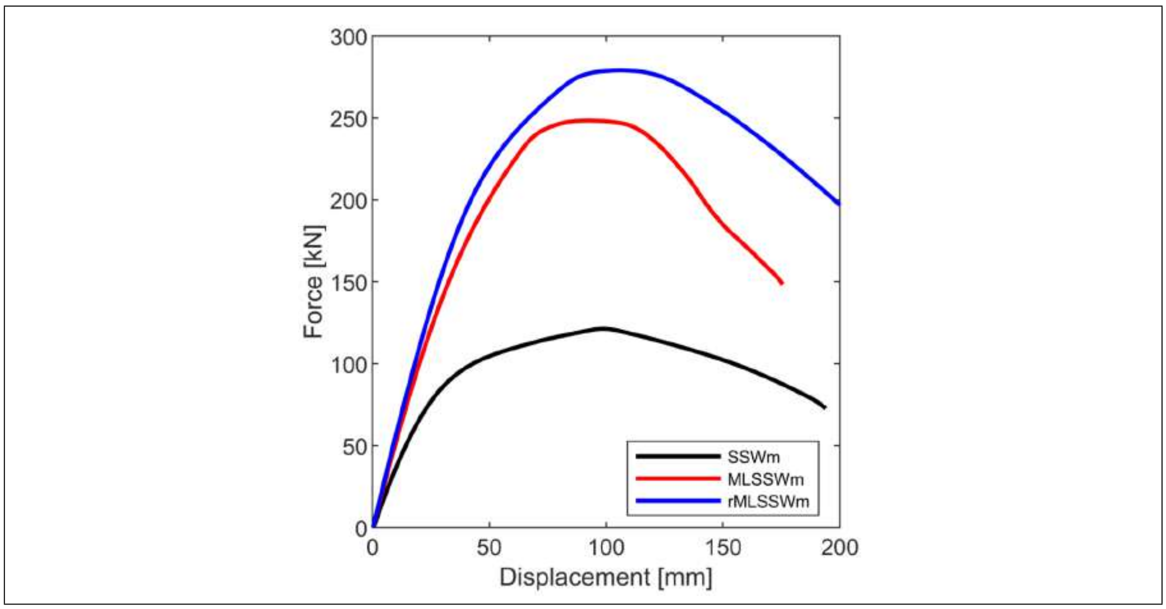

Figure 5.10. Monotonic test results from numerical models incorporating connection-level testing. (1 mm = 0.039 in; 1 kN = 224.8 lbf)

5.4.2. Parametric analysis program

A total of 30 analyses (see Table 5.9) were conducted for this study, considering various variables that were selected based on the available test data on SSWs from Guinez et al. (2019) and Estrella, Malek, et al. (2021), and wall configurations presented in the American Wood Council's Special Design Provisions for Wind and Seismic (SDPWS) (AWC, 2021). The variables included in the analyses are as follows: width-to-height wall aspect ratio (1:2, 1:1, or 1:0.7), type of overturning restraint system (continuous rod or conventional hold-down), type of multi-layered sheathing-to-frame connection (screwed or stapled), number of Type X GWB layers (one-ply or two-ply), and nail spacing (50 mm or 100 mm). The number of layers of Type X GWB (i.e., either one or two) is intended to replicate shear wall solutions that meet one-hour or two-hour fire-resistance rating, which is consistent with approved fire application solutions available in Chile. For each modeled wall, monotonic and cyclic analyses were performed. The models were developed considering model MLSSWm approximation from Table 5.2 using the test data at the connection level from the section 5.3.1 as an input for the multilayer sheathing-to-wood frame connections. To maintain a conservative approach in this analysis, the potential enhancements in stiffness, strength, and ductility/deformation capacity resulting from the reinforcement effect examined in the sections 5.3.2 and 5.4.1 were disregarded. This decision was primarily driven by the lack of experimental data available for evaluating the reinforcement effect specifically in stapled connections and for assessing the lateral response of MLSSWs with stapled connections. Test data summarized in Table 5.4, used in this section for validating numerical models (see Fig. 5.25 and Table 5.10 of supplemental material), are labeled following the same structure of wall types explored in the parametric analysis, but adding a “t” at the beginning referring to “test data”. The geometry of the test specimens is illustrated in Fig. 5.25 of the supplemental material. For both the experimental data and the parametric numerical evaluation of MLSSWs, the spacing of the fasteners used to attach the Type X GWB sheathing layers for fire protection comply with the minimum requirements of Eurocode 5 Part 1-2 (EN, 2004).

5.4.2.1. Parametric analysis results

Fig. 5.11 shows the monotonic response of selected wall types. The monotonic response of all wall groups and the cyclic response of MLSSWs with screwed connections and two Type X GWB layers are illustrated in Figs. 5.26 to 5.28 and 5.29, respectively, of the supplemental material. The reported displacement is the effective displacement of the wall measured at the top of the wall. The monotonic results are consistent with the findings reported inValdivieso, Guindos, et al. (2023), indicating that the inclusion of finish layers in the MLSSW configurations leads to increased stiffness and peak strength compared to SSWs. However, the influence of Type X GWB finish layers on the deformation capacity of MLSSWs is not significant, as discussed in more detail later. The cyclic response of the examined MLSSW specimens exhibited an elastic behavior up to a lateral drift range of approximately 1.0% to 2.4%, followed by a nonlinear response. Subsequently, progressive and gradual degradation in both strength and stiffness was observed after reaching the peak strength. As anticipated, the specimens displayed a notable level of redundancy due to the presence of multiple screwed/stapled and nailed connections, thereby enabling the structures to sustain high lateral drift levels without experiencing brittle failures. The MSTEW model effectively captured the cyclic response of the MLSSW under evaluation. Table 5.5 presents the fitted parameters for the MLSSW depicted in Fig. 5.11.

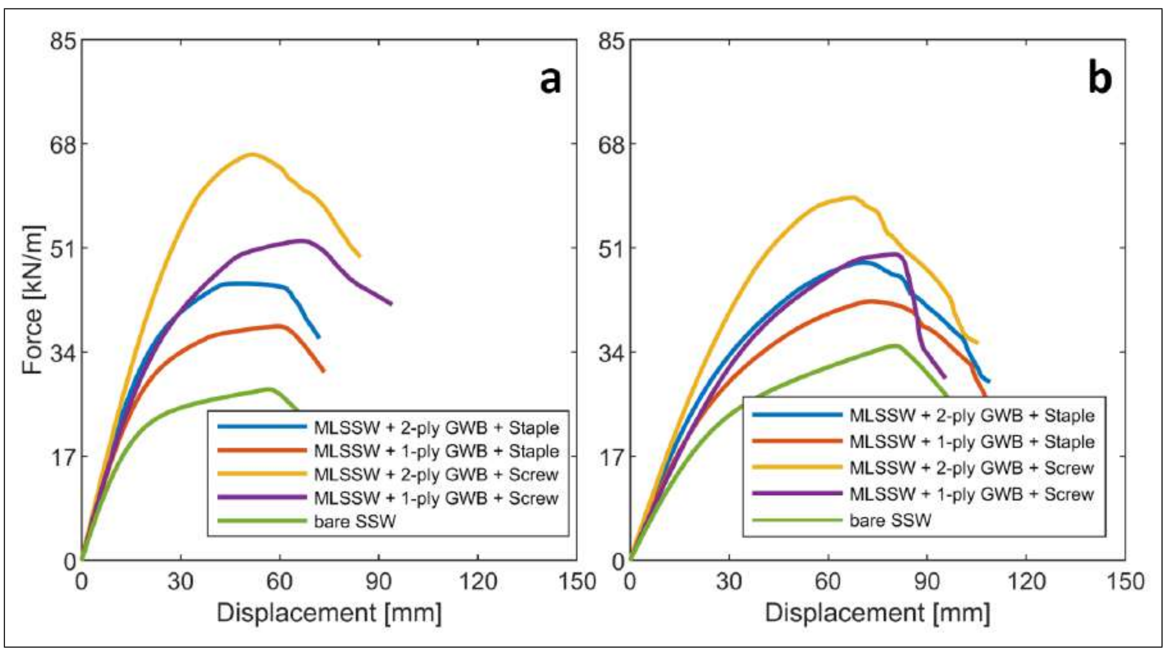

Figure 5.11. Monotonic response comparison between bare SSW and MLSSW with Type X GWB (one or two-ply) using stapled or screwed connections for 1:1 aspect ratio wall with (a) continuous rod system and (b) conventional hold-down. (1 mm = 0.039 in; 1 kN = 224.8 lbf)

Table 5.4. Summary of the assembly-level test data for validating the numerical model (see Table 5.10.

Wall size (L by H)	Wood Structural Panel			Gypsum Wallboard (GWB)		
	Thickness	Sheathing Nails	Spacing edge/field	Thickness and Type	Wallboard screws[f]	Spacing edge/field
2440x2481[a]	11.1	ϕ2.9x80[d]	100/200	None	-	-
2440x2440[b]	11.1	ϕ3.0x70[e]	50/100	None	-	-
2440x2481[a]	11.1	ϕ2.9x80[d]	100/200	(2) - 15, Type X	ϕ4.0x63.5 ϕ4.0x76.2	200/300
1200x2470[c]	11.1	ϕ3.0x70[e]	100/200	None	-	-
2400x2470[c]	11.1	ϕ3.0x70[e]	100/200	None	-	-
2400x2470[c]	11.1	ϕ3.0x70[e]	50/100	None	-	-
3600x2470[c]	11.1	ϕ3.0x70[e]	100/200	None	-	-

[a] Wall framing consisted of 41mm x 185 mm (2x8) C16 Chilean RP (INN, 2014) studs. Overturning restraint provided by ϕ38.1 mm ASTM A193 Grade B7 rods. Further details are in (Valdivieso, Guindos, et al., 2023). (1 mm = 0.039 in)

[b] Wall framing consisted of 35mm x 138 mm (2x6) C16 Chilean RP (INN, 2014) studs. Overturning restraint provided by ϕ44.5 mm rods grade 105. Further details are in (Estrella, Malek, et al., 2021).

[c] Wall framing consisted of 38mm x 138 mm (2x6) C16 Chilean RP (INN, 2014) studs. Overturning restraint provided by conventional hold-down Simpson Strong-Tie HD12. Further details are in (Guinez et al., 2019).

[d] OSB sheathing layer attached to frame with pneumatically driven wire coil spiral nails (80 x 2.9 x 6.5 mm) according to EN14592:2008+A1:2012 (BSI, 2008).

[e] OSB sheathing layer attached to frame with pneumatically driven wire coil common shank nails according to ASTM F1667 (ASTM, 2021).

[f] Type X GWB sheathing first layer attached to frame through the OSB with type “W” screws (63.5 x 4.0 x 8.0 mm). Type X GWB sheathing second layer attached to frame through the 1st Type X GWB and OSB with type “W” screws (76.2 x 4.0 x 8.0 mm). The application of a double layer of Type X GWB is intended to simulate a shear wall that meets a two-hour fire-resistance rating.

5.4.2.2. Engineering parameters developed from parametric analysis

From the monotonic and cycle numerical results, the same engineering parameters assessed in the connection-level experimental program were established according to EEEP: K_e; Δ_y; F_y; Δ_u; F_u; μ, $E_{H,i}$, ζ_{eq}; and k_{sec}. The resulting parameters from monotonic test results are summarized in Table 5.11 in the supplemental material. The engineering parameters are compared to evaluate the effect of each of the considered variables on the lateral response of all the analyzed wall types.

5.4.2.3. Strength

The parametric analysis of different MLSSW configurations showed the positive effect of finish layers on the peak strength compared to bare SSWs. MLSSWs with screwed and stapled connections showed a mean increase in strength of up to 57% and 30%, respectively, compared to bare SSWs. This difference in the peak strength increase is attributable to the strength difference between the fastener types. Comparing the effect of the number of finish layers, MLSSWs with two Type X GWB finish layers had a 70% higher increase in the peak strength than MLSSWs with one Type X GWB finish layers because of the larger number of fasteners used in the MLSSWs with two Type X GWB layers. Also, as the nail spacing is reduced from 100 mm to 50 mm an increase (i.e., up to 62%) of the strength was found (see Figs. 5.26 and 5.27 from the supplemental material). The results on strength confirm the findings of previous research on MLSSWs (Valdivieso, Guindos, et al., 2023) regarding: a) the positive effects of Type X GWB finish layers; and b) the fastener used to attach the finish layers to the wood frame having an even stronger influence than denser nailing patterns or stronger anchorages. These are the two most important design parameters to increase the capacity of timber shear walls (Guinez et al., 2019; Estrella et al., 2020; Estrella, Malek, et al., 2021). The type of anchorage significantly affects the peak strength. When the peak strength of MLSSWs is compared to that of bare SSWs, the difference is greater in walls with continuous rod systems than in those with conventional hold-downs. Specifically, the difference in walls equipped with continuous rod systems is at least 15% greater than that in walls equipped with conventional hold-downs. This difference is clearly illustrated in the comparison between bare SSWs and MLSSWs shown in Fig. 5.11. There is no clear difference in strength as the wall aspect ratio changes (see Figs. 5.27 and 5.28 from the supplemental material) which is consistent with SDPWS (AWC, 2021), where no reduction in the nominal strength (reported in section 4.3 of SDPWS AWC (2021)) is expected in walls of up to 1:2 width-to-height aspect ratio.

5.4.2.4. Stiffness

The results confirm the benefit of finish layers in the elastic and secant stiffness of MLSSWs over the consideration of bare SSWs. Walls with screwed and stapled multilayer connections showed a mean increase of up to 28% and 20% compared to bare SSWs, respectively. A mean increase of up to 33% was found when comparing MLSSWs with two Type X GWB finish layers to bare SSWs. Furthermore, a 128% higher mean increase was found when comparing between two and one Type X GWB finish layers cases. As the nail spacing is reduced from 100 mm to 50 mm the increase of the elastic stiffness with respect to bare SSWs was reduced by 51%. The impact of the anchorage type showed a difference in the elastic stiffness of less than 20%, which is consistent with the results reported in Estrella, Malek, et al. (2021). For walls with a 1:2 aspect ratio, up to -18% difference in the elastic stiffness was found compared to the other two cases, which is explained by the fact that the stiffer the wall (in shear) the more the overturning anchorage system controls the stiffness, which is consistent with the results reported in bare SSWs (Estrella, Malek, et al., 2021). Fig. 5.30 of the supplemental material presents the evolution of the secant stiffness per meter of wall as a function of the lateral drift for all wall configurations. All specimens show a clear degradation of the stiffness as the lateral drift of the wall increases, presenting a residual secant stiffness between 0.1 kN/mm/m to 0.2 kN/mm/m, which is attributable to the frame-to-frame interaction and the remaining field nailed OSB-to-frame connections. MLSSWs exhibit a linear degradation of secant stiffness at the 0.1% to 4% range of lateral drift, and then there is an important change in the degradation ratio at the 4% to 5% range of lateral drift (see Fig. 5.30 in the supplemental material). The change in the degradation ratio is attributable to the propagation of screws/staple failures along the top and bottom plate of the wall in the direction to the sturdy end studs. Wall types with two Type X GWB layers showed a higher degradation ratio compared to the case with only one layer. Also, the screwed MLSSWs showed higher increases and a faster degradation rate in the secant stiffness compared to the stapled MLSSWs, which is attributable to the difference in the fastener response.

5.4.2.5. Deformation Capacity

The deformation capacity of the different wall groups revealed no significant mean increase or decrease (less than 3%) of MLSSWs with respect to SSWs, which is important in the context of seismic design of LFTBs considering MLSSWs as lateral system. This result supports the experimental findings reported in Valdivieso, Guindos, et al. (2023) for a wide number of configurations, suggesting that deformation capacity is in general not adversely affected by the addition of the finish layers. However, when analyzing the response of MLSSWs from different wall groups there are some secondary effects that affect the deformation capacity. MLSSWs with 100 mm nail spacing and/or continuous rod systems showed an increase in deformation capacity of up to 7% compared to SSWs, whereas MLSSWs with 50 mm nail spacing and/or conventional hold-down systems showed a decrease in deformation capacity of up to 4% compared to SSWs. We attribute this dissimilar tendency to the fact that SSWs with 50 mm nail spacing and/or conventional shear walls tend to exhibit higher levels of deformation capacity where the rocking component of the lateral deformation is predominant. Then, in SSWs with 100 mm nail spacing and/or overturning restraint systems, there is space for an increase in the contribution of the rocking deformation to the lateral deformation of the wall, as was experimentally reported in MLSSWs (Valdivieso, Guindos, et al., 2023).

5.4.2.6. Energy dissipation and equivalent viscous damping

In Fig. 5.12, the evolution of the cumulative dissipated energy per wall meter as a function of the lateral drift is presented for selected wall configurations. The response of all wall groups is illustrated in Fig. 5.31 of the supplemental material. All wall types dissipate approximately the same amount of energy for lateral drifts smaller than 2%, but for larger displacements, the MLSSWs dissipate more energy, even when the walls are less ductile. Moreover, wall types with two Type X GWB layers have the highest level of dissipated energy due to the greater number of multi-layered connections. There is no significant difference in the equivalent viscous damping (ζ_{eq}) as a function of the lateral drift for each wall group (see Fig. 5.12 and Fig. 5.32 of the supplemental material). However, there is a clear reduction in ζ_{eq} as the aspect ratio of the wall increases, which is attributed to the influence of the rocking displacement on the lateral displacement of the wall as the aspect ratio increases. The mean ζ_{eq} values in MLSSWs were smaller (i.e., up to 36%) than those in bare shear walls, due to a more predominant increase in strength than in cumulative dissipated energy compared to SSWs. The ζ_{eq} values in MLSSWs with one Type X GWB layer were higher (i.e., 11%) than those with two layers. Stapled MLSSWs had higher (i.e., 20%) ζ_{eq} values than screwed MLSSWs which is explained by the different effects of the screwed and stapled connections on the increase of maximum capacity and stiffness in MLSSWs. Walls with continuous rod systems had higher ζ_{eq} values than those with conventional hold-down which is consistent with the difference in the values reported in previous studies (Guinez et al., 2019; Estrella et al., 2020; Estrella, Malek, et al., 2021). MLSSWs with a nail spacing of 100 mm had higher ζ_{eq} values (i.e., 17%) than those with a spacing of 50 mm. Finally, the mean ζ_{eq} values increased as the wall length increased, from 7.5% to 9.0% for walls with aspect ratios of 1:2 and 1:0.7, respectively.

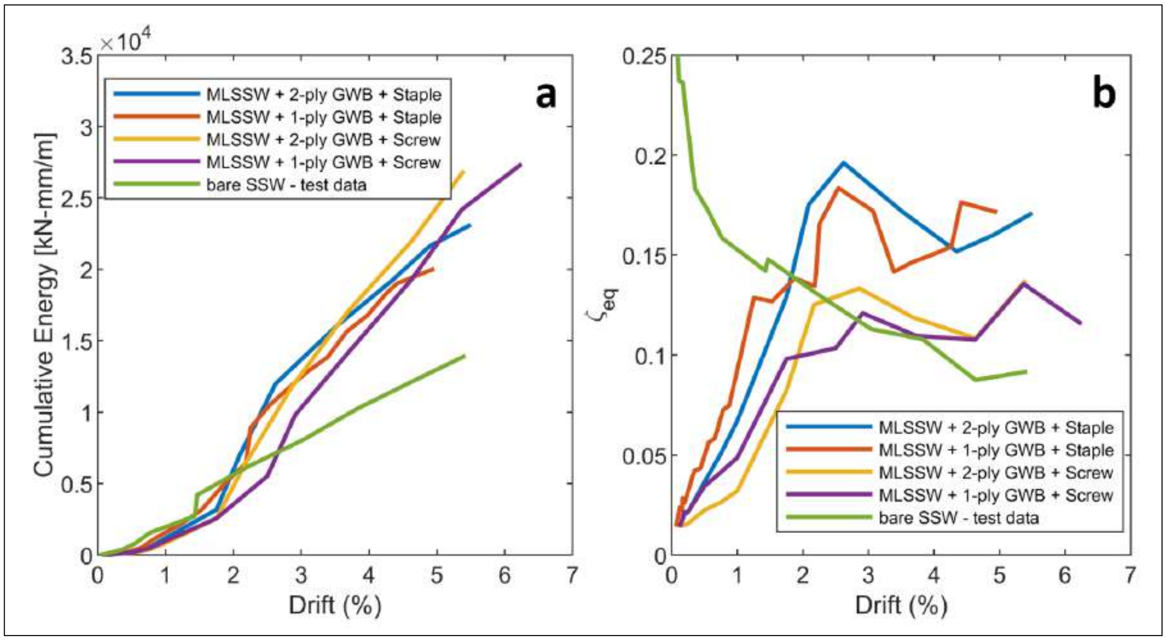

Figure 5.12. Comparison of (a) cumulative dissipated energy and (b) evolution of equivalent viscous damping as a function of lateral drift for bare SSW and MLSSW with Type X GWB (one or two-ply) using stapled or screwed connections in a 1:1 aspect ratio wall with continuous rod system. (1kN-mm =0.738 lbf-ft)

Table 5.5. MSTEW modeling parameters for MLSSWs as per Fig.5.11[a]. (1 mm = 0.039 in; 1 kN = 224.8 lbf; 1 kN/mm = 68.5 klf).

Wall Type	K_0 [kN/mm/m]	r_1	r_2	r_3	r_4	F_0 [kN/m]	F_I [kN/m]	Δ_u [mm]	α	β	F_{peak} [kN/m]
O1G-244-10-r3.8-Sc	2.2	0.043	-0.194	1.010	0.020	51.2	3.8	62.3	0.550	1.135	53.1
O1G-244-10-r3.8-St	2.0	0.015	-0.255	1.010	0.015	38.5	3.0	60.0	0.859	1.050	38.5
O2G-244-10-r3.8-Sc	2.5	0.107	-0.250	1.010	0.024	65.7	5.4	50.8	0.550	1.450	68.2
O2G-244-10-r3.8-St	2.2	0.064	-0.250	1.010	0.020	45.2	3.7	52.0	0.755	1.050	48.6
O1G-240-10-hd12-Sc	1.4	0.065	-0.315	1.050	0.025	48.0	2.7	69.2	0.550	1.096	47.0
O1G-240-10-hd12-St	1.3	0.080	-0.325	1.010	0.017	41.3	3.4	70.5	0.650	1.050	43.3
O2G-240-10-hd12-Sc	1.6	0.175	-0.336	1.010	0.023	59.5	2.6	60.9	0.805	1.141	60.2
O2G-240-10-hd12-St	1.3	0.150	-0.358	1.010	0.026	48.5	2.6	67.0	0.950	1.050	50.2

[a] K_0 is the initial stiffness of the hysteretic curve, r_1 to r_4 are dimensionless parameters that represent stiffness ratios at different parts of the curve, F_0 and F_I are strength parameters of the hysteretic curve (Folz & Filiatrault, 2004b), and Δ_u is the displacement at peak load. Parameters α ($\alpha > 0$) and β ($\beta > 0$) control the stiffness degradation and energy degradation, respectively.

5.5. Chapter Conclusions

In this investigation, the influence of finish layers (i.e., Type X GWB), their connections and the reinforcement effect on the cyclic lateral response of strong shear walls (SSWs) were analyzed numerically based on connection-level test results. Cyclic test results of connection-level tests were used for calibrating the MSTEW models used as an input for assembly-level numerical models. Results support the authors' previous experimental findings on 1:1 aspect ratio MLSSWs showing that finish layers improved almost all relevant engineering parameters. Further, the findings show that the response of MLSSWs is not controlled only by the extra connections of the finish layers, but also by the reinforcement effect of screws and Type X GWB layers. These sheathing layers modified the response of the fasteners that connect the OSB and the first Type X GWB sheathing layers by preventing them from pulling out and enhancing their deformation capacity. The main impact was observed in the nailed OSB-to-frame connection. At the assembly level, the inclusion of the reinforcement effect in the numerical model provides a better prediction of the lateral response of MLSSWs reported in Valdivieso, Guindos, et al. (2023) in terms of peak strength, stiffness, and ductility. Multi-layered connection-level tests show that a screwed connection has higher strength and stiffness than a stapled connection. The equivalent viscous damping tends to be similar in all the evaluated connection-level systems. However, the nailed connection has a larger displacement capacity than the screwed and stapled connections, especially under reversed cyclic loading. The test groups with staples also showed greater variability in their cyclic response, the implications of which are a topic for future research. The parametric numerical analysis demonstrates that MLSSWs with screwed multilayered connections present higher peak strength and stiffness, and almost the same deformation capacity, compared to stapled cases. The same relationship was found when comparing MLSSWs with two versus one Type X GWB finish layer. However, the effect of these finishes is less significant when there are more nails (i.e. reduced spacing) connecting the OSB sheathing layer, as the nails and the fasteners connecting the finish layers have a somewhat duplicative effect.

Additional research is needed to realize the potential of optimized fastener arrangements for even further improving the lateral response of MLSSWs. The impact of the overturning anchorage type on the lateral response of MLSSWs was mainly in the peak strength, as was previously reported on bare SSWs (Estrella, Malek, et al., 2021). There is no clear difference in terms of energy dissipated among the evaluated variables on MLSSWs. Taken together, these results shed light on the complexity of the finish layer interaction with MLSSW and the improvements in design procedures possible if these complexities could be incorporated. The integration of these findings into practice promises to foster the development of more robust, efficient, and sustainable timber-based construction solutions.

5.6. Supplemental Material - Figures

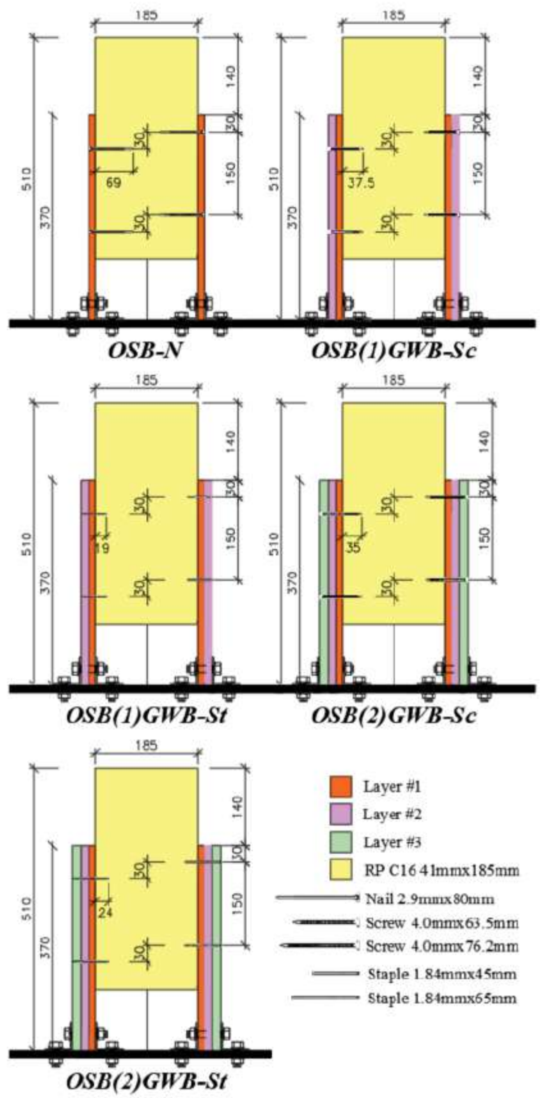

Figure 5.13. Multi-layered connection (i.e., connection-level) specimens for evaluation of the lateral response of isolated fasteners. All dimensions in millimeters (1 mm = 0.039 in).

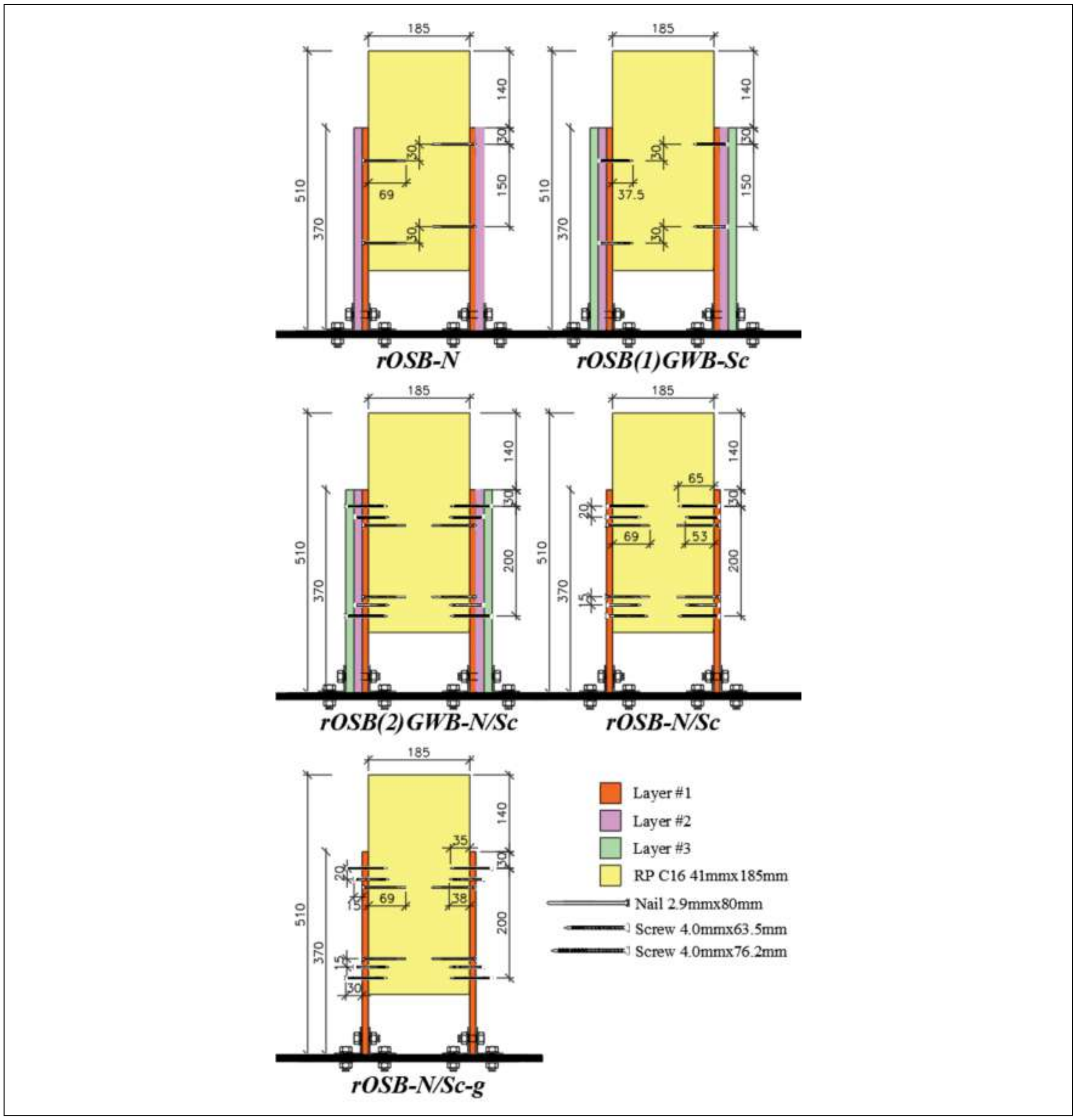

Figure 5.14. Multi-layered connection specimens for evaluation of the reinforcement effect. All dimensions in millimeters. (1 mm = 0.039 in).

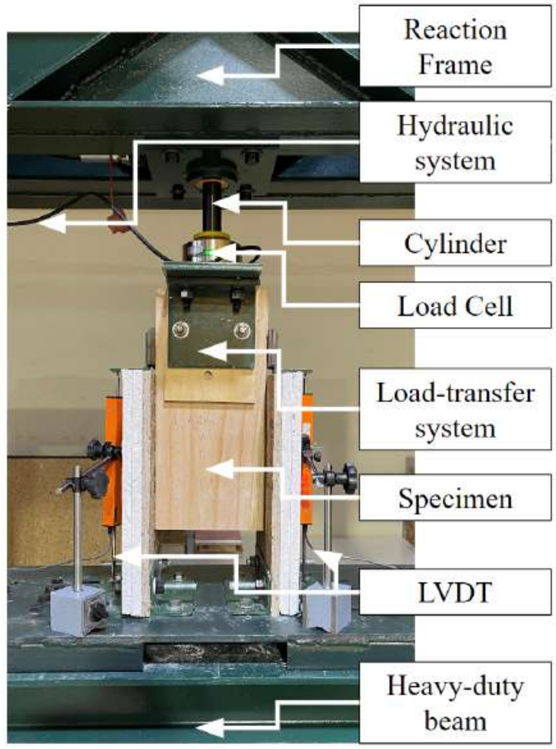

Figure 5.15. Connection-level test set-up.

Figure 5.16. Example of the failure modes identified in the connection-level test of the test group *OSB(1)GWB-St*. Label (1): excessive bending in the staple leading to the shearing-off of the fastener, and, label (2) pull-out of the staple from the frame leading to the detaching of the sheathing and fatigue failure of the fastener. In both cases, crushing on the wood and limited damage to the OSB and Type X GWB sheathings were observed.

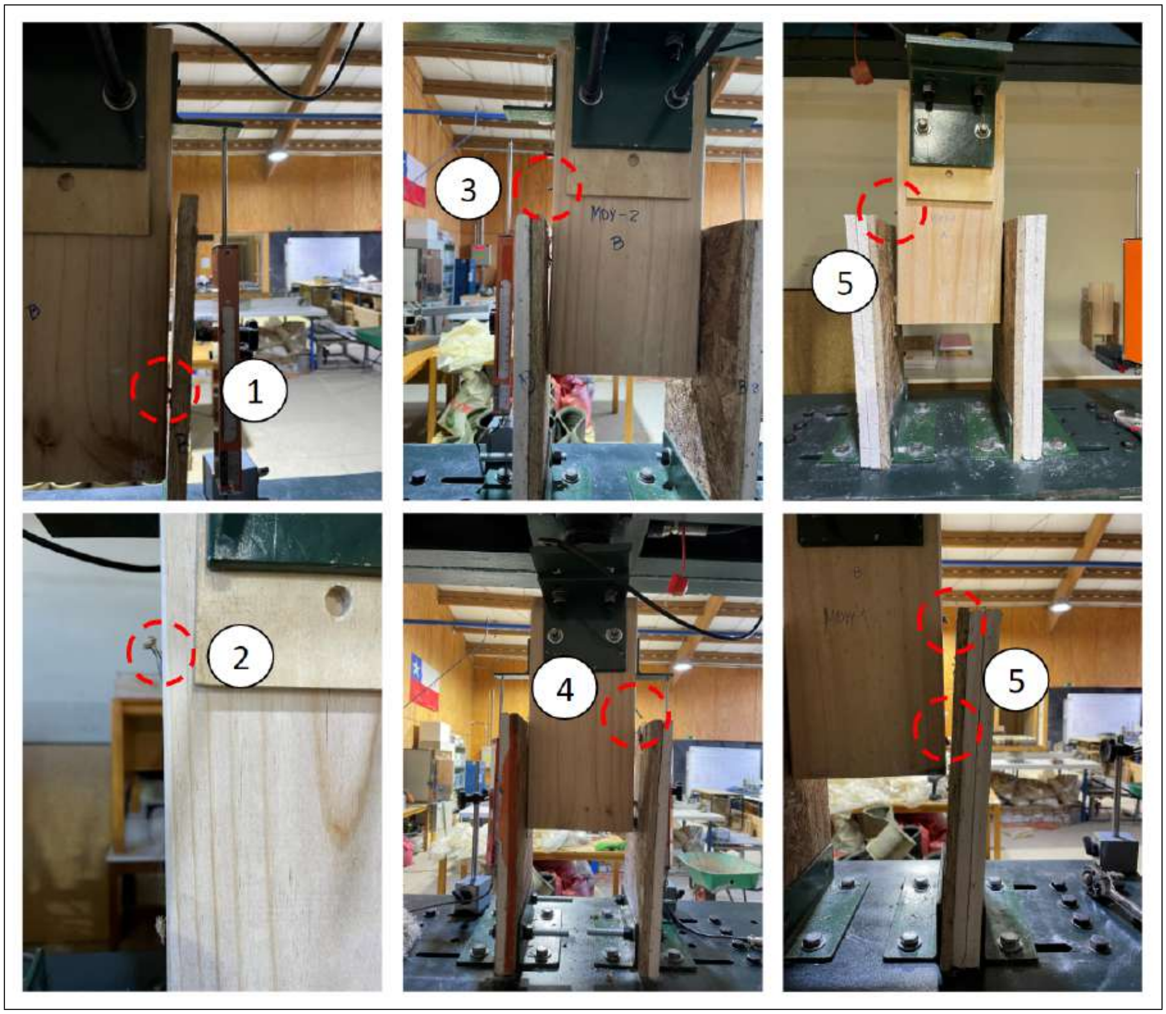

Figure 5.17. Example of the failure modes identified in the connection-level test of the test group *OSB-N*, *OSB(1)GWB-Sc*, and *OSB(2)GWB-Sc*. Label (1) excessive nail bending leading to fastener shearing. Label (2) nail pull-out or pull-through from the OSB-to-wood frame connection causing OSB detachment, accompanied by wood crushing and OSB panel fiber tearing. Label (3) excessive screw bending leading to fastener shearing. Label (4) screw pull-through from the GWB+OSB-to-wood frame connection resulting in sheathing detachment, with wood and panel crushing, and OSB and GWB tearing. Label (5) excessive screw bending causing fastener shearing, along with wood crushing and tearing in OSB.

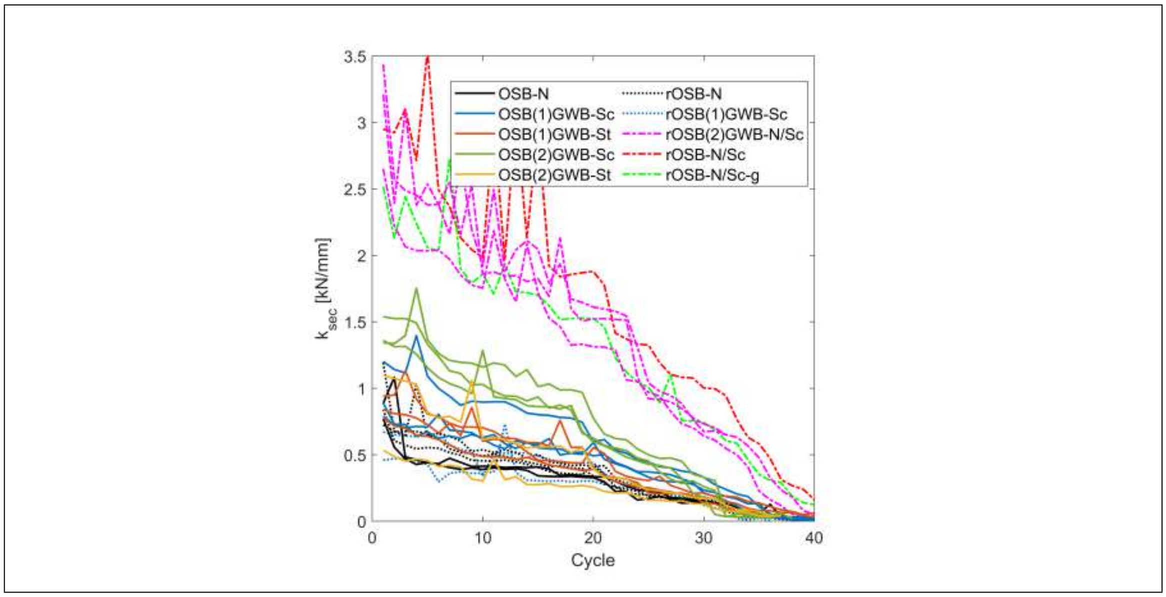

Figure 5.18. Secant stiffness evolution for connection-level test groups. (1 kN/mm = 68.5 klf)

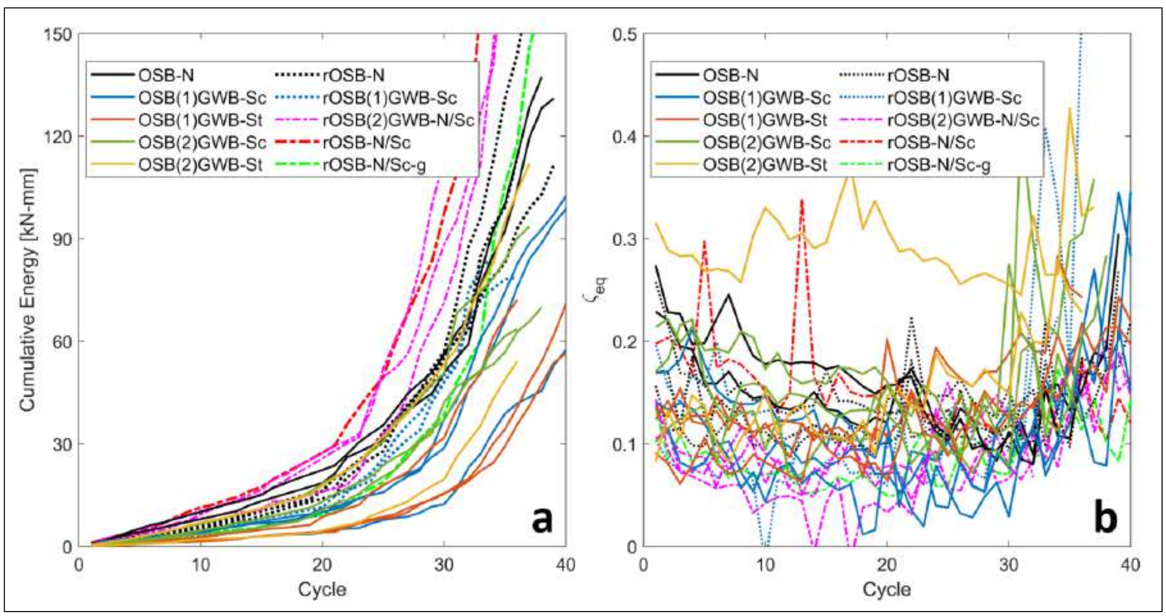

Figure 5.19. Evolution of (a) mean cumulative dissipated energy, and, (b) mean equivalent viscous damping for connection-level test groups. (1kN-mm = 0.738 lbf-ft)

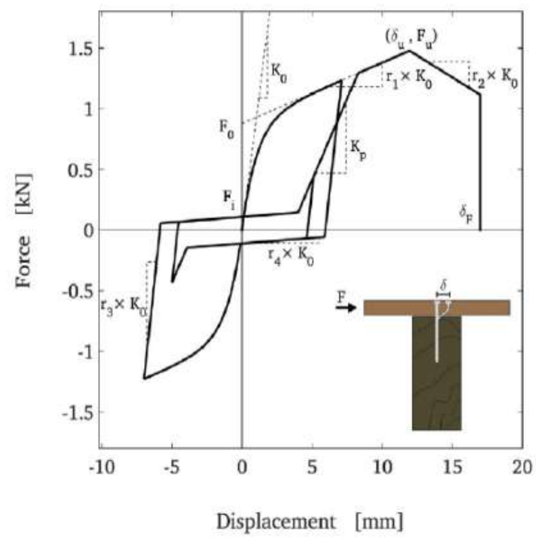

Figure 5.20. MSTEW model description. Reprinted from (Estrella et al., 2020). (1 mm = 0.039 in; 1 kN = 224.8 lbf)

For test group *rOSB(2)GWB-N/Sc*, two failure modes were identified: (i) pull-through of the nail from the sheathing-to-frame joint, leading to the detaching of the OSB and Type X GWB layers (see label 1 in Fig. S9), and, (ii) excessive bending of the nails and screws, leading to the shearing-off of the screws (again this is attributable to the reinforcement effect) (see label 2 in Fig. 5.21). On test groups *rOSB-N/Sc* and *rOSB-N/Sc-g*, two failure modes were identified: (i) excessive bending in the screw and nails leading to the yielding but not to the shearing-off of the fasteners (see label 3 in Fig. 5.21), and, (ii) pull-through of the nails from the OSB-to-frame joint leading to a minor detaching of the OSB sheathing because of the screws withdrawal strength (see label 4 in Fig. 5.21). In all cases, crushing in the wood and sheathing, and fiber tear in the OSB and GWB panels were observed.

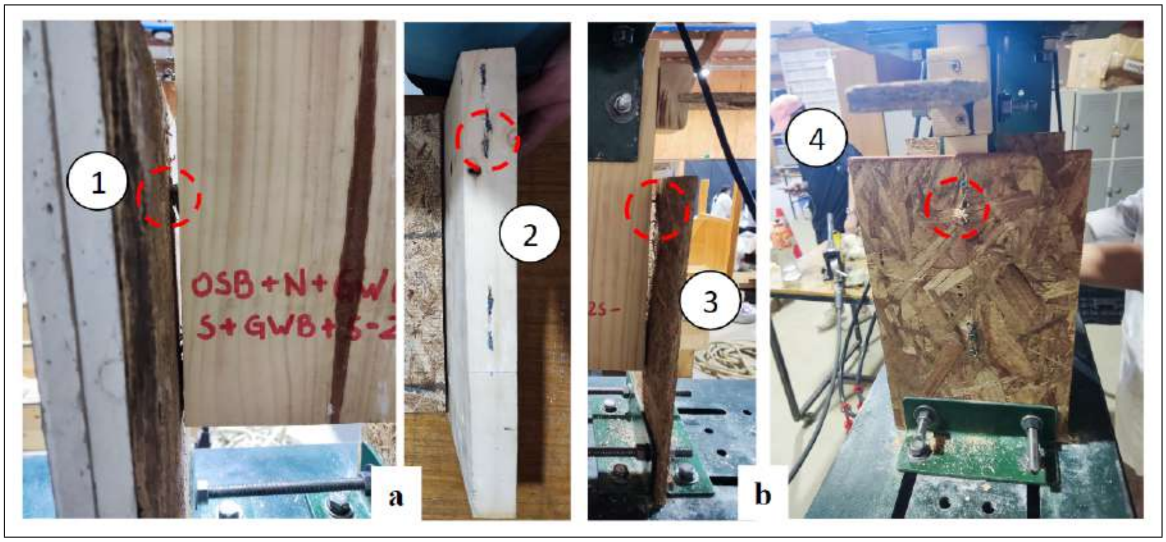

Figure 5.21. Failure modes identified in the connection-level test group: (a) *rOSB(2)GWB-N/Sc*, (b) *rOSB-N/Sc* and *rOSB-N/Sc-g*.

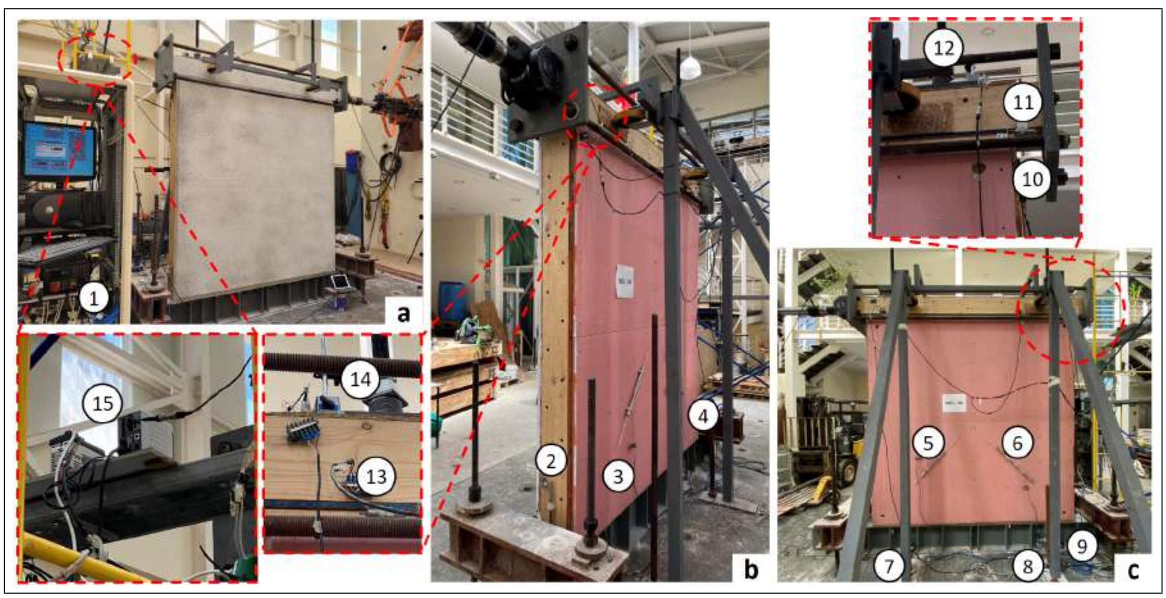

Figure 5.22. The MLSSW test setup (a) a front view showing the application of Digital Image Correlation, (b) a side view, and (c) a back view where transducers were installed. Labels (1) to (15) indicate the instrumentation detailed by (Valdivieso, Guindos, et al., 2023). This figure is reproduced from (Valdivieso, Guindos, et al., 2023).

Figure 5.23. Main failure modes observed in MLSSW specimens: (1) nail and screw failure pattern; (2) and (3) failure of the screwed Type X GWB+OSB-to-frame connection (in orange) for the 2nd layer and 1st layer, respectively; (4) and (6) pulling out of screws and nails; (5) and (9) local failure of the Type X GWB panels and OSB, respectively; (7) pulling through of nails and screws;(8) sheathing layers detachment from the wood-frames; and, (10) double shear failure of the screws. This figure is reproduced from (Valdivieso, Guindos, et al., 2023).

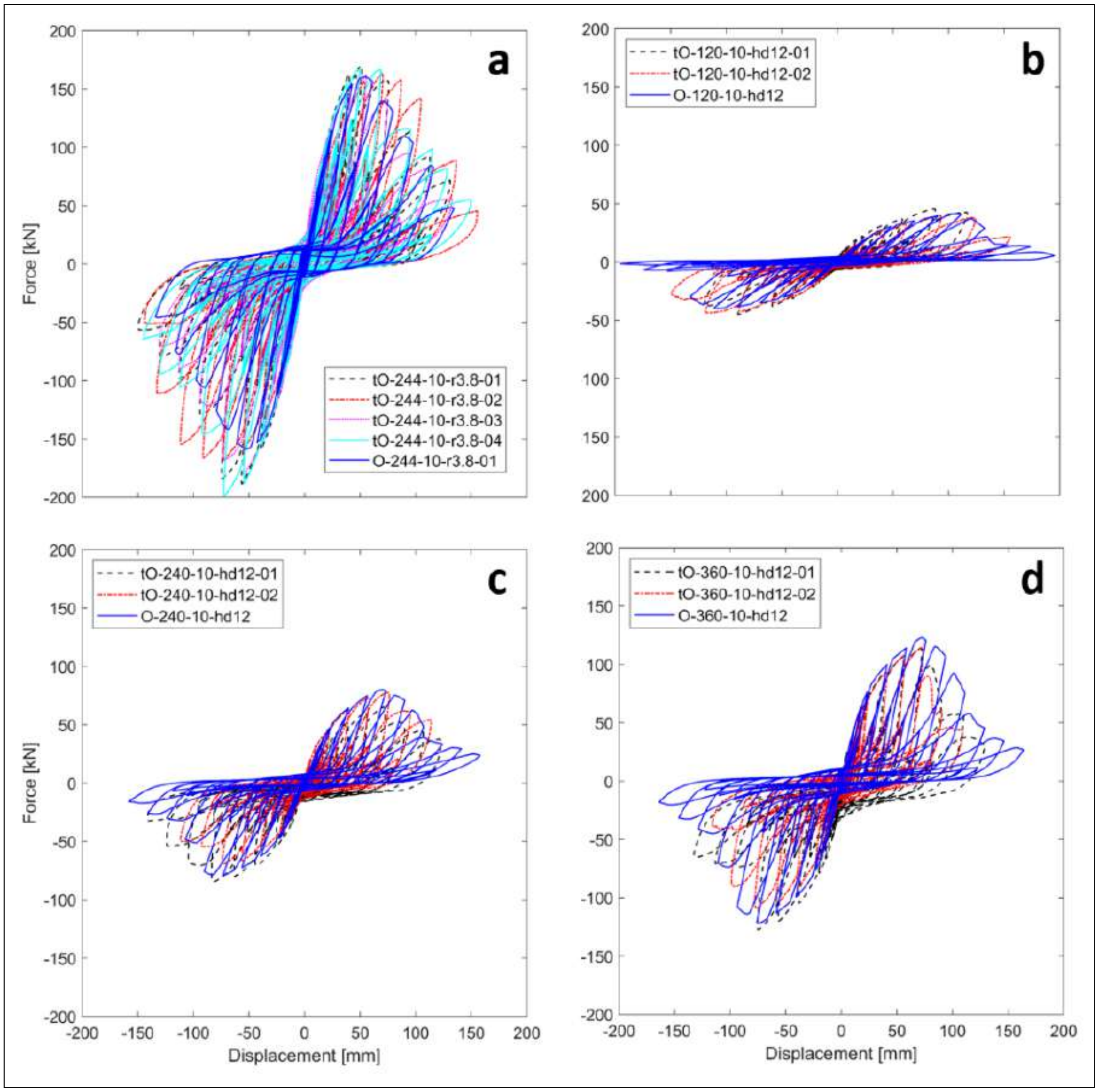

Figure 5.24. Cyclic response comparison of numerical model prediction and test data for wall type: (a) *O2G-244-10-r3.8-Sc* specimens 01 to 04 (Valdivieso, Guindos, et al., 2023), (b) *OSB-120-10-hd12* specimens 01 and 02 (Guinez et al., 2019), (c) *OSB-240-10-hd12* (Guinez et al., 2019), and, (d) *OSB-360-10-hd12* (Guinez et al., 2019). (1 mm = 0.039 in; 1 kN = 224.8 lbf)

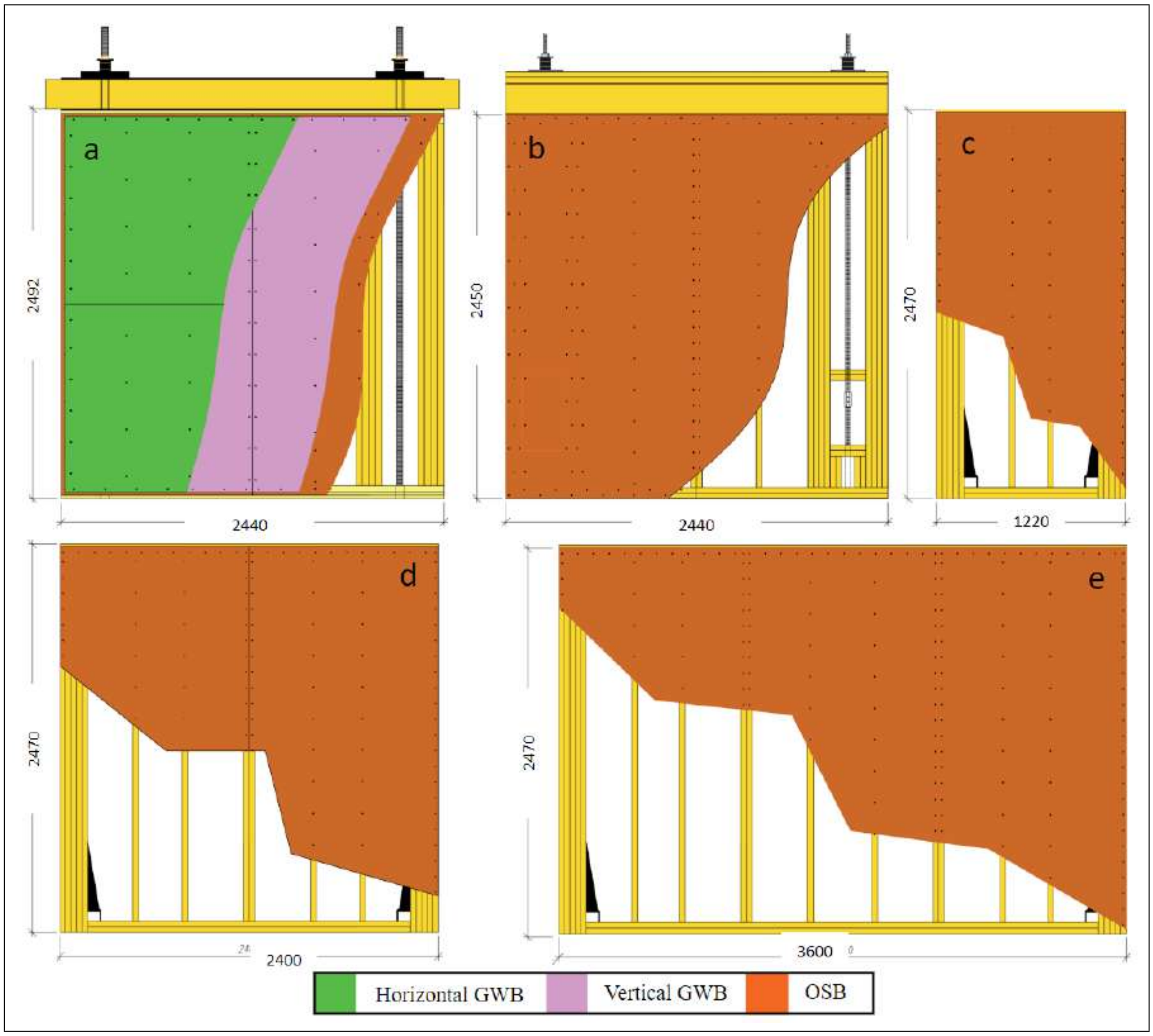

Figure 5.25. Shear walls configuration considered in the parametric analysis: (a) 1:1 aspect ratio MLSSW from Valdivieso, Guindos, et al. (2023), (b) bare strong shear wall with continuous rod system fromEstrella, Malek, et al. (2021); bare strong shear wall with conventional hold-down of (c) 1:2 aspect ratio, (d) 1:1 aspect ratio and (e) 1:0.7 aspect ratio from Guinez et al. (2019). Units in millimeters (1 mm = 0.039 in)

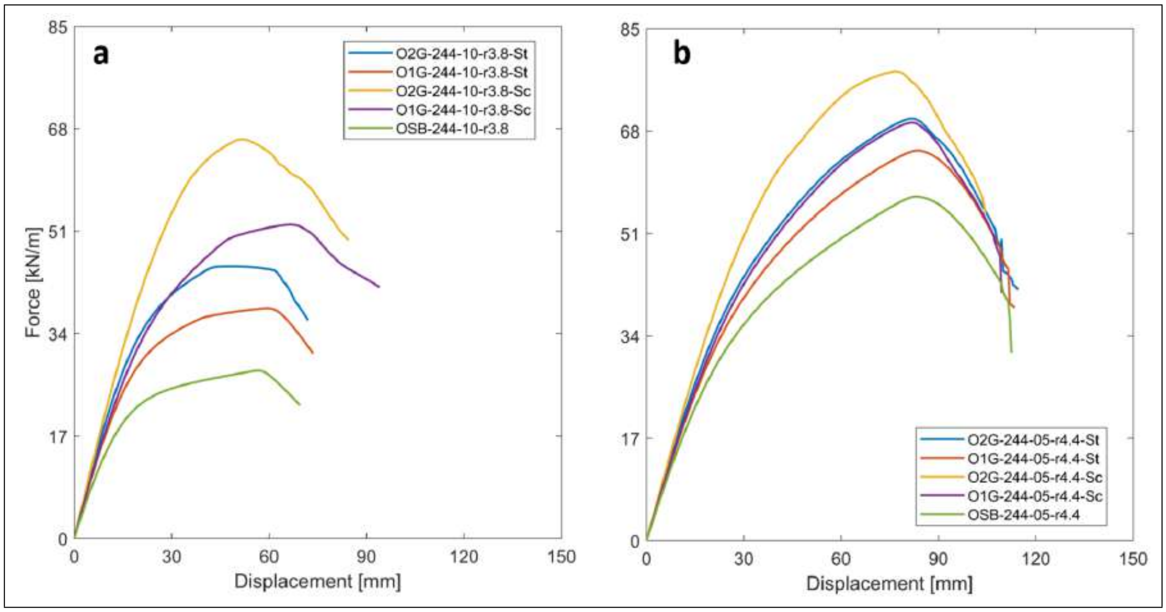

Figure 5.26. Monotonic response comparison of the evaluated wall groups (a) *A* and (b) *B* (group type as per Table 5.9). (1 mm = 0.039 in; 1 kN = 224.8 lbf)

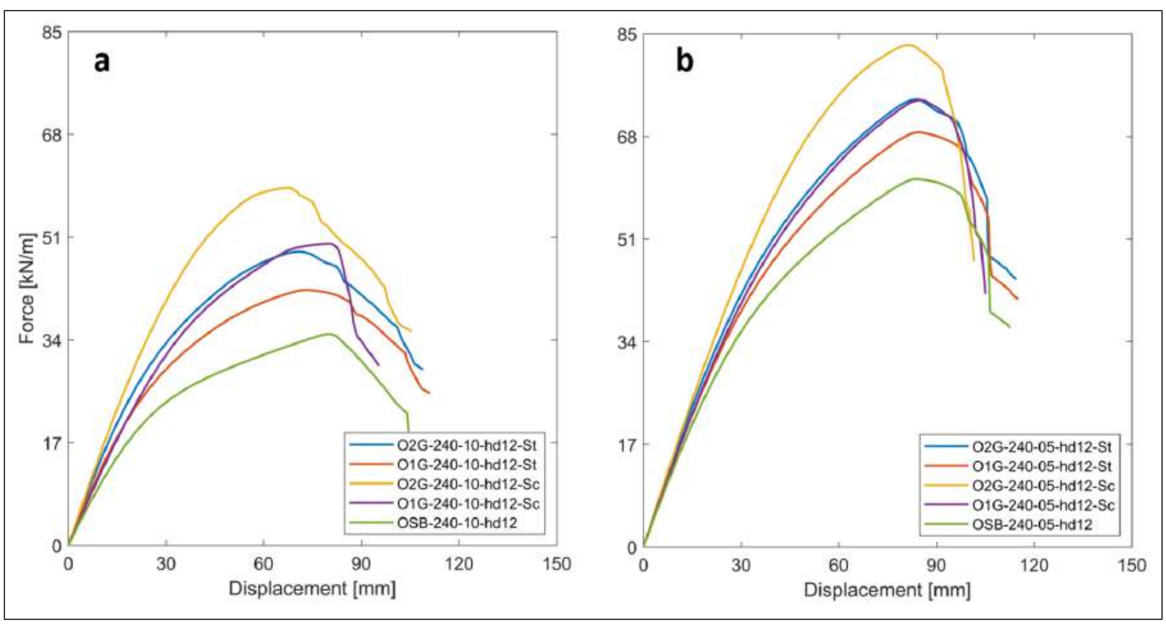

Figure 5.27. Monotonic response comparison of the evaluated wall groups (a) *C* and (b) *D* (group type as per Table 5.9). (1 mm = 0.039 in; 1 kN = 224.8 lbf)

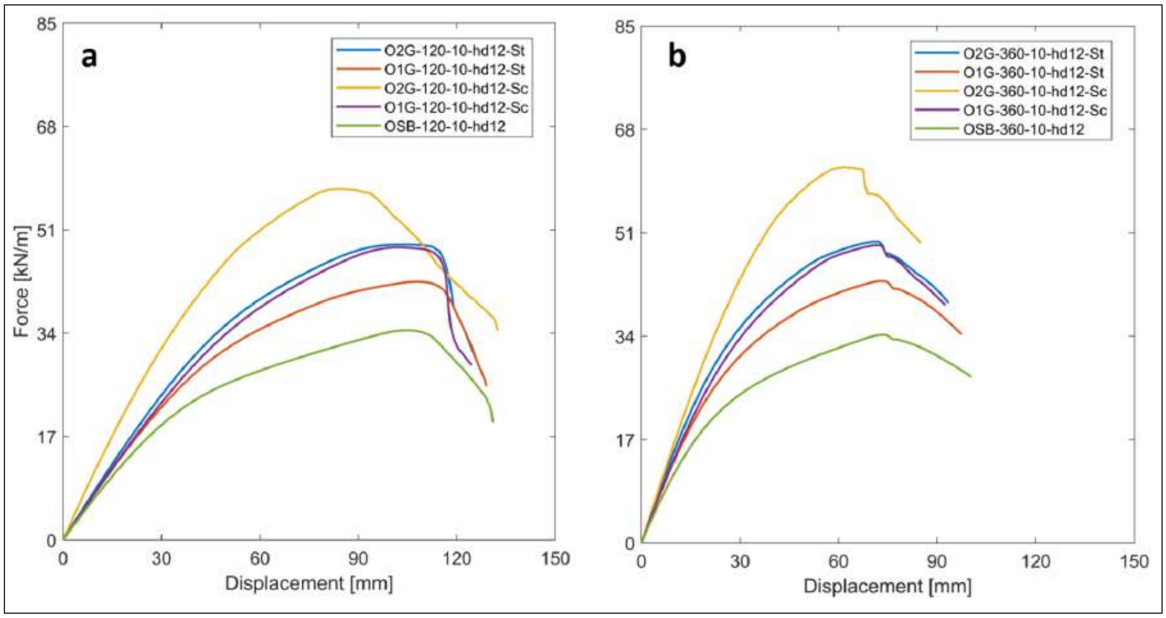

Figure 5.28. Monotonic response comparison of the evaluated wall groups (a) *E* and (b) *F* (group type as per Table 5.9). (1 mm = 0.039 in; 1 kN = 224.8 lbf)

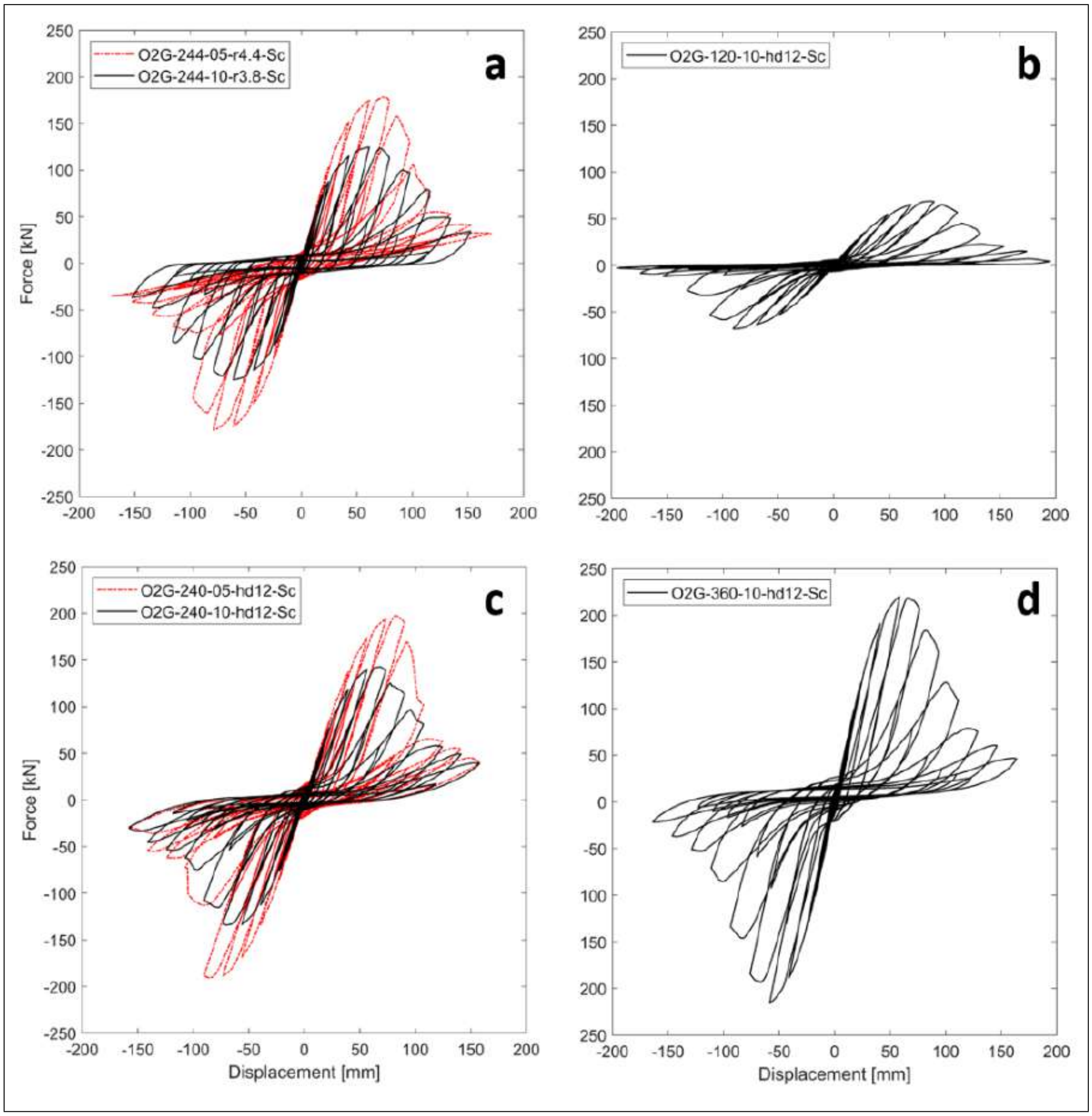

Figure 5.29. Example of the numerical cyclic response of MLSSW with screwed connections and two Type X GWB layers: (a) *O2G-244-10-r3.8-Sc* and *O2G-244-05-r4.4-Sc*; (b) *O2G-120-10-hd12-Sc*; (c) *O2G-240-10-hd12-Sc* and *O2G-240-05-hd12-Sc*; and (d) *O2G-360-10-hd12-Sc*. (1 mm = 0.039 in; 1 kN = 224.8 lbf)

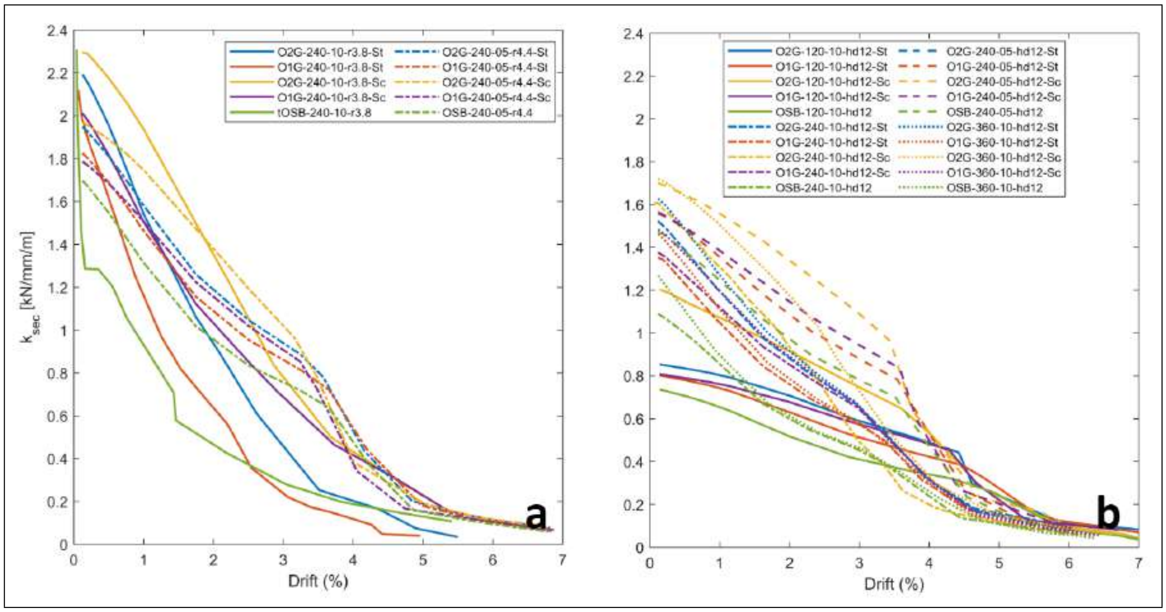

Figure 5.30. Secant stiffness degradation as a function of the lateral drift for wall groups: (a) *A* and *B*, and, (b) *C* to *F* (group type as per Table 5.9). (1 kN/mm = 68.5 klf)

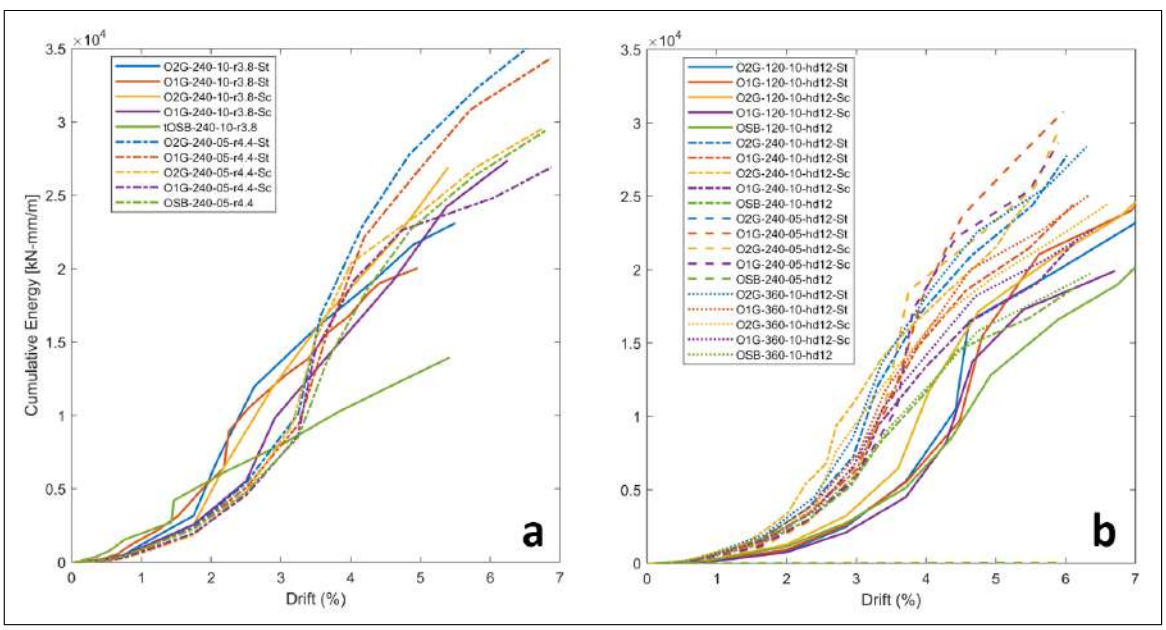

Figure 5.31. Cumulative dissipated energy as a function of the lateral drift for wall groups: (a) *A* and *B*, and, (b) *C* to *F* (group type as per Table 5.9). (1kN-mm = 0.738 lbf-ft)

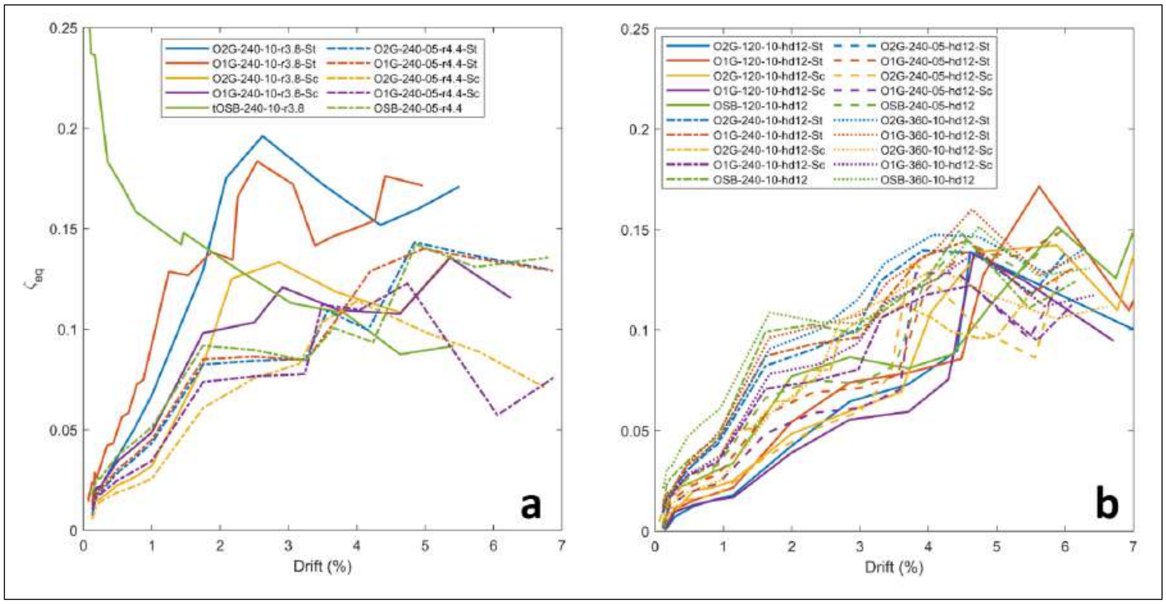

Figure 5.32. Evolution of the equivalent viscous damping as a function of the lateral drift for wall groups: (a) *A* and *B*, and, (b) *C* to *F* (group type as per Table 5.9).

5.7. Supplemental Material - Tables

Table 5.6. Engineering parameters from monotonic connection-level test results

Test Group	K_e [kN/mm]	Δ_y [mm]	F_y [kN]	Δ_u [mm]	F_u [kN]	F_{peak} [kN]
OSB-N[a]	0.90	1.9	1.7	31.5	1.5	1.9
OSB(1)GWB-Sc[a]	0.90	2.2	1.9	17.1	1.8	2.3
OSB(1)GWB-St	0.83	1.0	0.9	11.0	0.8	1.0
OSB(2)GWB-Sc[a]	1.89	1.0	1.9	14.4	1.9	2.3
OSB(2)GWB-St	0.51	1.9	1.0	16.6	0.9	1.1

[a] Repeated from (Valdivieso, Guindos, et al., 2023). (1 mm = 0.039 in; 1 kN = 224.8 lbf)

Table 5.7. MSTEW modeling parameters[a]. (1 mm = 0.039 in; 1 kN = 224.8 lbf; 1 kN/mm = 68.5 klf)

Wall Type	K_0 [kN/mm/m]	r_1	r_2	r_3	r_4	F_0 [kN/m]	F_I [kN/m]	Δ_u [mm]	α	β	F_{peak} [kN/m]
OSB-N[b]	1.050	0.020	-0.101	1.189	0.004	0.850	0.090	13.800	0.750	1.100	1.480
OSB(1)GWB-Sc[b]	0.9105	0.085	-0.140	1.010	0.005	0.909	0.0768	7.500	0.450	1.200	1.410
OSB(1)GWB-St	0.8329	0.045	-0.055	1.001	0.001	0.540	0.050	7.100	0.987	1.2092	0.8105
OSB(2)GWB-Sc[b]	1.892	0.050	-0.087	1.250	0.006	1.322	0.120	3.500	0.750	1.250	1.570
OSB(2)GWB-St	1.160	0.025	-0.050	1.180	0.008	0.451	0.090	6.9885	0.860	1.1045	0.6657

[a] K_0 is the initial stiffness of the hysteretic curve, r_1 to r_4 are dimensionless parameters that represent stiffness ratios at different parts of the curve, F_0 and F_I are strength parameters of the hysteretic curve (Folz & Filiatrault, 2004b), and Δ_u is the displacement at peak load. Parameters α ($\alpha > 0$) and β ($\beta > 0$) control the stiffness degradation and energy degradation, respectively.

[b] Taken from (Valdivieso, Guindos, et al., 2023).

Table 5.8. . Engineering parameters from monotonic connection-level test results for evaluating the reinforcement effect. (1 mm = 0.039 in; 1 kN = 224.8 lbf)

Test Group	K_e [kN/mm]	Δ_y [mm]	F_y [kN]	Δ_u [mm]	F_u [kN]	F_{peak} [kN]
rOSB-N	0.72	2.4	1.7	31.5	1.5	1.9
rOSB(1)GWB-Sc	0.90	2.0	1.8	31.1	1.7	2.1
rOSB(2)GWB-N/Sc	5.45	1.1	6.0	28.4	5.4	6.8
rOSB-N/Sc	2.83	2.0	5.7	17.7	5.4	6.8
rOSB-N/Sc-g	2.05	1.7	3.5	18.0	3.3	4.1
OSB(2)GWB-N/Sc-sum	3.42	1.4	4.8	31.5	5.0	6.3

The resulting combination of the previous variables (see Table 5.9) defines a wall-type label described as AAA-BBB-CC-DDDD-EE. The AAA refers to the sheathing layers (i.e., OSB or OyG = OSB + "y" layers of type X GWB). BBB and CC represent the wall width and nail spacing in centimeters, respectively. DDDD indicates the overturning restraint system type (i.e., "ry" for continuous rod system where "y" is the rod diameter in centimeters or "hdy" for a conventional hold-down system where "y" is the connector model). Finally, EE, represents the fastener type for attaching the Type X GWB layers (i.e., Sc for screws and St for staple).

Test data summarized in Table 5.10 are labeled following the same structure of wall types explored in the parametric analysis, but adding a "t" at the beginning referring to "test data".

Table 5.9. Wall types explored in the parametric analysis[a].

Sheathing Type	Fastener Type	Type of overturning restraint system: Continuous Rod (r)		Conventional Hold-down (hd)			
		Wall aspect ratio (width: height) 1:1				1:2	1:0.7
		Nail pattern (mm) 100	50	100	50	100	100
Wall Group		A	B	C	D	E	F
OSB	Nail	OSB-244-10-r3.8	OSB-240-05-r4.4	OSB-240-10-hd12	OSB-240-05-hd12	OSB-120-10-hd12	OSB-360-10-hd12
OSB + 1-layer Type X GWB	Screw	O1G-244-10-r3.8-Sc	O1G-240-05-r4.4-Sc	O1G-240-10-hd12-Sc	O1G-240-05-hd12-Sc	O1G-120-10-hd12-Sc	O1G-360-10-hd12-Sc
	Staple	O1G-244-10-r3.8-St	O1G-240-05-r4.4-St	O1G-240-10-hd12-St	O1G-240-05-hd12-St	O1G-120-10-hd12-St	O1G-360-10-hd12-St
OSB + 2-layers Type X GWB	Screw	O2G-244-10-r3.8-Sc	O2G-240-05-r4.4-Sc	O2G-240-10-hd12-Sc	O2G-240-05-hd12-Sc	O2G-120-10-hd12-Sc	O2G-360-10-hd12-Sc
	Staple	O2G-244-10-r3.8-St	O2G-240-05-r4.4-St	O2G-240-10-hd12-St	O2G-240-05-hd12-St	O2G-120-10-hd12-St	O2G-360-10-hd12-St

[a] Wall-types sheathed at both sides with OSB and one or two Type X GWB layers (i.e., labels start with O1G or O2G) are considered as MLSSW, whereas wall-types sheathed at both sides with only OSB are considered as bare SSW (i.e., label starts with OSB). (1 mm = 0.039 in)

Table 5.10. Summary of the assembly-level test data for validating the numerical model (see Fig. 5.25). (1 mm = 0.039 in).

Wall size (L by H)	Wood Structural Panel			Gypsum Wallboard (GWB)		
	Thickness	Sheathing Nails	Spacing edge/field	Thickness and Type	Wallboard screws[f]	Spacing edge/field
tOSB-244-10-r3.8[a]	11.1	ϕ2.9x80[d]	100/200	None	-	-
tOSB-244-05-r4.4[b]	11.1	ϕ3.0x70[e]	50/100	None	-	-
tO2G-244-10-r3.8-Sc[a]	11.1	ϕ2.9x80[d]	100/200	(2) - 15, Type X	ϕ4.0x63.5 ϕ4.0x76.2	200/300
tOSB-120-10-hd12[c]	11.1	ϕ3.0x70[e]	100/200	None	-	-
tOSB-240-10-hd12[c]	11.1	ϕ3.0x70[e]	100/200	None	-	-
tOSB-240-05-hd12[c]	11.1	ϕ3.0x70[e]	50/100	None	-	-
tOSB-360-10-hd12[c]	11.1	ϕ3.0x70[e]	100/200	None	-	-

[a] Wall framing consisted of 41mm x 185 mm (2x8) C16 Chilean RP (INN, 2014) studs. Overturning restraint provided by ϕ38.1 mm ASTM A193 Grade B7 rods. Further details are in (Valdivieso, Guindos, et al., 2023). (1 mm = 0.039 in)

[b] Wall framing consisted of 35mm x 138 mm (2x6) C16 Chilean RP (INN, 2014) studs. Overturning restraint provided by ϕ44.5 mm rods grade 105. Further details are in (Estrella, Malek, et al., 2021).

[c] Wall framing consisted of 38mm x 138 mm (2x6) C16 Chilean RP (INN, 2014) studs. Overturning restraint provided by conventional hold-down Simpson Strong-Tie HD12. Further details are in (Guinez et al., 2019).

[d] OSB sheathing layer attached to frame with pneumatically driven wire coil spiral nails (80 x 2.9 x 6.5 mm) according to EN14592:2008+A1:2012 (BSI, 2008).

[e] OSB sheathing layer attached to frame with pneumatically driven wire coil common shank nails according to ASTM F1667 (ASTM, 2021).

[f] Type X GWB sheathing first layer attached to frame through the OSB with type "W" screws (63.5 x 4.0 x 8.0 mm). Type X GWB sheathing second layer attached to frame through the 1st Type X GWB and OSB with type "W" screws (76.2 x 4.0 x 8.0 mm). The application of a double layer of Type X GWB is intended to simulate a shear wall that meets a two-hour fire-resistance rating.

Table 5.11. . Engineering parameters from monotonic assembly-level numerical models. (1 mm = 0.039 in; 1 kN = 224.8 lbf; 1 kN/mm = 68.5 klf)

Wall Type	K_e [kN/mm]	Δ_y [mm]	F_y [kN]	Δ_u [mm]	F_u [kN]	μ	F_{peak} [kN]
OSB-244-10-r3.8	3.77	16.3	61.6	69.1	54.4	4.2	68.0
O1G-244-10-r3.8-Sc	4.94	20.6	101.6	72.1	88.2	3.5	110.2
O1G-244-10-r3.8-St	4.45	19.1	84.9	73.7	74.6	3.9	93.2
O2G-244-10-r3.8-Sc	5.24	28.1	146.9	79.4	129.3	2.8	161.6
O2G-244-10-r3.8-St	4.42	25.7	113.5	94.1	101.7	3.7	127.2
OSB-240-05-r4.4	3.58	33.6	120.3	106.0	111.5	3.2	139.4
O1G-240-05-r4.4-Sc	3.99	38.9	155.0	102.4	135.5	2.6	169.4
O1G-240-05-r4.4-St	3.91	35.0	137.0	105.8	126.5	3.0	158.1
O2G-240-05-r4.4-Sc	4.55	37.2	169.6	98.8	152.1	2.7	190.1
O2G-240-05-r4.4-St	4.19	35.5	148.8	103.1	136.8	2.9	171.0
OSB-120-10-hd12	0.81	48.2	39.2	122.7	33.1	2.6	41.4
O1G-120-10-hd12-Sc	0.97	59.6	58.0	118.8	46.6	2.0	58.3
O1G-120-10-hd12-St	0.91	53.8	48.7	122.8	40.8	2.3	51.0
O2G-120-10-hd12-Sc	1.33	59.1	78.5	112.8	55.4	1.9	69.3
O2G-120-10-hd12-St	0.92	61.8	56.8	117.4	46.2	1.9	57.8
OSB-240-10-hd12	2.36	34.9	82.3	94.1	67.1	2.7	83.9
O1G-240-10-hd12-Sc	3.26	37.2	121.4	95.4	93.3	2.6	116.6
O1G-240-10-hd12-St	2.90	35.3	102.3	99.4	81.1	2.8	101.4
O2G-240-10-hd12-Sc	3.59	44.0	157.9	90.1	113.6	2.1	142.0
O2G-240-10-hd12-St	2.77	44.0	122.0	86.8	95.9	2.0	119.8
OSB-240-05-hd12	3.17	40.5	128.4	105.4	117.0	2.6	146.3
O1G-240-05-hd12-Sc	3.43	45.6	156.3	100.7	142.1	2.2	177.6
O1G-240-05-hd12-St	3.40	42.6	144.9	105.7	131.9	2.5	164.9
O2G-240-05-hd12-Sc	3.82	47.2	180.5	97.0	159.6	2.1	199.6
O2G-240-05-hd12-St	3.62	43.2	156.2	104.3	142.4	2.4	177.9
OSB-360-10-hd12	3.98	27.1	107.8	100.2	98.6	3.7	123.2
O1G-360-10-hd12-Sc	5.27	30.1	158.6	93.2	142.8	3.1	178.4
O1G-360-10-hd12-St	4.70	29.2	137.4	97.2	124.1	3.3	155.1
O2G-360-10-hd12-Sc	5.78	34.7	200.6	84.8	177.9	2.5	222.4
O2G-360-10-hd12-St	4.82	32.4	156.2	92.3	141.1	2.9	176.4

6. CHAPTER 6 - POTENTIAL FOR MITIGATING HURRICANE WIND IMPACT ON INFORMALLY-CONSTRUCTED HOMES IN PUERTO RICO UNDER CURRENT AND FUTURE CLIMATE SCENARIOS

6.1. Introduction

In 2023, the U.S. experienced 28 distinct weather and climate-related disasters that incurred costs of at least $1 billion, a record-breaking number (NOAA National Centers for Environmental Information (NCEI), 2024). Hurricanes (also known as typhoons and cyclones in other parts of the world), have been a major contributor to the economic impact of climate-related hazard events in the U.S., accounting for about 52% of the total costs since 1980 (NOAA National Centers for Environmental Information (NCEI), 2024). These climate-related events have a disproportionate impact on communities with limited resources (Dorkenoo et al., 2022). These effects can be even more significant in places like Puerto Rico where a significant segment of the population resides in informally-constructed housing (Acevedo, 2019; Rivera-Crespo & Colón Rodríguez, 2021). The destruction of homes has a profound and lasting impact on community recovery (Peacock et al., 2018; Rivera-Crespo & Colón Rodríguez, 2021). With the projected escalation of hurricane threats due to global climate change (Mudd et al., 2014b; Bhowmik et al., 2023), addressing the vulnerabilities of these communities in regions prone to hazards is crucial for fostering community resilience and reducing the impacts of future disasters. Employing interdisciplinary and participatory methods that involve communities in the hazard evaluation, mitigation, and recovery planning is vital (Hinojosa & Meléndez, 2018).

Here, we use the term "informally-constructed" to refer to housing erected by builders without formal training or by residents themselves, often with the assistance of friends and family. This form of construction stems from households' efforts to address personal housing needs within the constraints of available resources and local building practices; this construction is typically done without explicit alignment with building code standards and regulations (Algoed & Hernandez Torrales, 2019; Feliciano et al., 2022; Goldwyn et al., 2023). As a result of this process, the risk perceptions of the inhabitants, their construction knowledge, preferences and needs, and available resources play a pivotal role in shaping design and construction decisions, which in turn can either reduce or intensify the potential damage to the housing, impacting the resilience of the community (Cruzado & Pacheco-Crosetti, 2018; Rivera-Crespo & Colón Rodríguez, 2021; Goldwyn, Javernick-Will, & Liel, 2022; Talbot et al., 2022; Goldwyn et al., 2023). Puerto Rico's diverse array of housing types and construction techniques contributes to varying degrees of vulnerability to houses (Rivera-Crespo & Colón Rodríguez, 2021; Talbot et al., 2022).

Over the past three decades, Puerto Rico —a U.S. Caribbean archipelago with an estimated population of more than 3 million in 2023—has experienced several catastrophic hurricanes, including Hugo, George, Irma, and Maria. These hurricanes caused extensive damage to millions of homes (see Figure 6.1), and major disruption to everyday life (Partners, 2019; Rivera-Crespo & Colón Rodríguez, 2021). Hurricane Fiona, which occurred in September 2022, caused significant flooding, disrupting infrastructure and transportation connectivity, as well as damaging thousands of homes. Hurricane Fiona exacerbated the situation in communities still in the process of recovering from Hurricane Maria in 2017. Typical housing typologies in Puerto Rico include light-frame timber houses with corrugated metal panels as roof envelopes, which are particularly vulnerable to hurricane winds (FEMA Mitigation Assessment Team (MAT), 2018). Like housing construction, post-hurricane recovery and construction efforts in Puerto Rico, and many resource-limited communities, are often informally-constructed, and predominantly self-initiated and funded by homeowners (Opdyke et al., 2021; García, 2022; Talbot et al., 2022). The development of resilient housing needs to account for hazards like hurricanes, as well as the political and socioeconomic context, by advocating for sustainable, affordable, accessible, adaptable, and flexible housing through participatory, community-based design (Rivera-Crespo & Colón Rodríguez, 2021; Kuś et al., 2024).

This study assesses the hurricane wind performance of informally-constructed light-frame timber houses in hurricane scenarios, with a specific focus on the typical informal construction styles found in Puerto Rico, examining the extent to which possible mitigation strategies can improve this performance. We assess the housing performance using a component-based static wind assessment procedure that considers local materials and building practices and the uncertainties therein. Hurricane performance is quantified by wind structural fragility curves and the calculation of failure probabilities for both baseline and mitigated light-frame timber house typologies. These failure probabilities are compared to target consensus threshold values in the ASCE 7 Standard (ASCE, 2022), which is the basis of current building codes in the U.S. Furthermore, the paper assesses the implications of climate change on residential structures by revising hazard demands to account for potential increases in hurricane force winds in the Caribbean. Finally, in the interest of contributing to improved construction practices, we present recommended mitigation measures to informal contractors building housing in Puerto Rico and investigate their feasibility with local stakeholders.

6.2. Points of Departure

Residential light-frame timber houses, comprising about 90% of U.S. housing (Ellingwood et al., 2004), account for most of the economic losses from hurricanes, with an average annual cost of $5.4 billion in the U.S. (Li & Ellingwood, 2009). These losses have been increasing because of the growing coastal population, driven by migration towards the coast and urbanization, and due to climate change (Snaiki & Parida, 2023). During hurricanes, the most vulnerable component of a light-frame timber house is typically its envelope. Damage to the envelope can result in additional harm to the interior of the building from wind and precipitation (Ellingwood et al., 2004; Vickery, Quayyum, et al., 2023). Typical failure modes observed in the envelope are the uplift of roof panels, failures in the connections between the roof and walls due to uplift, and the breaking of windows and doors because of intense wind pressures or debris impact (Li & Ellingwood, 2009). Similarly, based on the vulnerability of Australian houses from the 1960s and 1970s to cyclonic winds, Henderson and Ginger (2007) found that the majority of damage occurs in roof cladding, but that the roof structure itself is also critical. Another study, focused on semi-engineered housing designs implemented post-Typhoon Yolanda in the Philippines

(Venable et al., 2021), identified initial roof panel losses due to panel or purlin connection failures as the critical failure mode, and found some houses exhibiting structural collapse from racking failures in wood and bamboo walls, worsened by roof reinforcements that inadvertently increased vulnerability.

Extensive research has been conducted on the response of residential structures in the U.S. to hurricane and tornado winds, using component-based performance-based wind engineering approaches (e.g., Ellingwood and Tekie (1999); Ellingwood et al. (2004); Lee and Rosowsky (2005); Li and Ellingwood (2006, 2009); van de Lindt and Dao (2009); Amini and van de Lindt (2014); Stoner and Pang (2021)). These studies typically rely on established literature to quantify the capacities and demands of the key components and define performance limit states used to construct structural fragility curves. These curves, incorporating elements like the roof envelope, roof-to-wall connection, and shear walls, represent the probability of failing performance states of interest.

Some of the past work has also assessed the performance of light-frame timber houses against certain established thresholds for performance, mostly showing that performance goals may not be met. For example, Stoner and Pang (2021) explored established thresholds for acceptable failure probabilities under tornado loads, referencing threshold failure probabilities in standards such as ASCE 7, the Eurocode, and the Netherlands. ASCE 7 (ASCE, 2022), which is relevant for this paper because it applies to U.S. construction, sets its target annual failure probability at 3.0 x 10^{-5} per year. However, Stoner and Pang (2021) find that residential light-frame timber housing design in 60% of the U.S. area would fail to meet the ASCE 7 (ASCE, 2022) threshold for tornados following current practice. They argue that reconsideration of the acceptable target probabilities may be appropriate. To assess the reliability of low-rise light-frame timber houses in hurricane-prone areas of the U.S., Li and Ellingwood (2006) developed a probabilistic framework, incorporating both structural fragility models and hurricane wind hazard models. They look specifically at one-story single-family light-frame timber houses and roof panel uplift failure, roof-to-wall connection failure due to uplift, and breakage of windows and doors under excessive wind pressure as limit states. From their results, we infer that the thresholds for roof-to-wall connection (i.e., life safety) do not meet ASCE 7 (ASCE, 2022) in most of the evaluated cases for both toe-nail and hurricane strap connection types. Expanding on prior research (e.g., Ellingwood et al. (2004); Lee and Rosowsky (2005)), van de Lindt and Dao (2009) introduced a performance-based wind engineering framework in order to enhance the performance of light-frame timber houses under hurricane winds. This methodology for the first time incorporates fragility analysis to assess four clearly-defined performance levels: occupant comfort, continued occupancy, life safety, and collapse prevention. The intent of their approach is to assist in directing the design of buildings to reduce post-hurricane losses to defined limits.

In Puerto Rico, envelope-related failure modes have been commonly observed in light-frame timber houses during recent hurricanes (FEMA Mitigation Assessment Team (MAT), 2018; Severino et al., 2018; Vickery, Quayyum, et al., 2023), as depicted in Figure 1. Window failures are less likely due to the use of jalousie-type windows. In addition, some wall lateral and sliding failures have been observed in past hurricanes in Puerto Rico. Of these shear wall failures, the predominant failure is the lateral failure due to the shear failure of the OSB or plywood sheathing-to-wood frame connection.

There have been a few studies that examine the hurricane performance of informally-constructed houses in Puerto Rico. For instance, Lochhead et al. (2022) found that the typical governing failure mode is roof panel loss due to tear-through at the fasteners used for attaching the corrugated metal panels to the roof structure. If this failure mode is avoided, failures at the purlin-to-truss connections and of the roof-to-wall connections also occur. To mitigate these issues, Lochhead et al. (2022) suggested two main strategies: enhancing the attachment of corrugated metal panels to the roof structure and the installation of hurricane straps at critical connections. Using the Hazus Hurricane Model, Vickery, Quayyum, et al. (2023) further showed that utilizing hurricane straps instead of toe-nails for the roof-to-wall connection and appropriate screws instead of nails for securing the corrugated metal panels to purlins lead to a significant reduction in annualized average hurricane losses. However, the studies by Lochhead et al. (2022) and by Vickery, Quayyum, et al. (2023) faced limitations due to the absence of connection-level test data for these mitigation measures, leading to approximations in the typologies of buildings considered and the failure analysis. Further, Lochhead et al. (2022) did not account for the implications of progressive failure and load redistribution as per Stewart et al. (2016), which are crucial for a more accurate assessment of structural failure. Moreover, our field work revealed that some proposed improvements for purlin-to-truss connections were not feasible at construction sites due to space restrictions. Thus, further research is needed in developing fragility curves considering performance levels for Puerto Rican informally-constructed house typologies, demonstrating the effectiveness of locally feasibility mitigation measures for improving performance.

Figure 6.1. (a) Typical undamaged Puerto Rican informally-constructed timber house [Photo from Polly Murray] and failure modes observed in housing structures in Puerto Rico from 2017's Hurricane Maria: (b) roof envelope damages; (c, d) failures in roof-to-wall connections; (e, f) rain intrusion damage due to roof envelope failure; and (g, h) shear wall failures and sliding. [Photos from Emily Alfred]

6.3. Hurricane Wind Performance Assessment

The performance of both baseline and mitigated housing typologies, defined below, was evaluated using a component-based performance-based wind engineering approach.

6.3.1. Wind Demands

The wind loads acting on structures were computed using the ASCE 7 (ASCE, 2022) methods and wind pressures for low-rise buildings, consistent with the approach taken by Li and Ellingwood (2006); Martin et al. (2011); Lochhead et al. (2022) and others. We use the 3-second wind speed gust, referred to as velocity, V, as intensity measure representing wind severity. The velocity is measured in miles per hour (mph), where 1 mph equals 0.447 meters per second (mps). From the velocity, we compute the velocity pressure at the average roof height, q_h, as detailed by Equation 6.1. In Eqn 6.1, q_h is in pounds per square foot or psf (1 psf = 47.88 N/m2).

$$q_h = 0.00256 K_z K_{zt} K_e V^2 \tag{6.1}$$

In Equation 6.1, K_z is the velocity pressure exposure coefficient, K_{zt} is the topographic factor and, K_e represents the ground elevation factor. The value of K_z is determined based on the structure's height and its exposure classification. Our assessment was primarily location-independent, due to the similar housing forms across the island. As such, we initially used a topography factor of 1.0 for computing wind structural fragility curves. However, to account for the acceleration effect caused by complex topography, such as hilly or mountainous landscapes, we considered topographic effects on the wind hazard, as outlined by Vickery, Liu, and Lin (2023) for Puerto Rico. The values used to define the wind demands are provided in Table 6.1.

From the velocity pressure at the average roof height, we determine the wind pressures, W, on the components of the houses, as outlined in Equation 2.

$$W = q_h K_d (GC_{pf} - GC_{pi}) \tag{6.2}$$

In this equation, K_d is the directionality factor, G is the gust factor, C_{pf} denotes the external pressure coefficient, and C_{pi} is the internal pressure coefficient. Pressure coefficients from Chapter 28 (Main Wind Force Resisting System–Envelope Procedure) were applied for shear walls and roof-to-wall connections and from Chapter 30 (Components and Cladding) for panels, fasteners, and purlin-to-truss connections (ASCE, 2022).

Table 6.1. Parameter values defining wind demands

Variable	Mean Value	Coefficient of Variation	Distribution Type	Data Source
K_z	by structure	0.14	Normal	Amani and van de Lindt (2014)
K_{zt}	1; by location	Deterministic	-	ASCE (2022); Vickery, Liu, and Lin (2023)
K_d	0.85	Deterministic	-	ASCE (2022); Stoner and Pang (2020)
K_e	1.0	Deterministic	-	ASCE (2022); Stoner and Pang (2020)
GC_pf	by panel	0.12	Normal	Amini and van de Lindt (2014)
GC_{pi}	0.55 (partially enclosed)	0.33	Normal	ASCE (2022); Lee and Rosowsky (2005)
Dead load	by component	0.10	Normal	ASCE (2022); Lee and Rosowsky (2005)

Finally, these wind pressures are used to determine through structural analysis the wind uplift forces on the roof panels and components and shear forces in the lateral force resisting system, considering the compensating effects of dead loads. As components failed, the wind uplift forces were modified to account for load redistribution. This redistribution has two aspects: 1) reduction in internal pressures with loss of components of the roof envelope, in this case corrugated metal panels, thereby reducing loads on the remaining components; and 2) redistribution of loads from a failed component to other nearby components in the load path. To account for the redistribution, the wind pressure calculations for the components of the light-frame timber houses were refined by adapting a methodology developed by Stewart et al. (2016), which was based on Henderson and Ginger (2011)'s and Konthesingha et al. (2015)'s experimental results. Initially intended for industrial buildings, this procedure has been adapted here for light-frame timber houses. The approach we used (shown in Figure 6.2a) was generated by starting with an initial C_{pi} value of 0.55 instead of 0.65, as suggested by the curve from Stewart et al. (2016), for the scenario of zero panels failing. This modification was made to establish an initial C_{pi} that is consistent with ASCE 7 pressure coefficients (ASCE, 2022). The negative constant C_{pi} for the scenario of four or more panels failing was then scaled by a factor of 0.55/0.65 = 0.85 times the Stewart et al. (2016) model. To account for the load redistribution, when a component fails, the load is redistributed to neighboring components, as depicted in Figure 6.2b. This redistribution is based on static analysis.

6.3.2. Components and Component Capacities

The wind loads are used to determine whether the components of interest, namely fasteners, roof panels, rafters, purlins, roof trusses, roof-to-wall connections, and/or shear walls have failed, by comparing the demand and capacity. These components are considered because they are linked to specific hurricane failure modes of housing that have been observed in Puerto Rico and elsewhere. To determine the component capacities (defined in Table 6.2), we built on Lochhead et al. (2022) and sourced data on component capacities from the existing literature. In addition, we conducted additional tests to refine

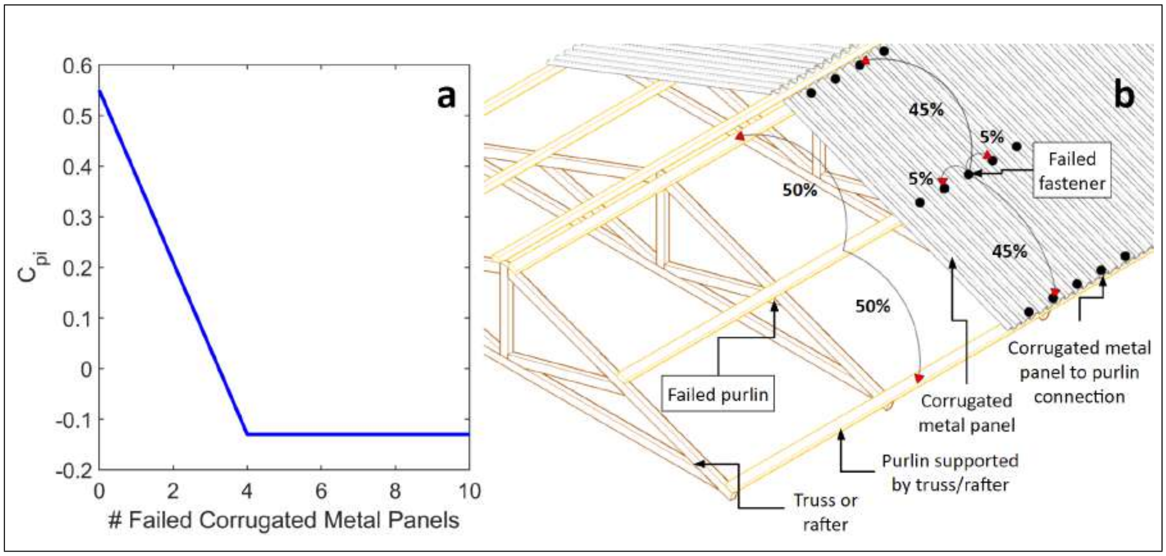

Figure 6.2. Implemented methodology for (a) reducing the internal pressure coefficient, C_{pi}, in response to failed corrugated metal panels in roof envelope, and (b) redistributing load on corrugated metal panels-to-purlins connections and purlins after failure of a purlin or fastener. The model in (a) is adapted from Stewart et al. (2016).

the capacities used for hurricane straps with different fastener arrangements (see Figure 6.3). We also gathered test results provided by Simpson Strong-Tie, to characterize the capacities of the hurricane straps with other fastener arrangements and screwed roof-to-wall and purlin-to-truss (or rafter) connections. Simpson Strong-Tie is the leading supplier of hurricane straps in the region.

6.3.3. Performance Assessments

The outcome of this study is an assessment of hurricane performance for baseline and mitigated housing typologies, represented by a set of fragility curves and, subsequently, an assessment of the annual probability of failure, which can be compared to target risk levels in established codes and standards.

Table 6.2. Parameter values defining component capacities[a]

Variable	Component	Mean Value	Coefficient of Variation	Distribution Type	Data Source
Wood strength	Bending Shear	F_b = 7.2 ksi F_s = 0.9 ksi	0.16 0.15	Normal Truncated[g]	ASTM (2006)
Corrugated metal panel to purlin connections[b,c]	by limit state		0.40-0.25	Normal Truncated[g]	Tear-out capacity (Mahendran & Tang, 1999); Pull-out capacity (Thurton et al., 2013), COV (Li and Ellingwood (2006) Stewart et al. (2018));
Purlin-to-truss[d] connections	Cleat	by calculation	0.40	Normal Truncated[g]	AWC (2018)
	SDWS22500[e]	0.5 kip	0.10		test data provided by Simpson Strong-Tie
Roof-to-wall connections	Toe-nailed	0.3 kip	0.30	Normal Truncated[g]	Cheng (2004)
	Hurricane Strap	1.7 kip	0.10		Test data from authors (Figure 6.3) and/or provided by Simpson Strong-Tie
	SDWC15600[f]	1.9 kip			Test data provided by Simpson Strong-Tie
Shear wall Strength	Baseline case (Table 6.5)	0.16 klf	0.12	Normal Truncated[g]	Test data as per report N-191 Vasquez et al. (2012), Doudak and Smith (2009)
	Mitigated case (Table 6.5)	0.90 klf			AWC (2021), Valdivieso, Guindos, et al. (2023)

[a] Unit conversion: 1 ksi = 6.895 MPa; 1 kip = 4.448 kN; 1 klf = 14.594 kN/m

[b] Our assumption considered the likelihood of improper fastener installation during construction. Specifically, we estimated that around 3% of all fasteners might not align correctly with the purlin, thereby diminishing their capacity. Following Stewart et al. (2018), we modeled this scenario using a triangular distribution, where a misaligned fastener has a mean capacity 80% lower than a correctly installed fastener.

[c] The failure of corrugated metal panel-to-purlin connections is contingent upon assessing the uplift limit state, which is based on the tear-out and pull-out capacity of the connection.

[d] This also applies to purlin-to-rafter connections.

[e] Timber screw with a 0.22 in (5.6 mm) shank diameter, 5 in (127.0 mm) in total length, and 3 in (76.2 mm) of thread length.

[f] Fully-threaded screw with a shank diameter of 0.155 in (3.9 mm) and a length of 6 in (152.4 mm).

[g] To prevent negative values in component capacity, a normal truncated distribution was employed, which cuts off at zero capacity, while maintaining a valid probability density function.

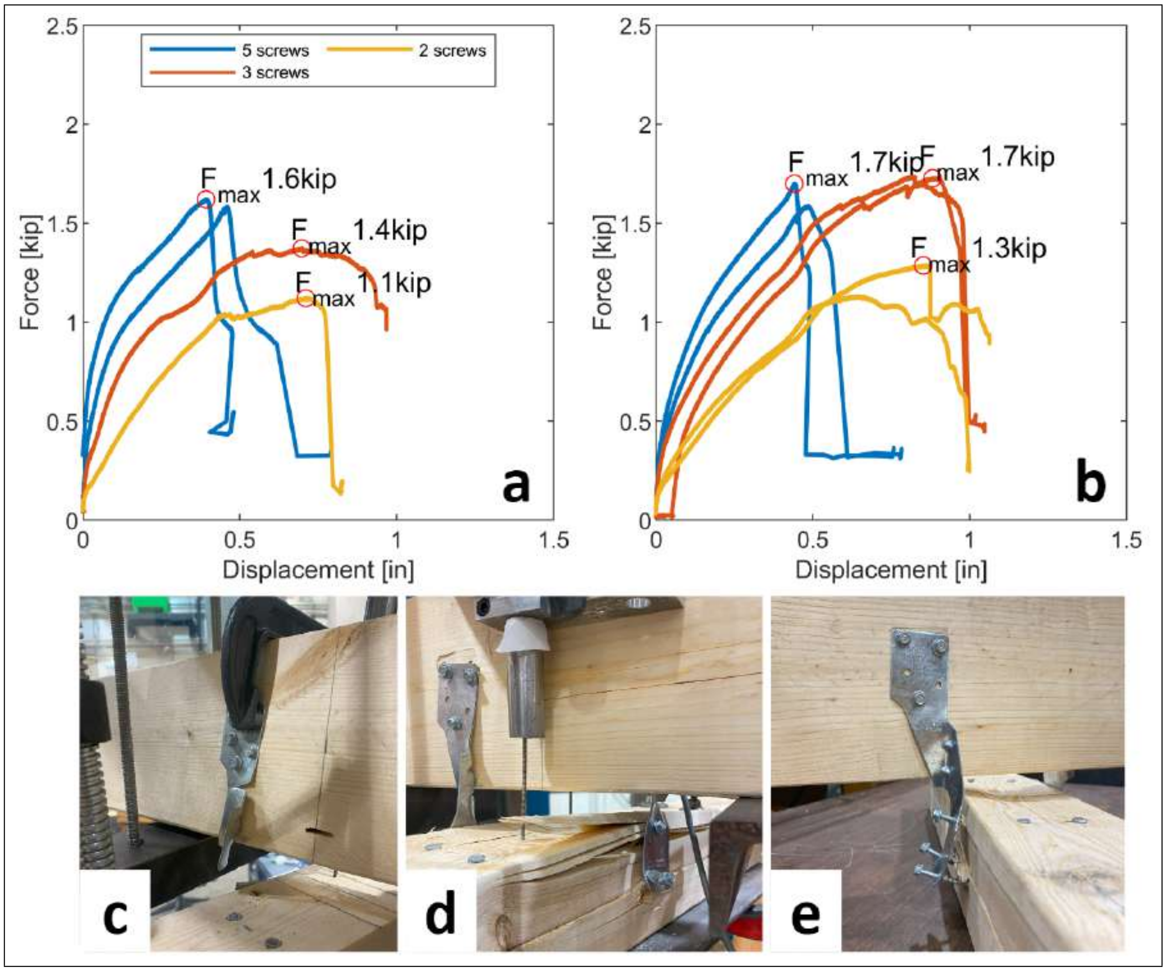

Figure 6.3. Monotonic uplift test results used to define the component capacities for hurricane straps used at roof-to-wall connections: with (a) SD screws as recommended by Simpson Strong-Tie and (b) Gripe Rite brand screws, which are commonly found in Puerto Rican hardware stores. These tests also identify the various failure modes in the uplift tests of hurricane straps, including (c) tensile failure of the connector, (d) plate splitting, and (e) screw pull-out. Unit conversion: 1 kip = 4.448 kN; 1 in = 25.4 mm

6.3.3.1. Performance Levels of Interest

Table 6.3 details the performance levels considered for evaluating the response of informally-constructed light-frame timber houses in Puerto Rico. These levels quantify

Roof Envelope, *Roof Structure*, and *Shear Wall* performance (see Figure 6.4). Their definition was informed by definitions in Vickery et al. (2006) and van de Lindt and Dao (2009). For example, the *Roof Envelope* failure impedes continued occupancy because it induces water intrusion in the house. This failure mode occurs if there is loss of 4 or more roof panels. The *Roof Structure* failure is taken as a failure of life safety because it causes the entire detachment of the roof from the shear walls, and the *Shear Wall* failure is a failure of collapse prevention because it causes the entire collapse of the house.

Figure 6.4. Damage photos showing (a) roof envelope, (b) roof-to-wall connection, and (c) shear wall failure modes after Hurricane Maria (2017). [Photos from Emily Alfred]

6.3.3.2. Wind Fragility Curves

The wind fragility curves represent the probability of exceeding a specified performance level (i.e., failure of that performance level), as a function of wind speed. We employed a Monte Carlo simulation approach to incorporate uncertainties in wind loads and component capacities in the development of the fragility curve. Tables 6.1 and 6.2 identify the load and capacity parameters treated as uncertain, respectively. The key uncertain variables on the loading side are GC_{pf}, GC_{pi} and K_z, based on the work by Lee and Rosowsky (2005). Other variables, i.e. K_d and K_e, are less influential and are therefore treated deterministically. For the capacities, the key uncertain variables are roof envelope-to-purlin connection capacities, roof-to-wall connection capacities, and shear walls strengths as they highly influence the defined performance levels (see Table 6.3).

For each structure of interest, the analysis was repeated at multiple wind speeds, with each wind speed associated with 500 realizations of the load and resistance variables, generated independently. We verified that 500 realizations were sufficient to yield stable values for the annual probability of failure. In each realization, the failure mechanisms associated with each performance level are assessed. For a performance level encompassing multiple criteria or sub-criteria, the occurrence of any one of these is sufficient to constitute a failure at that performance level. Subsequently, the instances of failure at each wind speed are tallied and normalized by the total number of simulations (i.e., 500) to calculate the failure probability for each performance level.

Table 6.3. Definition of the performance levels and failure criteria

Performance Level	Associated Failure Mode	Component-Specific Mechanism	Criteria[a]	Sub-criteria[a]
Roof Envelope (Continued Occupancy)	Loss of 4 or more roof panels[b]	Failure of panel-to-purlin connection (fastener pullout or panel tear-out)	A minimum of two panel-to-purlin connections, or ten percent of the panel-to-purlin connections, whichever is higher[c]	-
		or		
		Failure of purlin at the edge of the panel[c]	Shear or bending failure of purlin material	-
			or	
			Failure of all purlin-to-truss[d] connections at edge purlin	Failure of the connection (i.e., connector or fastener) or shear/bending failure of the connected truss/rafter material
Roof Structure (Life Safety)	Loss of uplift capacity of the roof	Failure of 3 or more roof to wall connections	Uplift failure of roof to wall connection	-
Shear Wall (Structural Integrity)	Loss of shear wall lateral capacity	Failure of at least one shear wall line	Lateral failure of the shear wall line	-

[a] For a criterion or sub-criterion that encompasses multiple possibilities, the fulfillment of any one criterion is sufficient to classify the performance level as failed.

[b] Following damage state 1 for roof cover failure, as per Vickery et al. (2006).

[c] Lochhead et al. (2022) assumed that the failure of a purlin at the edge of the roof is sufficient to engage the failure of the associated corrugated metal panel. This assumption is founded on engineering principles and the understanding that failure at the edge of the corrugated metal panel could lead to excessive uplift, thereby precipitating its failure.

[d] This criterion also applies to purlin-to-rafter connections.

[e] Previous research has highlighted the challenge in setting performance expectations (van de Lindt & Dao, 2009). In this study, we argue that the failure of three or more roof-to-wall connections is sufficient to jeopardize the entire roof's attachment to the wall. This assertion is based on observations that the fragility curve remains constant beyond this threshold of three failed connections.

6.3.3.3. Roof Failure Probabilities

The annual probability of failure, Pf,1, for the light-frame timber house typologies represents the annual probability of failure of the structure, considering the wind hazard curves and the fragilities. The calculated annual probability of failure for specific locations, focusing on the Roof Structure performance level (i.e., life safety), is evaluated against the threshold stated in Table 1.3-1 of ASCE 7 (ASCE, 2022) for Risk Category II buildings $P_{f,1}$ of 3.0 x 10^{-5} per year. This comparison is based on a failure scenario that is not abrupt and does not lead to extensive progressive damage. Risk Category II buildings include residential, office buildings, and commercial structures not designated as essential facilities.

The calculation for the annual probability of failure is based on a Poisson distribution model. This model calculates the mean annual probability of exceedance, λ_f, by convolving the hazard curve with the fragility curves as in Equation 6.3:

$$\lambda_f = \sum_{i=1}^{N} P(F|v_i) \left| \frac{d\lambda(v_i)}{dv_i} \right| \Delta v_i \tag{6.3}$$

where $P(F|v_i)$ represents the fragility curve, i.e., the probability of failure for a specific performance level at a given wind speed v_i. Here, $\lambda(v_i)$, denotes the annual probability of exceedance associated with the hazard curve at any given wind speed v_i. The annual probability of failure is calculated following Equation 6.4.

$$P_{f,1} = 1 - \exp^{-\lambda_f} \tag{6.4}$$

6.3.3.4. Wind hazard curves: current and future climate

We considered the wind hazard curve at multiple locations across Puerto Rico. The locations are San Juan, Mayagüez, Ponce, Arecibo, Santa Isabel, Guayama, Fajardo, Carolina, and Gurabo, selected based on their representation of diverse damage levels observed after Hurricane Maria in 2017, as reported in Severino et al. (2018). We developed the hazard curve using the ASCE 7 (ASCE, 2022, n.d.) online hazard tool, which reports wind speeds for return periods of 10, 25, 50, 100, 300, 700, 1700, 3000, and 10,000 years. These speeds account for the topographic factor as per Vickery, Liu, and Lin (2023). Subsequently, we fit a Weibull distribution to these data points based on Li and Ellingwood (2006). This distribution was then used to derive the annual probability of exceedance, λ, for wind speeds of interest ranging from 0 mph to 200 mph, as demonstrated in Figure 6.5a for Gurabo, Puerto Rico. This hazard curve is representative of our current climate, considering the historical record (Vickery, Quayyum, et al., 2023). The resultant Weibull distribution for each location is depicted in Figure 6.5b, with the computed Weibull parameters for all locations reported in Table 6.8. The wind hazard is more significant in the eastern coast (i.e., Gurabo) and slightly less in the western coast (i.e., Mayagüez), indicating the geographical variation in hurricane risk exposure across Puerto Rico.

Due to climate change, wind speeds are likely to increase in the North Atlantic Ocean because of increased sea temperatures leading to more frequent tropical storm formation. To incorporate the effects of climate change on the computed hazard curves, we make use of research by Mudd et al. (2014b) and Bhowmik et al. (2023). Mudd et al. (2014b) used the worst-case future climate change scenario from the Intergovernmental Panel on Climate Change (IPCC) fifth assessment report, specifically the high-forcing Representative Concentration Pathway (RCP) 8.5 scenario with 8.5 W/m² radiative forcing by 2100, to quantify expected hazards at the Northeast US coastline, specifically, for New York City. Bhowmik et al. (2023) focused on the sixth IPCC assessment report, adopting the RCP 4.5 scenario, which projects 4.5 W/m² radiative forcing by 2100, to project the hurricane hazard curve for the year 2060. Bhowmik et al. (2023) produces wind hazard curves for a site in South Carolina. The studies similarly show increases in wind speeds for different hurricane return periods, with results indicating a consensus on wind speeds increasing by a factor of 1.2 to 1.4 for a 100-year return period hurricane event. Due to the absence of specific studies for Puerto Rico, scaling factors from these studies for the North Atlantic Ocean were applied to adjust the local hazard curves as an estimate of the range of future climate scenarios. We applied a uniform scaling factor across all locations, though not uniformly across all wind speeds. Instead, we adjusted the scaling factor for each wind speed based on the findings from Mudd et al. (2014b) and Bhowmik et al. (2023). The impact of these scenarios on hurricane hazards, such as in Gurabo, is illustrated in Figure 5a. Table S1 provides the assumed hazard curves considering climate change.

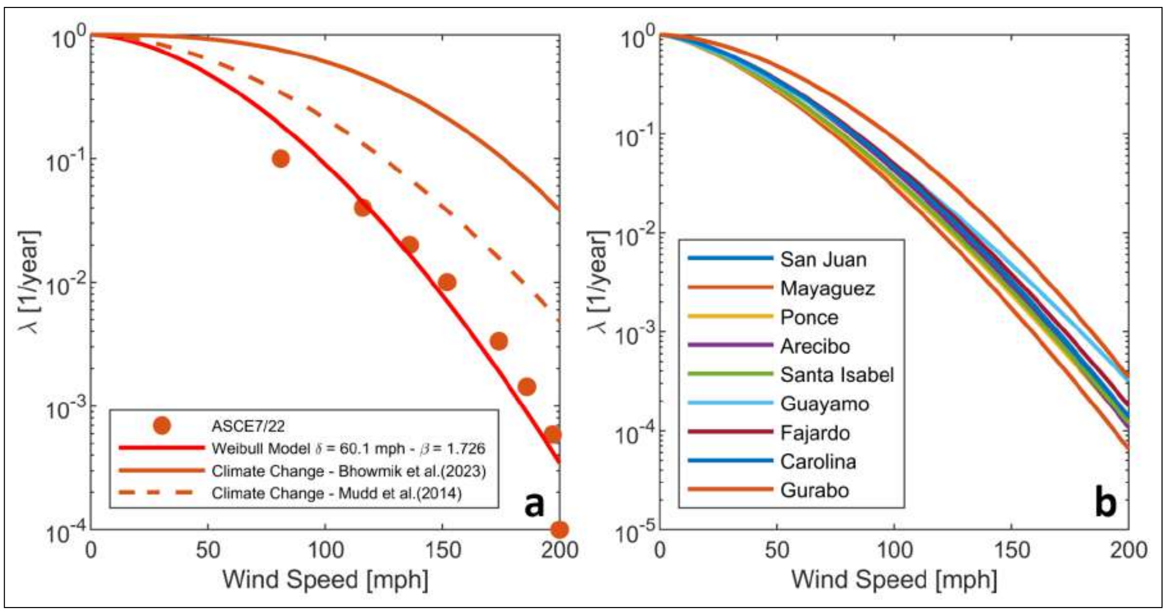

Figure 6.5. Wind hazard curves (a) in Gurabo, showing derivation of the current climate Weibull model, and as adjusted for climate change, and (b) for the current climate in all the considered locations. The locations are mapped in Figure 12. Unit conversion: 1 mph = 0.477 mps.

6.4. Light-frame timber house typologies

We defined typologies of informally-constructed houses based on our field observations and insights shared with us by NGOs involved with post-hurricane reconstruction efforts in Puerto Rico. Our fieldwork consisted of site visits, interviews, a survey, and capacity-building trainings conducted between 2019 and 2023 (Goldwyn et al., 2021; Goldwyn, Javernick-Will, & Liel, 2022; Goldwyn et al., 2023; Murray et al., 2023).

6.4.1. Baseline Typologies

The dimensions of the baseline typologies, outlined in Table 6.4, reflect typical one-story light-frame housing construction in Puerto Rico. The dimensions for the light-frame timber house baseline typology are 16 ft by 24 ft (4.88 m by 7.32 m), with a story height of 8 ft (2.44 m) and a roof slope of 21 degrees. We consider baseline typologies with both gable and hip roof shapes (see Figure 6.6). The roof envelope consists of corrugated metal panels connected to the purlins. The designation of flat 2x4 purlin means that the purlin is installed horizontally, with the wider side lying flat against the truss or rafter, providing a broader surface area for support, but less bending resistance. We found this to be the most common configuration during fieldwork. The roofs extend to 0.5 ft (0.15 m) eaves. The roof structural system is assumed to be wood trusses in most cases, though we also consider a case with rafters for the gable roof. We consider only light-frame timber houses. Even so, the fragility results for Roof Envelope and Roof Structure performance levels are applicable to houses with wood frame roofs and masonry-infilled reinforced concrete frames because the roofs and roof-to-wall connections have the same capacity (based on data on connections used in those situations and statements in Murray et al. (2023) and Vickery, Quayyum, et al. (2023)). However, we did not calculate the fragility curves for the Shear Wall performance level for masonry-infilled reinforced concrete frames due to the lower likelihood wall (lateral) failure. Southern Yellow Pine is assumed for all wood in the roof structures, being the most available local material. All cases are classified as partially enclosed, based on fieldwork observations; windows are typically of the miami or jalousie type.

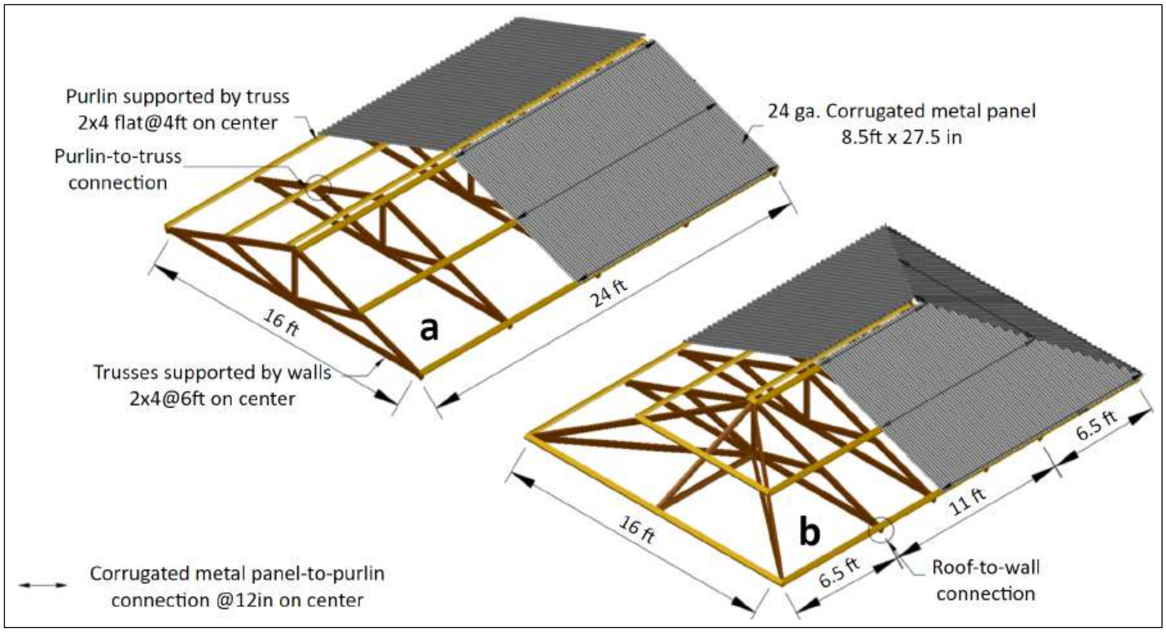

Figure 6.6. Baseline (a) gable and (b) hip roof typologies. Unit conversion: 1 ft = 0.305 m; 1 in = 25.4 mm.

Table 6.4. Baseline typology matrix[a]

Item	Baseline Typology Gable 1	Gable 2	Hip
Roof shape	Gable	Gable	Hip
Roof structure	Wood trusses	Wood rafters	Wood trusses
Shear wall material	2x4 Wood frame studs and 0.5 in plywood sheathing	2x4 Wood frame studs and 0.5 in plywood sheathing	2x4 Wood frame studs and 0.5 in plywood sheathing
Total height	8 ft	8 ft	8ft

[a] Unit conversion: 1 in = 25.4 mm; 1 ft = 0.305 m.

6.4.2. Mitigated Typologies

The mitigation measures proposed in this study draw on findings from surveys previously conducted with those involved in the informal construction industry (described in Goldwyn, Javernick-Will, and Liel (2022)) and focus group conversations with Puerto Rican builders during training exercises (described in Goldwyn et al. (2023)). Surveys of individuals in the construction industry highlighted the significance of mitigating light-frame timber houses, with 89% of respondents anticipating damage or destruction due to hurricane winds. Those respondents expressed a particular concern for reinforcing the roof envelope, showing interest in thicker panels, additional fasteners, or tie-down cables, drawing on their personal experiences from past hurricanes (Goldwyn, Javernick-Will, & Liel, 2022). In relation to hurricane straps and enhancing the roof-to-wall connection, only 45% of respondents identified strengthening this connection as crucial for hurricane mitigation. Despite the widespread availability of hurricane straps in Puerto Rican hardware stores, survey results (Goldwyn, Javernick-Will, & Liel, 2022) and subsequent training sessions (Goldwyn et al., 2023) revealed uncertainty about the choice of fasteners (nails vs. proprietary screws vs. conventional screws) and concerns about the quantity of fasteners needed, especially in terms of its effects on the integrity of the wooden components of the roof. Trainees at capacity-building events explained their confusion with existing catalogs on hurricane straps and other mitigation materials sold at hardware stores, saying “it’s more complicated than it should be” and “it’s not accessible to people” (Goldwyn et al., 2023). In addition, during fieldwork in March and October 2022, we observed several examples of residents and local NGO staff incorrectly installing hurricane straps horizontally (rather than vertically, see labels “a” and “b” in Figure 6.7) at the purlin-to-truss connection due to space limitations. Examples of the training exercise conducted in June 2023 are illustrated in Figure 6.7.

This study proposes incremental mitigation strategies for the roof envelope, roof structure, and shear walls in both existing and new buildings, informed by the previously described survey data from the informal construction sector and dialogues with Puerto Rican builders (Goldwyn, Javernick-Will, & Liel, 2022; Goldwyn et al., 2023), as well as damage observations post-Hurricanes Maria and Fiona (FEMA Mitigation Assessment Team (MAT), 2018; Severino et al., 2018). These mitigation measures are intended to address the interests of the local building community, and to investigate mitigation measures that

Figure 6.7. Observed incorrect installation of hurricane straps at connections between (a) purlins and rafters, and (b) roofs and walls during fieldwork. Collaborative Training and Practical Workshops with two key local NGOs in Puerto Rico focusing on reconstruction efforts after Hurricane Maria. These activities involved direct participation and assessment of proposed mitigation measures for (c) shear walls, as well as (d) hurricane straps and (e) fully-threaded screws for roof-to-wall connections. Other training activities are described in Goldwyn et al. (2023).

are not well understood. Accordingly, the proposed mitigation measures include improving corrugated metal panel-to-purlin connections, roof-to-truss connections, truss/rafter and purlin spacing, purlin-to-truss/rafter connections, corrugated metal panel thickness, and lateral strength of shear walls. Eight enhanced typologies, based on the baseline cases in Table 6.4, are established, each progressively integrating the proposed mitigation measures. Table 6.5 provides detailed descriptions of the proposed mitigation measures, including the specific combinations considered. For instance, in the case of the baseline gable with trusses (referred to as Gable 1 in Table 6.4), applying all mitigation measures to the roof envelope and roof structure (namely, RE) leads to the creation of an improved typology, Gable RE.

Reflecting the reality of informal construction, none of these mitigated typologies explicitly satisfy design loads and criteria of American building standards adopted in Puerto Rico (i.e., in IRC 2018, IBC 2018, ASCE 7). Yet, the fully mitigated case is more consistent with the requirements of these documents, including corrugated metal panels attached to purlins using screws, with purlin spacing not exceeding 2 ft (0.6 m), roof-to-wall connections reinforced with hurricane straps or screws, and shear walls reinforced with sheathing panels at least 3/8 in (9.5 mm) thick, complemented by hold-downs as an overturning restraint system. However, the fully mitigated gable case does not entirely meet the building code standards regarding truss and rafter spacing—mandated to be no more than 2 ft (0.6 m). Neither the fully mitigated hip nor the gable cases align with building codes requiring OSB panels for roof sheathing.

6.5. Results: Hurricane wind performance of housing typologies

Figures 6.8 to 6.10 present fragility curves for baseline and mitigated light-frame timber house typologies, including gable truss, hip truss, and gable rafter cases. In general, the baseline cases show poor performance, with Roof Envelope failures possible with wind speeds less than a Category 1 storm, and Roof Structure failures likely in a Category 2 storm. These observations are consistent with field observations after Hurricanes Maria and Fiona made by the authors, NGO workers, and Severino et al. (2018).

Among the baseline cases, the gable cases with trusses and rafters (Figure 6.8a and Figure 6.10a) exhibited similar performance (6% and less than 1% difference in median wind speed were observed at the *Roof Envelope* and *Roof Structure* or *Shear Walls* performance levels, respectively), suggesting that wood failure in the roof structure is not a significant factor in hurricane wind resistance. The hip truss case demonstrated superior baseline *Roof Structure* performance to the gable in terms of annual probability of failure (up to 76% better) due to the lower pressures on hip roofs and the larger number of roof to wall connections. In all cases, the *Roof Envelope* failure typically occurs at the lowest wind speed, followed by the *Roof Structure* and *Shear Wall* failures. However, the sequence of these failure modes depends on a systematic consideration of the load transfer from one component to another. If any link in the path is weaker, then the sequence of the failure modes can be altered. For example in the hip roof baseline case, the *Roof Envelope* performance is slightly worse than the gable roof cases, due to longer purlin spans associated with the roof geometry impacting roof envelope integrity (see the comparison between Figure 6.8a and 6.9a).

Table 6.5. Mitigated typology matrix[a,b]

Group	ID	Item	Baseline	Mitigated
Roof Envelope and Structure[c]	RE_1	Corrugated panel-to-purlin connection	nail	screws
		Corrugated panel-to-purlin connection spacing	12 in exterior/ 12 in interior	4 in exterior/ 4 in interior
	RE_2	Purlin and truss/rafter member size	2x4	2x6
		Purlin-to-truss[d] connection	nailed	screwed[e]
	RE_3	Truss/Rafter spacing	6 ft	2ft - 3ft[f]
		Purlin spacing	4 ft	2 ft
Roof-to-Wall	R2W	Roof-to-wall connection	toe-nailed	hurricane straps or fully-threaded screws
Shear Wall	SW	Shear wall sheathing layers	one-side	both-sides
		Shear wall overturning restraint system	none	conventional hold-down

[a] The term "Fully Mitigated" is used to denote the combined implementation of the RE, R2W, and SW mitigation measures.

[b] Unit conversion: 1 in = 25.4 mm; 1 ft = 0.305 m.

[c] The term "RE" refers to the combined action of RE_1, RE_2, and RE_3.

[d] This item also applies to mitigation of purlin-to-rafter connections.

[e] In Lochhead et al. (2022) hurricane straps were considered for purlin-to-truss connections. However, our subsequent fieldwork in Puerto Rico found that there is not enough space to place hurricane straps making them less effective than screwed connections.

[f] For hip roof designs, we considered typologies with the spacing of trusses at 2 ft and 3 ft. In contrast, for gable roof configurations, trusses or rafters are spaced at 2 ft. This distinction in spacing reflects the structural differences and requirements between the two roof shapes.

We also note that, in some cases, the fragility curve does not display a monotonically increasing trend that is typical of fragility curves, e.g. Figure 6.8a. This perhaps surprising trend occurs because of the change in the sign of C_{pi} resulting from the failure of the roof envelope such that the chance of the uplift failure of the corrugated metal panel goes down, which happens when 3 corrugated metal panels fail, as shown in Figure 6.2a. Due to the sign change, the probability of failure for the performance levels decreases instead of continuing to increase following the C_{pi} sign alteration at specific wind speeds.

The fragility curves developed herein for both the gable and hip roof baseline typologies, particularly for *Roof Envelope* and *Roof Structure* performance levels, showed less favorable outcomes compared to the typical formally-constructed American light-frame timber house typologies studied by Li and Ellingwood (2006) and van de Lindt and Dao (2009). Here, we compare our gable and hip roof baseline case fragility curves with the roof panel with overhang and roof-to-wall connection fragility curves from those studies, which consider North American residential housing in the southeast, gulf coast and eastern seaboard states. Despite some differences in assumptions, the performance of the baseline typologies in our case are up to 200% worse in terms of the median wind speed at failure. These performance differences between Puerto Rico and other North American housing typologies primarily stem from the absence of OSB sheathing in the roof envelope (instead, corrugated metal panels are fastened directly onto the purlins without intermediate sheathing) and the wider truss and purlin spacing in Puerto Rican informally-constructed light-frame timber houses. Where sheathing and narrowing spacing of the roof support structure are used in typical formal construction, there is a more extensive nailing pattern for attaching the corrugated metal panel to purlins.

The effect of the mitigation measures is to dramatically improve performance, leading to up to 140%, 220% and 135% increase in median wind speeds at the *Roof Envelope*, *Roof Structure*,and *Shear Wall* limit states, respectively. In particular, the median speed at *Roof Envelope* failure changes from occurring below a Category 1 wind speed, to a Category 3 or 4 wind speed. The mitigation measures delay a median *Roof Structure* failure to a

Category 5 storm. In mitigated cases, despite the expectation of increased stress on the wood frame of the roof, wood failure does not significantly impact the response of the houses to hurricane winds because the roof structures are strong enough. This observation is again evidenced by the similar responses observed between gable cases with trusses and those with rafters (see Figure 6.8b and 6.10b), even though the rafters are much weaker.

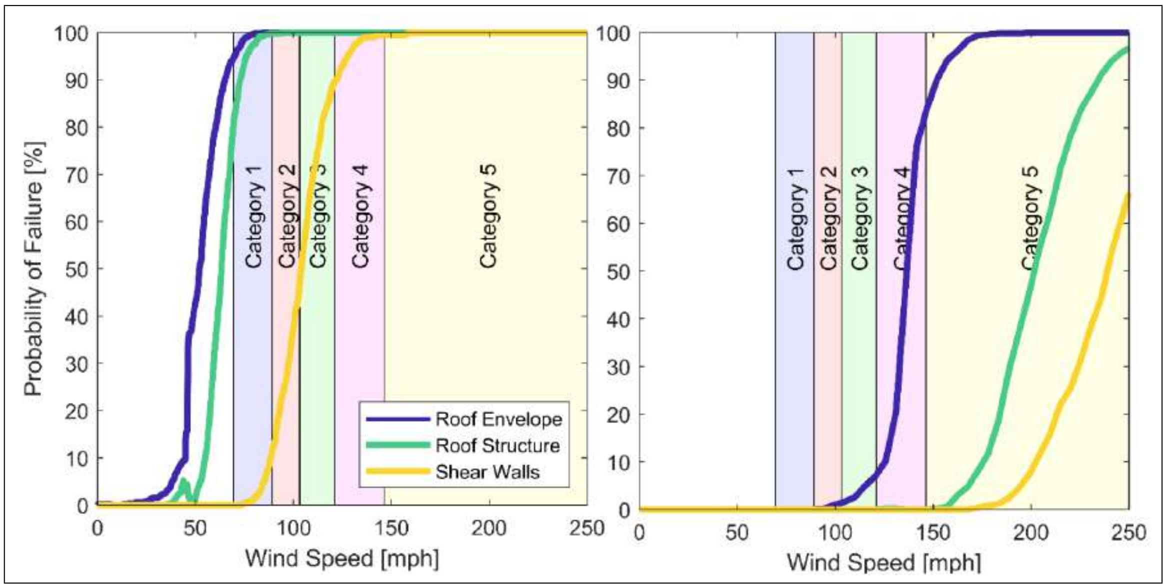

Figure 6.8. Wind fragility curve for gable roof with trusses: (a) baseline and (b) fully mitigated case. (On this figure and subsequent figures, wind speed is delineated into storm categories, based on the The Saffir-Simpson Team (2019) scale). Unit conversion: 1 mph = 0.477 mps.

Figure 6.11 provides the average annual probability of failure for the Roof Structure (life safety) performance level for all selected sites for the cases considering all mitigation measures. (These results include only the gable with truss, as the rafter results are similar; the full set of data is provided in Tables 6.9-6.11). The baseline cases have terrible performance, with annual failure probabilities several orders of magnitude over those found in previous studies and established targets. However, our results for the fully mitigated cases of informally-constructed light-frame timber house typologies indicate a lower annual failure probability than those reported for typical houses by Li and Ellingwood (2006). However, only the fully mitigated hip case with trusses spaced 2 ft on center meets the criteria

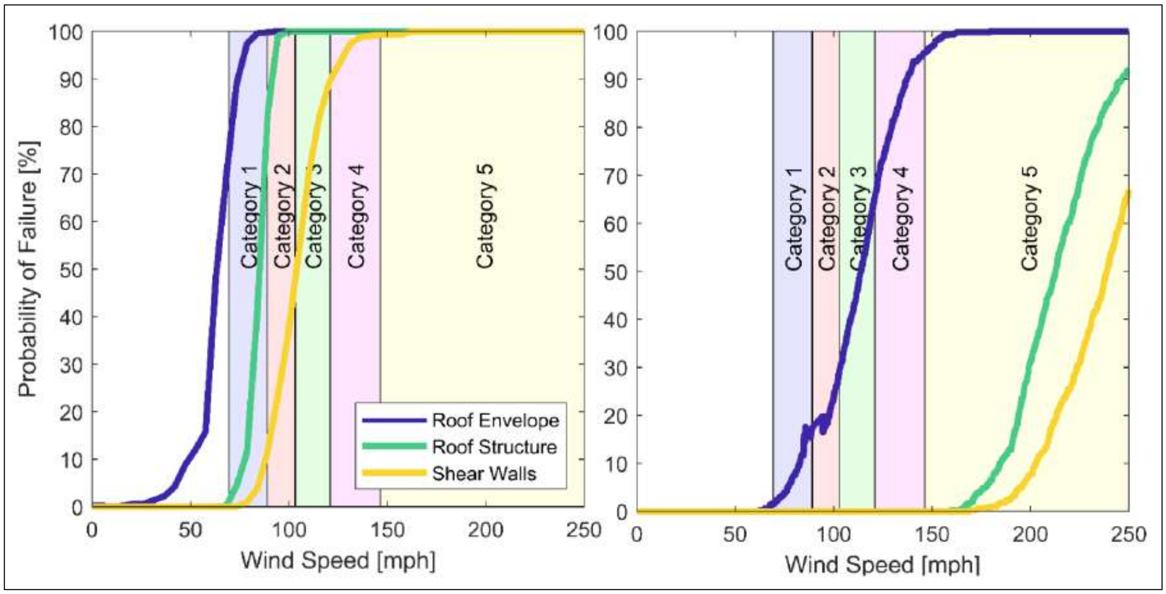

Figure 6.9. Wind fragility curve for the hip roof with trusses: (a) baseline and (b) fully mitigated case with trusses at 3 ft on center. Unit conversion: 1 mph = 0.477 mps.

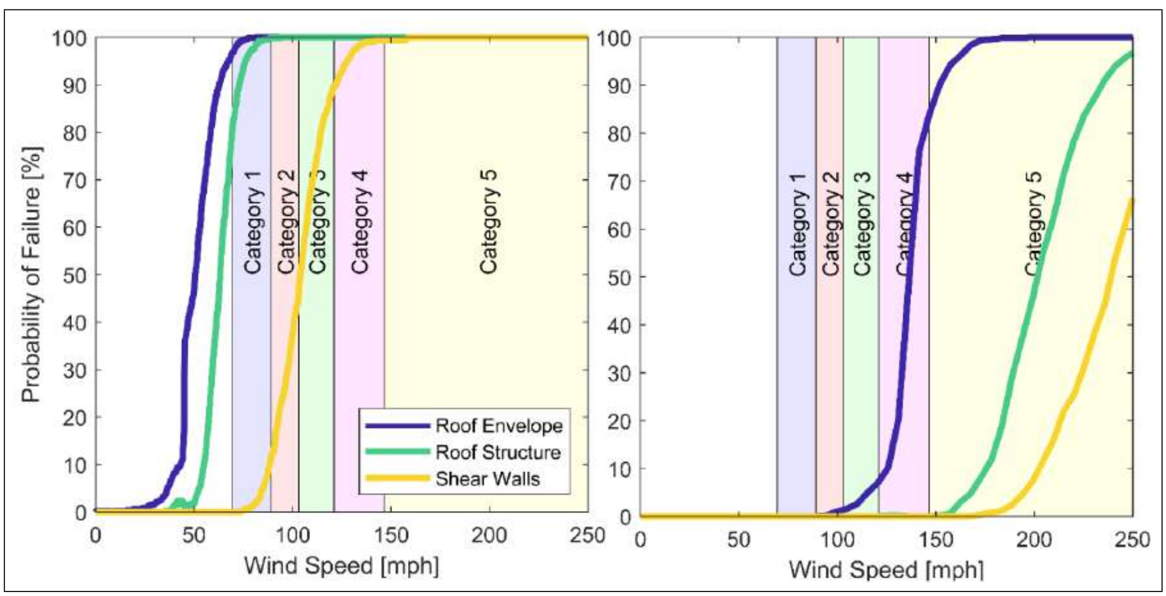

Figure 6.10. Wind fragility curve for gable case with rafters: (a) baseline and (b) fully mitigated case. Unit conversion: 1 mph = 0.477 mps.

set in the ASCE 7 (ASCE, 2022) standards, which limits the annual probability of failure to 3.0 x 10^{-5} per year.

Figure 6.12 examines the annual probability of failure for fully mitigated gable and hip cases across different locations. The results for the fully mitigated gable case indicate that southern/western locations are closest to reaching the target the ASCE 7 (ASCE, 2022) failure probabilities, while northern/eastern areas have more vulnerability due to the greater wind hazard in those areas. This failure pattern aligns with the damage observed on the island following Hurricane Maria in 2017, as noted by FEMA Mitigation Assessment Team (MAT) (2018) and Severino et al. (2018), and the differences in hurricane hazard. For fully mitigated hip case with trusses at 3 ft on center, with the exception of the Gurabo municipality, all analyzed locations showed annual probabilities of failure that either meet or are close to meeting the ASCE 7 (ASCE, 2022) target criteria, as indicated by the greener dots in Figure 6.12. As highlighted in Severino et al. (2018) and Vickery, Liu, and Lin (2023), Gurabo is uniquely vulnerable due to topographical factors that amplify wind speeds, resulting in increased damage.

To further explore the design implications of the failure probabilities, we also disaggregate the wind speeds that contribute to 90% of the calculated annual probability of failure for both gable and hip roof typologies with trusses, across various performance levels (Figure 6.13 and Figure 6.14). We refer to the wind speed range that contributes 90% of the failure (i.e., from 5^{th} to 95^{th} percentile) as the “critical failure range”. This disaggregation is illustrated in Figures 6.13 and 6.14 for the gable cases, and Figures 6.17 and 6.18 for the hip cases, while Table 6.6 provides a summary of the critical failure range for each typology and performance level. In comparison to the gable case, the hip case demonstrates a critical failure range that is 16% higher across all performance levels, indicating again the higher wind speeds associated with failure in the hip cases. Likewise, the implementation of all proposed mitigation strategies led to significant increases in the wind speed range for both roof types. These results show that the baseline cases fail well below the design wind speed. In contrast, the fully mitigated cases’ critical failure range encompasses or is above the design wind speed, despite not being explicitly designed. Only the Roof Envelope performance level is below the design wind speed.

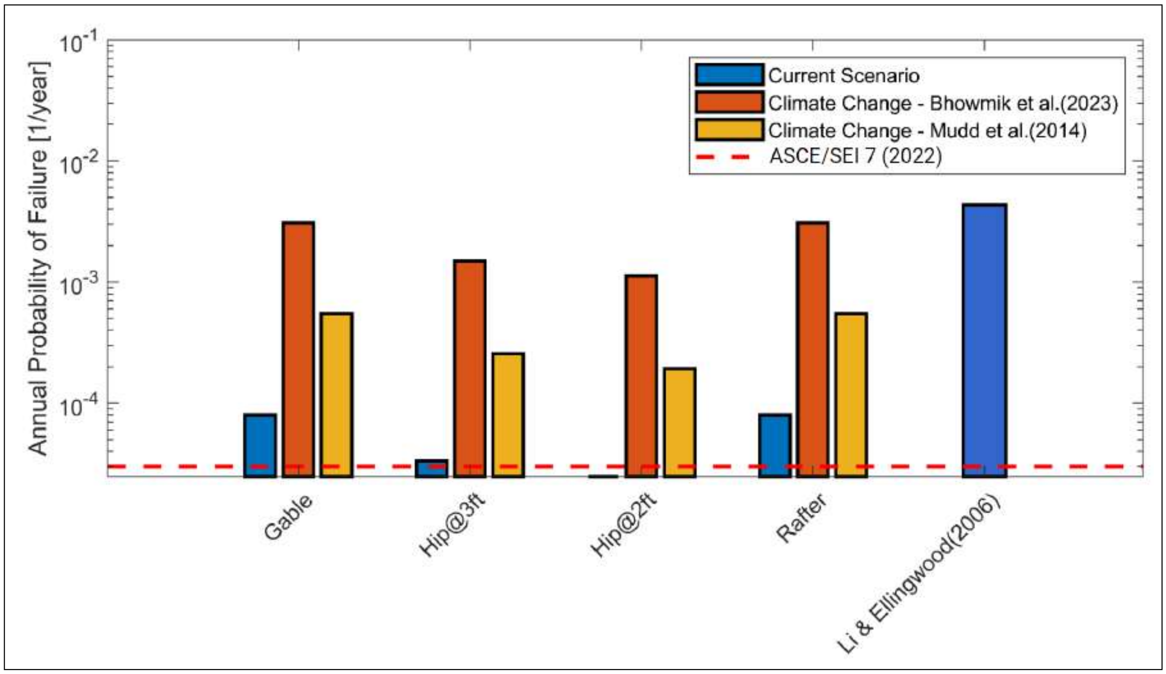

Figure 6.11. Comparison of the computed annual probability of failure of *Roof Structure* (life safety) performance level for the fully mitigated cases against Li and Ellingwood (2006) and ASCE 7 (ASCE, 2022) thresholds. For comparison, baseline cases have annual probabilities of failure ranging from 1.4x10^{-1} to 3.4x10^{-1} and are illustrated in Figures 6.15 and 6.16.

Table 6.6. Wind speed range contributing to the 90% of the annual probability of failure under the current climate scenario

Performance Level	Critical failure range wind speed [5^{th}, 95^{th} percentiles] mph (1 mph = 0.447 mps)			
	Gable	Gable- Fully mitigated	Hip	Hip- Fully mitigated
Roof Envelope	[53,117]	[108,172]	[47,121]	[76,150]
Roof Structure	[44,115]	[127,186]	[80,137]	[163,187]
Shear Wall	[88,150]	[171,187]	[88,150]	[171,187]

6.5.1. Contribution of proposed mitigation measures

In order to explore the effectiveness of individual mitigation strategies, Figures 6.15 and 6.16 showcase the impact of each proposed mitigation measure, both individually and in combination as outlined in Table 6.5, on the annual probability of failure for the

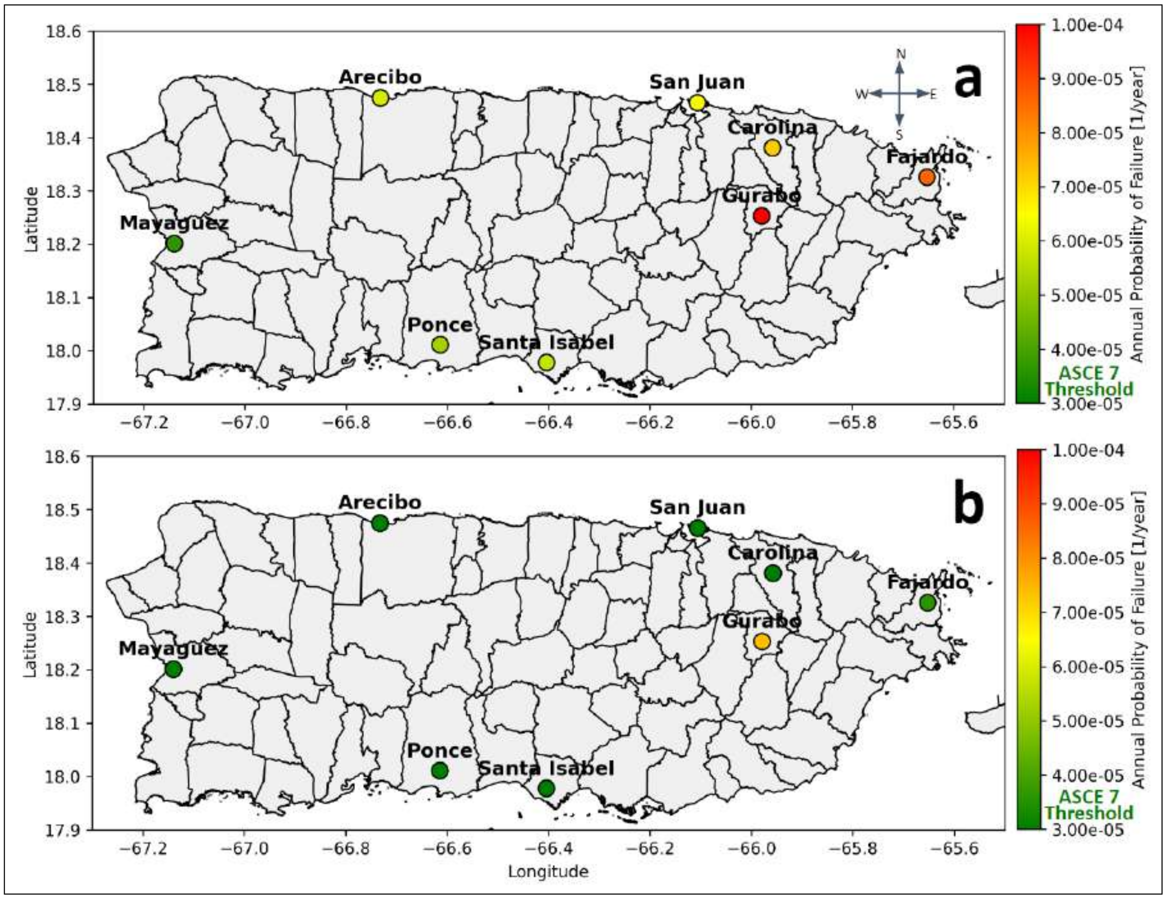

Figure 6.12. Annual probability of failure related to the Roof Structure (life safety) performance level across various locations on the island for mitigated (a) gable case and (b) hip case with trusses at 3 ft on center.

Roof Structure performance level. These figures reveal (comparing the baseline case and R2W) that, in both gable and hip cases, the most effective individual mitigation measure is reinforcing the roof-to-wall connection, either through installation of hurricane straps or fully-threaded screws at this location. This approach significantly reduces the annual probability of failure by increasing the capacity of the crucial roof-to-wall connection by up to six times, making it a priority in strengthening efforts. Regarding the roof envelope and roof structure (RE) enhancements, the most beneficial for improving the *Roof Structure* performance level compared to baseline case is reducing the spacing of trusses (or rafters) and purlins (i.e., RE_3), for the gable (up to 67% reduction in annual probability of failures) and hip (up to 20%) cases. This mitigation has the effect of reducing the uplift

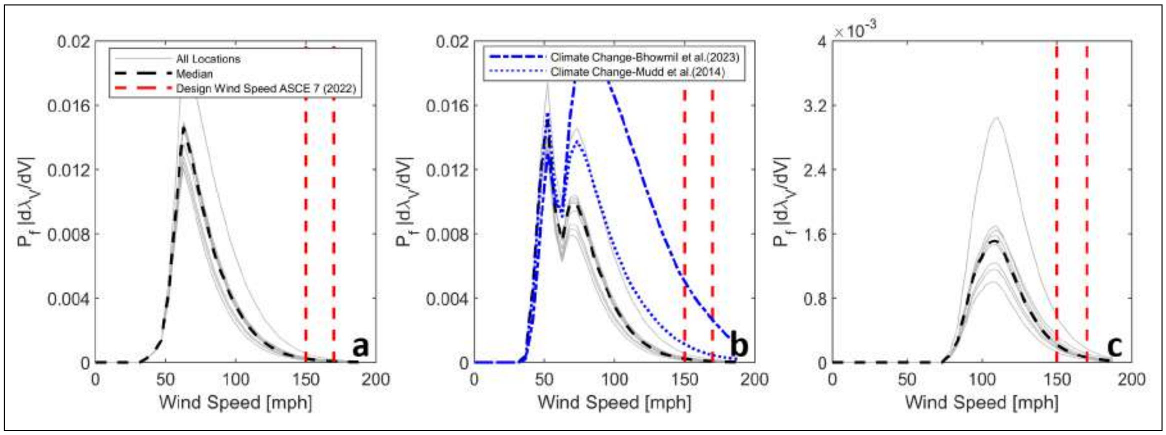

Figure 6.13. For the baseline gable case, disaggregation of the wind speed contribution to the probability of failure for (a) *Roof Envelope*, (b) *Roof Structure*, and (c) *Shear Wall* performance levels. The design wind speeds represent the range across the locations considered. Unit conversion: 1 mph = 0.477 mps.

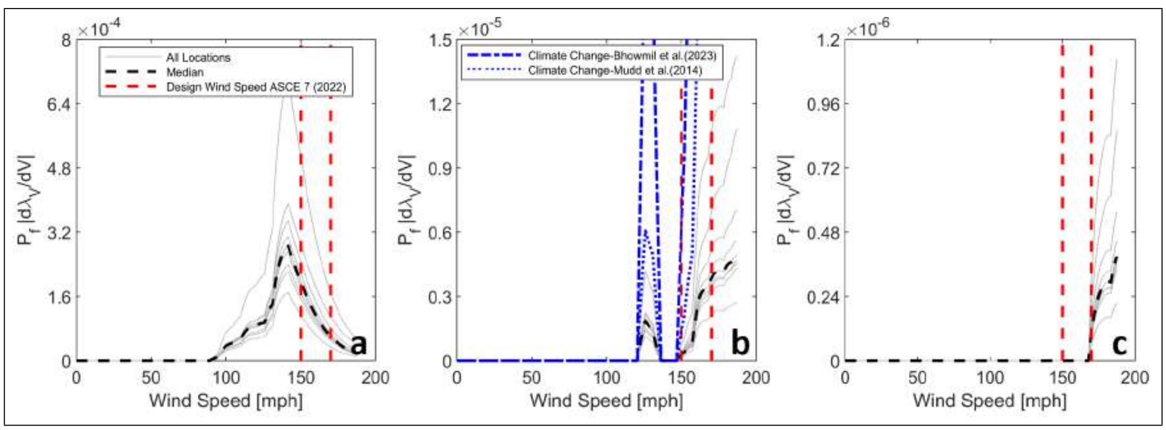

Figure 6.14. For the fully mitigated gable case, disaggregation of the wind speed contribution to the probability of failure for (a) *Roof Envelope*, (b) *Roof Structure*, and (c) *Shear Wall* performance levels. The design wind speeds represent the range across the locations considered. Unit conversion: 1 mph = 0.477 mps.

force on the roof-to-wall connection because there are more trusses to attach to the walls, and thereby delaying the likelihood of failure. Although not shown, RE_3 also improves the fragility for the *Roof Envelope* performance level by 62% compared to baseline performance. The second most beneficial mitigation measure on *Roof Structure* performance, labeled RE_2, involves: a) increasing the dimensions of wooden components in trusses (or rafters) and purlins to produce higher uplift strength in toe-nails, and b) using screwed purlin-to-truss connections. However, RE_2 exhibits a negligible impact (less than 4%) on reducing the annual probability of failure for the *Roof Envelope* performance level when compared to the baseline performance. Improving both the thickness of corrugated metal panels and the spacing of corrugated metal panel-to-purlin fasteners (RE_1) improves the *Roof Envelope* performance by 30% for the gable case and by 66% for the hip case. However, the RE_1 approach alone actually worsens the *Roof Structure* performance because strengthening the envelope means that larger forces are transferred to the weak roof structure and roof-to-wall connections when the envelope does not fail—unless that structure and connections are also mitigated. All of the RE measures are more effective than the sum of the individual RE_1 and RE_2, but it is slightly less effective than implementing RE_3 alone; essentially, the more mitigated the roof structure from RE_1 and RE_2,the higher the uplift load transferred to the shear wall through the roof-to wall connection. These results show that to achieve the performance criteria set by ASCE 7 (ASCE, 2022), it is essential to combine roof-to-wall reinforcement with improvements to the roof envelope and roof structure. In particular, combining roof envelope and roof structure enhancements means that the structure is able to produce a continuous and effective load path to shear walls, reducing annual failure probabilities more than if either set of modifications were made alone. This underscores the importance of adopting a system thinking approach in designing or mitigating houses.

Mitigating the roof envelope and structure is crucial, yet without applying mitigation measures to the shear walls, its performance could be compromised (refer to Table 6.11 to evaluate the differences between baseline, RE+R2W, and the fully-mitigated cases). Implementing shear wall mitigation measures enhances the continuity of the load path to the foundation. While not displayed here, shear wall mitigation measures (SW) improve the baseline annual probability of failure for the *Shear Wall* performance level from $1.97\text{x}10^{-2}$ to as small as $7.11\text{x}10^{-7}$.

We conducted additional fieldwork in June 2023 to assess the feasibility of the mitigation measures explored in this engineering assessment, i.e., those outlined in Table 6.5 and Figures 6.15 and 6.16. This assessment involved sharing the proposed mitigation measures with approximately thirty builders and fifteen hardware store employees, and then briefly interviewing them to assess their likelihood of implementing these measures. Interviewees shared that they believed that the proposed mitigation measures would enhance the safety of their houses, provide shelter for neighbors, and contribute to improved mental well-being by increasing preparedness for future hurricanes. Almost 70% of the interviewees selected the roof-to-wall and corrugated metal panel-to-purlin connections as critical areas for fortification in a house, complementing the engineering findings that these are key for enhancing *Roof Envelope* and *Roof Structure* performance.

However, the interviewees also raised concerns about barriers to implementation, particularly cost, especially the costs of fully-threaded screws for roof-to-wall connections (R2W), thicker corrugated metal panels (RE_1), screws instead of nails for the corrugated metal panel-to-purlin connection (RE_1), and 2x6 rather than 2x4 wood members in the roof structure (RE_2). The interviewees also indicated that a lack of knowledge on how to execute the proposed mitigation measures was a significant barrier, affecting the adoption of closer spacing for the fasteners for the corrugated metal (RE_1), reduced spacing for purlins, trusses, or rafters (RE_3), and sheathing on shear walls (SW).

The builder interviewees also noted material availability issues for the screws to attach the purlin to trusses or rafters (RE_2), for the hurricane straps and fully-threaded screws at the roof-to-wall connection (R2W), and for the 2x6 wood members (RE_2). However, hardware store employee interviewees did not view material availability as an obstacle, attributing the lack of adoption primarily to a lack of customer awareness around the proposed mitigation measures. These results also suggest that cost misconceptions may also be an important barrier. Goldwyn et al. (2023) previously found that builders saw value in sharing information about costs, and the cost to benefit ratio of protecting roof connections in your house with hurricane straps more widely. Both builders involved with local

NGOs and hardware store employees cited cost, complexity, lack of understanding, and the additional time required as barriers for implementing hip roof designs, despite our findings (and those of others, e.g., Vickery, Quayyum, et al. (2023)) suggesting hip roofs are highly advantageous over gable roofs. Therefore, it is crucial to effectively communicate the long-term advantages of the suggested mitigation strategies to the community.

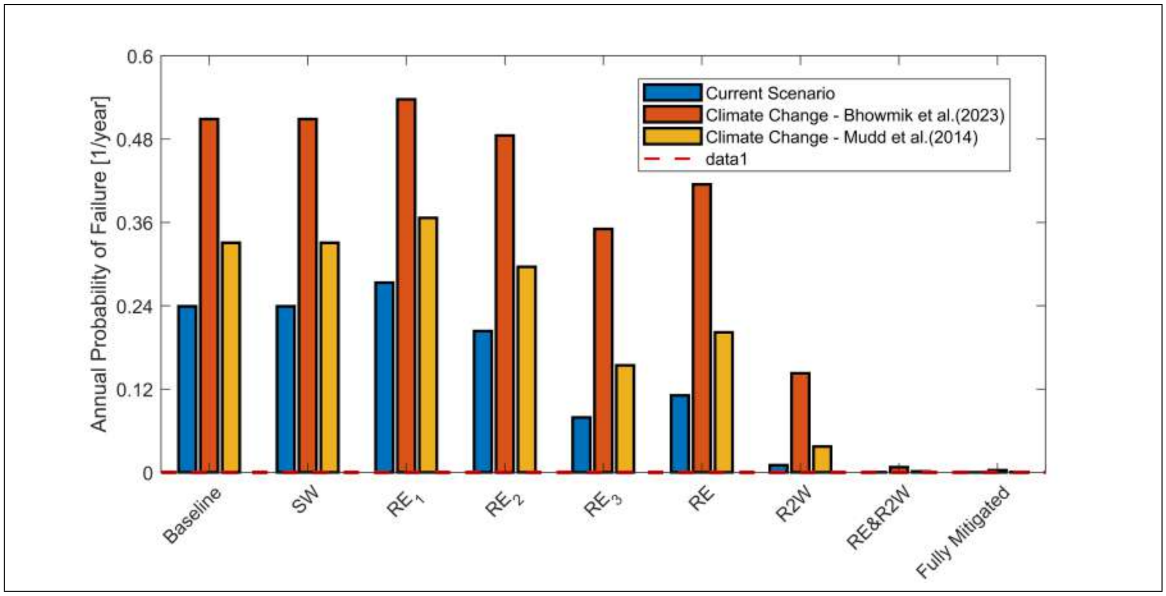

Figure 6.15. For the gable roof structure, contribution of each proposed mitigation measure to reduce the annual probability of failure associated with the *Roof Structure* performance level.

6.5.2. Effect of climate change

Climate change significantly escalates failure risks for these structures, with probabilities of failure potentially doubling to quintupling based on the roof shape and climate scenarios in both baseline and mitigated cases. This increase is derived from the amplified hazard in the climate change scenarios considered; for example, in Gurabo, a 100 mph (45 mps) wind speed's annual likelihood increases from 8.96 x 10^{-2} to 2.09 x 10^{-1} (a factor of more than two) and to 6.05 x 10^{-1} (a factor of almost seven) for the Mudd et al. (2014b) and Bhowmik et al. (2023) climate change scenarios, respectively. In addition, the critical failure range changes from [127,186] mph ([57,83] mps) in the current climate scenario

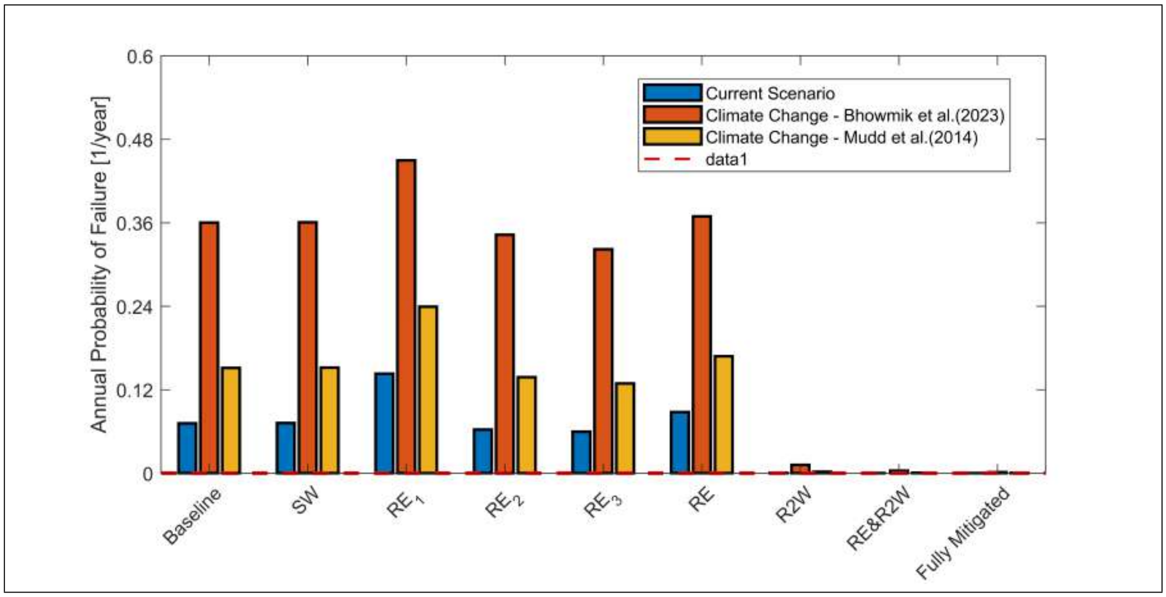

Figure 6.16. For the hip roof structure, contribution of each proposed mitigation measure to reduce the annual probability of failure associated with the *Roof Structure* performance level.

to [156,187] mph ([70, 84] mps) for the fully mitigated gable case under Bhowmik et al. (2023) climate change scenario (see Table 6.7). Failing to proactively adjust for the non-stationary future climate implies that the upper and lower limits of the critical failure range of wind speeds will increase over time, leading to the obsolescence of existing design wind speeds and inadequacies of practices that may have implicitly satisfied the current design targets. This observation adds urgency to the need to mitigate, as the annualized failure risk is increasing, regardless of the future climate model considered.

Table 6.7. Wind speed range contributing to the 90% of the Roof Structure annual probability of failure under various climate scenarios

Climate Scenario	Critical failure range wind speed [5^{th},95^{th} percentiles] mph (1 mph = 0.447 mps)			
	Gable	Gable- Fully mitigated	Hip	Hip- Fully mitigated
Current	[44,115]	[127,186]	[80,137]	[163,187]
Bhowmik et al. (2023)	[51,158]	[156,187]	[85,166]	[165,187]
Mudd et al. (2014a)	[46,136]	[132,187]	[82,154]	[165,187]

6.6. Limitations and Future Work

This research focuses exclusively on the impacts of wind and does not encompass risks associated with hurricane-induced flooding or storm surges. Likewise, our analysis considers only structural damage caused by hurricane winds, excluding considerations such as water intrusion and impacts from debris. The house typologies were established through fieldwork observations and are confined to single-story residential homes. However, these typologies are based on a simplification of house shapes, and results could vary for unusual geometry or construction practices. Lochhead et al. (2022) and Vickery, Quayyum, et al. (2023) partially addressed the limitation related to building stories in our study, showing greater risk for two-story buildings. Additionally, we recognize that the definition of the performance levels, as described in Table 6.3, can significantly influence the fragility curve response for the typologies under review. Moreover, the coefficients of variation used for wind demands and components, especially those not derived from experimental data, can also greatly affect the calculated probability of failure.

Future research should focus on refining the fragility models to accommodate changing climate scenarios and tackle scenarios involving multiple hazards, as Puerto Rico has recently experienced earthquakes and floods as well as high winds. These events have placed residents in a dilemma regarding the choice of the most suitable structural system, since heavier construction is preferable for winds and in many cases flooding (elevation is possible), but not earthquakes Goldwyn et al. (2021); Goldwyn, Vega, et al. (2022).

Finally, we assess the ASCE 7 (ASCE, 2022) threshold for annual probability of failure, but we emphasize the need for a more nuanced approach for Puerto Rico, considering its specific hurricane risks and socioeconomic context. Since the threshold from ASCE 7 (ASCE, 2022) applies broadly to various hazards and diverse U.S. contexts, future research should consider how and if these targets—and the associated building code requirements—should be varied to be more aligned with building practices and the changing nature of hurricanes due to climate change on the island to meet community expectations.

6.7. Chapter Conclusions

This study conducted a comprehensive assessment of hurricane performance of light-frame timber houses in Puerto Rico, focusing on developing fragility curves across three critical limit states: roof envelope failure, roof structure failure, and shear wall failures for both gable and hip roof types. This analysis used a component-based probabilistic method that considered how wind demands would contribute to roof envelope, structure, and wall failure at a range of wind speeds. A key aspect was evaluating the probability of failure for the baseline typologies and assessing how various mitigation measures reduce this probability, comparing these probabilities of failure to target performance level and findings from other studies. Additionally, the research investigated the projected impact of two climate change scenarios on the probability of failure of the light-frame timber house typologies.

These assessments demonstrated the poor performance of the existing informally-constructed housing stock, with high risk of roof envelope and structure failure in hurricanes. The implementation of all proposed mitigation measures significantly reduced the probabilities of failure. Among the mitigation measures, reinforcing the roof-to-wall connection emerged as the most effective strategy in reducing the probability of failure associated with *Roof Structure* (life safety) performance level. The results showed that improvements to the roof structure through increasing the number (smaller spacing) and dimension of wood component is the next most effective strategy. Reinforcing the envelope through improvements to the panel and panel to structure connections improve the *Roof Envelope* performance, but can have detrimental effects on the *Roof Structure* performance if pursued without increasing the quality and number of roof to wall connections.

The fully mitigated cases showed substantial improvements, on par with that performance found with other more formally constructed North American housing even without fully complying with all aspects of building codes and standards. Even so, they did not consistently meet the ASCE 7 (ASCE, 2022) target for an adequately low probability of failure. The study also revealed that the future climate change scenarios considered have the potential to dramatically increase the probability of failure across all evaluated cases and performance levels. In these scenarios, the baseline typologies' performance becomes even more unacceptable, driving the need for design and mitigation strategies that meet these future climate conditions.

The interviews we conducted identified both resource constraints and knowledge gaps as significant obstacles preventing Puerto Rican communities from adopting the suggested mitigation measures for roof-to-wall and corrugated metal panel-to-purlin connections. These findings underscore the need to develop strategies to overcome some of the real and perceived cost barriers, and to improve understanding of these mitigation measures among local builders. A key aspect of the needed capacity building is to convey the long-term advantages of these mitigation strategies and to accommodate both current and anticipated future demands resulting from climate change.

Looking ahead, this research aims to set the stage for achieving safer and more resilient informally-constructed housing within Puerto Rican communities by identifying key challenges. Overcoming these challenges will involve an active collaboration with local stakeholders to boost knowledge and transfer the application of cost-effective strategies, particularly those focused on the roof to wall connections, aimed at reinforcing houses against hurricane winds. These efforts will be especially critical given the expected increases in frequency of hurricane-force winds, which indicates even worse performance by the end of the century without changes in building practices. Nevertheless, the results suggest that dramatic improvements are possible in performance with available materials and technologies. The improvements may reach close to a target level performance of modern standards and that achieved by typical light frame timber housing in North America without explicitly following all the detailing requirements of codes and standards. The ultimate goal of this endeavor is to enhance the resilience of communities in Puerto Rico and similar areas, preparing them to face the escalating hurricane threats in a progressively changing climate.

6.8. Supplementary Material - Figures

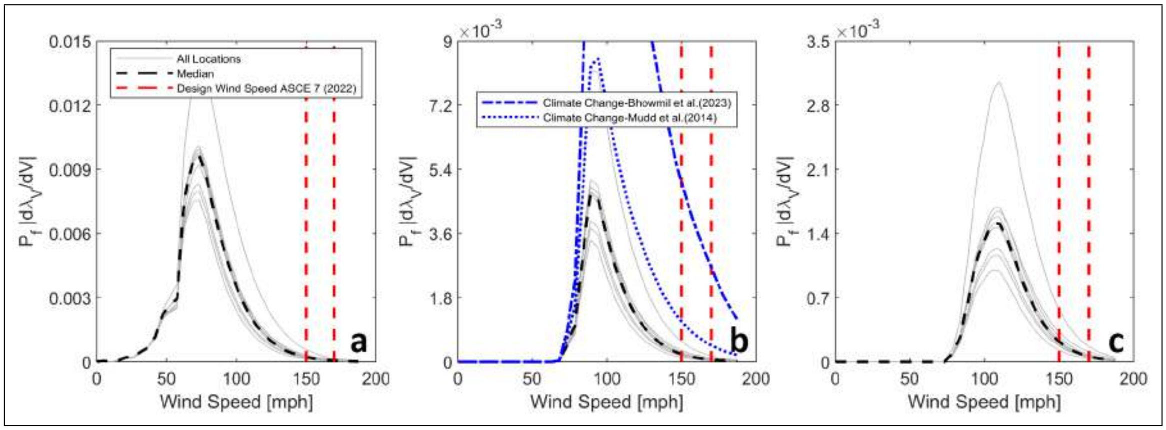

Figure 6.17. For the baseline hip case, disaggregation of the wind speed contribution to the probability of failure for (a) *Roof Envelope*, (b) *Roof Structure*, and (c) *Shear Wall* performance levels. The design wind speeds represent the range across the locations considered. Unit conversion: 1 mph = 0.477 mps.

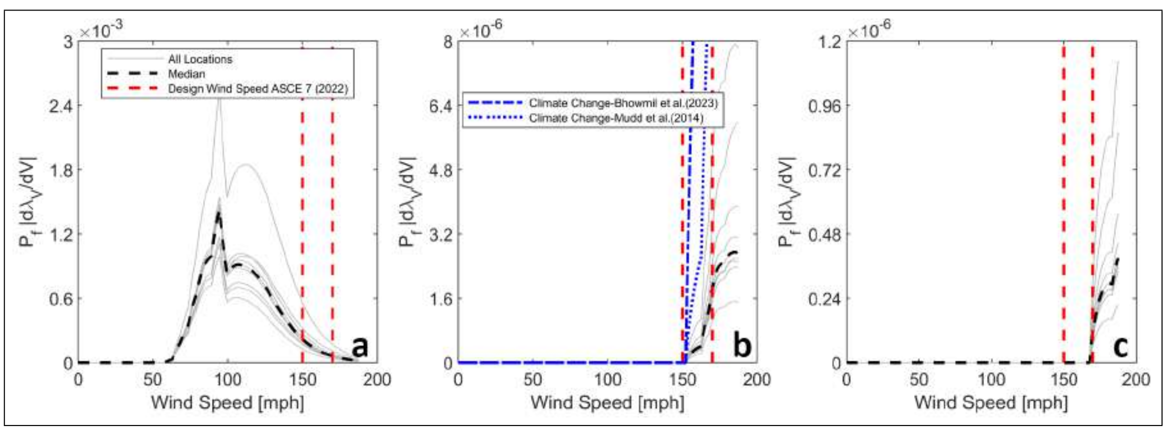

Figure 6.18. For the fully mitigated hip case with trusses at 3 ft on center, disaggregation of the wind speed contribution to the probability of failure for (a) *Roof Envelope*, (b) *Roof Structure*, and (c) *Shear Wall* performance levels. The design wind speeds represent the range across the locations considered. Unit conversion: 1 mph = 0.477 mps.

6.9. Supplementary Material - Tables

Table 6.8. Adjusted Weibull parameters for all selected locations in Puerto Rico. (Unit conversion: 1 mph = 0.477 mps)

Location	Current Scenario		Climate Change Scenario			
			Bhowmik et al. (2023)		Mudd et al. (2014a)	
	δ [mph]	β	δ [mph]	β	δ [mph]	β
San Juan	47.5	1.532	98.7	2.174	62.0	1.576
Mayagüez	41.6	1.442	91.2	2.112	53.9	1.474
Ponce	42.6	1.429	91.9	2.046	55.1	1.458
Arecibo	47.2	1.532	103.0	2.298	61.2	1.569
Santa Isabel	43.6	1.444	94.0	2.076	56.4	1.474
Guayama	46.2	1.424	97.1	1.981	59.6	1.451
Fajardo	48.6	1.523	104.3	2.232	62.9	1.557
Carolina	48.0	1.531	104.4	2.285	62.2	1.567
Gurabo	60.1	1.726	129.1	2.703	77.9	1.772

Table 6.9. Computed annual probability of failure for the evaluated locations for the current climate scenario and *Roof Envelope* performance level

Case	Location								
	San Juan	Mayagüez	Ponce	Arecibo	Santa Isabel	Guayama	Fajardo	Carolina	Gurabo
Gable	2.15e-01	1.70e-01	1.80e-01	2.12e-01	1.87e-01	2.10e-01	2.24e-01	2.19e-01	3.08e-01
Gable-RE_1	1.53e-01	1.17e-01	1.26e-01	1.50e-01	1.31e-01	1.52e-01	1.61e-01	1.57e-01	2.34e-01
Gable-RE_2	2.16e-01	1.71e-01	1.81e-01	2.14e-01	1.88e-01	2.12e-01	2.26e-01	2.21e-01	3.10e-01
Gable-RE_3	8.92e-02	6.34e-02	7.09e-02	8.72e-02	7.47e-02	9.27e-02	9.67e-02	9.23e-02	1.55e-01
Gable-RE	4.79e-03	2.88e-03	3.75e-03	4.55e-03	4.05e-03	6.71e-03	5.87e-03	5.19e-03	1.17e-02
Gable-R2W	2.15e-01	1.70e-01	1.80e-01	2.12e-01	1.87e-01	2.10e-01	2.24e-01	2.19e-01	3.08e-01
Gable-SW	2.15e-01	1.70e-01	1.80e-01	2.12e-01	1.87e-01	2.10e-01	2.24e-01	2.19e-01	3.08e-01
Gable-RE+R2W	4.79e-03	2.88e-03	3.75e-03	4.55e-03	4.05e-03	6.71e-03	5.87e-03	5.19e-03	1.17e-02
Gable Mitigated	4.79e-03	2.88e-03	3.75e-03	4.55e-03	4.05e-03	6.71e-03	5.87e-03	5.19e-03	1.17e-02
Hip	1.78e-01	1.39e-01	1.48e-01	1.76e-01	1.54e-01	1.76e-01	1.87e-01	1.82e-01	2.65e-01
Hip-RE_1	6.89e-02	4.77e-02	5.42e-02	6.71e-02	5.73e-02	7.34e-02	7.57e-02	7.17e-02	1.26e-01
Hip-RE_2	1.71e-01	1.31e-01	1.41e-01	1.69e-01	1.47e-01	1.70e-01	1.80e-01	1.75e-01	2.60e-01
Hip-RE_3	4.29e-02	2.88e-02	3.35e-02	4.16e-02	3.56e-02	4.76e-02	4.80e-02	4.49e-02	8.38e-02
Hip-RE	2.92e-02	1.97e-02	2.28e-02	2.83e-02	2.43e-02	3.26e-02	3.27e-02	3.06e-02	5.71e-02
Hip-R2W	1.71e-01	1.31e-01	1.41e-01	1.69e-01	1.47e-01	1.70e-01	1.80e-01	1.75e-01	2.60e-01
Hip-SW	1.71e-01	1.31e-01	1.41e-01	1.69e-01	1.47e-01	1.70e-01	1.80e-01	1.75e-01	2.60e-01
Hip-RE+ R2W	2.92e-02	1.97e-02	2.28e-02	2.83e-02	2.43e-02	3.26e-02	3.27e-02	3.06e-02	5.71e-02
Hip Mitigated	2.92e-02	1.97e-02	2.28e-02	2.83e-02	2.43e-02	3.26e-02	3.27e-02	3.06e-02	5.71e-02
Hip@2ft Mitigated	2.92e-02	1.97e-02	2.28e-02	2.83e-02	2.43e-02	3.26e-02	3.27e-02	3.06e-02	5.71e-02
Rafter	2.43e-01	1.97e-01	2.07e-01	2.40e-01	2.14e-01	2.36e-01	2.51e-01	2.46e-01	3.34e-01
Rafter-RE_1	1.53e-01	1.17e-01	1.26e-01	1.50e-01	1.31e-01	1.52e-01	1.61e-01	1.57e-01	2.34e-01
Rafter-RE_2	2.16e-01	1.71e-01	1.81e-01	2.14e-01	1.88e-01	2.12e-01	2.26e-01	2.21e-01	3.10e-01
Rafter-RE_3	8.92e-02	6.34e-02	7.09e-02	8.72e-02	7.47e-02	9.27e-02	9.67e-02	9.23e-02	1.55e-01
Rafter-RE	4.79e-03	2.88e-03	3.75e-03	4.55e-03	4.05e-03	6.71e-03	5.87e-03	5.19e-03	1.17e-02
Rafter-R2W	2.15e-01	1.70e-01	1.80e-01	2.12e-01	1.87e-01	2.10e-01	2.24e-01	2.19e-01	3.08e-01
Rafter-SW	2.15e-01	1.70e-01	1.80e-01	2.12e-01	1.87e-01	2.10e-01	2.24e-01	2.19e-01	3.08e-01
Rafter-RE+R2W	4.79e-03	2.88e-03	3.75e-03	4.55e-03	4.05e-03	6.71e-03	5.87e-03	5.19e-03	1.17e-02
Rafter Mitigated	4.79e-03	2.88e-03	3.75e-03	4.55e-03	4.05e-03	6.71e-03	5.87e-03	5.19e-03	1.17e-02

Table 6.10. Computed annual probability of failure for the evaluated locations for the current climate scenario and *Roof Structure* performance level

Case	Location								
	San Juan	Mayagüez	Ponce	Arecibo	Santa Isabel	Guayama	Fajardo	Carolina	Gurabo
Gable	2.41e-01	1.97e-01	2.06e-01	2.38e-01	2.13e-01	2.34e-01	2.49e-01	2.45e-01	3.29e-01
Gable-RE_1	2.76e-01	2.27e-01	2.37e-01	2.73e-01	2.45e-01	2.67e-01	2.84e-01	2.80e-01	3.69e-01
Gable-RE_2	2.04e-01	1.63e-01	1.73e-01	2.02e-01	1.79e-01	2.00e-01	2.13e-01	2.08e-01	2.90e-01
Gable-RE_3	7.72e-02	5.54e-02	6.16e-02	7.55e-02	6.49e-02	8.03e-02	8.36e-02	7.99e-02	1.34e-01
Gable-RE	1.09e-01	7.91e-02	8.73e-02	1.07e-01	9.18e-02	1.11e-01	1.17e-01	1.12e-01	1.83e-01
Gable-R2W	9.38e-03	5.78e-03	7.28e-03	8.96e-03	7.82e-03	1.22e-02	1.12e-02	1.01e-02	2.17e-02
Gable-SW	2.41e-01	1.97e-01	2.06e-01	2.38e-01	2.13e-01	2.34e-01	2.49e-01	2.45e-01	3.29e-01
Gable-RE+R2W	2.08e-04	1.21e-04	1.68e-04	1.96e-04	1.82e-04	3.37e-04	2.67e-04	2.29e-04	5.41e-04
Gable Mitigated	6.42e-05	3.64e-05	5.29e-05	5.97e-05	5.74e-05	1.16e-04	8.56e-05	7.16e-05	1.75e-04
Hip	6.93e-02	4.79e-02	5.44e-02	6.75e-02	5.76e-02	7.38e-02	7.61e-02	7.21e-02	1.27e-01
Hip-RE_1	1.42e-01	1.06e-01	1.15e-01	1.39e-01	1.21e-01	1.42e-01	1.51e-01	1.46e-01	2.25e-01
Hip-RE_2	6.02e-02	4.11e-02	4.71e-02	5.85e-02	4.99e-02	6.50e-02	6.65e-02	6.27e-02	1.13e-01
Hip-RE_3	5.75e-02	3.98e-02	4.52e-02	5.60e-02	4.79e-02	6.17e-02	6.33e-02	5.99e-02	1.06e-01
Hip-RE	8.60e-02	6.15e-02	6.84e-02	8.41e-02	7.21e-02	8.89e-02	9.29e-02	8.89e-02	1.48e-01
Hip-R2W	2.42e-04	1.36e-04	2.00e-04	2.24e-04	2.17e-04	4.43e-04	3.25e-04	2.70e-04	6.69e-04
Hip-SW	6.97e-02	4.82e-02	5.48e-02	6.79e-02	5.80e-02	7.42e-02	7.65e-02	7.25e-02	1.28e-01
Hip-RE+ R2W	7.00e-05	3.92e-05	5.82e-05	6.48e-05	6.33e-05	1.31e-04	9.48e-05	7.85e-05	1.95e-04
Hip Mitigated	2.61e-05	1.46e-05	2.20e-05	2.42e-05	2.39e-05	5.08e-05	3.58e-05	2.95e-05	7.37e-05
Hip@2ft Mitigated	1.93e-05	1.07e-05	1.62e-05	1.78e-05	1.77e-05	3.78e-05	2.65e-05	2.17e-05	5.45e-05
Rafter	1.89e-01	1.48e-01	1.57e-01	1.86e-01	1.64e-01	1.86e-01	1.97e-01	1.92e-01	2.76e-01
Rafter-RE_1	2.76e-01	2.27e-01	2.37e-01	2.73e-01	2.45e-01	2.67e-01	2.84e-01	2.80e-01	3.69e-01
Rafter-RE_2	2.04e-01	1.63e-01	1.73e-01	2.02e-01	1.79e-01	2.00e-01	2.13e-01	2.08e-01	2.90e-01
Rafter-RE_3	7.72e-02	5.54e-02	6.16e-02	7.55e-02	6.49e-02	8.03e-02	8.36e-02	7.99e-02	1.34e-01
Rafter-RE	1.09e-01	7.91e-02	8.73e-02	1.07e-01	9.18e-02	1.11e-01	1.17e-01	1.12e-01	1.83e-01
Rafter-R2W	9.38e-03	5.78e-03	7.28e-03	8.96e-03	7.82e-03	1.22e-02	1.12e-02	1.01e-02	2.17e-02
Rafter-SW	2.41e-01	1.97e-01	2.06e-01	2.38e-01	2.13e-01	2.34e-01	2.49e-01	2.45e-01	3.29e-01
Rafter-RE+R2W	2.08e-04	1.21e-04	1.68e-04	1.96e-04	1.82e-04	3.37e-04	2.67e-04	2.29e-04	5.41e-04
Rafter Mitigated	6.42e-05	3.64e-05	5.29e-05	5.97e-05	5.74e-05	1.16e-04	8.56e-05	7.16e-05	1.75e-04

Table 6.11. Computed annual probability of failure for the evaluated locations for the current climate scenario and *Shear Wall* performance level

Case	Location								
	San Juan	Mayagüez	Ponce	Arecibo	Santa Isabel	Guayama	Fajardo	Carolina	Gurabo
Gable	3.01e-02	1.97e-02	2.33e-02	2.90e-02	2.49e-02	3.44e-02	3.41e-02	3.16e-02	6.15e-02
Gable-RE_1	1.14e-02	7.12e-03	8.84e-03	1.09e-02	9.49e-03	1.44e-02	1.34e-02	1.22e-02	2.58e-02
Gable-RE_2	3.01e-02	1.97e-02	2.33e-02	2.90e-02	2.49e-02	3.44e-02	3.41e-02	3.16e-02	6.15e-02
Gable-RE_3	4.58e-02	3.21e-02	3.64e-02	4.46e-02	3.84e-02	4.92e-02	5.03e-02	4.76e-02	8.33e-02
Gable-RE	1.18e-01	8.64e-02	9.49e-02	1.16e-01	9.96e-02	1.20e-01	1.26e-01	1.21e-01	1.94e-01
Gable-R2W	3.01e-02	1.97e-02	2.33e-02	2.90e-02	2.49e-02	3.44e-02	3.41e-02	3.16e-02	6.15e-02
Gable-SW	1.28e-06	7.11e-07	1.09e-06	1.18e-06	1.19e-06	2.63e-06	1.79e-06	1.45e-06	3.66e-06
Gable-RE+R2W	1.18e-01	8.64e-02	9.49e-02	1.16e-01	9.96e-02	1.20e-01	1.26e-01	1.21e-01	1.94e-01
Gable Mitigated	2.30e-06	1.28e-06	1.95e-06	2.12e-06	2.12e-06	4.63e-06	3.19e-06	2.60e-06	6.54e-06
Hip	3.01e-02	1.97e-02	2.33e-02	2.90e-02	2.49e-02	3.44e-02	3.41e-02	3.16e-02	6.15e-02
Hip-RE_1	4.65e-02	3.25e-02	3.69e-02	4.53e-02	3.90e-02	5.00e-02	5.12e-02	4.84e-02	8.52e-02
Hip-RE_2	3.01e-02	1.97e-02	2.33e-02	2.90e-02	2.49e-02	3.44e-02	3.41e-02	3.16e-02	6.15e-02
Hip-RE_3	4.51e-02	3.11e-02	3.55e-02	4.39e-02	3.76e-02	4.89e-02	4.98e-02	4.70e-02	8.42e-02
Hip-RE	1.05e-01	7.71e-02	8.44e-02	1.03e-01	8.86e-02	1.06e-01	1.12e-01	1.08e-01	1.71e-01
Hip-R2W	3.01e-02	1.97e-02	2.33e-02	2.90e-02	2.49e-02	3.44e-02	3.41e-02	3.16e-02	6.15e-02
Hip-SW	1.28e-06	7.11e-07	1.09e-06	1.18e-06	1.19e-06	2.63e-06	1.79e-06	1.45e-06	3.66e-06
Hip-RE+ R2W	1.05e-01	7.71e-02	8.44e-02	1.03e-01	8.86e-02	1.06e-01	1.12e-01	1.08e-01	1.71e-01
Hip Mitigated	2.30e-06	1.28e-06	1.95e-06	2.12e-06	2.12e-06	4.63e-06	3.19e-06	2.60e-06	6.54e-06
Hip@2ft Mitigated	2.30e-06	1.28e-06	1.95e-06	2.12e-06	2.12e-06	4.63e-06	3.19e-06	2.60e-06	6.54e-06
Rafter	3.01e-02	1.97e-02	2.33e-02	2.90e-02	2.49e-02	3.44e-02	3.41e-02	3.16e-02	6.15e-02
Rafter-RE_1	1.14e-02	7.12e-03	8.84e-03	1.09e-02	9.49e-03	1.44e-02	1.34e-02	1.22e-02	2.58e-02
Rafter-RE_2	3.01e-02	1.97e-02	2.33e-02	2.90e-02	2.49e-02	3.44e-02	3.41e-02	3.16e-02	6.15e-02
Rafter-RE_3	4.58e-02	3.21e-02	3.64e-02	4.46e-02	3.84e-02	4.92e-02	5.03e-02	4.76e-02	8.33e-02
Rafter-RE	1.18e-01	8.64e-02	9.49e-02	1.16e-01	9.96e-02	1.20e-01	1.26e-01	1.21e-01	1.94e-01
Rafter-R2W	3.01e-02	1.97e-02	2.33e-02	2.90e-02	2.49e-02	3.44e-02	3.41e-02	3.16e-02	6.15e-02
Rafter-SW	1.28e-06	7.11e-07	1.09e-06	1.18e-06	1.19e-06	2.63e-06	1.79e-06	1.45e-06	3.66e-06
Rafter-RE+R2W	1.18e-01	8.64e-02	9.49e-02	1.16e-01	9.96e-02	1.20e-01	1.26e-01	1.21e-01	1.94e-01
Rafter Mitigated	2.30e-06	1.28e-06	1.95e-06	2.12e-06	2.12e-06	4.63e-06	3.19e-06	2.60e-06	6.54e-06

7. CONCLUSIONS AND FUTURE WORK

7.1. Overview

In addressing the urgent need for resilient and sustainable communities, this study underscores the critical role of evaluating timber residential structures against seismic and hurricane hazards. The shift towards timber in construction, especially in disaster-stricken regions across the globe, marks a significant move towards sustainable architecture and engineering that meets both housing needs and environmental concerns. By thoroughly investigating the resilience of timber structures to earthquakes and hurricanes, this dissertation outlines a strategy for developing residential spaces that are not only sustainable and efficient but also capable of withstanding earth- and climate-related hazards, thereby enabling faster disaster recovery. Through a better understanding of the behavior of timber structures subjected to extreme loads associated with earthquake and wind hazards, the research presented in this thesis advocates for the development of more precise design methods. These methods not only enhance the structural efficiency of timber buildings, making them more competitive, but also empower engineers and researchers to integrate considerations of sustainability and resilience into building design. In doing so, the self-recovery of vulnerable communities is supported by making possible the implementation of cost-effective mitigation strategies that are accessible to these communities, and contributing to social justice in the wake of disasters. Thus, the findings of this thesis not only challenge existing design paradigms, but also pave the way for more sustainable building practices.

This study uses both numerical and experimental methods to analyze the effects of transverse shear walls, diaphragm stiffness, and gravity loads on shear wall performance in light-frame timber buildings under earthquake loads, using full-scale cyclic and scaled shake table tests. It explores the impact of Type X GWB on lateral responses and aims to refine predictive models for seismic resilience. Additionally, it assesses hurricane wind performance on informally-constructed light-frame timber houses, developing fragility curves for critical failure modes and evaluating mitigation measures. The study also considers future climate change scenarios, aiming to enhance resilience through improved design and mitigation strategies.

7.2. Contributions

Table 7.1 summarizes the theoretical and practical contributions of each chapter, while the specific conclusions of each chapter are presented in the following paragraphs.

Chapter 2 emphasized the importance of incorporating system effects into the structural design of light-frame timber buildings, particularly under seismic conditions. The impact of transverse shear walls, the out-of-plane bending stiffness of the diaphragms, and the influence of gravity loads on the lateral response of non-planar wood-frame shear walls with details representative of mid-rise timber buildings was examined. Two types of wall-to-wall perpendicular connections were evaluated, highlighting the advantages of slotted over screwed connections, particularly in terms of ease of installation and cyclic response. Furthermore, a study on a T-shaped wood-frame shear wall revealed significant improvements in lateral stiffness and strength for non-planar shear walls compared to planar ones, due to the effect of transverse shear walls. However, these enhancements were offset by a reduced deformation capacity in the T-shaped shear wall relative to its planar counterpart. Nevertheless, when the effects of diaphragms and gravity loads are considered alongside transverse shear walls, the mean deformation capacity becomes comparable to that of planar shear walls. Designing with system effects in mind leads to buildings that are stronger, stiffer, and have nearly the same deformation capacity as those designed with planar shear walls. Consequently, this leads to a lower wall density, necessitating an urgent reconsideration of seismic performance factors in light of these system effects. The study demonstrated that the collector beam in a wood-frame diaphragm primarily determines the impact of the diaphragm's out-of-plane bending stiffness on the lateral response of wood-frame shear walls. Additionally, it was found that high stress concentration at the web-to-flange connections can lead to premature failure of the nailed OSB-to-wood frame connections, a problem that can be mitigated by specifying a denser nail pattern.

In **Chapter 3**, the study delved deeper into the system effects on light frame timber buildings through shake table testing. The findings highlighted the significant influence of the interactions between structural components (i.e., system effects) on the building performance against lateral loads. The critical system effects identified were the effect of transverse shear walls, the out-of-plane bending stiffness of the diaphragms, and gravity loads, which collectively reduce story drift demands, enhance lateral stiffness, and increase the damping ratio of light frame timber buildings compared to current analytical and numerical models. This chapter emphasizes the need for refining current analytical models to better capture the system effects and proposes a first simplistic numerical model. This model aims to achieve system effects in the design of light-frame timber buildings, hence achieving safer and more efficient structural designs.

Chapter 4 investigated the influence of the finish layers used for fire protection, such as Type X GWB, on the cyclic lateral response of wood-frame strong shear walls. The effect of finish layers leads to increased values of stiffness and strength, without compromising the deformation capacity of a wood-frame shear wall. This increased strength could potentially result in a lower wall density in building designs, while the increased stiffness means that the drift demand will be reduced. Moreover, the increased stiffness could lead to an overestimation of the building's natural period, and consequently, an underestimation of the seismic demands on the building. A numerical and analytical model was proposed and demonstrated the ability to accurately replicate the experimental findings. Additionally, it provided the shear strength and stiffness input values essential for designing light-frame timber buildings, taking into account the impact of Type X GWB finish layers in the scenario of a wood-frame shear wall with two layers of Type X GWB on each side, corresponding to a 2-hour fire-rated shear wall. This chapter also highlighted the need for further research to fully understand and integrate the effect of finish layers into seismic design methodologies.

Chapter 5 expands on the impact of Type X GWB finish layers and their connections on the lateral response of wood-frame strong shear walls, exploring configurations not covered in **Chapter 4**. Through a combination of parametric numerical analysis and experimental data, this chapter assesses how different factors—such as the quantity of Type X GWB layers per side, the type of fasteners for securing these layers, the overturning restraint system, and the wall's aspect ratio—affect the performance of the shear walls. Additionally, the study sought to explain why shear walls with multiple Type X GWB finish layers do not have less deformation capacity than those without finish layers. The key to this phenomenon lies in the fact that Type X GWB finish layers and their connections not only bolster strength and stiffness but also enhance the performance of internal connections. This reinforcement allows nails and internal screws to increase their deformation capacity, as the pull-out of these connections is effectively counteracted by the reinforcing effect of the finish layers.

Chapter 6 studied the hurricane performance of light-frame timber houses in Puerto Rico, with emphasis on the development of fragility curves and the evaluation of the impact of both current and future climate change scenarios. Annual probabilities of failure were calculated and compared with the thresholds set by ASCE 7 (ASCE, 2022). Assessments revealed high failure risks in Puerto Rico's informally-constructed houses against hurricanes. Effective mitigation, especially reinforcing the roof to wall connections, significantly lowered failure probabilities. However, resource and knowledge gaps impede the adoption of these measures, highlighting a need for enhanced support and awareness to communities. The chapter underlined the urgency of updating building standards in response to anticipated climate changes, with a focus on bolstering community resilience to escalating hurricane risks.

Overall, this thesis has made significant contributions by providing valuable insights into the design and resilience of light-frame timber structures. The need for a holistic approach to structural design has been underscored, incorporating not just traditional issues but also overlooked aspects such as finish layers, system effects, and climate change impacts. The findings and recommendations of this thesis pave the way for the development of more robust, efficient, and sustainable timber building practices, especially in regions that are vulnerable to seismic and hurricane activities. Furthermore, many findings of this research have rendered solutions that may be significantly cost-competitive, which are strongly needed to really achieve a broader adoption of more sustainable structural designs in developing countries where economical aspects commonly govern any design decision. Proper consideration of wall finishes and system effects may make timber construction more feasible than less sustainable alternatives in developing countries such as Chile or Puerto Rico.

Table 7.1. Summary of contributions by dissertation chapter

Chapter/Citation	Theoretical Contributions	Practical Contributions
Chapter 2. **Valdivieso, D.**, Almazan, J.L, Lopez-Garcia, D. , Montano, J., Liel, A., & Guindos, P. (2024). System effects in T-shaped timber shear walls: effects of transverse walls, diaphragms, and axial loading. *Earthquake Engineering & Structural Dynamics*.	This study quantifies the system effects at the assembly level in non-planar T-shaped shear walls, identifying key failure modes that dictate their behavior under lateral cyclic loading. To my knowledge, this is the first presentation of the hysteretic response of a non-planar T-shaped wood-frame shear wall configuration, providing fresh perspectives on structural performance.	This study demonstrates how non-planar shear walls, the effects of diaphragm out-of-plane bending stiffness, and gravity loads can affect performance and therefore design requirements. Transverse shear walls enhance all engineering parameters, except deformation capacity, compared to planar shear walls. Yet, considering diaphragm and gravity load effects alongside transverse shear walls, mean deformation becomes comparable to that of planar shear walls. Additionally, a practical guideline is introduced for estimating the stiffness of wall-to-wall perpendicular connections. This guideline ensures the engagement of transverse shear walls in the in-plane lateral response, akin to the monolithic elements in concrete shear walls. Moreover, mitigation measures are proposed for addressing stress concentrations at the joint between longitudinal and transverse shear walls, enhancing overall structural integrity.

Chapter/Citation	Theoretical Contributions	Practical Contributions
Chapter 3. **Valdivieso, D.**, Quizanga, D., Almazan, J.L, Guindos, P., Lopez-Garcia, D. , Liel, A., Lopez, N., & Hernandez, F. (Under Review). Shake Table Testing for System Effects Analysis in a 1:2 Scale Three-Story Light Frame Timber Building. *Earthquake Spectra,* Submitted 02/24.	The study demonstrates that system effects greatly impact the dynamic response of light frame timber buildings with U- and L-shaped shear walls. It shows that these interactions lead to increased lateral stiffness, decreased story drift demands, and higher damping ratios, thus challenging the accuracy of existing numerical and analytical models by pointing out their underestimation of these essential factors.	Due to the effects of system effects, this study demonstrates the need to improve seismic design standards. The study introduced a numerical model formulation designed to incorporate system effects into the design of light-frame timber buildings. This approach involves adjusting existing analytical models as outlined in the SDPWS (ANSI/ AWC, 2021), enabling a more comprehensive consideration of how these buildings respond to seismic forces.
Chapter 4. **Valdivieso, D.**, Guindos, P., Montaño, J., & Lopez-Garcia, D. (2023). Experimental investigation of multi-layered strong wood-frame shear walls with nonstructural Type X gypsum wallboard layers under cyclic load. *Engineering Structures*, 282, 115797.	The study demonstrates that fire protection layers can enhance all engineering parameters of a wood-frame strong shear wall without leading to brittle failure modes. This challenges the 'conservative' approach of excluding finish layers in the design of light-frame timber buildings and supports the argument for improving structural efficiency by considering the structural effects of fire protection in light-frame timber buildings.	The study proposes design strength values and a dual approach, numerical and analytical, for integrating Type X GWB finish layers in the seismic design of light-frame timber buildings. This enables practical engineers to incorporate these layers in timber structures to enhance resilience against seismic loads.

Chapter/Citation	Theoretical Contributions	Practical Contributions
Chapter 5. Valdivieso, D., Lopez-Garcia, D. , Liel, A., & Guindos, P. (Under Review). Reinforcement Effects and Parametric Study of the Lateral Response of Multi-layered Wood-Frame Shear Walls: An Experimental and Numerical Investigation. *Journal of Structural Engineering/ASCE Library,* Submitted 06/23.	The research investigates the impact of Type X finish layers utilized for fire protection, quantifying the reinforcement effect these layers offer. This reinforcement effect is primarily why the deformation capacity of multi-layered wood-frame shear walls is fundamentally comparable to that of bare wood-frame shear walls. Furthermore, it demonstrates how this reinforcement effect can be numerically incorporated at the assembly level, drawing from data obtained from connection-level testing.	In the design of light-frame timber buildings, incorporating finish layers necessitates careful attention to two crucial aspects: the selection of fasteners for attaching these layers and the quantity of finish layers applied per side. These factors, namely the type of fastener and the number of finish layers per side, are paramount in influencing the peak strength, stiffness, deformation capacity, and energy dissipation of the shear walls.
Chapter 6. Valdivieso, D., Liel, A., Javernick-Will, A., Goldwyn, B., Lopez-Garcia, D., & Guindos, P. (under review). Potential for Mitigating Hurricane Wind Impact on Informally-Constructed Homes in Puerto Rico under Current and Future Climate Scenarios*International Journal of Disaster Risk Reduction.* Submitted 03/24.	The study enhances knowledge on the effects of hurricanes on informally-constructed light-frame timber homes by creating fragility curves for different performance levels. It pinpoints the most impactful mitigation strategies for lowering annual failure probabilities. Furthermore, the study identifies the wind speed critical failure ranges linked to failure probabilities and compares against current design values and assesses how anticipated climate change scenarios could affect these outcomes.	This research offers actionable insights for enhancing the resilience of light-frame timber houses in Puerto Rico against hurricanes, identifying the roof to wall connection as particularly critical. By identifying the most effective mitigation measure for reducing annual probability of failure, particularly reinforcing roof-to-wall connections, it provides a clear path for improving housing safety and sustainability in face of current and future climate change scenarios.

7.3. Future Research

This thesis describes an in-depth structural analysis at various levels (connection, assembly, and building) to investigate the impact of system effects and fire protection finish layers on the lateral response of wood-frame structures. Additionally, the resilience of informally-constructed timber houses in Puerto Rico under current and future climate scenarios has also been examined. The subsequent paragraphs outline future directions for research in these areas. Regarding system effects, future work should include more experimental investigations on non-planar shear walls with details different from those of the walls tested in this thesis, particularly at the assembly level. Of particular importance is the accurate characterization of T-, L-, and U-shaped shear walls, both wood-frame and CLT, with varying details in the overturning restraint systems, such as conventional or continuous hold-downs. The development of robust numerical models that can accurately simulate the nonlinear response of non-planar shear walls is also essential. These models should be based on connection-level data and validated against assembly-level experimental results. Another interesting issue is a more exhaustive analysis of system effects at the global level (rather than at the local level), such as for instance the global overturning of diaphragms leading to global areas under tensile forces versus globally compressed areas.

Furthermore, some of the system effects researched in this investigation may be equally or even more relevant in other timber structural systems, such as mass timber systems, and in particular cross laminated timber systems (CLT). In the latter structural typology, rigid deformations of shear walls (sliding and rocking) are known to be even larger than in light frame timber buildings, therefore system effects considerations might be of significant relevance. Regarding the evaluation of fire protection finish layers in timber buildings, further research should aim at broadening the test matrix at both the connection and assembly levels. This includes examination of shear walls with different details at different stories of a building, as finish layers might play a more crucial role at the upper stories. Attention should also be paid to experimental tests of shear walls with varying aspect ratios, one or two Type X GWB layers, different hold-down types, and stapled connections.

These tests will deepen our understanding of multi-layered strong shear walls and enhance the accuracy of the proposed nonlinear numerical model.

With improved numerical models that account for system effects and the effects of finish layers, the focus should shift to the assessment of these effects at the building level. The goal is to quantify seismic performance factors that account for these effects. In doing so such effects are incorporated into the seismic design practice, thereby more efficient structural designs will be achieved. Additionally, in the context of Performance-Based Earthquake Engineering, future research should concentrate on establishing performance metrics for timber buildings that take into account both system and finish effects. This includes, as an example, the development of damage fragility curves for structural components with non-planar configurations and the incorporation of finish layers as key structural contributors.

In terms of building resilient communities in Puerto Rico (and other countries in the world), while current and future climate scenarios and their impact on the failure probability of informal constructions have been evaluated, a more detailed analysis is needed. This should involve the development of a unified climate change scenario for the entire island and the consequent re-evaluation of the probability of failure. This will not only assist policymakers in revising design codes but also play a crucial role in informing and engaging local communities in taking proactive preparatory measures. Given Puerto Rico's recent experiences with earthquakes and hurricanes (the latter causing intensive floodings), future research should also focus on evaluating the annual probability of failure from multiple hazards and proposing mitigation measures to reduce the vulnerability to these compounded risks.

REFERENCES

Acevedo, N. (2019). *Housing is key to puerto rico's recovery. will 2019 see promised funding, solutions?* NBC News. Retrieved from https://www.nbcnews.com/news/latino/housing-key-puerto-rico-s-recovery-will-2019-see-promised-n959776 (Accessed: February 29, 2024)

Algoed, L., & Hernandez Torrales, M. (2019). The land is ours. vulnerabilization and resistance in informal settlements in puerto rico: Lessons from the cano martin pena community land trust. *Radical Housing Journal*, *1*(1), 29–47.

Amini, M. O., & van de Lindt, J. W. (2014). Quantitative insight into rational tornado design wind speeds for residential wood-frame structures using fragility approach. *Journal of Structural Engineering*, *140*(7), 04014033.

APA. (2012). *Panel design specification.* (The Engineering Wood Association)

ASCE. (n.d.). *ASCE 7 hazard tool.* https://asce7hazardtool.online/. American Society of Civil Engineers. (Accessed June to November 2023)

ASCE. (2022). *Minimum design loads for buildings and other structures*. Reston, VA: American Society of Civil Engineers. (ASCE/SEI 7-22)

Asiz, A., Chui, Y. H., Doudak, G., Ni, C., & Mohammad, M. (2011). Contribution of plasterboard finishes to structural performance of multi-storey light wood frame buildings. *Procedia Engineering*, *14*, 1572–1581.

ASTM. (2006). Standard practice for establishing clear wood strength values [Computer software manual]. West Conshohocken, Pennsylvania. (Standard D2555-06)

ASTM. (2006). *Standard practice for static load test for shear resistance of framed walls for buildings astm e564-06.* (ASTM International: West Conshohocken)

ASTM. (2016). *Standard test methods for shear modulus of wood-based structural panels astm e3044-16.* (ASTM International: West Conshohocken)

ASTM. (2019). *Standard test methods for cyclic (reversed) load test for shear resistance* *of vertical elements of the lateral force resisting systems for buildings astm e2126-19.* (ASTM International: West Conshohocken)

ASTM. (2021). *Standard specification for driven fasteners: Nails, spikes, and staples.* (ASTM F1667. West Conshohocken, PA: ASTM)

ATC. (2007). *Interim testing protocols for determining the seismic performance characteristics of structural and nonstructural components.* Applied Technology Council. (FEMA 461. Washington, USA)

AWC. (2018). *National design specification for wood construction*. Leesburg, VA: American Wood Council. (ANSI/AWC NDS-2018)

AWC. (2021). *Special design provisions for wind and seismic.* (ANSI/AWC SDPWS-2021. Leesburg, VA: American Wood Council)

Bagheri, M., Doudak, G., & Gong, M. (2019). Impact of out-of-plane stiffness of the diaphragm on deflection of wood light-frame shear walls. *International Journal of Civil & Environmental Engineering*, *13*(7), 359-364.

Bagheri, M. M. (2018). *Study of deflection of single and multi-storey light frame wood shear walls* (Unpublished doctoral dissertation). Université d'Ottawa/University of Ottawa.

Bahmani, P., & van de Lindt, J. W. (2016). Experimental and numerical assessment of woodframe sheathing layer combinations for use in strength-based and performance-based design. *Journal of Structural Engineering*, *142*(4), E4014001.

Benedetti, F., Jara-Cisterna, A., Grandon, J., Astroza, N., & Opazo-Vega, A. (2022). Numerical analysis of the seismic performance of light-frame timber buildings using a detailed model. *Buildings*, *12*(7), 981. doi: 10.3390/buildings12070981

Berwart, S., Estrella, X., Montaño, J., Santa-María, H., Almazán, J. L., & Guindos, P. (2022). A simplified approach to assess the technical prefeasibility of multistory wood-frame buildings in high seismic zones. *Engineering Structures*, *257*, 114035.

Bhowmik, S., Pang, W., & Stoner, M. (2023, July 9-13). Probabilistic modeling of north atlantic ocean hurricane spawn considering climate change. In *Proceedings of the 14th international conference on applications of statistics and probability in civil* *engineering, icasp14.* Dublin, Ireland.

Botzen, W. W., Deschenes, O., & Sanders, M. (2019). The economic impacts of natural disasters: A review of models and empirical studies. *Review of Environmental Economics and Policy*.

Boughton, G. (1988). Full scale structural testing of houses under cyclonic wind loads. In *Proceedings of the international timber engineering conference, forest products society* (Vol. 2, p. 82-88). Madison, WI.

Brueggen, B. (2009). *Performance of t-shaped reinforced concrete structural walls under multi-directional loading* (Unpublished doctoral dissertation). University of Minnesota.

BSI. (2008). *BS EN 14592: 2008+ A1: 2012. timber structures–dowel-type fasteners–requirements.*

Carcamo, S., María, H., & Zisis, S. (2018). Wood frame shear wall model for a finite element program through a shell element. In *Proceedings of the world conference on timber engineering.* Seoul, Republic of Korea.

Carcamo, S. I. (2017). *Modelo de muros marco plataforma para un programa de elementos finitos mediante elementos are* . Universidad Federico Santa Maria, Valparaiso. ([Tesis para optar al titulo de Ingeniero Civil en Obras Civiles])

Carrero, T., Montano, J., Santa-Maria, H., & Guindos, P. (2020). Static and dynamic performance of direct hybrid connections of cross-laminated timber with steel, concrete and laminated strand lumber composites. *Latin American Journal of Solids and Structures*, *17*.

Casagrande, D., Grossi, P., & Tomasi, R. (2016). Shake table tests on a full-scale timber-frame building with gypsum fibre boards. *European Journal of Wood and Wood Products*, *74*(3), 425–442.

Ceccotti, A. (2008). New technologies for construction of medium-rise buildings in seismic regions: the xlam case. *Structural Engineering International*, *18*(2), 156–165.

Ceccotti, A., Sandhaas, C., Okabe, M., Yasumura, M., Minowa, C., & Kawai, N. (2013).

Sofie project–3d shaking table test on a seven-storey full-scale cross-laminated timber building. *Earthquake Engineering & Structural Dynamics*, *42*(13), 2003–2021.

Chen, Z., Chui, Y. H., Doudak, G., & Nott, A. (2016). Contribution of type-x gypsum wall board to the racking performance of light-frame wood shear walls. *Journal of Structural Engineering*, *142*(5), 04016008.

Cheng, J. (2004). Testing and analysis of the toe-nailed connection in the residential roof-to-wall system. *Forest Products Journal*, *54*(4).

Collins, M., Kasal, B., Paevere, P., & Foliente, G. (2005a). Three-dimensional model of light frame wood buildings. ii: Experimental investigation and validation of analytical model. *Journal of Structural Engineering*, *131*(4), 684-692.

Collins, M., Kasal, B., Paevere, P., & Foliente, G. (2005b). Three-dimensional model of light frame wood buildings. i: Model description. *Journal of Structural Engineering*, *131*(4), 676-683.

Comerio, M. (1998). *Disaster hits home: New policy for urban housing recovery*. Berkeley, CA: University of California Press.

Constantin, R. (2016). *Seismic behaviour and analysis of u-shaped rc walls* (Unpublished doctoral dissertation). EPFL. (https://doi.org/10.5075/epfl-thesis-7133)

Cramer, S. M., Friday, O. M., White, R. H., & Sriprutkiat, G. (2003). Mechanical properties of gypsum board at elevated temperatures. In *Proceedings of the fire and materials 2003: 8th international conference* (pp. 33–42). San Francisco, CA, USA: Interscience Communications Limited.

Cruzado, H. J., & Pacheco-Crosetti, G. E. (2018). General overview and case studies of damages in puerto rico due to hurricane maria. In *Proceedings of the forensic engineering 2018: Forging forensic frontiers* (pp. 986–996). Reston, VA.

D'Arenzo, G., Schwendner, S., & Seim, W. (2021). The effect of the floor-to-wall interaction on the rocking stiffness of segmented clt shear-walls. *Engineering Structures*, *249*, 113219.

Dinehart, D. W., & Blasetti, A. S. (2012). Comparison of energy dissipation, stiffness, and damage of structural oriented strand board (osb), conventional gypsum, and viscoelastic gypsum shearwalls subjected to cyclic loads. *Buildings*, *2*(3), 173–202.

Dolan, J., & Heine, C. (1997). *Sequential phased displacement tests of wood framed shear walls with corners.* Blacksburg, VA. (Prepared for the NAHB Research Center, Inc. by Virginia Polytechnic Institute and State University)

Dolan, J. D., & Madsen, B. (1992). Monotonic and cyclic nail connection tests. *Canadian Journal of Civil Engineering*, *19*(1), 97–104.

Dorkenoo, K., Scown, M., & Boyd, E. (2022). A critical review of disproportionality in loss and damage from climate change. *Wiley Interdisciplinary Reviews: Climate Change*, *13*(4), e770.

Doudak, G., & Smith, I. (2009). Capacities of osb-sheathed light-frame shear-wall panels with or without perforations. *Journal of Structural Engineering*, *135*(3), 326–329.

Ellingwood, B. R., Rosowsky, D. V., Li, Y., & Kim, J. H. (2004). Fragility assessment of light-frame wood construction subjected to wind and earthquake hazards. *Journal of Structural Engineering*, *130*(12), 1921–1930. doi: 10.1061/(ASCE)0733-9445(2004)130:12(1921)

Ellingwood, B. R., & Tekie, P. B. (1999). Wind load statistics for probability-based structural design. *Journal of Structural Engineering*, *125*(4), 453–463.

EN. (2004). *Eurocode 5 - design of timber structures - part 1-1: General – common rules and rules for buildings.* (1995-1-1:2004+AC:2006+A1:2008, Brussels, Belgium: CEN, European Committee for Standardization)

Estrella, X., Guindos, P., Almazan, J. L., & Malek, S. (2020). Efficient nonlinear modeling of strong wood frame shear walls for mid-rise buildings. *Engineering Structures*, *215*, 110670.

Estrella, X., Guindos, P., Almazán, J., Malek, S., Santa María, H., Montaño, J., & Berwart, S. (2021). Seismic performance factors for timber buildings with woodframe shear walls. *Engineering Structures*, *248*, 113185.

Estrella, X., Malek, S., Almazan, J. L., Guindos, P., & Santa Maria, H. (2021). Experimental study of the effects of continuous rod hold-down anchorages on the cyclic response of wood frame shear walls. *Engineering Structures*, *230*, 111641.

Federal Emergency Management Agency. (2012). *Seismic evaluation and retrofit of multi-unit wood-frame buildings with weak first stories* (Tech. Rep. No. FEMA P807). Washington, DC: Applied Technology Council.

Feliciano, D., Arroyo, O., Liel, A., Murray, P., & Carrillo, J. (2022). A framework to assess the seismic vulnerability of informally constructed houses: A case study in villavicencio, colombia. In *Proceedings of the 12th national conference in earthquake engineering.* Salt Lake City.

FEMA Mitigation Assessment Team (MAT). (2018). Hurricanes irma and maria in puerto rico: Building performance observations, recommendations, and technical guidance [Computer software manual]. `https://www.fema.gov/sites/default/files/2020-07/mat-report_hurricane-irma-maria-puerto-rico_2.pdf`. (FEMA P-2022)

Filiatrault, A., Christovasilis, I. P., Wanitkorkul, A., & van de Lindt, J. W. (2010). Experimental seismic response of a full-scale light-frame wood building. *Journal of Structural Engineering*, *136*(3), 246–254.

Filiatrault, A., Fischer, D., Folz, B., & Uang, C. M. (2001). Shake table testing of a full-scale two-story woodframe house. In *Proceedings of the structures 2001: A structural engineering odyssey.* Washington, D.C., USA.

Filiatrault, A., Fischer, D., Folz, B., & Uang, C. M. (2002). Seismic testing of two-story woodframe house: Influence of wall finish materials. *Journal of Structural Engineering*, *128*(10), 1337–1345.

Fiorino, L., Macillo, V., & Landolfo, R. (2017). Shake table tests of a full-scale two-story sheathing-braced cold-formed steel building. *Engineering Structures*, *151*, 633–647.

Foliente, G. (1995). Discussion of "narrow plywood shear panels" by bl schmid, rj nielsen, and rr linderman. *Earthquake Spectra*, *11*(1), 161-163.

Foliente, G., Paevere, P., Macindoe, L., Banks, R., & Kasal, B. (2000). System effects and load-sharing in an l-shaped woodframe house. In *Proceedings of the world* *conference on timber engineering.*

Foliente, G. C. (1996). Issues in seismic performance testing and evaluation of timber structural systems. In *International wood engineering conference.* New Orleans, USA.

Folz, B., & Filiatrault, A. (2004a). Seismic analysis of woodframe structures. ii: Model implementation and verification. *Journal of Structural Engineering*, *130*(9), 1361–1370.

Folz, B., & Filiatrault, A. (2004b). Seismic analysis of woodframe structures. i: Model formulation. *Journal of Structural Engineering*, *130*(9), 1353–1360.

Fonseca, F. S., Rose, S. K., & Campbell, S. H. (2002). *Nail, wood screw, and staple fastener connections.* (Consortium of Universities for Research in Earthquake Engineering)

Fothergill, A., & Peek, L. (2004). Poverty and disasters in the united states: A review of recent sociological findings. *Natural Hazards*, *32*, 89–110. doi: 10.1023/B:NHAZ.0000026792.76181.d9

García, I. (2022). Deemed ineligible: Reasons homeowners in puerto rico were denied aid after hurricane maría. *Housing Policy Debate*, *32*(1), 14–34.

Girhammar, U., & Källsner, B. (2008). Effect of transverse walls on capacity of wood-framed wall diaphragms without tie-downs. In *Proceedings of the 10th world conference on timber engineering.* Miyazaki, Japan.

Goldwyn, B., Javernick-Will, A., & Liel, A. (2021). Dilemma of the tropics: Changes to housing safety perceptions, preferences, and priorities in multihazard environments. *Natural Hazards Review*, *22*(3), 04021012.

Goldwyn, B., Javernick-Will, A., Liel, A., & Koschmann, M. (2022). Designing a communication practice to build community capacity for safer housing. In *Proceedings of the construction research congress 2022* (p. 229-239).

Goldwyn, B., Javernick-Will, A., & Liel, A. B. (2022). Multi-hazard housing safety perceptions of those involved with housing construction in puerto rico. *Sustainability*, *14*(7), 3802.

Goldwyn, B., Vega, Y. G., Javernick-Will, A., & Liel, A. B. (2022). Identifying misalignments between the informal construction sector's perceptions and engineering assessments of housing safety in future disasters for capacity development. *International Journal of Disaster Risk Reduction*, *77*, 103105.

Goldwyn, B., Velasquez, C., Liel, A. B., Javernick-Will, A., & Koschmann, M. (2023). Capacity-building to support safer housing through appropriate hurricane strap use. *Natural Hazards Review*, *24*(3), 04023026.

Gonzalez, P., Valdivieso, D., Lopez, A., Perez, E., Gonzalez, A., Neira, J., ... Burgos, C. (2020). Experimental study of wall joints in cross laminated timber panels through cyclic test. In *Proceedings of the 17th world conference on earthquake engineering.* Sendai, Japan.

Goodall, S. I., & Gupta, R. (2011). Improving the performance of gypsum wallboard in wood frame shear walls. *Journal of Performance of Constructed Facilities*, *25*(4), 287–298.

Group, E. (2022). *Technical guidelines for type x gypsum wallboard.* (Accessed on: May 26, 2022. [Online]. Available: www.gyplac.com/es-cl/productos/gyplac-portafolio/placas-de-yeso/yeso-carton-resistente-fuego/)

Guinez, F., Santa Maria, H., & Almazan, J. L. (2019). Monotonic and cyclic behaviour of wood frame shear walls for mid-height timber buildings. *Engineering Structures*, *189*, 100–110.

Henderson, D. J., & Ginger, J. D. (2007). Vulnerability model of an australian high-set house subjected to cyclonic wind loading. *Wind and Structures*, *10*(3), 269-286.

Henderson, D. J., & Ginger, J. D. (2011). Response of pierced fixed corrugated steel roofing systems subjected to wind loads. *Engineering Structures*, *33*(12), 3290-3298.

Hernandez, F., Diaz, P., Astroza, R., Ochoa-Cornejo, F., & Zhang, X. (2021). Time variant system identification of superstructures of base-isolated buildings. *Engineering Structures*, *246*, 112697.

Hinojosa, J., & Meléndez, E. (2018). The housing crisis in puerto rico and the impact of hurricane maria. *Centro*, *24*.

Hopkins, A., Fell, B., Deierlein, G., & Miranda, E. (2014). *Large-scale tests of seismically enhanced planar walls for residential construction* [Report No. 186]. Stanford, USA.

INN. (1997). *Norma Chilena Oficial NCh 935/1 Of1997 Prevención de incendio en edificios - Ensayo de resistencia al fuego - Parte 1: Elementos de construcción en general.* Instituto Nacional de Normalización,Santiago, Chile. (in Spanish)

INN. (2009). *Norma Chilena Oficial NCh 433 f1996 Mod2009 Diseño Sismico de Edificios.* Instituto Nacional de Normalización, Santiago, Chile. (in Spanish)

INN. (2014). *Norma Chilena Oficial NCh 1198 Of2014 Madera - Construcciones en Madera – Cálculo.* Instituto Nacional de Normalización, Santiago, Chile. (in Spanish)

Isoda, H., Matsuda, M., Tesfamariam, S., & Tamori, S. (2021). Shake table test of full-size wooden houses versus wall test result: Comparison of load-deformation relationship. *Journal of Performance of Constructed Facilities*, *35*(5), 04021043.

Jayamon, J., Charney, F., Flores, F., & Line, P. (2016, August). Influence of wall load-displacement shape on seismic performance of wood-frame shear wall structures. In *Proceedings of the world conference on timber engineering.*

Jayamon, J. R., Line, P., & Charney, F. A. (2018). State-of-the-art review on damping in wood-frame shear wall structures. *Journal of Structural Engineering*, *144*(12), 03118003.

Juang, J.-N., Cooper, J., & Wright, J. (1988). An eigensystem realisation algorithm using data correlations (era/dc) for modal parameter identification. *Control - Theory and Advanced Technology*, *4*(1), 5–14.

Kharrazi, M. H. K., Ventura, C. E., Prion, H. G. L., Taylor, G. W., Lord, J. F., & Turek, M. (2002, June). Experimental evaluation of seismic response of woodframe residential construction. In *Proceedings of the 4th structural speciality conference of the canadian society for civil engineering* (pp. 1–9).

Kircher, C. A., Reitherman, R. K., Whitman, R. V., & Arnold, C. (1997). Estimation of earthquake losses to buildings. *Earthquake Spectra*, *13*(4), 703–720.

Kochkin, V., & McKee, S. (2001). *Wood shear walls with corners.* Upper Marlboro, MD. (Prepared for the U.S. Department of Housing and Urban Development Office of Policy Development and Research by NAHB Research Center, Inc.)

Koliou, M., van de Lindt, J. W., & Hamburger, R. O. (2018). Nonlinear modeling of wood-frame shear wall systems for performance-based earthquake engineering: Recommendations for the asce 41 standard. *Journal of Structural Engineering*, *144*(8), 04018095.

Kolozvari, K., Kalbasi, K., Orakcal, K., & Wallace, J. (2021). Three-dimensional shear-flexure interaction model for analysis of non-planar reinforced concrete walls. *Journal of Building Engineering*, *44*, 102946.

Konthesingha, K. C., Stewart, M. G., Ryan, P., Ginger, J., & Henderson, D. (2015). Reliability based vulnerability modelling of metal-clad industrial buildings to extreme wind loading for cyclonic regions. *Journal of Wind Engineering and Industrial Aerodynamics*, *147*, 176-185.

Krawinkler, H., Parisi, F., Ibarra, L., Ayoub, A., & Medina, R. (2001). *Development of a testing protocol for woodframe structures* (Tech. Rep.). Consortium of Universities for Research in Earthquake Engineering. (CUREE Report W-02, Task 1.3.2, Richmond (CA))

Kremer, P. D., & Symmons, M. A. (2015). Mass timber construction as an alternative to concrete and steel in the australia building industry: a pestel evaluation of the potential. *International Wood Products Journal*, *6*(3), 138-147.

Kuś, A., Mota, N., van Bueren, E., Carmona Báez, A., & Asselbergs, T. (2024). Designing for a flow: Navigating temporalities in housing considerations in low-income and hazard-prone caribbean contexts. *Buildings*, *14*(2), 327.

Lam, F., Prion, H. G., & He, M. (1997). Lateral resistance of wood shear walls with large sheathing panels. *Journal of Structural Engineering*, *123*(12), 1666–1673.

Lee, K. H., & Rosowsky, D. V. (2005). Fragility assessment for roof sheathing failure in high wind regions. *Engineering Structures*, *27*(6), 857-868.

Leung, T., Asiz, A., Chui, Y., Hu, L., & Mohammad, M. (2010). Predicting lateral deflection and fundamental natural period of multi-storey wood frame buildings. In *Proceedings of the 11th world conference on timber engineering.* Trentino, Italy.

Li, Y., & Ellingwood, B. R. (2006). Hurricane damage to residential construction in the us: Importance of uncertainty modeling in risk assessment. *Engineering Structures*, *28*(7), 1009-1018.

Li, Y., & Ellingwood, B. R. (2009). Framework for multihazard risk assessment and mitigation for wood-frame residential construction. *Journal of Structural Engineering*, *135*(2), 159-168.

Line, P., Hohbach, D., & Waltz, N. (2021). Gypsum wallboard finish contribution to the racking strength of wood-frame shear walls with representative multi-story details. In *Proceedings of the world conference on timber engineering.* Santiago, Chile.

Lochhead, M., Goldwyn, B., Venable, C., Liel, A. B., & Javernick-Will, A. (2022). Assessment of hurricane wind performance and potential design modifications for informally constructed housing in puerto rico. *Natural Hazards*, *112*(2), 1165-1189.

Lopez, N., Berwart, S., Guindos, P., & Montano, J. (2023). Modelacion de muros de madera en entramado ligero mediante elementos frame y link en software etabs para edificios de mediana altura. In *Proceedings of the congreso chileno de sismologia e ingenieria sismica - achisina.* Valparaiso, Chile.

Mahendran, M., & Tang, R. B. (1999). Pull-through strength of high tensile steel cladding systems. *Australian Structural Engineering Transactions*, *2*(1), 37-50.

Mao, C., Shen, Q., Shen, L., & Tang, L. (2013). Comparative study of greenhouse gas emissions between off-site prefabrication and conventional construction methods: Two case studies of residential projects. *Energy and Buildings*, *66*, 165-176.

Martin, K. G., Gupta, R., Prevatt, D. O., Datin, P. L., & van de Lindt, J. W. (2011). Modeling system effects and structural load paths in a wood-framed structure. *Journal of Architectural Engineering*, *17*(4), 134–143.

McDowall, C. (1984). Qualitative assessment of whole house structural response to lateral wind loads. In *Proceedings of the pacific timber engineering conference* (Vol. 1,

p. 519-526).

Mudd, L., Wang, Y., Letchford, C., & Rosowsky, D. (2014a). Assessing the impact of climate change on the us east coast hurricane hazard: Wind and rain. In *Proceedings of the structures congress 2014* (p. 1426-1436).

Mudd, L., Wang, Y., Letchford, C., & Rosowsky, D. (2014b). Hurricane wind hazard assessment for a rapidly warming climate scenario. *Journal of Wind Engineering and Industrial Aerodynamics*, *133*, 242–249.

Mukherji, A. (2017). *Post-disaster housing recovery.* Oxford Research Encyclopedia of Natural Hazard Science. Retrieved from `https://doi.org/10.1093/acrefore/9780199389407.013.82` (Retrieved 25 Feb. 2024)

Murray, P. B., Feliciano, D., Goldwyn, B. H., Liel, A. B., Arroyo, O., & Javernick-Will, A. (2023). Seismic safety of informally constructed reinforced concrete houses in puerto rico. *Earthquake Spectra*, *39*(1), 5-33.

NOAA National Centers for Environmental Information (NCEI). (2024). *U.s. billion-dollar weather and climate disasters.* Retrieved from `https://www.ncei.noaa.gov/access/billions/` doi: 10.25921/stkw-7w73

Opdyke, A., Goldwyn, B., & Javernick-Will, A. (2021). Defining a humanitarian shelter and settlements research agenda. *International Journal of Disaster Risk Reduction*, *52*, 101950.

Orellana, P., Santa María, H., Almazán, J., & Estrella, X. (2021). Cyclic behavior of wood-frame shear walls with vertical load and bending moment for mid-rise timber buildings. *Engineering Structures*, *240*, 112298.

Paevere, P. (2002). *Full-scale testing, modeling and analysis of light-frame structures under lateral loading* (Unpublished doctoral dissertation). University of Melbourne, Melbourne, Australia.

Pan, Y., Ventura, C. E., Bebamzadeh, A., & Motamedi, M. (2021). Modeling of a shake-table tested retrofitted wood-frame building subjected to subduction ground motions. *Earthquake Engineering & Structural Dynamics*, *50*(9), 2510–2528.

Pang, W., & Hassanzadeh Shirazi, S. M. (2013). Corotational model for cyclic analysis of light-frame wood shear walls and diaphragms. *Journal of Structural Engineering*, *139*(8), 1303–1317.

Pang, W. C., Rosowsky, D. V., Pei, S., & van de Lindt, J. W. (2007). Evolutionary parameter hysteretic model for wood shear walls. *Journal of Structural Engineering*, *133*(8), 1118-1129.

Partners, E. C. (2019). *Keep safe: A guide for resilient housing design in island communities.* `https://www.enterprisecommunity.org/resources/keep-safe-guide-resilient-housing-design-island-communities`. (Accessed February 29, 2024)

Peacock, W. G., Dash, N., Zhang, Y., & Van Zandt, S. (Eds.). (2018). *Post-disaster sheltering, temporary housing and permanent housing recovery*.

Pei, S., & van de Lindt, J. (2011). Seismic numerical modeling of a six-story light-frame wood building: comparison with experiments. *Journal Earthquake Engineering*, *15*(6), 924-941.

Pei, S., & van de Lindt, J. W. (2009). Coupled shear-bending formulation for seismic analysis of stacked wood shear wall systems. *Earthquake Engineering & Structural Dynamics*, *38*(14), 1631–1647.

Perez, E., Yanez, S., Gonzalez, P., Valdivieso, D., & Burgos, C. (2018). Experimental analysis of wall joints in cross-laminated timber panels requested by cyclic load. In *Proceedings of the world conference on timber engineering.* Seoul, Republic of Korea.

Quizanga, D., Almazan, J., Valdivieso, D., Lopez-Garcia, D., & Guindos, P. (2024). Shaking table test of a timber building equipped with a novel cost-effective, impact-resilient seismic isolation system. *Journal of Building Engineering*, *82*, 108402. doi: 10.1016/j.jobe.2023.108402

Rahmanian, I. (2011). *Thermal and mechanical properties of gypsum boards and their influences on fire resistance of gypsum board based systems* (Unpublished doctoral dissertation). The University of Manchester (United Kingdom).

Reyes, V., Graf, W. P., & Arnold, S. F. (2010). Strengthening of existing light-framed buildings with gypsum shear walls using a newly developed fiber reinforced polymer (frp) assembly. In *Proceedings of the improving the seismic performance of existing buildings and other structures* (pp. 1204–1212).

Rivera-Crespo, O., & Colón Rodríguez, Y. (2021). Casas resilientes en puerto rico: resistir al desastre redefiniendo la vivienda. *Revista de Arquitectura (Bogotá)*, *23*(2), 84-93. doi: 10.14718/RevArq.2021.2793

Ruggeri, E., D'Arenzo, G., Fossetti, M., & Seim, W. (2022). Investigating the effect of perpendicular walls on the lateral behavior of cross-laminated timber shear walls. *Structures*, *46*, 1679-1695.

Ruggeri, E. M., D'Arenzo, G., Cavoli, D. L., Cottonaro, R. D., & Fossetti, M. (2023). Experimental investigation on the lateral performance of clt shear walls connected to perpendicular walls. *Procedia Structural Integrity*, *44*, 464–471.

Sartori, T., Casagrande, D., Tomasi, R., & Piazza, M. (2012). Shake table test on 3-storey light-frame timber building. In *Proceedings of the world conference on timber engineering.* Auckland, New Zealand.

Sartori, T., & Tomasi, R. (2013). Experimental investigation on sheathing-to-framing connections in wood shear walls. *Engineering Structures*, *56*, 2197–2205.

Seible, F., Filiatrault, A., & Uang, C. (1999). *Proceedings of the invitational workshop on seismic testing, analysis and design of woodframe construction.* Richmond, USA: Consortium of Universities for Research in Earthquake Engineering. (CUREE Publication No. W-01)

Seim, W., Kramar, M., Pazlar, T., & Vogt, T. (2016). Osb and gfb as sheathing materials for timber-framed shear walls: Comparative study of seismic resistance. *Journal of Structural Engineering*, *142*(4), E4015004.

Severino, K., Figueroa, D. I., Hinojosa, J., Roman, N., & Melendez, E. (2018). *Puerto rico one year after hurricane maria* (Tech. Rep.). Center for Puerto Rican Studies, Hunter College.

Simpson Strong-Tie. (2021). *Strong-rod® systems: Seismic and wind restraint system guide.* (`https://sstoolbox.widen.net/view/pdf/mgxhrd0gvs/F`

-L-SRS21.pdf?t.download=true&ul=cjmyin)

Snaiki, R., & Parida, S. S. (2023). Climate change effects on loss assessment and mitigation of residential buildings due to hurricane wind. *Journal of Building Engineering*, *69*, 106256.

Stewart, M. G., Ginger, J. D., Henderson, D. J., & Ryan, P. C. (2018). Fragility and climate impact assessment of contemporary housing roof sheeting failure due to extreme wind. *Engineering Structures*, *171*, 464-475.

Stewart, M. G., Ryan, P. C., Henderson, D. J., & Ginger, J. D. (2016). Fragility analysis of roof damage to industrial buildings subject to extreme wind loading in non-cyclonic regions. *Engineering Structures*, *128*, 333-343.

Stoner, M. (2020). *Performance of cross-laminated timber as a residential building material subject to tornado events* (Unpublished doctoral dissertation). Clemson University, Clemson, USA.

Stoner, M., & Pang, W. (2020). Simulated performance of cross-laminated timber residential structures subject to tornadoes. *Frontiers in Built Environment*, *6*, 88.

Stoner, M., & Pang, W. (2021). Tornado hazard assessment of residential structures built using cross-laminated timber and light-frame wood construction in the us. *Natural Hazards Review*, *22*(4), 04021032.

Sugiyama, H., & Isono, R. (1983). The effect of perpendicularly arranged wall on the shear strength of plywood sheathed wall. In *Proceedings of the 1983 annual meeting, architectural institute of japan.* Tokyo, Japan.

Suzuki, S. (1990). Effect of cross-walls on lateral stiffness of light-frame buildings. In *Proceedings of the international timber engineering conference.* Tokyo, Japan.

Swensen, S., Deierlein, G. G., & Miranda, E. (2016). Behavior of screw and adhesive connections to gypsum wallboard in wood and cold-formed steel-framed wallettes. *Journal of Structural Engineering*, *142*(4), E4015002.

Talbot, J., Poleacovschi, C., & Hamideh, S. (2022). Socioeconomic vulnerabilities and housing reconstruction in puerto rico after hurricanes irma and maria. *Nat Hazards*, *110*, 2113–2140. Retrieved from https://doi.org/10.1007/

s11069-021-05027-7 doi: 10.1007/s11069-021-05027-7

Tamagnone, G., Rinaldin, G., & Fragiacomo, M. (2020). Influence of the floor diaphragm on the rocking behavior of clt walls. *Journal of Structural Engineering*, *146*(3), 04020010.

The Saffir-Simpson Team. (2019). *The saffir-simpson hurricane wind scale.* https://www.nhc.noaa.gov/pdf/sshws.pdf.

Thurton, D. A. W., Sabnis, G., & Raval, P. (2013). Performance of various semi-engineered roof deck systems under high velocity winds. *Scientia Iranica*, *20*(1), 34-43.

Tomasi, R., Sartori, T., Casagrande, D., & Piazza, M. (2015). Shaking table testing of a full-scale prefabricated three-story timber-frame building. *Journal Earthquake Engineering*, *19*(3), 505-534.

Tyrell, T. (2007). *Full-scale three dimensional wood structure test project.* (Detailed information available at: http://www.strongtie.com/news/industry/wall-bracing/3Dtest/index.html. Accessed 15 October 2008.)

Uang, C. M., & Gatto, K. (2003). Effects of finish materials and dynamic loading on the cyclic response of woodframe shearwalls. *Journal of Structural Engineering*, *129*(10), 1394–1402.

Ugalde, D., & Lopez-Garcia, D. (2020). Analysis of the seismic capacity of chilean residential rc shear wall buildings. *Journal of Building Engineering*, *31*, 101369.

UNISDR. (2005). *Hyogo framework for action 2005–2015: Building the resilience of nations and communities to disasters* (Tech. Rep.). Geneva: The United Nations International Strategy for Disaster Reduction. (Extract from the final report of the World Conference on Disaster Reduction (A/CONF. 206/6))

Valdivieso, D., Guindos, P., & Lopez-Garcia, D. (2022, June). Monotonic and cyclic characterization of multilayer sheathing-to-wood frame connection. In *Proceedings of the 12th us national conference on earthquake engineering.* Salt Lake City, USA.

Valdivieso, D., Guindos, P., Montaño, J., & Lopez-Garcia, D. (2023). Experimental investigation of multi-layered strong wood-frame shear walls with nonstructural type x gypsum wallboard layers under cyclic load. *Engineering Structures*, *282*, 115797.

Valdivieso, D., Lopez-Garcia, D., Almazán, J., Montaño, J., & Guindos, P. (2023). Testing the influence of 3d coupling effects on the lateral response of non-planar t-shape wood frame shear walls. In *Proceedings of the world conference on timber engineering.* Oslo, Norway. (DOI: 10.52202/069179-0283)

van de Lindt, J. W. (2008). Experimental investigation of the effect of multiple earthquakes on woodframe structural integrity. *Practice Periodical on Structural Design and Construction*, *13*(3), 111–117.

van de Lindt, J. W., & Dao, T. N. (2009). Performance-based wind engineering for wood-frame buildings. *Journal of Structural Engineering*, *135*(2), 169-177.

van de Lindt, J. W., & Liu, H. (2007). Nonstructural elements in performance-based seismic design of wood frame structures. *Journal of Structural Engineering*, *133*(3), 432–439.

van de Lindt, J. W., Pei, S., Liu, H., & Filiatrault, A. (2010). Three-dimensional seismic response of a full-scale light-frame wood building: Numerical study. *Journal of Structural Engineering*, *136*(1), 56–65.

van de Lindt, J. W., Pei, S., Pryor, S. E., Shimizu, H., & Isoda, H. (2010). Experimental seismic response of a full-scale six-story light-frame wood building. *Journal of Structural Engineering*, *136*(10), 1262–1272.

van de Lindt, J. W., Pryor, S. E., & Pei, S. (2011). Shake table testing of a full-scale seven-story steel–wood apartment building. *Engineering Structures*, *33*(3), 757–766.

Vasquez, L., Hernandez, G., Campos, R., & Gonzalez, M. (2012). *Caracterizacion mecanica de muros estructurales de madera* (Tech. Rep. No. Reporte N°191). Chile: Instituto Forestal.

Venable, C., Liel, A. B., Kijewski-Correa, T., & Javernick-Will, A. (2021). Wind performance assessment of postdisaster housing in the philippines. *Natural Hazards Review*, *22*(4), 04021033.

Ventura, C. E., Motamedi, M., Pan, Y., Tesfamariam, S., & Xiong, H. (2023). Drift- and energy-based seismic performance assessment of retrofitted wood frame shear wall buildings: Shake table tests. *Earthquake Engineering & Structural Dynamics*, *52*(6), 1844–1860.

Vickery, P. J., Liu, F., & Lin, J. X. (2023). Development of topographic wind speedups and hurricane hazard maps for puerto rico. *Journal of Structural Engineering*, *149*(10), 04023130.

Vickery, P. J., Quayyum, S., Liu, F., Mudd, L. A., Lavelle, F. M., Rozelle, J., ... Zuzak, C. (2023). Hazus hurricane wind model for the us caribbean territories: Hazard modeling and development of residential damage functions. *Natural Hazards Review*, *24*(4), 04023033.

Vickery, P. J., Skerlj, P. F., Lin, J., Twisdale Jr, L. A., Young, M. A., & Lavelle, F. M. (2006). Hazus-mh hurricane model methodology. ii: Damage and loss estimation. *Natural Hazards Review*, *7*(2), 94-103.

Viveiros, J., & Sturtevant, L. (2014). *Planning for post-disaster recovery briefing papers: Affordable housing.* Washington DC: American Planning Association, Federal Emergency Management Association.

Westenenk, B., de la Llera, J., Junemann, R., Hube, M., Besa, J., Luders, C., ... Jordan, R. (2013). Analysis and interpretation of the seismic response of rc buildings in concepcion during the february 27, 2010, chile earthquake. *Bulletin of Earthquake Engineering*, *11*(1), 69–91.

White, T., & Ventura, C. (2007, June). Seismic behaviour of residential wood-frame construction in british columbia: Part ii–performance requirements. In *Proceedings of the ninth canadian conference on earthquake engineering.*

White, T. W., & Ventura, C. (2007, June). Seismic behavior of residential wood-frame construction in british-columbia: Part i—modeling and validation. In *Proceedings of the 9th canadian conference on earthquake engineering* (pp. 935–944).

Winkel, M., & Smith, I. (2010). Structural behavior of wood light-frame wall segments subjected to in-plane and out-of-plane forces. *Journal of Structural Engineering*, *136*(7), 826-836.

Wolfe, R. W. (1983). *Contribution of gypsum wall board to racking resistance of light-frame walls* (Vol. 439; Tech. Rep.). US Department of Agriculture, Forest Service, Forest Products Laboratory.

Zhang, Z., & Li, B. (2016). Seismic performance assessment of slender t-shaped reinforced concrete walls. *Journal of Earthquake Engineering*, *20*(8), 1342-1369. (DOI: 10.1080/13632469.2016.1140097)

APPENDIX

A. CO-AUTHORED SHAKE TABLE TEST OF AN ISOLATED LIGHT-FRAME TIMBER BUILDING JOURNAL ARTICLE

Shaking table test of a timber building equipped with a novel cost-effective, impact-resilient seismic isolation system

Abstract: In most cases, construction of Light Frame Timber Buildings (LFTBs) in areas of high seismic hazard requires strong wood frame shear walls and continuous rod systems, which increases the cost of LFTBs. Frictional seismic isolation might be applied to protect LFTBs against extreme ground motions and mitigate the cost of continuous rod systems. However, there are no experimental studies on the response of LFTBs equipped with frictional isolation and subjected to extreme seismic ground motions that might cause impacts between the slider and the perimetral ring or between the isolated base and the perimetral moat wall. This study explores the potential of using impact-resilient frictional isolators as a feasible so- lution to alleviate stiffening and overturning costs of LFTBs while making them resilient to impacts in case of extreme events. This issue has been researched by evaluating the response of a 1:2 scaled 3-story LFTB isolated with a novel Impact Resilient Double Concave Frictional Pendulum recently developed by the authors. The specimen was subjected to a suite of shaking table tests (white noise, harmonics signals, and seismic records), including strong ground motions such as the Concepcion record (2010 Maule, Chile earthquake, Mw = 8.8) scaled to 130%. Results indicate that despite being subjected to extreme excitations, peak acceleration ratios (i.e., the ratio of peak floor acceleration to peak ground acceleration) did not exceed 0.75, and story drift ratios were smaller than 0.52% in most cases. Thus, the superstructure remained in the elastic range without damage. The study demonstrates the potential of achieving effective seismic protection of LFTBs using Impact Resilient devices. In addition, this paper presents a numerical model developed with experimental data, which provides insight into modeling issues such as, for instance, damping properties.

Reference: Quizanga, D., Almazán, J. L., **Valdivieso, D.**, López-García, D., and Guindos, P. (2024). Shaking table test of a timber building equipped with a novel cost-effective, impact-resilient seismic isolation system. *Journal of Building Engineering, 82, 108402*. `https://doi.org/10.1016/j.jobe.2023.108402`

B. ABSTRACTS AND LINKS TO CONFERENCE PAPERS

Notation: [a] presenter, [b] Universidad Andres Bello or [c] Universidad de Santiago de Chile undergraduate student.

- **Reference:** Quizanga, D., **Valdivieso, D.**, Almazan J.[a], Guindos P. and Lopez-Garcia D. (2023) Estudio experimental en mesa vibratoria de una estructura de madera de 3 pisos de entramado ligero con aisladores sísmicos friccionales resilientes a impacto. *XIII Congreso Chileno de Sismología e Ingeniería Sísmica ACHISINA 2023*, Viña del Mar, Chile, October 24–26, 2023.

  Abstract: The construction of buildings has contributed significantly to environmental pollution. For this reason, various countries have implemented public policies aimed at reducing the carbon footprint through the use of wood in construction. On the other hand, base isolation is an effective technology for seismic protection, primarily applied in concrete and steel buildings. However, the cost of its implementation (isolator devices, isolation base, perimeter moat wall) has been one of the main factors limiting its use. This paper presents the results of a shaking table test of a 3-story light frame timber building at a 1:2 scale, isolated with frictional pendulum devices, which are resilient to impact. The experimental results indicated that the superstructure did not sustain damage, even when subjected to extreme ground motions (demands higher than the maximum possible earthquake). The use of these devices could eliminate the need for constructing a perimeter wall, as they can absorb the effects of the eventual impact of the sliders against their inner ring in a controlled manner.

  Link: `https://www.eabstract.cl/paper/view-proceeding?id=3514`

- **Reference: Valdivieso, D.**, Liel A.[a] and Javernick-Will, Amy. (2023) Hurricane Wind Performance and Mitigation Strategies for Informally Constructed Houses in Puerto Rico. *In proceedings ASCE Inspire 2023*, Arlington, Virginia, United States, November 16–18, 2023.

  Abstract: This paper examines the performance of wood-based informally constructed houses in Puerto Rico, where resource-limited communities are vulnerable to climate-related hazards including hurricanes. Informally constructed housing is potentially vulnerable to hurricane and earthquake events but with significant variation depending on housing characteristics. This paper assesses the hurricane performance of representative housing typologies through a component-based performance-based wind engineering assessment framework. Results show that strengthening the roof envelope and roof-to-wall connections is essential for increasing the resilience of informally constructed wood houses in Puerto Rico. These upgrades are feasible for many builders and households, but challenges related to cost, appropriate construction, and material availability remain.

  Link: `https://ascelibrary.org/doi/10.1061/9780784485163.038`

- **Reference: Valdivieso, D.**[a], Liel A., Aravena A.[c], Hellman A.[c], Miranda J.[c] and Silva F.[c] (2023) Collapse Fragility of a 5-story CLT Structure under Chilean Subduction Earthquake Records. *14th International Conference on Applications of Statistics and Probability in Civil Engineering, ICASP14*, Dublin, Ireland, July 9-13, 2023.

Abstract: Mass timber structures have been used in North America, Europe, and Oceania, and are currently being evaluated in Latin America for midrise buildings in order to reduce the housing deficit and the contribution of the construction industry to greenhouse gas emissions. In highly seismic-prone areas, it is essential to provide resilient timber structures where structural and non-structural components adequately protect life safety and limit earthquake-induced damage and repair costs. In this paper, the Performance-Based Earthquake Engineering (PBEE) framework is employed to assess the probability of collapse of a government-subsidized 5-story platform-type cross-laminated timber (CLT) residential building designed under the draft of the Chilean seismic design code for CLT structures. The building model involved a full 3D representation of the building structure. Wall-to-foundation/floor connections and the overturning restraint system (i.e. hold-downs) were modeled explicitly to represent their hysteretic response. The collapse assessment determined a probability of 8.5% at the spectral acceleration of the predominant period (at 2% in the 50-year ground motion intensity) for a building with the mentioned characteristics, making it suitable for construction in Chile. Further research is needed to achieve loss estimation under the PBEE framework, such as quantifying damage fragility curves of representative engineering details for Chilean construction.

Link: `http://www.tara.tcd.ie/handle/2262/103415`

- **Reference: Valdivieso, D.**[a], Lopez-Garcia D., Montaño J. and Guindos P. (2023) Testing of strong multi-layered wood frame shear walls with non-structural layers. *World Conference on Timber Engineering WCTE 2023*, Oslo, Norway, June 2023.

Abstract: In areas of high seismic activity it is important to provide Light Frame Timber Buildings (LFTBs) with enhanced levels of lateral stiffness and strength,

as well as to prevent excessive levels of non-structural (NSC) damage. Chilean wood-frame shear walls are usually sheathed at both sides with OSB and covered by one/two-ply type X gypsum wallboard (GWB) fastened to the frame with narrow patterns of nailsor screws. Theresult is a multi-layered strong shear wall (MLSSW), which is not considered as such by design codesand mechanical models. Theobjective of this paper is to report an experimental evaluation of typical Chilean MLSSWs, with emphasis on the influence ofNSCs. Connectionlevel and assembly-level of 1:1 aspect ratio shear walls were evaluated through experimental tests. Results showed increments of 53% and 160% in elastic stiffness and maximum capacity, respectively, while keeping virtually the same deformation capacity and energy dissipation of equivalent bare (non-GWB finished) shear walls. It is postulated that such increases may arise from the high embedment strength of the GWB, and that the deeply screwed GWBmay prevent nails from pulling out during hysteresis cycles. It is concluded that GWBs have a significant structural influence on MLSSWs, and such influenceshould be taken into account in structural design.

Link: `https://www.proceedings.com/069179-0282.html`

- **Reference: Valdivieso, D.**[a], Lopez-Garcia D., Almazan J., Montaño J. and Guindos P. (2023) Testing the influence of 3D coupling effects on the lateral response of non-planar T-shape wood frame shear walls. *World Conference on Timber Engineering WCTE 2023*, Oslo, Norway, June 2023.

Abstract: Cumulative shear wall overturning (CSWO) is a common response of structural models of multistoryLight-Frame Timber Buildings (LFTBs) under lateral loads. Governed by holdown uplift and shear wall (SW) bending, large CSWO occurs in LFTBs due to the light self-weight of wood and the dominant rocking flexibility of stiff SWs. Even though CSWO is paramount in seismic design because of its effect on the flexibility of LFTBs (making hard to achieve the inter-story drift limits), this phenomenon is not incorporated into the structural models of LFTBs. For instance, in the design of LFTBs for lateral loads it is assumed that SWs behave as planar isolated elements. However, CSWO may be influenced by 3D coupling effects (3D-SWCE) in non-planar SWs such as T or L assemblies. This paper describes a large full-scale experiment of a 7.32 m x 5.1 m assembly, performed to gather insight into 3D-SWCEs through the cyclic evaluation of a non-planar T-shape SW. Resultsshowed an asymmetricbehaviour of the T-shape SW with increments of 20% and 98% in elastic stiffness and maximum capacity, respectively, with respect to those of a planar SW.It is concluded that 3D-SWCEs have a significant structural influence on the response of LFTBs.

Link: `https://www.proceedings.com/069179-0283.html`

- **Reference:** Aravena A.[c], Hellman A.[c], Miranda J.[c], Silva F.[c] and **Valdivieso, D.**[a] (2023) Collapse Probability of a 5-story CLT Structure Under Chilean Subduction Earthquake Records. *World Conference on Timber Engineering WCTE 2023*, Oslo, Norway, June 2023.

  Abstract: Mass timber structures have been utilized in North America, Europe, and Oceania, and are being evaluated in Latin America to decrease the housing shortage and the construction industry's contribution to greenhouse gas emissions. In Chile, where seismic activity is common, it is crucial to provide resilient timber structures that safeguard life safety and reduce earthquake-induced damage and repair costs. The Performance-Based Earthquake Engineering (PBEE) framework offers a practical alternative for designing more efficient timber buildings and assessing the risks related to seismic hazards, potential damage, and economic losses. In this paper, the PBEE framework is employed to assess the likelihood of a government-subsidized 5-story cross-laminated timber building collapsing under seismic stress in Chile. The probabilistic seismic hazard analysis (PSHA) was used for hazard site characterization, and the collapse probability analysis indicated a probability of less than 0.1% for a building with the mentioned characteristic, making it suitable for construction in Chile. Further research is required to achieve loss estimation under the PBEE framework, such as quantifying damage fragility curves of representative engineering details for Chilean construction.

Link: `https://www.proceedings.com/069179-0355.html`

- **Reference:** Armanent G, Ugarte J., Carcamo S., Sierra A.[a], **Valdivieso, D.**, Ugarte J.J. (2023) Tamango Building: Typological exploration for a 12-story wooden apartment building in a seismic area. *World Conference on Timber Engineering WCTE 2023*, Oslo, Norway, June 2023.

  Abstract: In 2020, Tallwood was commissioned to build a 12-story building with a mixed commercial and residential program in Coyhaique, the gateway to Chilean Patagonia and one of the most virgin territories in the world, but also a city that has one of the worst pollution rates in Latin America andispart of one of the countries with the highest seismicity in the world. This article explains the process and methodology behind the architectural and structural solution for the ”Tamango” building, which today has a constructionpermit and is in the final phase of economic studies to start the construction of its 12-story tower and 21,112m2, which includes 2,806m2 for offices and commerce on a reinforced concrete plate and 9,528m2 for 68 apartments distributed in a hybrid structure of LVL columns and beams, CLT and reinforced concrete composite slabs, and vertical cores of reinforced concrete.

Link: `https://www.proceedings.com/069179-0515.html`

- **Reference:** Carcamo S.[a] and **Valdivieso, D.** (2023) Morphologic study of hybrid tall building towards and interdisciplinary design. *World Conference on Timber Engineering WCTE 2023*, Oslo, Norway, June 2023.

  Abstract: Interdisciplinary design for tall wood buildings (TWBs) is a challenging task mainly due to the ongoing research on the behaviour of TWBs and to achieve cost-effective designs that allow the construction industry to improve the sustainability of the building inventory. Although more than 40 TWBs projects have been built, the lack of a guide regarding the distribution of structural elements increases the time that preliminary design requires, which commonly implies several iterations of different proposals. Based on the morphologic study of six TWBs, this paper analyses qualitatively timber buildings with reinforced concrete cores and study different parameters that should be taken into consideration in the early stage of the project, in order to achieve a healthy structure in a reduced time period. A comparative table with a range of values for each proposed parameter is presented. A range of values for the different studied parameters are presented as a guideline for the RC core typology.

  Link: `https://www.proceedings.com/069179-0516.html`

- **Reference:** Uribe J.[b] and **Valdivieso, D.**[a] (2023) Python-based plate model to simulate the effect of knotty areas on sawn timber. *World Conference on Timber Engineering WCTE 2023*, Oslo, Norway, June 2023.

  Abstract: This paper introduces a computational python-based model of a timber plate of Pinus Radiata D. Don specie grown in Chile. The effect of knotty areas is considered for the simulation of stiffness and resistance in a simply supported plate subjected to out-of-plane bending assessing the failure with the Von Mises normalized and Tsai-Wu criteria. The computational model is implemented based on the Reissner-Mindlin plate theory, considering a rectangular orthotropic model to simulate the behavior of wood. When the knotty area ratio (KAR) reaches its maximal value, 1, stiffness and resistance decrease by 19% and 56%, respectively. Through the Monte-Carlo method, 500 wooden plates are simulated by randomly distributing the lengths of internodes and whorls, which shows a difference of 14% in vertical displacement. It is concluded that the open-source numerical model was able to capture the effect of the knotty areas on the bending behavior of timber elements. The next step involves the calibration of the input parameters of the numerical model from the test results.

Link: `https://www.proceedings.com/069179-0052.html`

- **Reference: Valdivieso, D.**, Guindos P. and Lopez-Garcia D. (2022) Monotonic and cyclic characterization of multilayer sheathing-to-wood frame connection. *12th US National Conference on Earthquake Engineering*, Salt Lake City, USA, June 2022.

  Abstract: Light frame timber building (LFTB) is one of the structural systems evaluated by the Chilean construction industry to eventually replace concrete and steel buildings, which will improve the sustainability of the building inventory. Since Chile is subjected to high levels of seismic activity, it is then important to understand the dynamic behavior of LFTBs designed for earthquake loads. However, current mechanical models do not consider the multiple layers (structural and non-structural) of shear walls. In this paper, the monotonic and cyclic characterization of the wood frame-to-OSB nailed connection and the multilayer sheathing (OSB+GYB)-to-wood frame connection (screwed or stapled) are evaluated through experimental tests. Six engineering parameters were

established from monotonic test results based on the Equivalent Energy Elastic-Plastic (EEEP) approach. Results of load-slip connection tests were used to calibrate the MSTEW hysteretic model. This joint level sheathing-to-frame model will be incorporated into a future multilayer wood-frame shear wall model that takes into consideration the contribution of finishes layers such as the ones used for fire protection in LFTBs.

Link: `https://eeri.org/what-we-offer/digital-library/?lid=13050`

- **Reference:** Villegas, J.[b] and **Valdivieso, D.**[a] (2021) Numerical analysis of the cyclic behaviour of CLT walls made with Radiata Pine grown in Chile. *World Conference on Timber Engineering WCTE 2020-2021*, Santiago, Chile, August 2021.

  Abstract: In this research, the nonlinear behaviour of different configurations of CLT shear walls subjected to monotonic and cyclic lateral loads were studied through numerical simulations in OpenSees software. The shear and tension CLT wall-to-foundation joints were modelled with a nonlinear behaviour, whereas the CLT panel was modelled as a linear-elastic element. For this, firstly, each joint configuration was modelled using the SAWS constitutive model to represent their hysteretic responses. The SAWS parameters were calibrated against the experimental force-displacement curves obtained by the Materials Research Laboratory of Civil Engineering Department at Universidad de Santiago de Chile (LIMUS) in cyclic load tests carried out in CLT shear and tension connection samples. Joint models' results show good fitting between numerical and experimental responses for both shear and tension connections. Additionally, wall configurations with different aspect ratios, the number of shear keys, and the gravitational load applied above the panel were numerically studied by

using the calibrated SAWS parameters for each joint. These wall configurations were computationally subjected to monotonic and cyclic loads according to DIN EN 12512 toward determining hysteretic properties of each wall, such as strength, elastic stiffness, ductility, and equivalent viscous damping. Finally, the influence of each controlled variable on the walls' hysteretic properties was studied.

C. QUESTIONNAIRE USED IN INTERVIEWS WITH LOCAL NGO BUILDERS AND HARDWARE STORE EMPLOYEES TO IDENTIFY BARRIERS IN IMPLEMENTING PROPOSED MITIGATION MEASURES.(ENGLISH)

This appendix contains the presentation handouts distributed to NGO builders and hardware store employees at the workshop held in June 2023. Additionally, it showcases the blueprints of the structure constructed in the hands-on activity.

C.1. NGO Builders

Part 1. Before Presentation

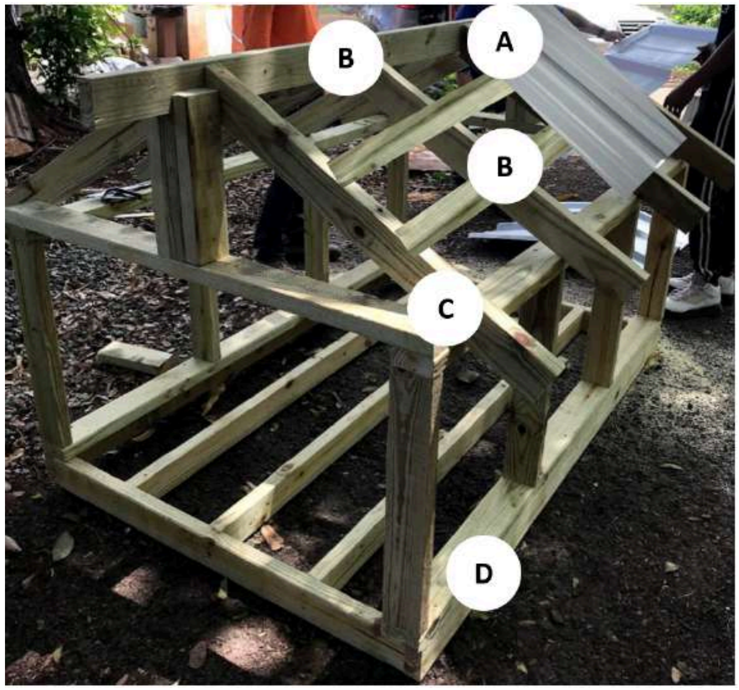

1. What connection from the continuous load path of the structure illustrated in the picture do you believe is the most critical to improve hurricane outcomes? (see picture on the screen)
    a. Zinc-to-purlin (A)
    b. Internal roof connections (B)
    c. Connections between roof and walls(C)
    d. Connections between walls and foundation (D)
2. What connection from the continuous load path of the structure illustrated in the picture do you believe is the least critical to improve hurricane outcomes? (see picture on the screen)
    a. Zinc-to-purlin (A)
    b. Internal roof connections (B)
    c. Connections between roof and walls(C)
    d. Connections between walls and foundation (D)

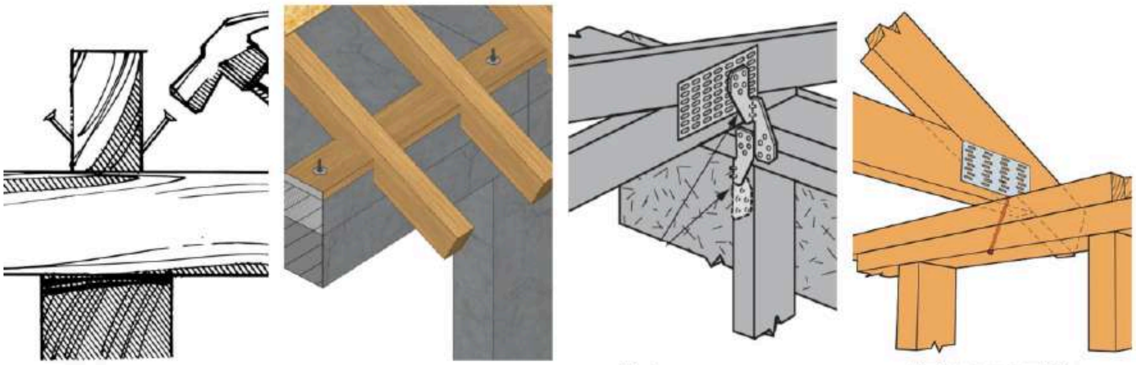

Union Clavada | Union con barra de acero | Union con amarre metalico | Union con tornillo de hilo continuo

3. What do you believe are effective strategies for strengthening/building the roof-to-wall connection? Select all the effective options. (see picture on the screen)
    a. Using nails to connect the truss/rafter to the walls
    b. Using metallic straps that connect the truss/rafter to the walls
    c. Using steel bars that connect the roof to the concrete
    d. Using fully-threaded screws that connect the truss/rafter to the wall
    e. Other, please describe

    Why? Explain your selection (in 2-3 sentences)

    ____
    ____
    ____

4. How likely do you think it is that a category 4 or 5 hurricane will affect Puerto Rico in the next five years?
    a. Not likely at all
    b. Unlikely
    c. Neutral
    d. Likely
    e. Extremely likely

    Do you believe that climate change makes hurricanes more likely?

    a. yes
    b. no

5. Was your home or the one of someone you know damaged in Hurricane Maria?
    a. yes
    b. no

    If yes, why was the home damaged?

    i. It was damaged because of the way it was built
    ii. It was destroyed because of the Panel-fastener interface (Roof panels ripped off)
    iii. It was destroyed because of Roof-to-wall connection

iv. It was destroyed because of the Purlin-to-truss connection
v. It was destroyed because of the Wall collapse
vi. Other, please describe in 2-3 sentences:

____
____
____

Part 2. After Presentation

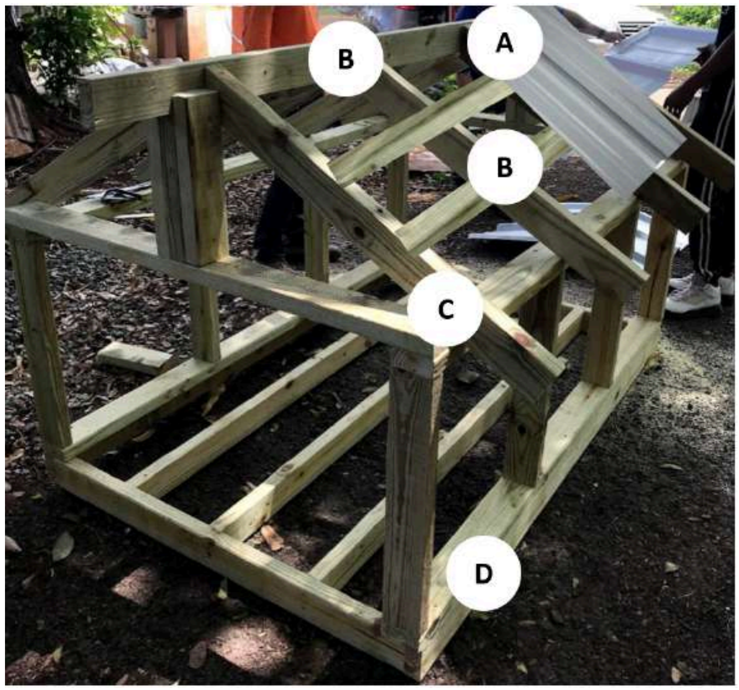

6. What connection from the continuous load path of the structure illustrated in the picture do you believe is the most critical to improve hurricane outcomes? (see picture on the screen)
   a. Zinc-to-purlin (A)
   b. Internal roof connections (B)
   c. Connections between roof and walls(C)
   d. Connections between walls and foundation (D)
7. What connection from the continuous load path of the structure illustrated in the picture do you believe is the least critical to improve hurricane outcomes? (see picture on the screen)
   a. Zinc-to-purlin (A)
   b. Internal roof connections (B)
   c. Connections between roof and walls(C)
   d. Connections between walls and foundation (D)

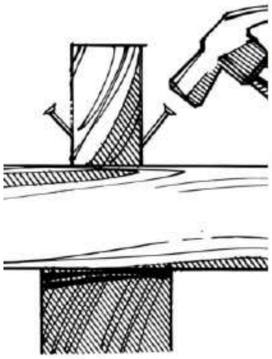

Union Clavada

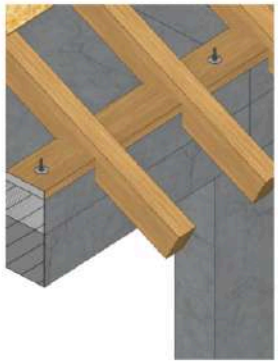

Union con barra de acero

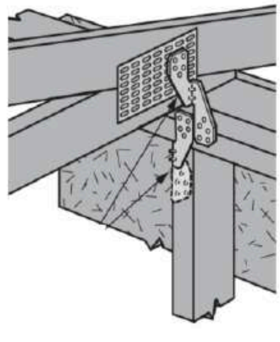

Union con amarre metalico

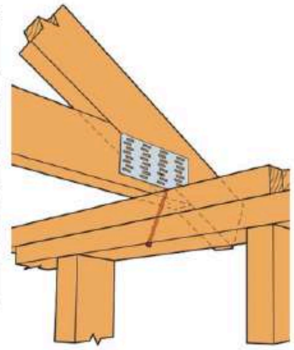

Union con tornillo de hilo continuo

8. What do you believe are effective strategies for strengthening/building the roof-to-wall connection? Select all the effective options. (see picture on the screen)
    a. Using nails to connect the truss/rafter to the walls
    b. Using metallic straps that connect the truss/rafter to the walls
    c. Using steel bars that connect the roof to the concrete
    d. Using fully-threaded screws that connect the truss/rafter to the wall
    e. Other, please describe

    Why? Explain your selection (in 2-3 sentences)

9. If you changed your responses from beforehand, what did you learn that made you change your answer? Please describe in 2-3 sentences

10. Do you feel the information shared in this training is valuable to share with others?
    a. Not valuable at all
    b. Slightly valuable
    c. Moderately valuable
    d. Valuable
    e. Super valuable

    Do you plan to share this information with others?
    a. yes
    b. no
    c. maybe

    Why or why not? (Please describe in 2-3 sentences)

11. If you are interested in sharing this information, which of the following do you believe would help you to reach more people to share the information from this training? Select all that are applicable.
    a. Translated materials in multiple languages
    b. Collaboration with local community organizations
    c. Municipal support and endorsement
    d. Island/US government support and endorsement
    e. Access to affordable building materials
    f. Engaging local media for wider coverage
    g. Training programs for local builders and contractors
    h. Workshops and educational events for homeowners and the community
    i. Others, Please describe in 2-3 sentences:

____
____
____

12. What 1 or 2 other things do you want to learn about strengthening a house under hurricane wind?
    1)____
    ____
    2)____
    ____

13. If you are looking for more information, who or where would you turn to for advice on safer housing construction? Select all that are applicable.
    a. Churches
    b. Municipal government
    c. island/US government
    d. Hardware stores
    e. Friends, family, or neighbors
    f. Social media (e.g., Facebook or YouTube)
    g. Community-based organizations
    h. Other, please describe briefly:

____
____
____

14. What guidance for mitigation may be challenging for the average builder/homeowner to implement based on cost, difficulty, material availability, lack of understanding, or time constraints? Please select all that apply.

Guidance for Mitigation	Cost	Difficulty	Material Availability	Lack of Understanding	Time
A hipped roof					

Bracing or sheathing on all walls					
Install the hurricane strap connectors for securing the roof-to-walls					
Install screws for securing the roof-to-walls					
Install screws for securing the purlin to truss/rafter					
Install truss/rafter or purlins with reduced spaced					
Install lateral bracing on the roof					
Install 2x6 or 2x8 instead of 2x4 wood elements					
Install thicker Zinc					
Install Zinc to the purlins with fasteners @ 150mm					
Install Zinc to the purlins with screws instead of nails					

15. In what situation might a builder not incorporate the guidance for mitigation? Please choose no more than 3.
    a. Limited knowledge or awareness of hurricane mitigation practices
    b. Lack of access to quality building materials and resources
    c. Financial constraints
    d. Time constraints and pressure to complete construction quickly
    e. Resistance to change and adherence to traditional building methods
    f. Lack of knowledge about building codes and regulations
    g. Lack of construction supervision to ensure hurricane mitigation measures are built
    h. Cost-cutting pressures that discourage mitigation
    i. Limited availability of skilled labor with the necessary expertise
    j. Inadequate understanding of the potential impact of hurricanes in the region
    k. Other
    l. I cannot think of a situation
16. What do you see as the benefits of living in a house that is built using the proposed guidance for mitigation? Please describe in 2-3 sentences: ____
____
____

C.2. Hardware Store Employees

Survey for Non-Trainees

English

1. What do you recommend people do to improve hurricane outcomes for wood frame houses?
   ____
   ____
   ____
   ____
2. What is surprising in these recommendations?
   ____
   ____
   ____
3. What do you see as the main benefits of following this guidance for mitigation when building?
   ____
   ____
   ____
4. How would you describe the methods for and importance of strengthening this roof-to-wall connection for a group of customers?
   ____
   ____
   ____
5. What 1 or 2 things do you think your customers most need to learn about strengthening a house under hurricane wind?
   1)____
   ____
   2)____
   ____
6. In relation to the guidance for mitigation, What [resources, information, training…] do you believe would help you to reach more customers with advice about building wood frame houses for hurricanes? Please describe
   ____
   ____
   ____
7. Which of the items from the guidance for mitigation do you think an average builder/person may find challenging due to factors such as cost, difficulty, material availability, lack of understanding, or time? Please select all that apply.

Guidance for Mitigation	Cost	Difficulty	Material Availability	Lack of Understanding	Time

Install the hurricane strap connectors for securing the roof-to-walls					
Install screws for securing the roof-to-walls					
Install screws for securing the purlin to truss/rafter					
Install truss/rafter or purlins with reduced spacing					
Install 2x6 or 2x8 instead of 2x4 wood elements					
Install thicker Zinc					
Fasten Zinc to the purlins with fasteners @ 150mm					
Fasten Zinc to the purlins with screws instead of nails					

8. In what situation might one of your customers not incorporate the guidance for mitigation? Please select
    a. Limited knowledge or awareness of hurricane mitigation practices
    b. Lack of access to quality building materials and resources
    c. Financial constraints
    d. Time constraints and pressure to complete construction quickly
    e. Resistance to change and adherence to traditional building methods
    f. Lack of knowledge about building codes and regulations
    g. Lack of construction supervision to ensure hurricane mitigation measures are built
    h. Cost-cutting pressures that discourage mitigation
    i. Limited availability of skilled labor with the necessary expertise
    j. Inadequate understanding of the potential impact of hurricanes in the region
    k. Other
    l. I cannot think of a situation

D. JUNE 2023 WORKSHOP DOCUMENTATION

This appendix contains the presentation handouts distributed to NGO builders and hardware store employees at the workshop held in June 2023. Additionally, it showcases the blueprints of the structure constructed in the hands-on activity and photographs of all activities conducted during the June 2023 workshop.

D.1. NGO Builders

University of Colorado Boulder

Huracanes en Puerto Rico ¿Cómo preparar su casa de madera para el siguiente evento?

Objetivos

Al finalizar esta actividad, esperamos que:

- Pueda identificar y aplicar los diferentes elementos de la guía de mitigación ante vientos huracanados
- Aplique el concepto de camino de carga continuo al analizar y construir una estructura de madera
- Identifique los efectos de la aplicación de la guía de mitigación ante vientos huracanados

Hicimos entrevistas y encuestas con más de 400 constructores, empleados de ferreterías, residentes, ingenieros, y arquitectos en todo Puerto Rico para **entender los desafíos con la seguridad de viviendas.**

60+ entrevistas

Observaciones de la situación actual

~350 encuestas

Las percepciones de peligros (o desastres) naturales y la seguridad de viviendas en el trabajo de construcción informal

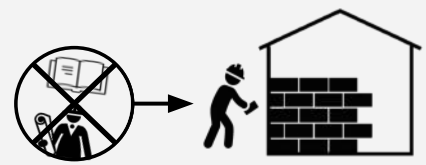

Según las experiencias de los constructores y los residentes, analizamos **el desempeño esperado de las viviendas de madera o de concreto** en los huracanes y terremotos.

Observaciones de la situación actual

+

Inventario de ferreterías

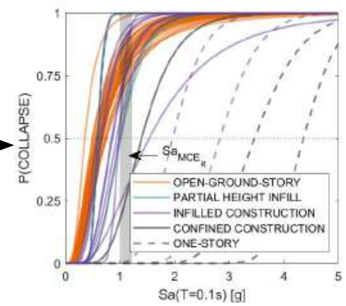

Análisis estructural & recomendaciones priorizadas

Análisis estructural del desempeño en los huracanes y los terremotos

Encuesta de entrada (15 minutos)

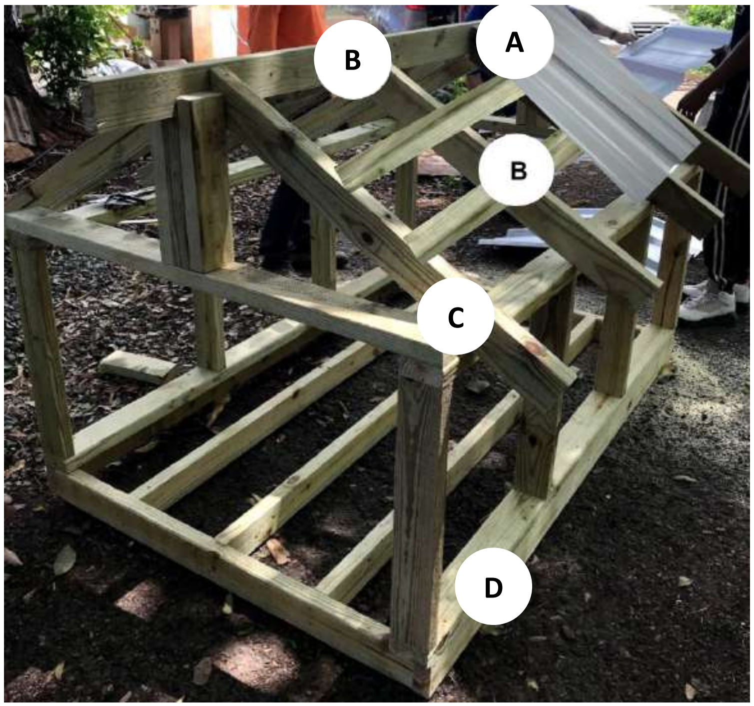

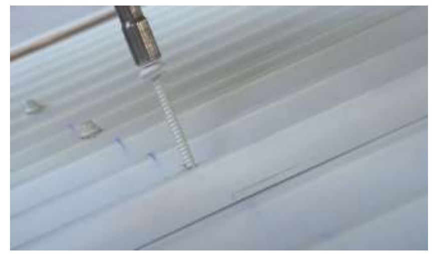

A – Cinc a Purlins

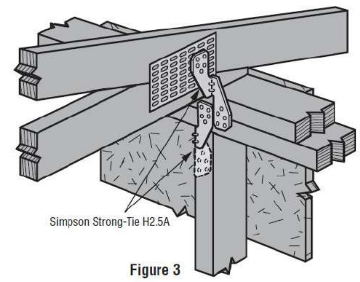

C – Conexiones Techo a Muros

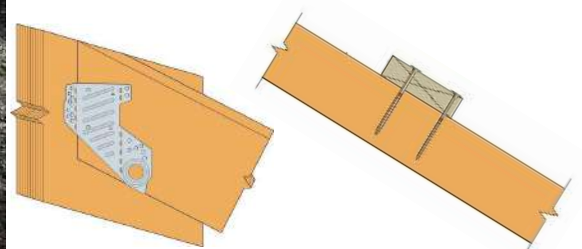

B – Conexiones Internas del Techo

D – Conexiones Muro a Fundación

Encuesta de entrada (15 minutos)

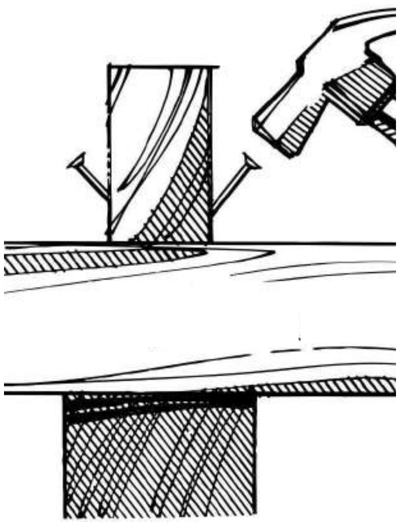

Unión Clavada

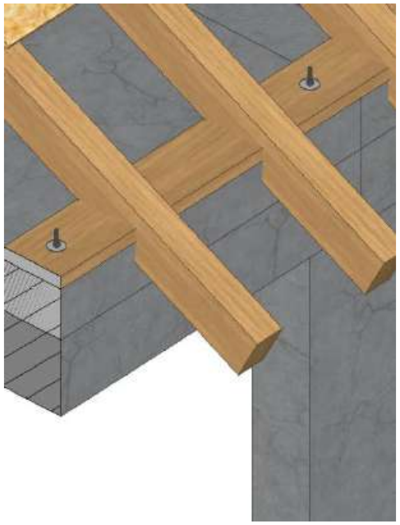

Unión con barra de acero

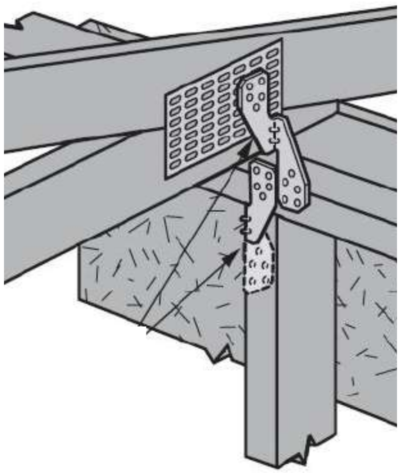

Unión con amarre metálico

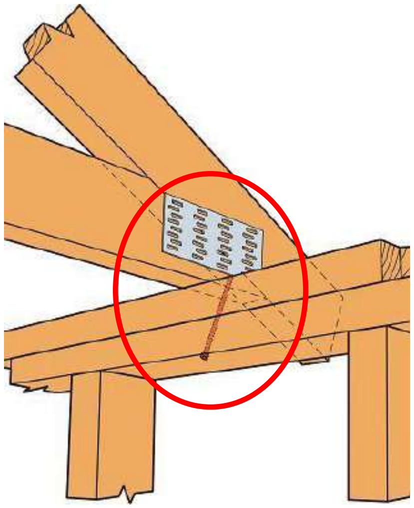

Unión con tornillo de hilo continuo

Huracanes son amenazas que producen grandes pérdidas económicas a los habitantes de Puerto Rico.

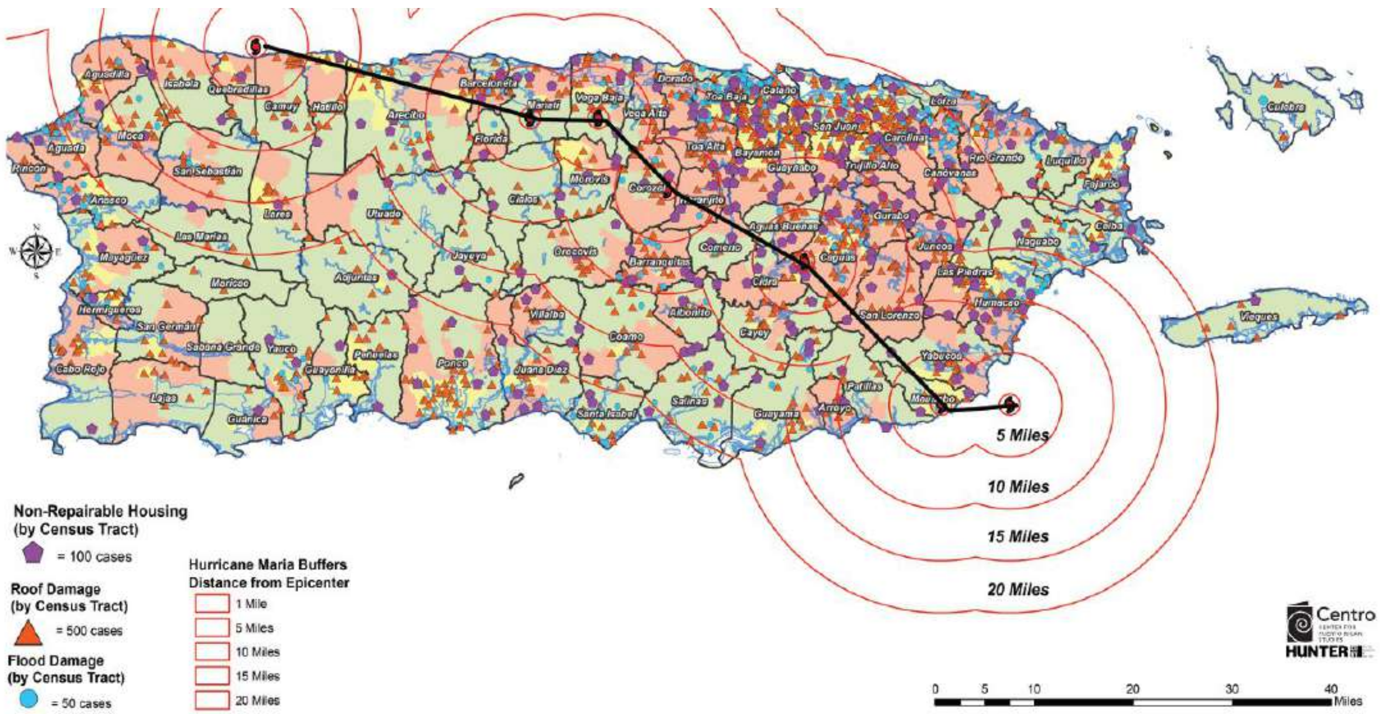

Fuente: Center for Puerto Rican Studies

Los daños a las casas de los puertorriqueños incrementan la vulnerabilidad de las familias truncando su desarrollo. Es necesario trabajar para el desarrollo de estructuras resilientes a futuros eventos.

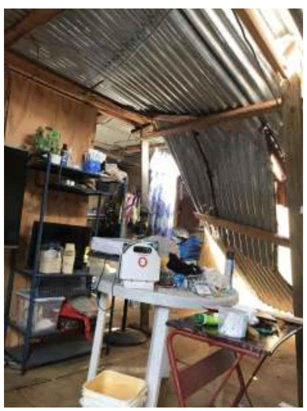

Estos se categorizan según un rango de velocidad de vientos y se puede atribuir un cierto nivel de daño esperado.

Cat.1 74 – 95 mph
Cat.2 96 – 110 mph
Cat.3 111 - 129 mph
Cat.4 130 - 156 mph
Cat.5 > 157 mph

Fuente: BBC

¿Cómo afectan los vientos huracanados a una estructura?

Fuente: Disaster Safety

Los vientos huracanados inducen diferentes tipos de movimientos en la estructura que deben ser prevenidos para evitar la falla.

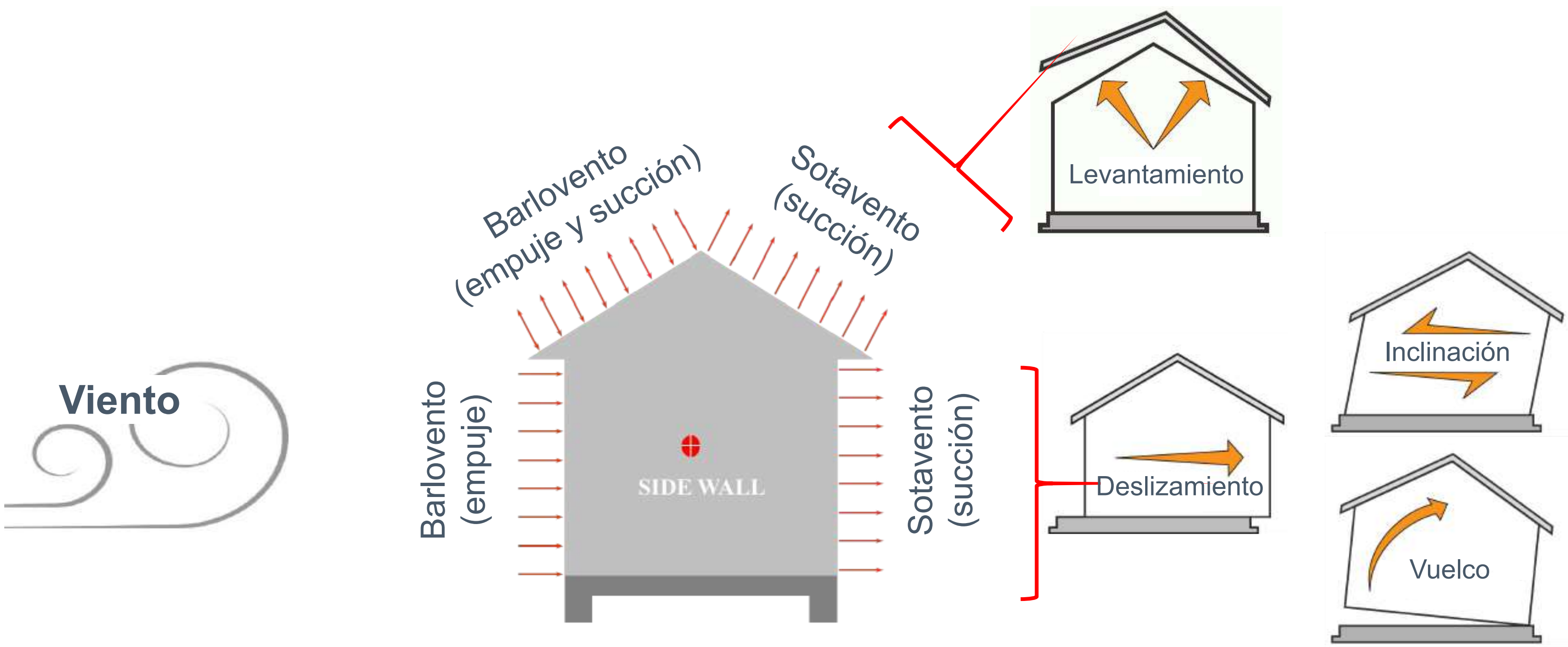

Fuente: Simpson Strong-Tie

Independiente de la naturaleza del movimiento, es necesario garantizar una transferencia de carga continua a la fundación.

12

En huracanes pasados, como el Huracán María en 2017, produjo una falla progresiva de las estructuras asociada al camino de carga continuo. La falla de un componente produce una redistribución de la fuerza del viento en el resto.

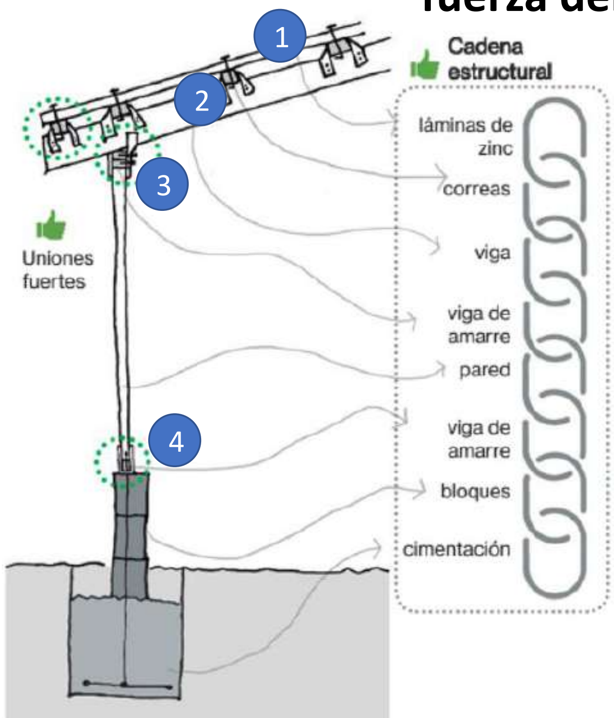

Fuente: Habitat para la Humanidad

1. Cobertura de metal
2. Entramado de madera de la estructura de techo: Purlins y trusses/vigas
3. Anclaje del techo a los muros
4. Anclaje de los muros a las fundaciones

Uno de los principales modos de fallas evidenciados en casas construidas de manera informa en Puerto Rico fue el desprendimiento de la cobertura metálica.

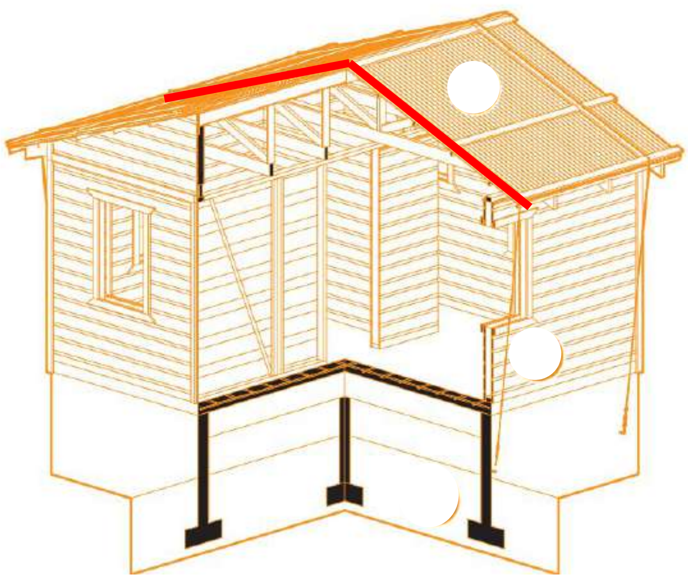

Razones para este tipo de fallas:

- ✔ Techos muy planos

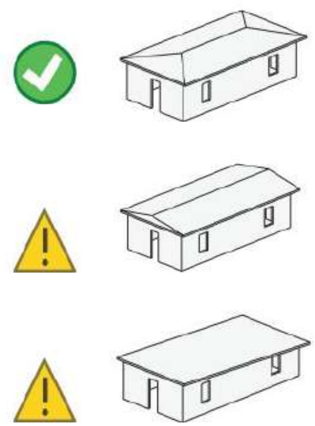

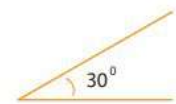

Mejor ángulo de techo: Resiste más el viento.

Fuente : Habitat para la Humanidad

Uno de los principales modos de fallas evidenciados en casas construidas de manera informa en Puerto Rico fue el desprendimiento de la cobertura metálica

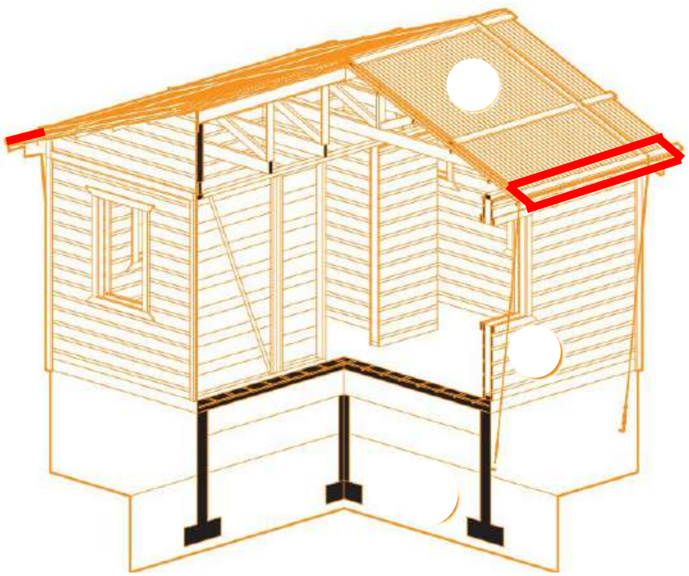

Razones para este tipo de fallas:

- ✔ Utilización de aleros largos y extensión del techo principal de la vivienda para hacer corredores o terrazas techadas

Fuente : Habitat para la Humanidad

Uno de los principales modos de fallas evidenciados en casas construidas de manera informa en Puerto Rico fue el desprendimiento de la cobertura metálica.

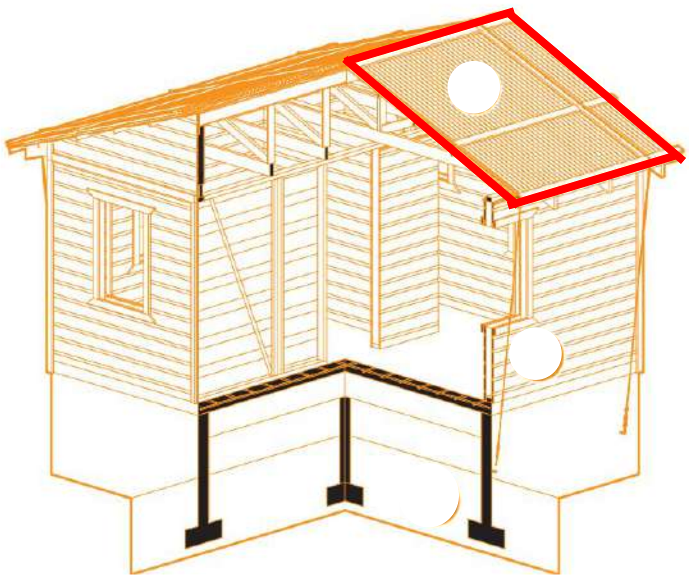

Razones para este tipo de fallas:

- ✔ Uso de fijaciones inadecuadas.

Fuente : Habitat para la Humanidad

Uno de los principales modos de fallas evidenciados en casas construidas de manera informa en Puerto Rico fue el desprendimiento de la cobertura metálica.

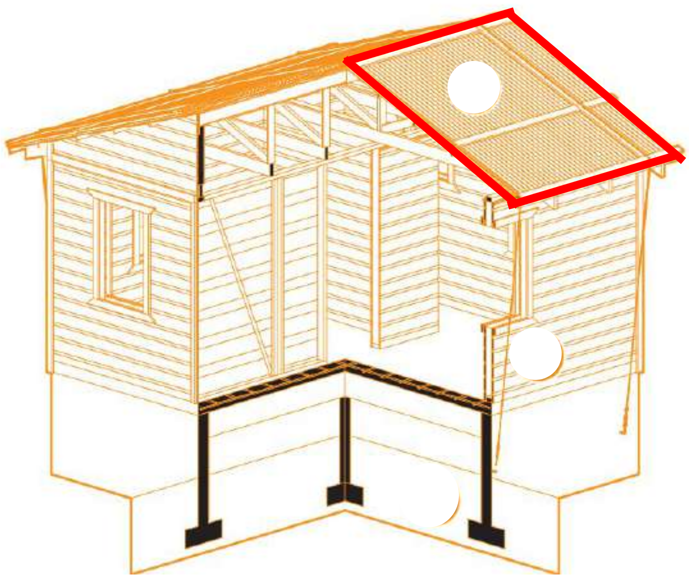

Razones para este tipo de fallas:

- ✔ Dispuestos muy espaciados entre sí: disponerlos cada **6in**

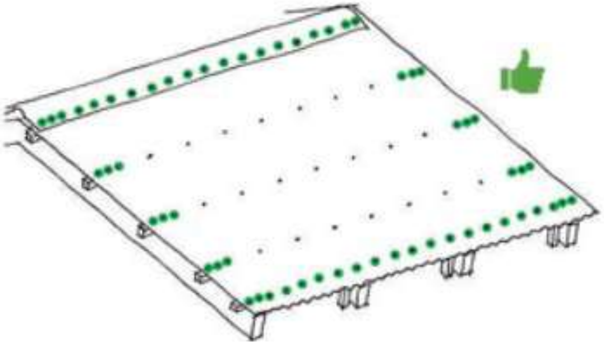

Fuente : Habitat para la Humanidad

Si las placas de cinc se instalan correctamente, la estructura de techo debe ser lo suficientemente fuerte para transmitir las cargas a los muros.

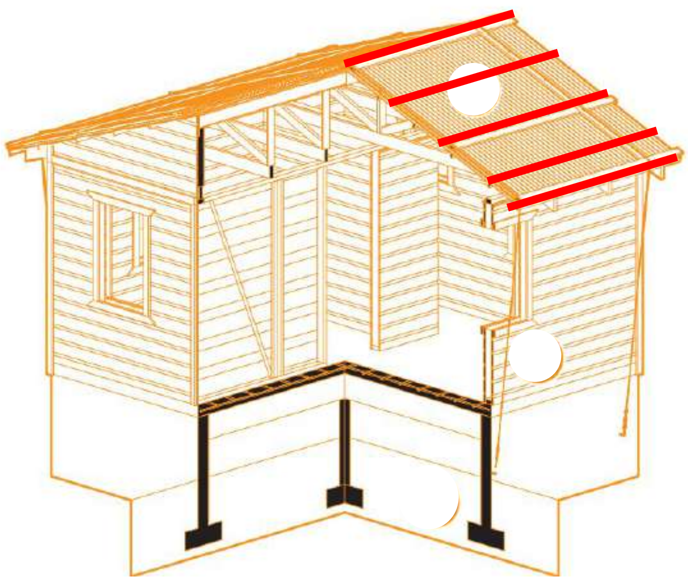

Razones para este tipo de fallas:

✔ Purlins instalados con espaciamientos muy holgados (instaladas cada 4ft cuando debería ser **2ft**)

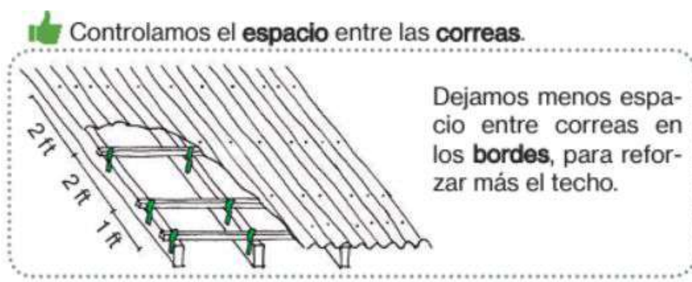

Fuente : Habitat para la Humanidad

Si las placas de cinc se instalan correctamente, la estructura de techo debe ser lo suficientemente fuerte para transmitir las cargas a los muros.

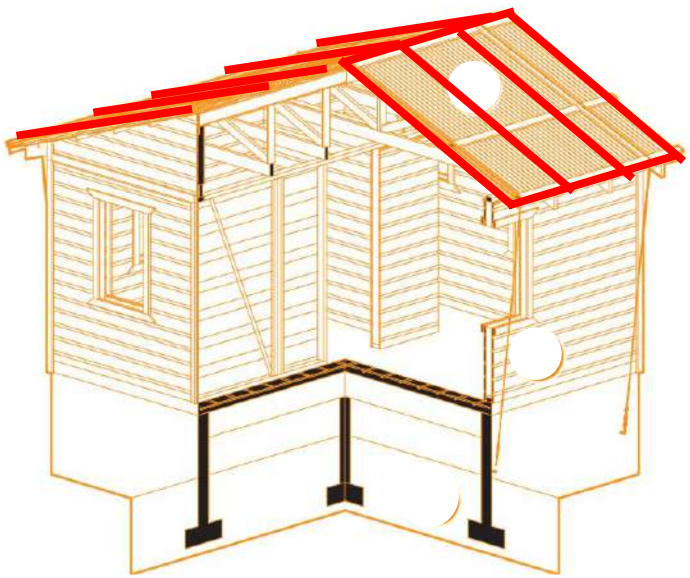

Razones para este tipo de fallas:

- ✔ Espaciamiento entre trusses/armaduras o vigas de techo muy grande para el tamaño de las vigas de madera (espaciados cada 6ft cuando debería ser **4ft o 2ft**).
- ✔ Utilización de vigas muy pequeñas para la luz solicitante (2x4 donde se debería usar **2x6 o 2x8**).

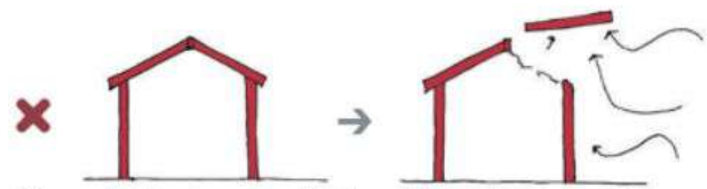

Si nuestro techo no está bien reforzado y sus uniones no son fuertes, incluso un viento suave puede levantarlo.

Fuente : Habitat para la Humanidad

Si las placas de cinc se instalan correctamente, la estructura de techo debe ser lo suficientemente fuerte para transmitir las cargas a los muros.

Razones para este tipo de fallas:

- ✔ Conexiones inadecuadas entre los elementos

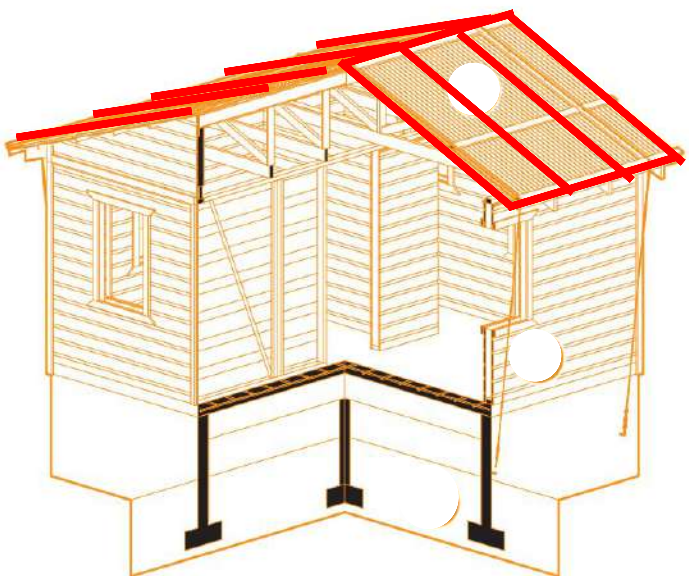

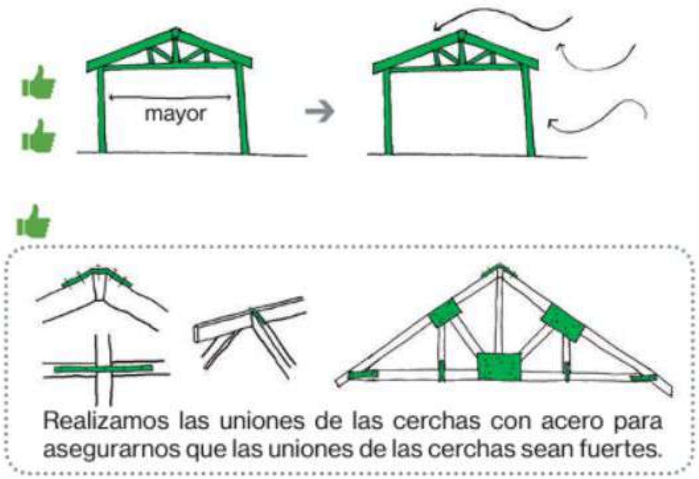

Realizamos las uniones de las cerchas con acero para asegurarnos que las uniones de las cerchas sean fuertes.

Fuente : Habitat para la Humanidad

Si las placas de cinc se instalan correctamente, la estructura de techo debe ser lo suficientemente fuerte para transmitir las cargas a los muros.

Razones para este tipo de fallas:

- ✔ Conexiones inadecuadas entre los elementos

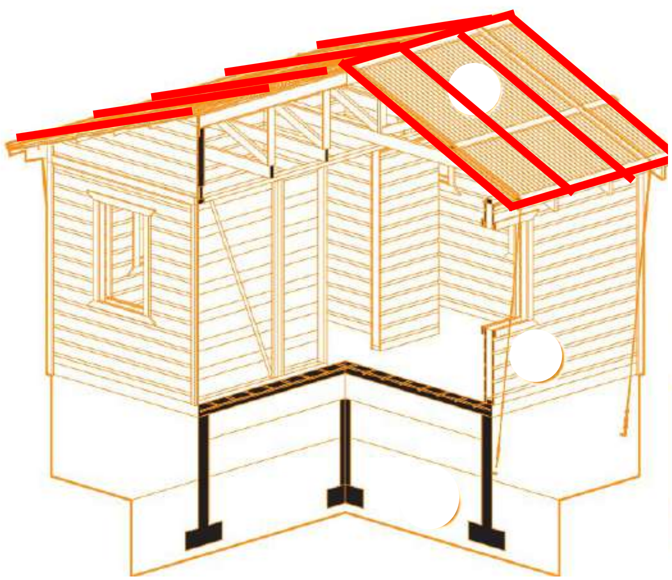

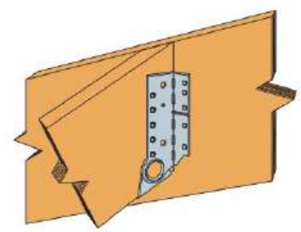

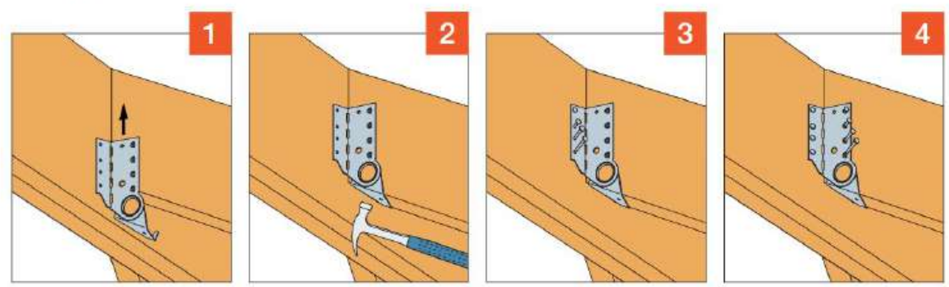

Fuente : Habitat para la Humanidad & Simpson Strong-Tie

Asegurada la estructura de techo, el siguiente problema puede resultar del desprendimiento completo de techo debido a una débil conexión a los muros.

Razones para este tipo de fallas:

- ✔ El uso de clavos tipo lancero para resolver la unión

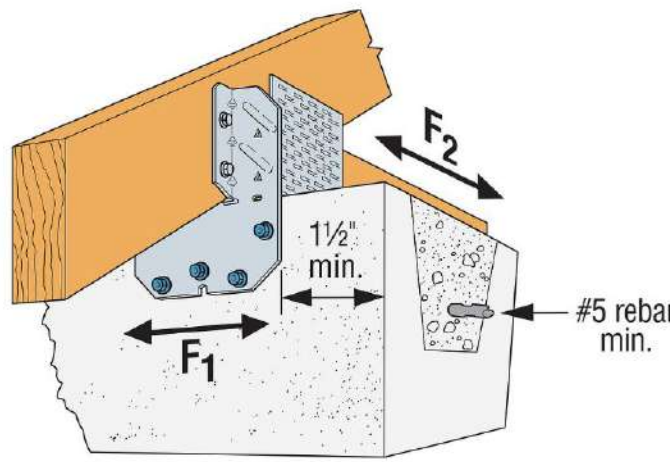

HM9 Attaching Truss to Masonry

Fuente: Disaster Safety

Los muros también son los encargados de amarrar el techo a la fundación y deben resistir las fuerzas de levante. Aquí las conexiones en el entramado de madera del muro es clave.

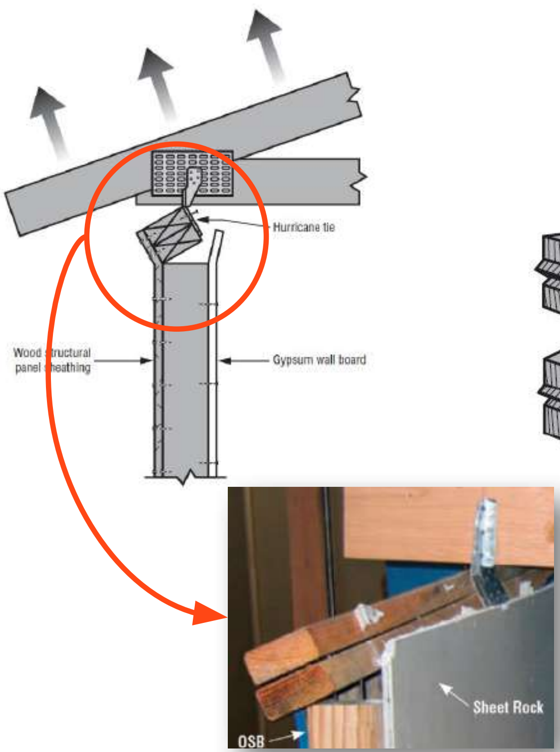

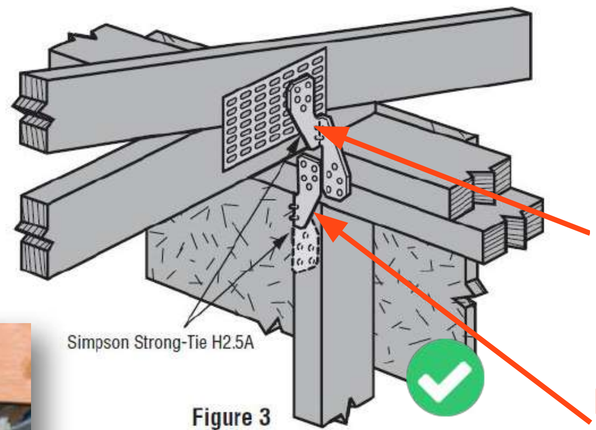

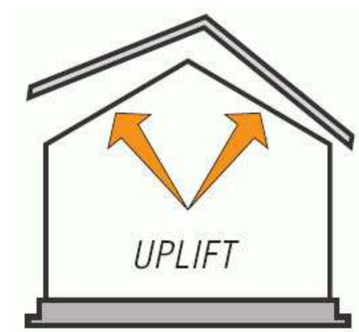

Fuente: Simpson Strong-Tie

Si bien los muros han demostrado un menor porcentaje de falla en eventos pasados, se deben asegurar para transmitir las cargas laterales del huracán.

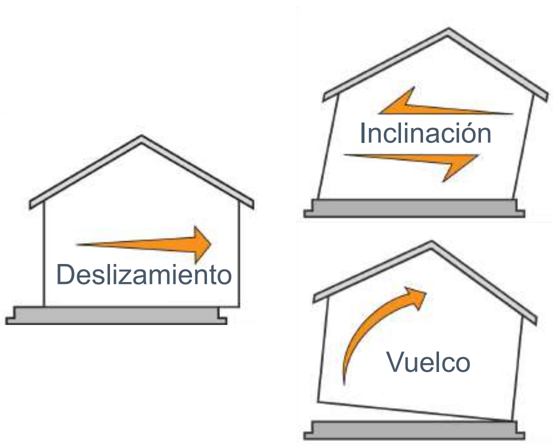

Fuente: Simpson Strong-Tie

Se debe evitar la falla por apilamiento del frame de madera considerando algún tipo de elemento arriostrante.

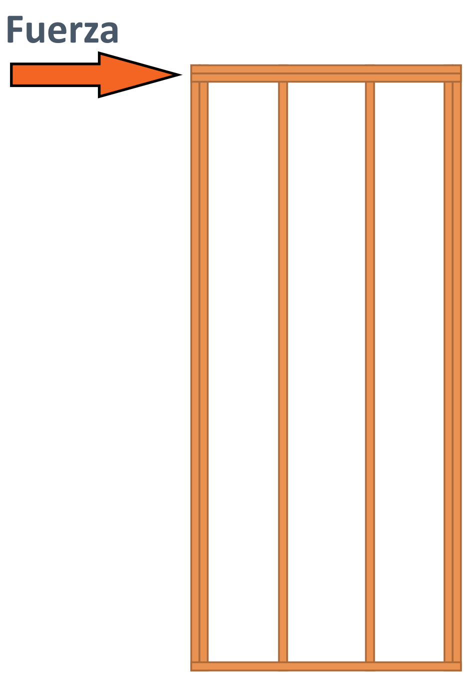

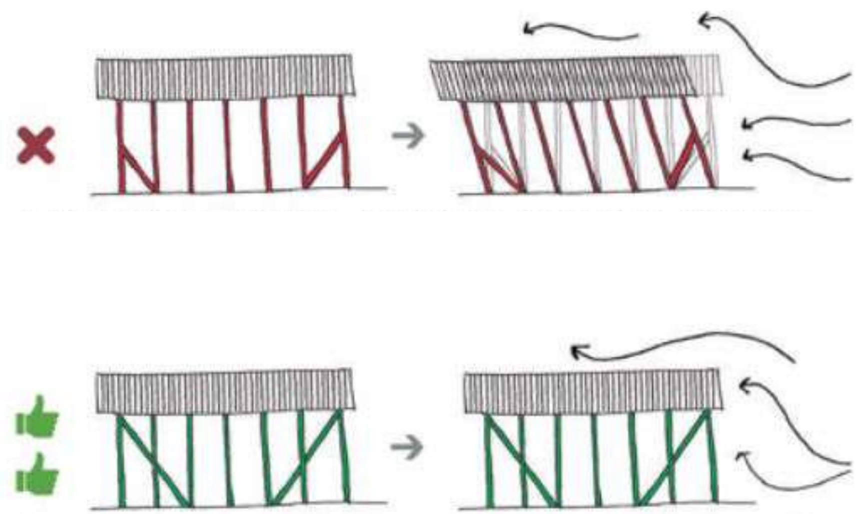

Fuente: Simpson Strong-Tie

Se debe evitar la falla por apilamiento del entramado de madera considerando algún tipo de elemento arriostrante.

Fuerza

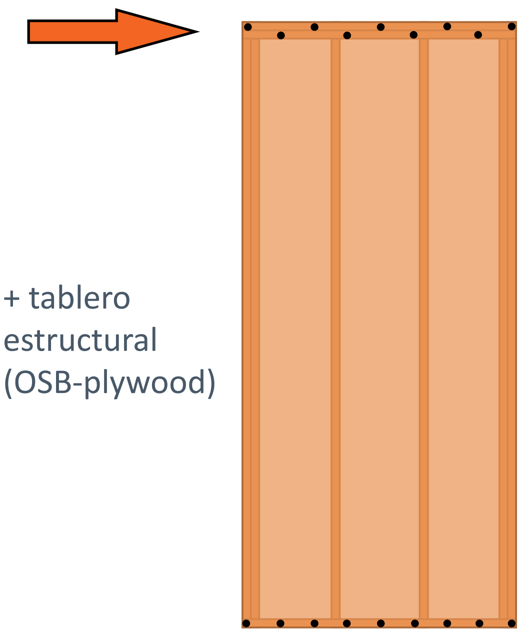

+ tablero estructural (OSB-plywood)

Fuente: Simpson Strong-Tie

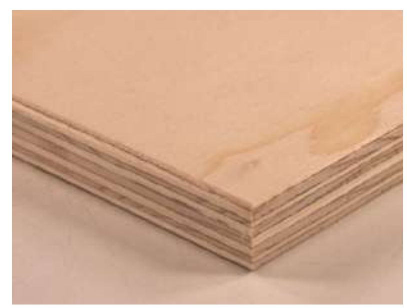

Para evitar la falla por deslizamiento, los muros deben ser anclados apropiadamente a la fundación o a los niveles aledaños

Fuerza

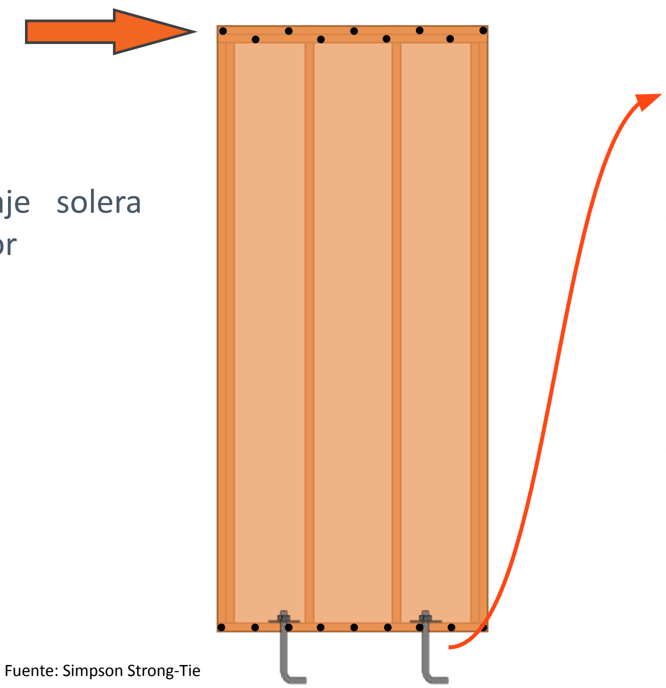

+anclaje solera inferior

Fuente: Simpson Strong-Tie

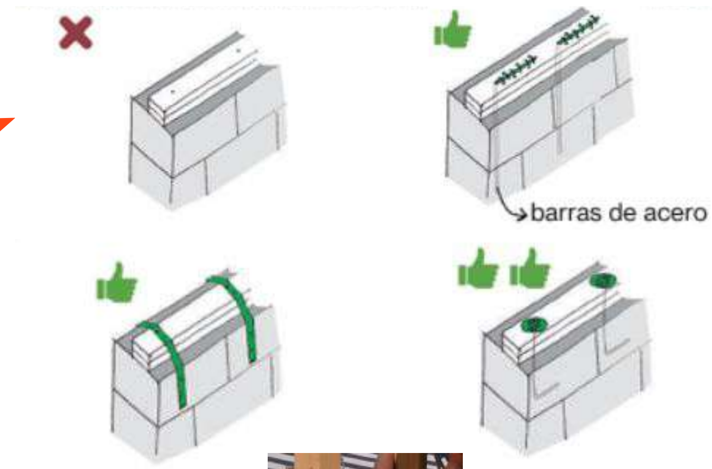

Para evitar la falla por vuelco, se debe disponer algún tipo de anclaje anti-vuelco.

Fuerza

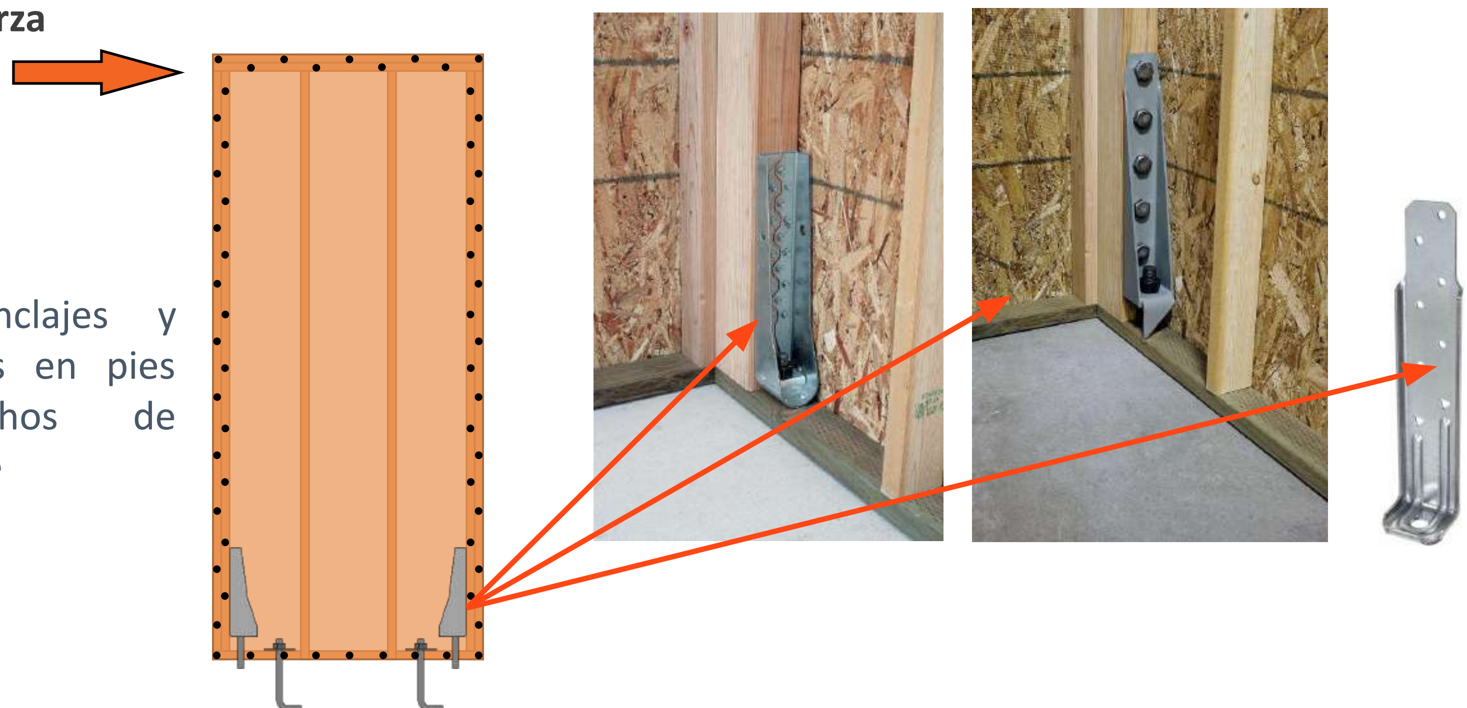

\+ anclajes y clavos en pies derechos de borde

Fuente: Simpson Strong-Tie

El detallamiento del anclaje anti-vuelco es primoridal para garantizar un adecuado traspaso de la carga lateral a las fundaciones.

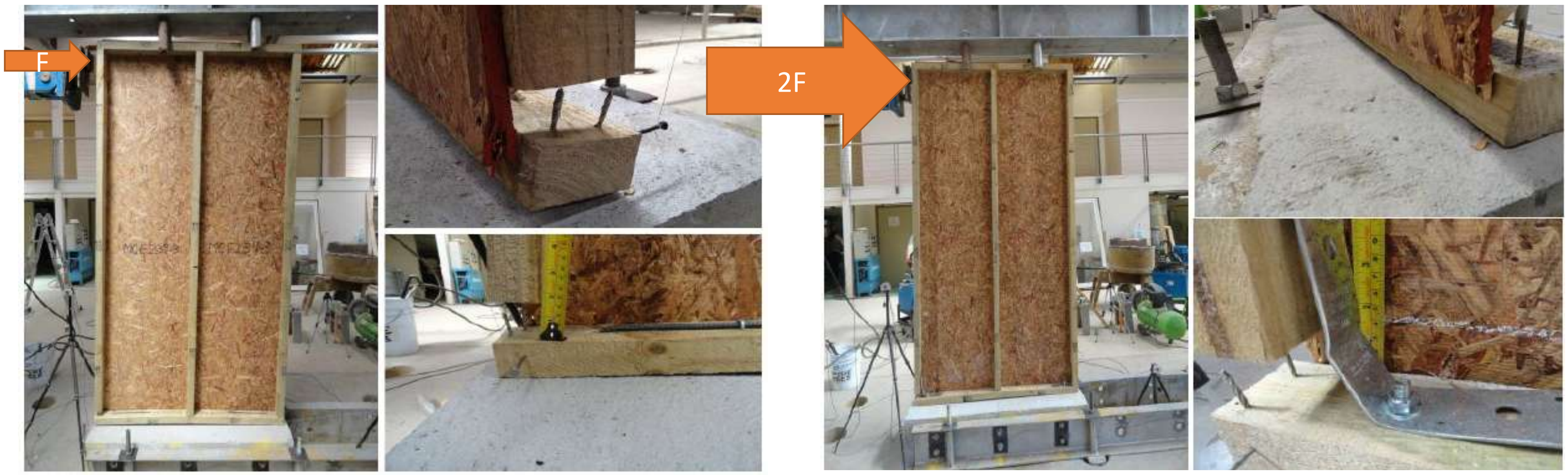

Disponer un simple conector en el borde permite resistir el **doble de la carga**

Fuente: INFOR Chile

¿Cuales son los efectos de la aplicación de las medidas de mitigación identificadas anteriormente? Veamos el caso actual de las casas:

De un total de **10 casas en su barrio**, se espera que **fallen 10 casas** en un evento **CT 1**

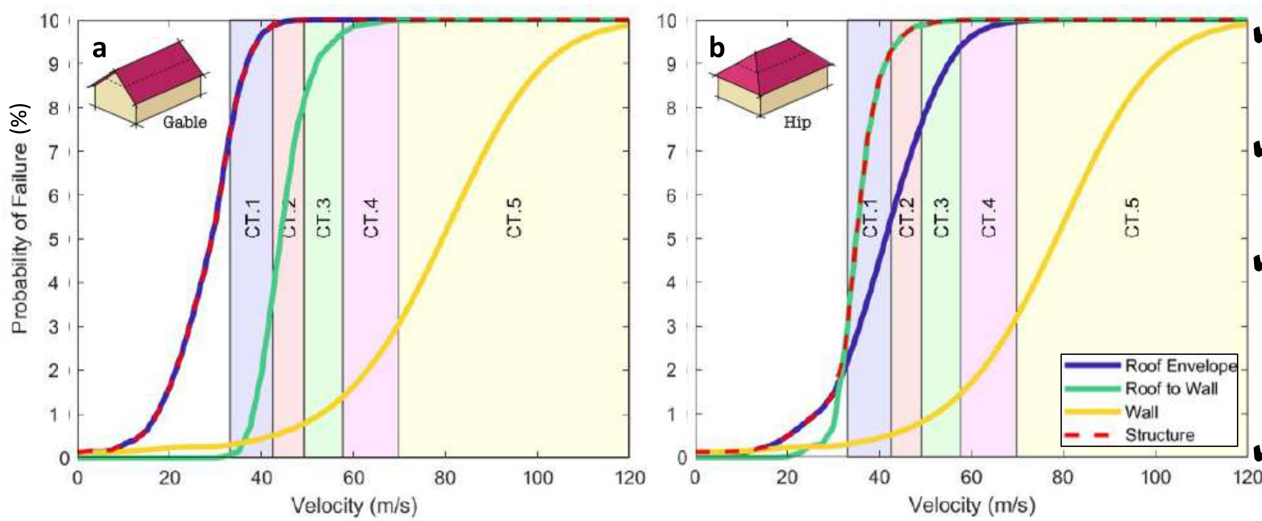

- ✔ Clavo para unir el zinc a las correas cada 300mm
- ✔ Cerchas cada 1.8m y correas cada 1.2m
- ✔ Clavos lancero para union correas a cerchas/vigas y de techo a muros
- ✔ Vigas de 2x4 SYP para el entramado de techo y correas
- ✔ CGI 26 gauge

¿Cuáles son los efectos de la aplicación de las guías de mitigación identificadas anteriormente? Veamos el caso actual de las casas:

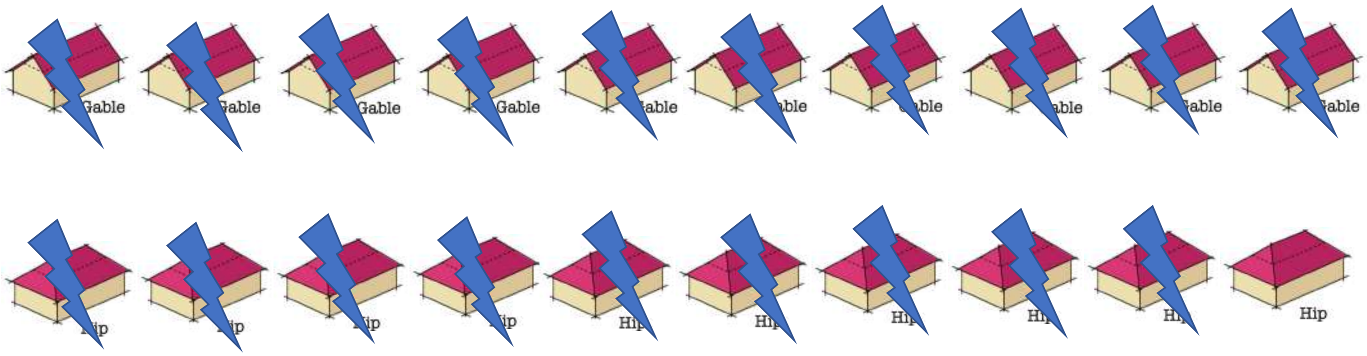

Cuales son los efectos de la aplicación de las medidas de mitigación identificadas anteriormente?

De un total de **10 casas en su barrio**, se espera que **fallen 10 casas** en un evento **CT 5 con altas velocidades**

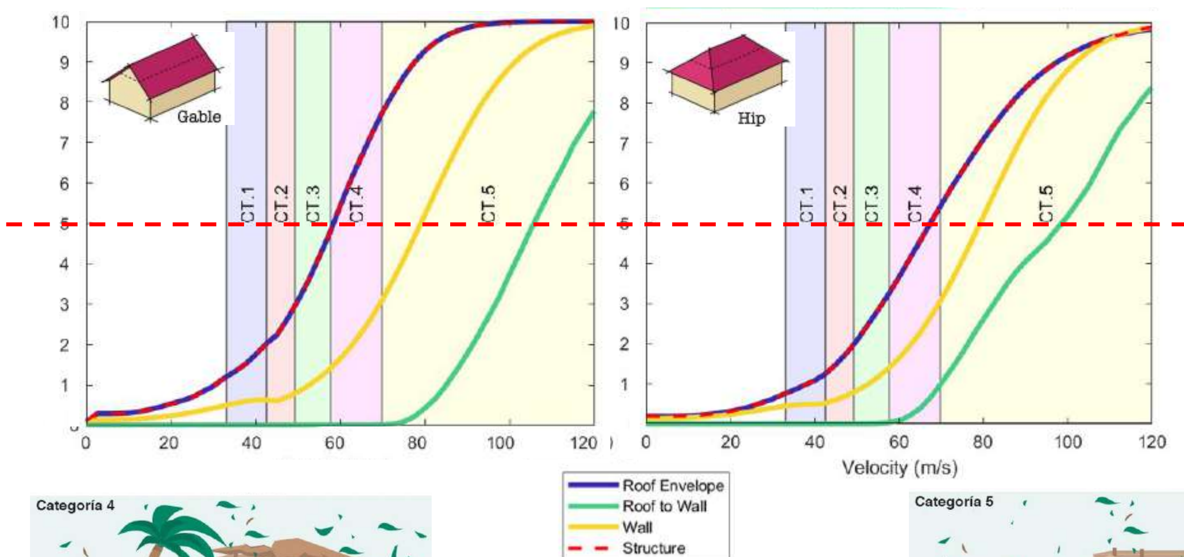

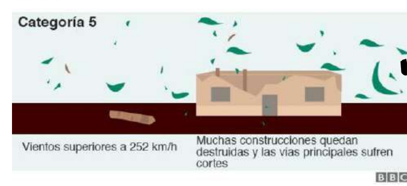

- ✔ Clavo para unir el zinc a las correas cada 150mm
- ✔ Cerchas cada 0.6m y correas cada 0.6m
- ✔ Tornillos para union correas a cerchas/vigas y H2.5 de techo a muros
- ✔ Vigas de 2x6 SYP para el entramado de techo y correas
- ✔ CGI 24 gauge

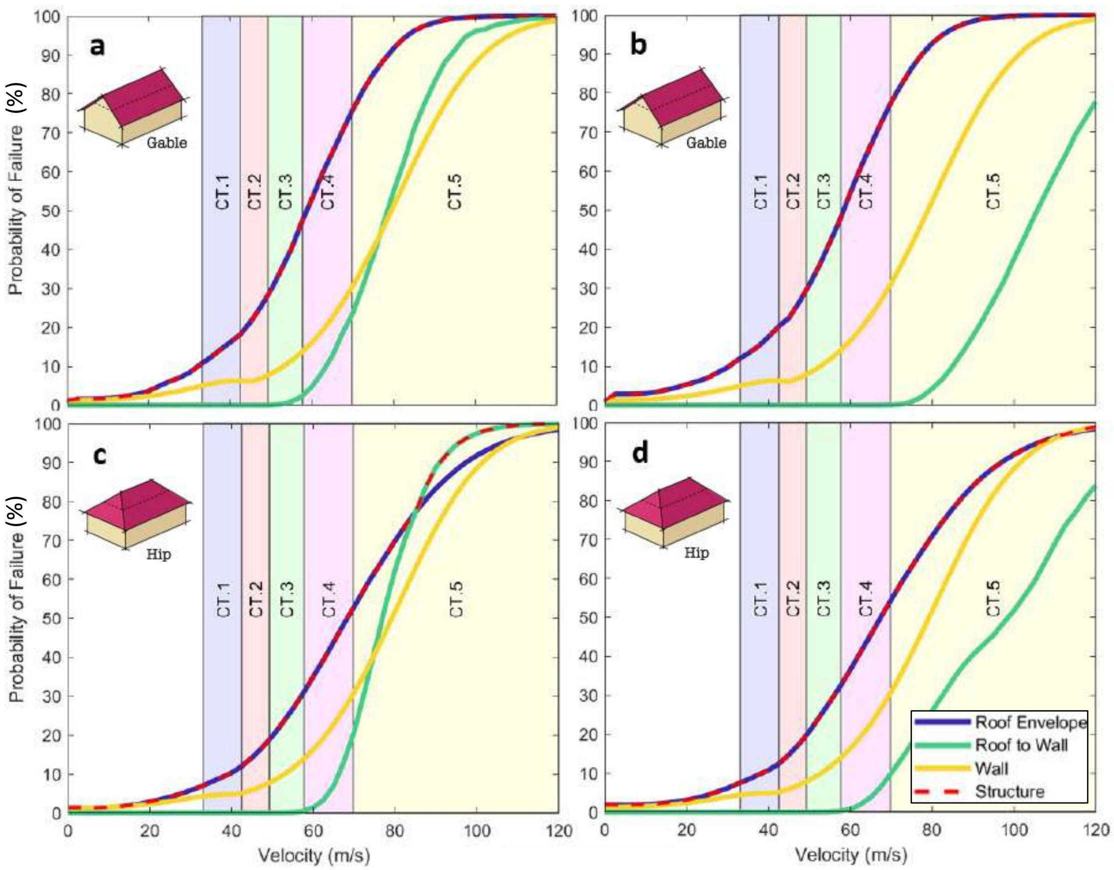
a
b
c
d
Gable
Gable
Hip
Hip
CT.1
CT.2
CT.3
CT.4
CT.5
Probability of Failure (%)
Velocity (m/s)
Roof Envelope
Roof to Wall
Wall
Structure

¿Cuáles son los efectos de la aplicación de las guías de mitigación identificadas anteriormente?

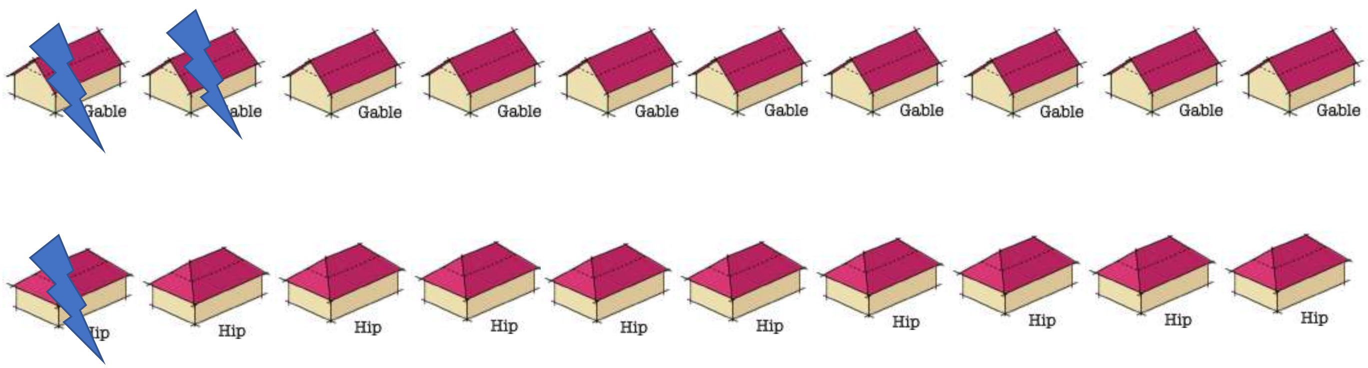

¿Cuáles son los efectos de la aplicación de las guias de mitigación identificadas anteriormente?

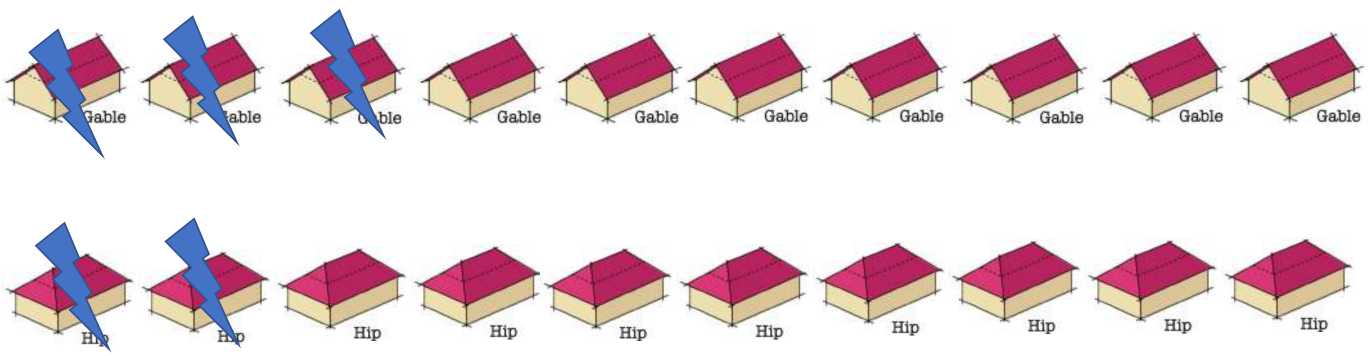

¿Cuáles son los efectos de la aplicación de las medidas de mitigación identificadas anteriormente?

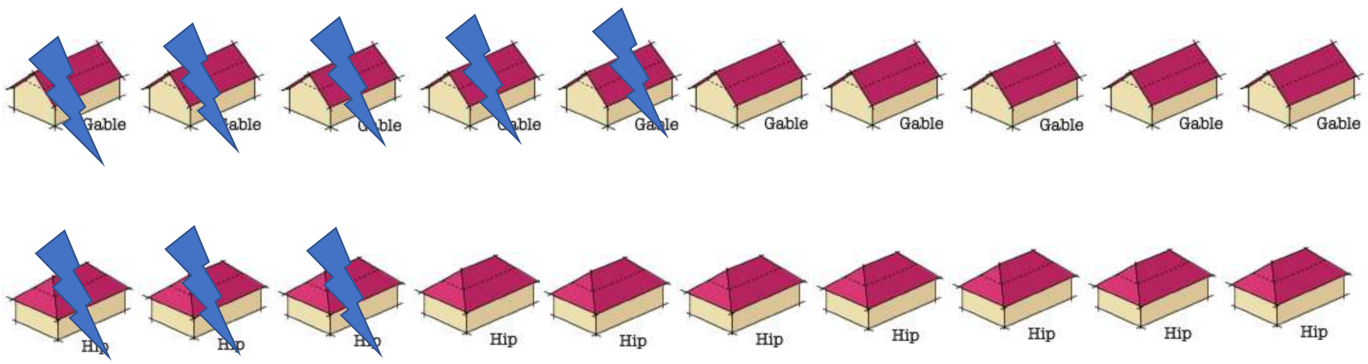

¿Cuáles son los efectos de la aplicación de las medidas de mitigación identificadas anteriormente?

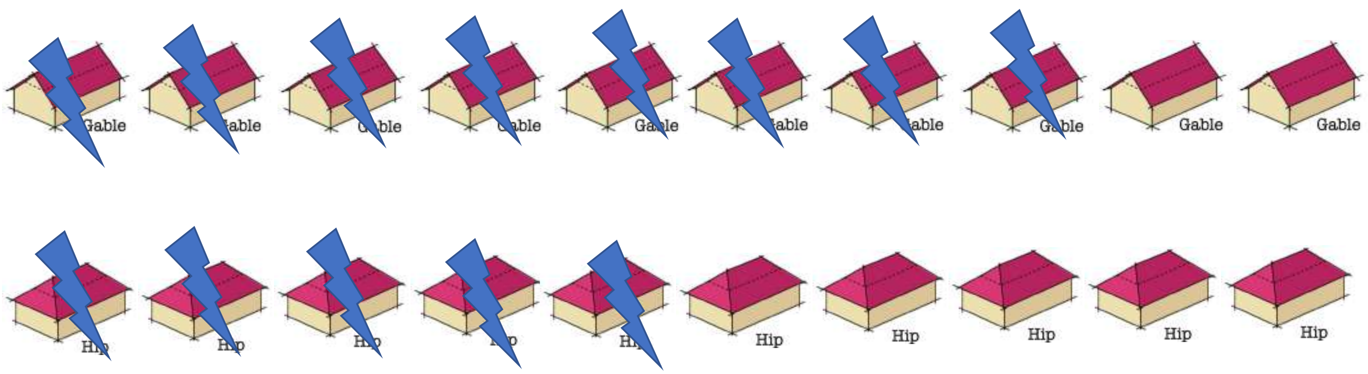

Objetivos

Al finalizar esta actividad, esperamos que:

- Pueda identificar y aplicar los diferentes elementos de la guía de mitigación ante vientos huracanados
- Aplique el concepto de camino de carga continuo al analizar y construir una estructura de madera
- Identifique los efectos de la aplicación de la guía de mitigación ante vientos huracanados

University of Colorado **Boulder**

Huracanes en Puerto Rico ¿Cómo preparar su casa de madera para el siguiente evento?

diego.valdivieso@colorado.edu

Encuesta de salida (25 minutos)

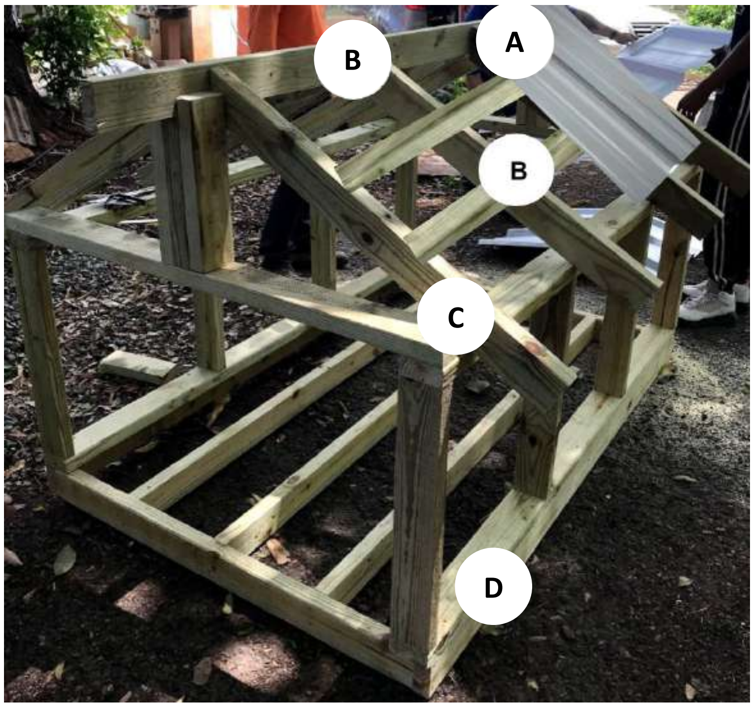

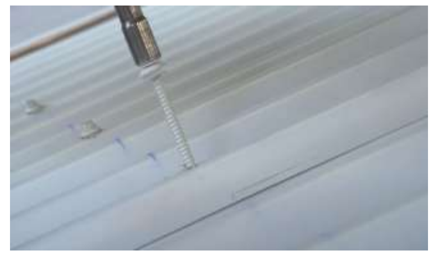

A – Cinc a Purlins

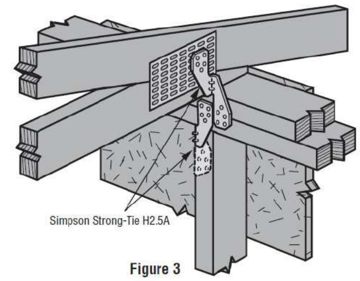

C – Conexiones Techo a Muros

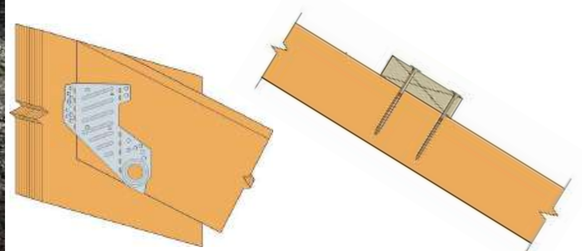

B – Conexiones Internas del Techo

D – Conexiones Muro a Fundación

Encuesta de entrada (15 minutos)

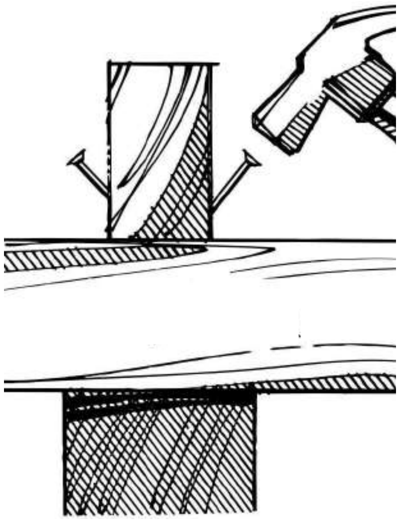

Unión Clavada

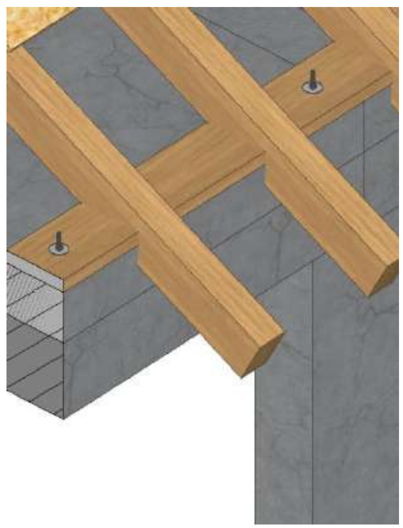

Unión con barra de acero

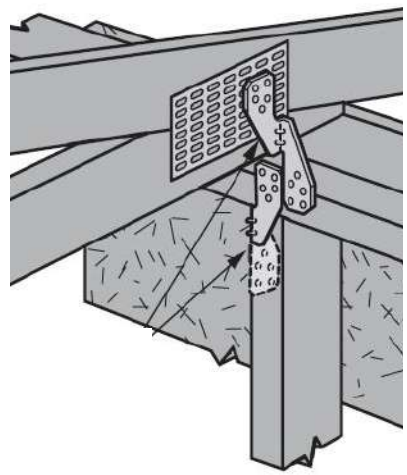

Unión con amarre metálico

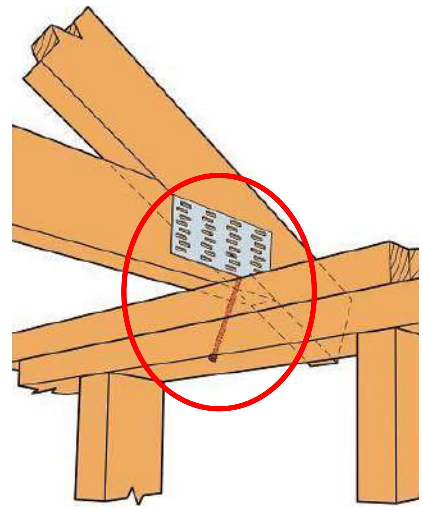

Unión con tornillo de rosca continua

D.2. Hardware Store Employees

University of Colorado **Boulder**

Huracanes en Puerto Rico ¿Cómo preparar su casa de madera para el siguiente evento?

Unión techo a muros

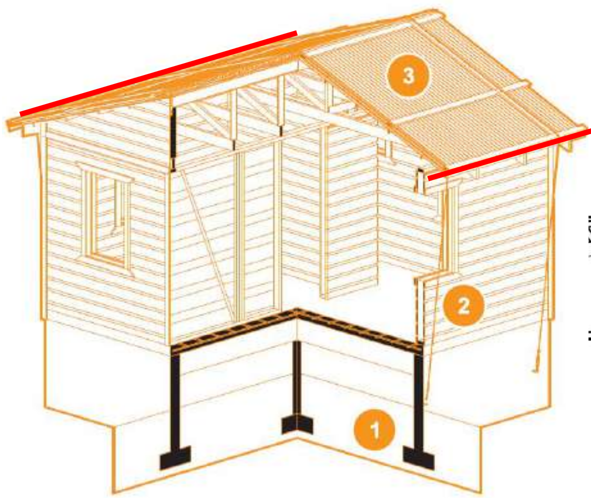

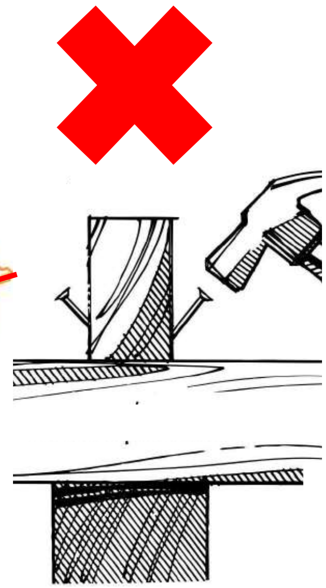

Unión Clavada

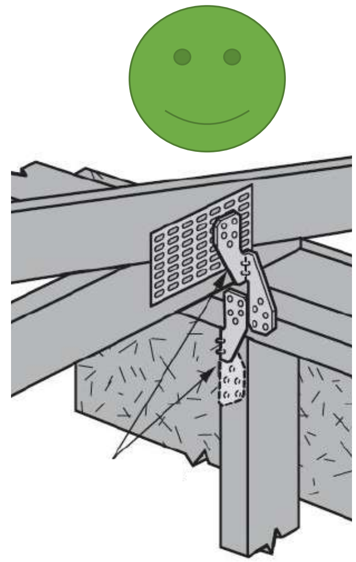

Unión con amarre metálico

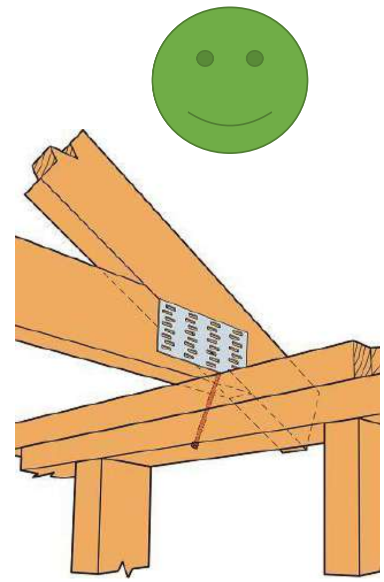

Unión con tornillo de hilo continuo

Unión cinc a purlins

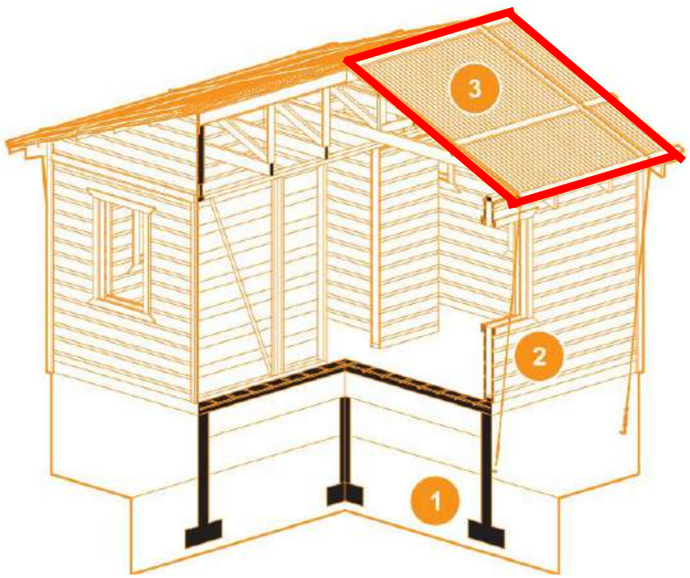

Unión cinc a purlins

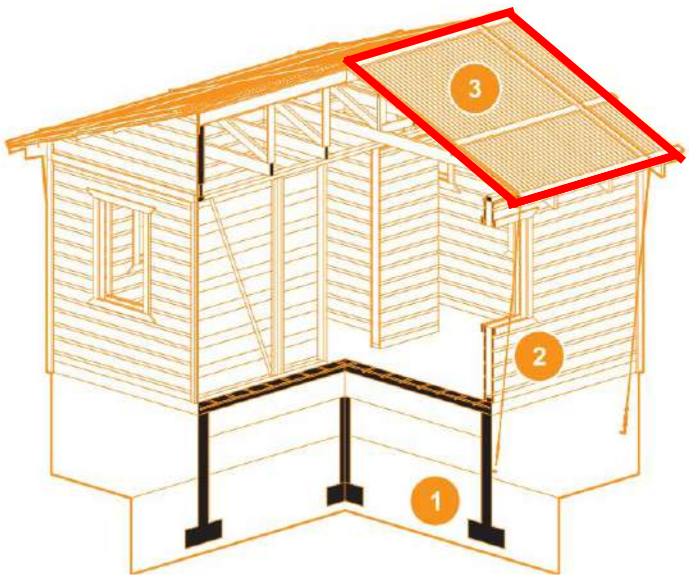

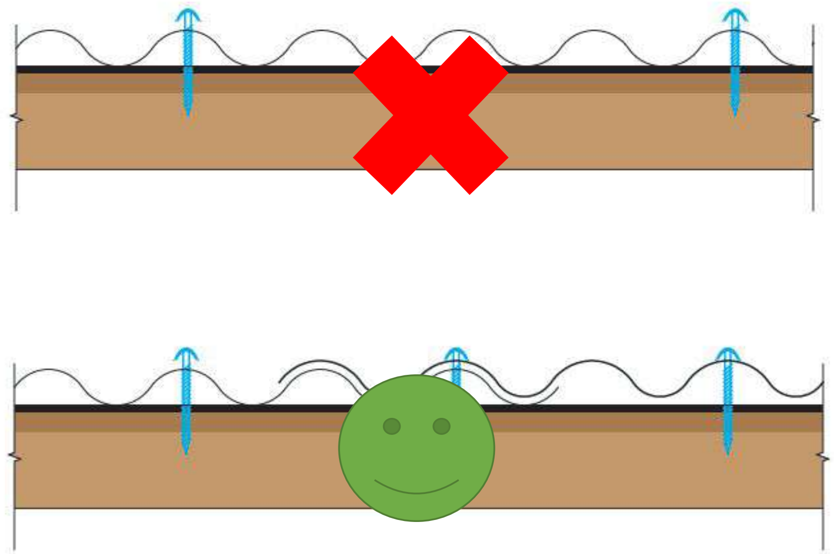

Distanciamiento purlins

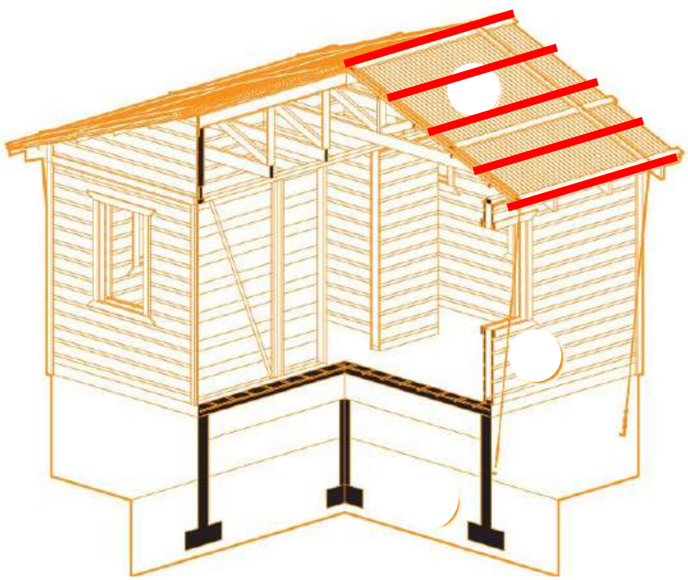

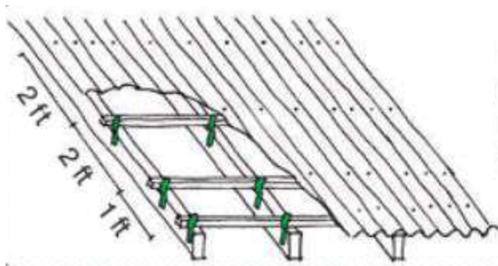

Dejamos menos espacio entre correas en los **bordes**, para reforzar más el techo.

Distanciamiento trusses/vigas

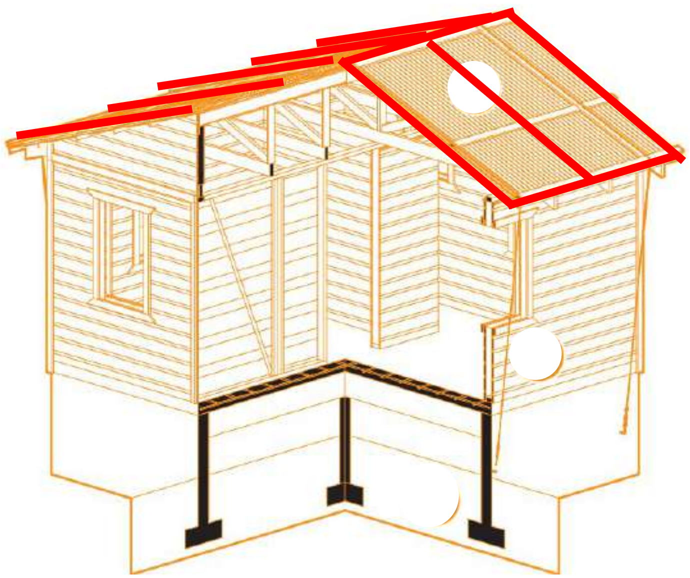

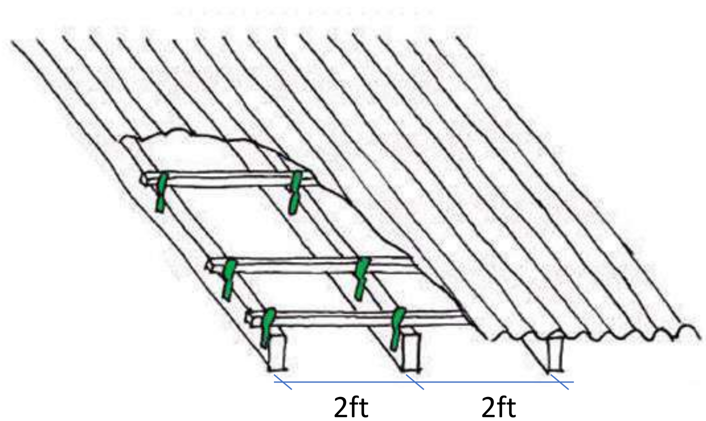

344

Refuerzo de los muros

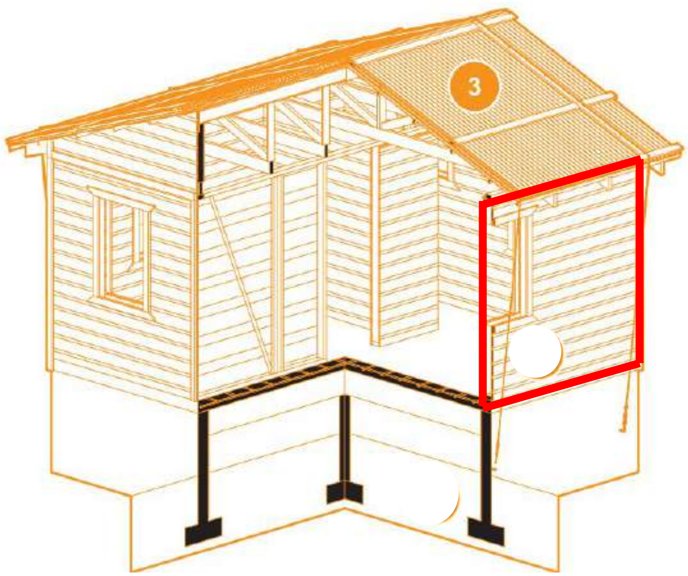

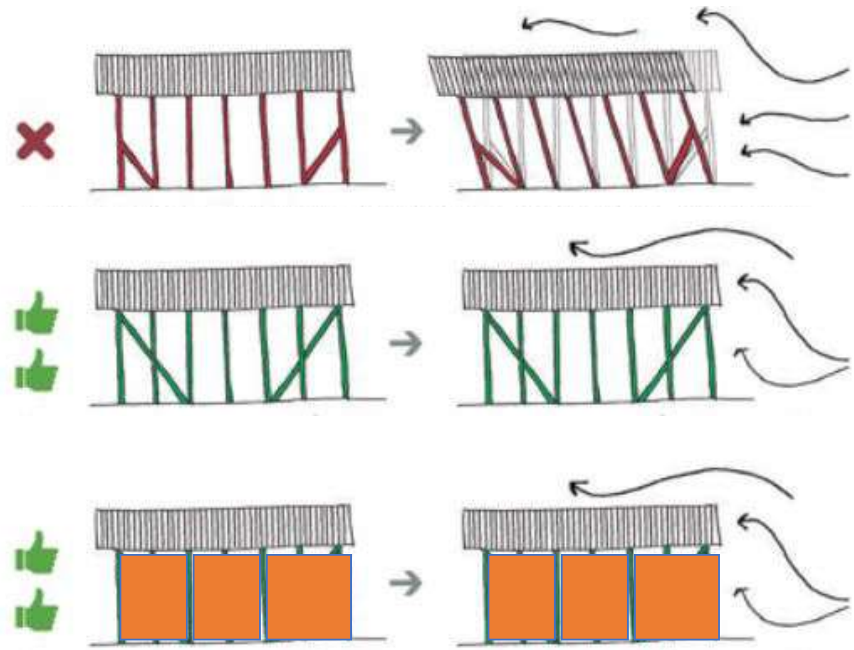

7

University of Colorado Boulder

Huracanes en Puerto Rico ¿Cómo preparar su casa de madera para el siguiente evento?

D.3. Hands-on Activity

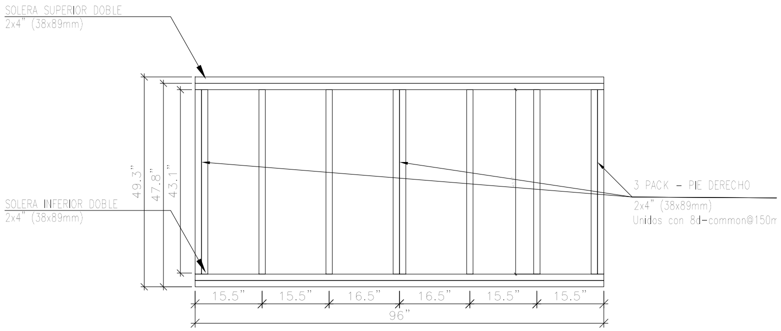

ELEVACIÓN MURO TIPO - L = 96"
DETALLE DEL ENTRAMADO - 4 UNIDADES
ESC 1:25

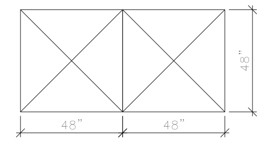

DETALLE DE DIAGRAMADO
OSB DE MURO L=96"
ESC 1:50

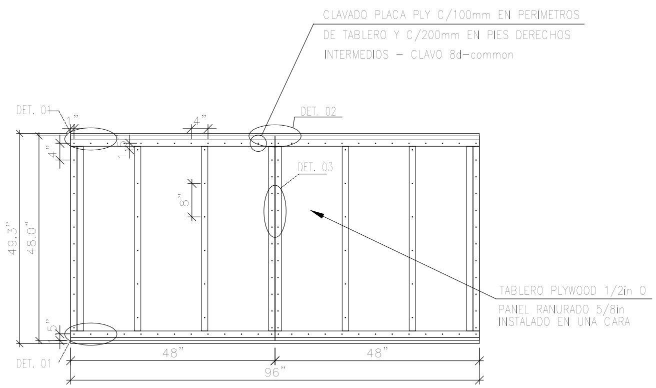

ELEVACIÓN MURO TIPO - L = 96"
DETALLE DE CLAVADO DEL TABLERO AL FRAME CON CLAVO 8d
ESC 1:25

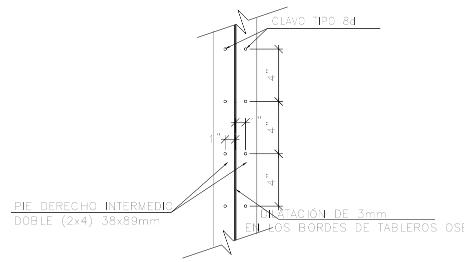

DETALLE 03
JUNTA DILATACIÓN Y DISTANCIAS AL BORDE DE CLAVOS
EN UNIÓN DOS TABLEROS VERTICALES DE OSB
ESC. 1:7.5

Modificaciones
Revisión | Fecha | Descripción

Centro UC
de Innovación
en Madera

PUERTO RICO
PROJECT

Ubicación:

Beneficiario:
CU-Boulder

Profesionales:
Diego Valdivieso

Contenido:
HANDS-ON 1/4

Especialidad:
Estructuras

Orientación:

Dibujó: D.V.C
Escala: Indicada

Lámina: E01

Versión: 02

Fecha: 06/15/2023

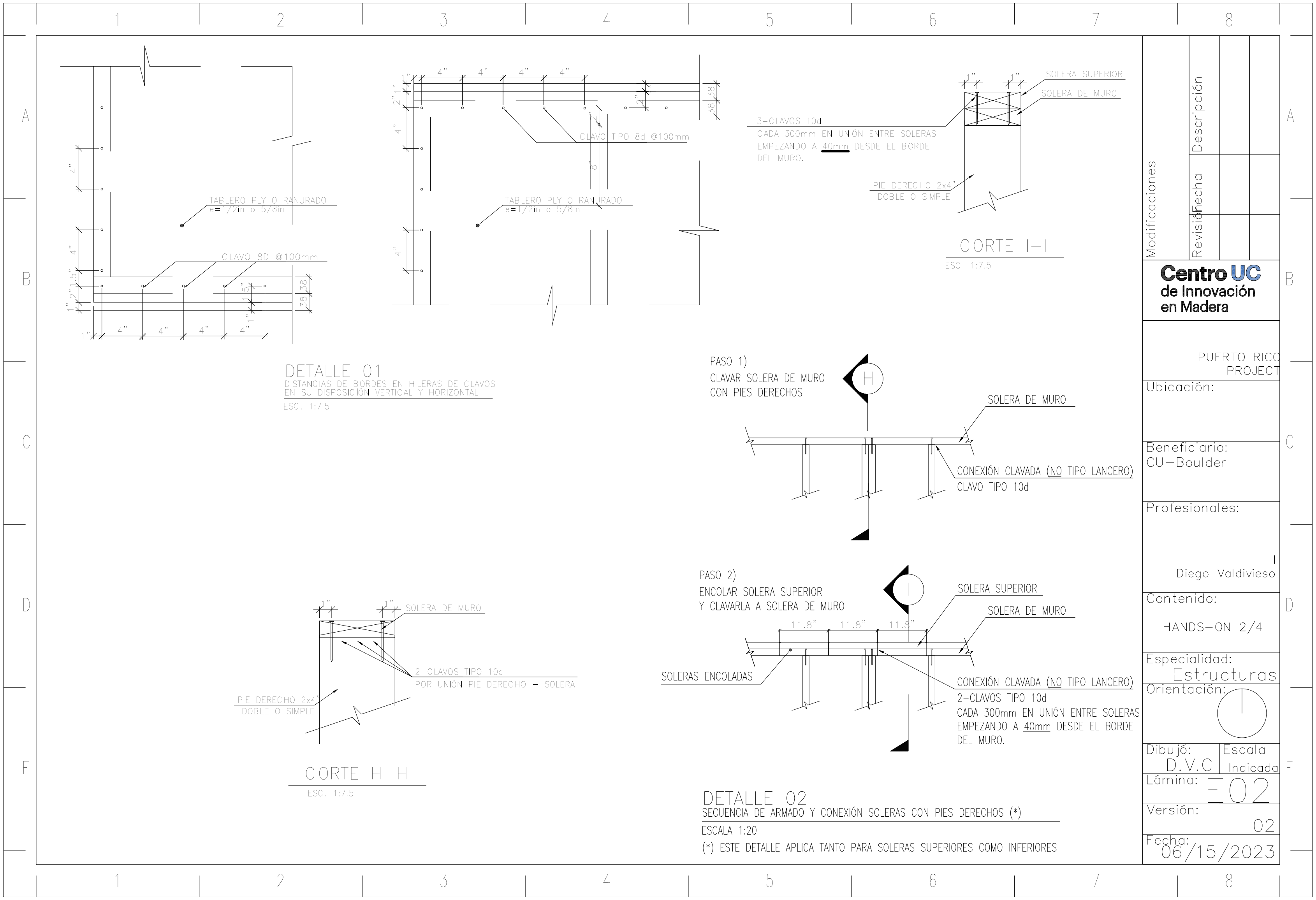
TABLERO PLY O RANURADO
e=1/2in o 5/8in
CLAVO 8D @100mm
4"
1"
38
DETALLE 01
DISTANCIAS DE BORDES EN HILERAS DE CLAVOS
EN SU DISPOSICIÓN VERTICAL Y HORIZONTAL
ESC. 1:7.5
CLAVO TIPO 8d @100mm
TABLERO PLY O RANURADO
e=1/2in o 5/8in
3-CLAVOS 10d
CADA 300mm EN UNIÓN ENTRE SOLERAS
EMPEZANDO A 40mm DESDE EL BORDE
DEL MURO.
SOLERA SUPERIOR
SOLERA DE MURO
PIE DERECHO 2x4"
DOBLE O SIMPLE
CORTE I-I
ESC. 1:7.5
PASO 1)
CLAVAR SOLERA DE MURO
CON PIES DERECHOS
H
SOLERA DE MURO
CONEXIÓN CLAVADA (NO TIPO LANCERO)
CLAVO TIPO 10d
PASO 2)
ENCOLAR SOLERA SUPERIOR
Y CLAVARLA A SOLERA DE MURO
I
SOLERA SUPERIOR
SOLERA DE MURO
11.8"
11.8"
11.8"
SOLERAS ENCOLADAS
CONEXIÓN CLAVADA (NO TIPO LANCERO)
2-CLAVOS TIPO 10d
CADA 300mm EN UNIÓN ENTRE SOLERAS
EMPEZANDO A 40mm DESDE EL BORDE
DEL MURO.
SOLERA DE MURO
2-CLAVOS TIPO 10d
POR UNIÓN PIE DERECHO - SOLERA
PIE DERECHO 2x4"
DOBLE O SIMPLE
CORTE H-H
ESC. 1:7.5
DETALLE 02
SECUENCIA DE ARMADO Y CONEXIÓN SOLERAS CON PIES DERECHOS (*)
ESCALA 1:20
(*) ESTE DETALLE APLICA TANTO PARA SOLERAS SUPERIORES COMO INFERIORES
Modificaciones
Revisión
Fecha
Descripción
Centro UC
de Innovación
en Madera
PUERTO RICO
PROJECT
Ubicación:
Beneficiario:
CU-Boulder
Profesionales:
Diego Valdivieso
Contenido:
HANDS-ON 2/4
Especialidad:
Estructuras
Orientación:
Dibujó:
D.V.C
Escala
Indicada
Lámina:
E02
Versión:
02
Fecha:
06/15/2023

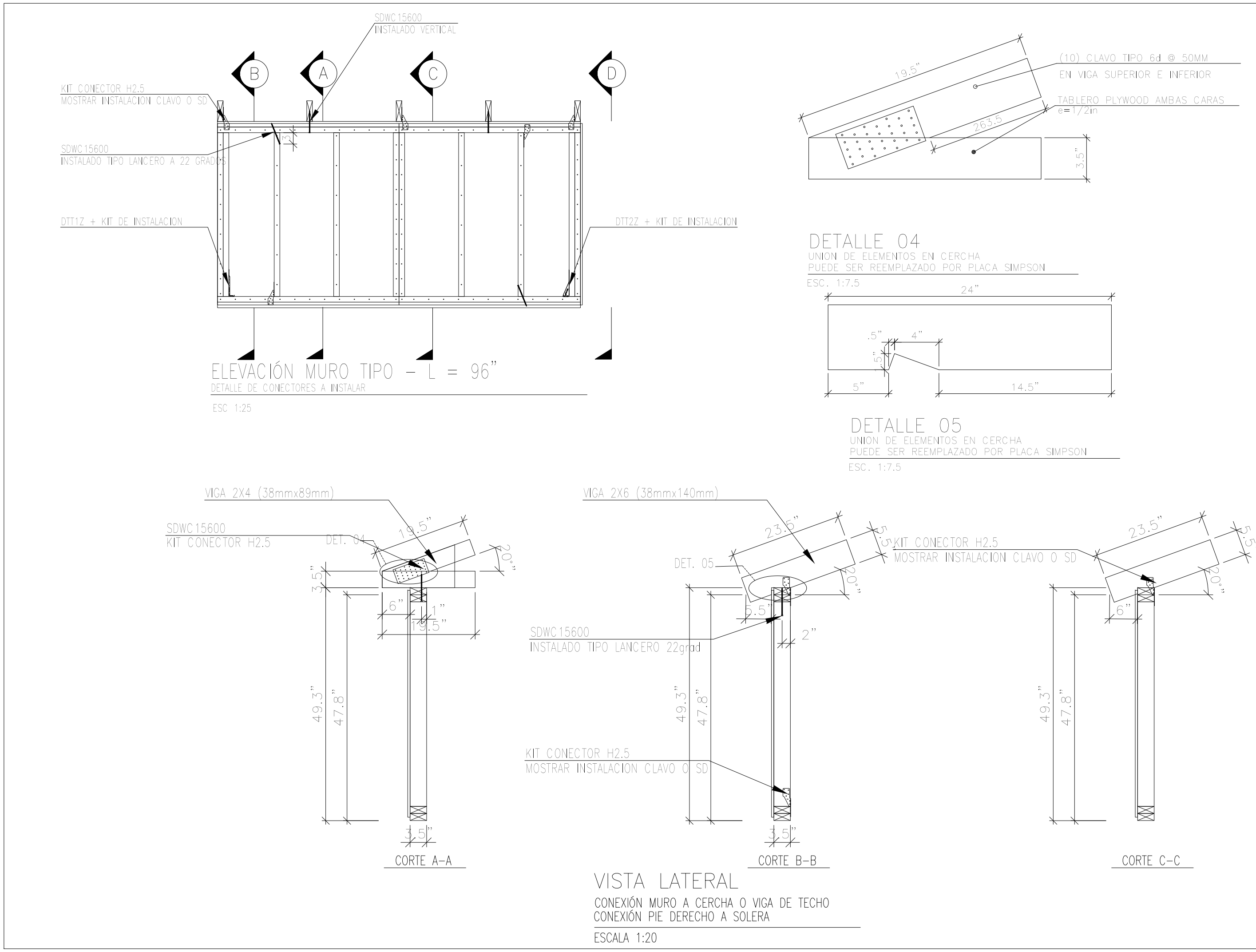

Modificaciones	Revisión	Fecha	Descripción

Centro UC de Innovación en Madera

PUERTO RICO PROJECT

Ubicación:

Beneficiario: CU-Boulder

Profesionales:

Diego Valdivieso

Contenido: HANDS-ON 3/4

Especialidad: Estructuras

Orientación:

Dibujó: D.V.C | Escala Indicada

Lámina: E03

Versión: 04

Fecha: 06/13/2023

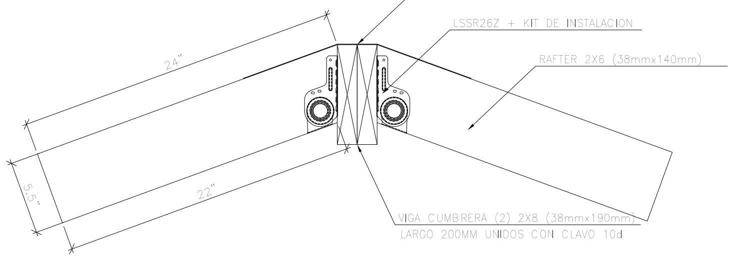

DETALLE 07
CUMBRERA DE TECHO USANDO RAFTER
SOLUCION 2
ESC. 1:7.5

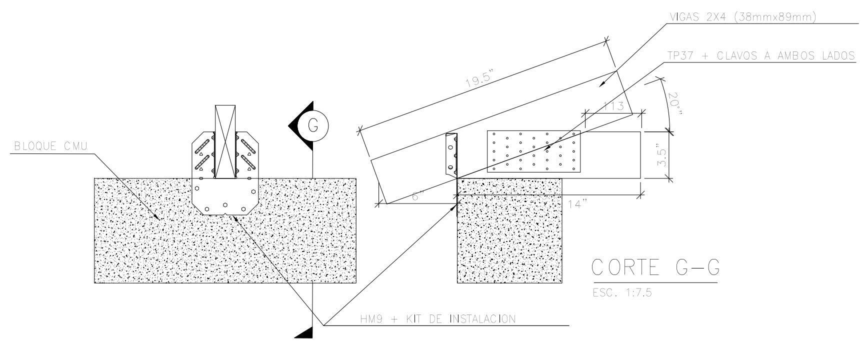

CORTE G–G
ESC. 1:7.5

DETALLE 07
CUMBRERA DE TECHO USANDO RAFTER

Modificaciones	Revisión	Fecha	Descripción

Centro UC de Innovación en Madera

PUERTO RICO PROJECT

Ubicación:

Beneficiario: CU–Boulder

Profesionales: Diego Valdivieso

Contenido: HANDS–ON 4/4

Especialidad: Estructuras

Orientación:

Dibujó: D.V.C

Escala Indicada

Lámina: E04

Versión: 04

Fecha: 06/13/2023

D.4. Pictures of the Workshop

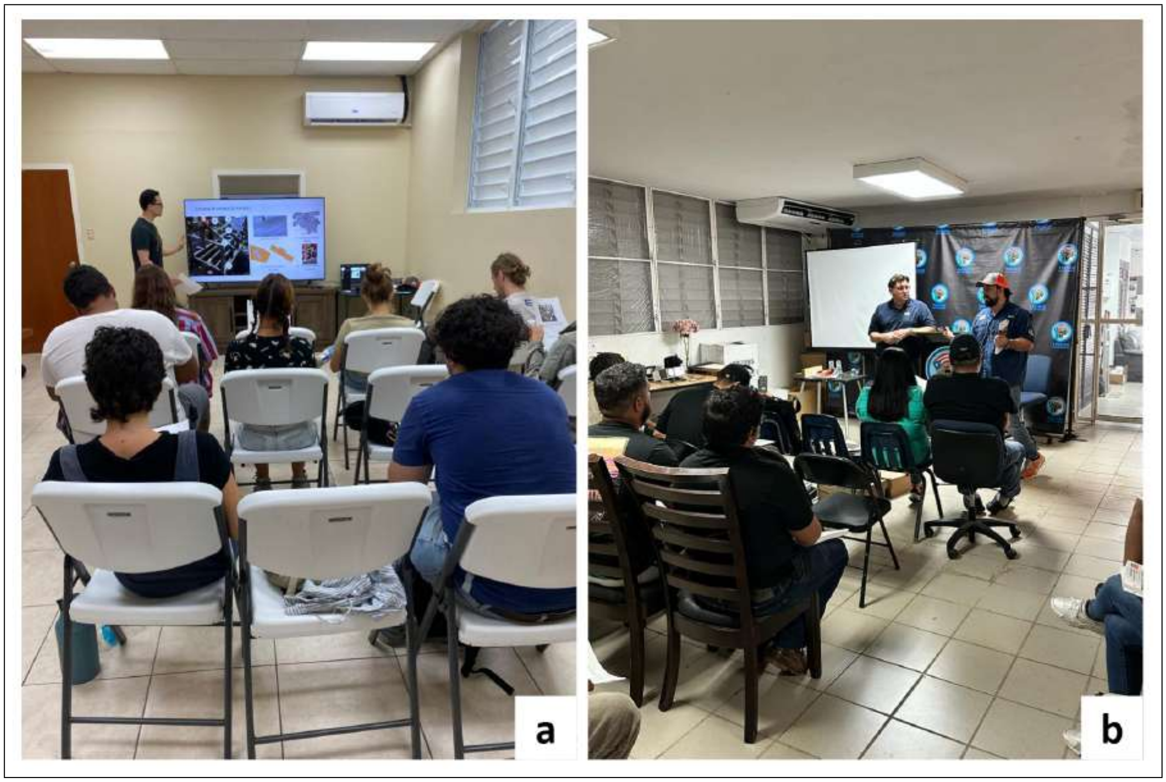

Figure D.1. Lecture delivered to two Puerto Rican local NGOs involved in post-Hurricane Maria reconstruction efforts in 2017: (a) Protechos and (b) Techos para mi Gente.

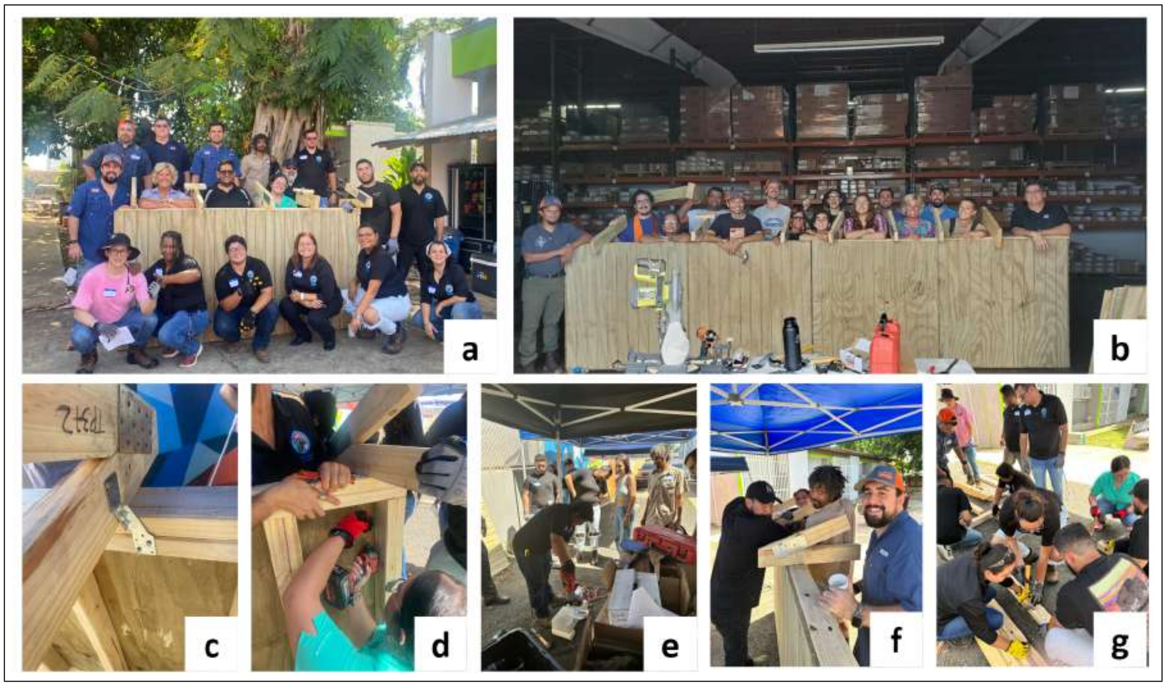

Figure D.2. Collaborative Training and Workshops with Local NGOs (a) 'Techos para mi Gente' and (b) 'Protechos' in Puerto Rico. These sessions included hands-on involvement in evaluating mitigation techniques for (a-b) shear walls, and implementing roof-to-wall connections: (c) hurricane straps, (d) fully-threaded screws, and (e) hurricane straps for timber to masonry/concrete connections. Additional activities featured (f) truss installation over shear walls with a 0.5 ft (0.15m) eave, and (g) the attachment of truss plates for upper-to-bottom chord connections in trusses.